THE DEVELOPMENT OF MODEL TECHNIQUES FOR PREDICTION OF CREEP STRAINS APPLIED TO STEAM TURBINE CASINGS

by

R. A. Bellamy

Thesis submitted to the University of Nottingham for the degree of Doctor of Philosophy, May 1973.

CONTAINS PULLOUTS

CONTENTS

	Page no.
Summary	v
Notation	vii
1 Introduction	1.1
2 Basis for Creep Work	
2.1 Survey of Literature	
2.1.1 Mechanism of creep in metals	2.1
2.1.2 Theoretical analysis of uniaxial creep	2.2
2.1.3 Theoretical analysis of multiaxial creep	2.8
2.1.4 Use and experimental test of theory	2.10
2.1.5 Variable load and temperature	2.11
2.1.6 Uniaxial calibration in creep	2.12
2.1.7 The work of P.A.T. Gill	2.15
2.1.8 Antimony and Arsenic alloys of lead	2.17
2.1.9 Chill casting and the solidification of metals	2.18
2.2 Similarity conditions for creep	
2.2.1 Similarity conditions	2.21
2.2.2 Application to engineering materials	2.23
2.2.3 Application to two particular materials	2.25
2.2.4 Comparison with Frederick	2.27
3 The Model Material	
3.1 Selection of model material	
3.1.1 Requirements of model material	3.1
3.1.2 Selection of 1.2% Sb 0.12% As lead alloy	3.2
3.2 Calibration of model material	
3.2.1 The uniaxial test rig	3.3
3.2.2 The uniaxial specimens	3.4
3.2.3 Uniaxial tests and results	3.5

	Page no.
3.2.4 Analysis of results	3.6
3.2.5 Discussion	3.10
3.2.6 Conclusions	3.15
4 The Model	
4.1 The model design	
4.1.1 Selection of model design	4.1
4.1.2 Coordinate system for model	4.1
4.2 Elastic analysis of model	
4.2.1 Production of Araldite models	4.3
4.2.2 Loading of Araldite models	4.4
4.2.3 Results	4.7
4.2.4 Discussion	4.9
4.2.5 Conclusions	4.12
5 Model Manufacture	
5.1 Production of castings	
5.1.1 Chill casting	5.1
5.1.2 The crucible	5.1
5.1.3 The mould	5.2
5.1.4 Development of casting technique	5.4
5.1.5 Casting quality	5.9
5.2 Machining of castings	5.13
6 Model Test Equipment	
6.1 Model loading equipment	
6.1.1 Design parameters	6.1
6.1.2 The sealing shaft	6.1
6.1.3 The clamping rig	6.2
6.1.4 The pressure rig	6.5
6.1.5 Performance of equipment	6.6

	Page no.
6.2 Instrumentation and recording equipment	
6.2.1 Strain gauges on lead	6.7
6.2.2 General instrumentation and recording	6.9
6.2.3 The model strains	6.10
6.2.4 Clamping load	6.12
6.2.5 Pressure measurement	6.12
6.2.6 Scan starting time and voltage check	6.13
6.2.7 Ultra Violet recorder	6.13
6.3 Test arrangement and processing of results	
6.3.1 Test arrangement	6.14
6.3.2 Test procedure	6.15
6.3.3 Processing of results	6.16
7 The Model Creep Tests	
7.1 Test parameters	
7.1.1 Pressure and bolt loading	7.1
7.1.2 Measurement positions	7.2
7.1.3 Measurement intervals and test times	7.4
7.1.4 Summary of tests	7.5
7.2 Test 2 (elastic casings)	
7.2.1 Results	7.7
7.2.2 Discussion	7.7
7.3 Model creep results (test 4 to test 9)	
7.3.1 Meridional strains in the casing	7.9
7.3.2 Hoop strains in the casing	7.10
7.3.3 Hoop strains in the flange fillet radius	7.10
7.4 Meridional strains in the casing	
7.4.1 Clamping strains	7.12
7.4.2 General features of Test 9	7.17
7.4.3 Comparison of Tests 4 to 8 with Test 9	7.20
7.4.4 Comparison of Tests 6 to 9 with predicted behaviour	7.22

		Page no.
7.5	Hoop strains in the casing	
7.5.1	General features of Tests 4 to 9	7.25
7.5.2	Comparison of Tests 8 and 9 with predicted behaviour	7.27
7.6	Hoop strains in the flange fillet radius	
7.6.1	General features of Test 9	7.29
7.6.2	Comparison of Tests 4 to 8 with Test 9	7.30
7.7	Errors	
7.7.1	Build up of errors	7.32
7.7.2	Errors in predicted elastic stresses	7.32
7.7.3	Errors in predicted creep law	7.33
7.7.4	Errors in predicted creep strains	7.37
7.7.5	Errors in measured creep strains	7.38
7.7.6	Discussion	7.39
8	Conclusions	
9	Recommendations for Further Work	
9.1	The immediate program	9.1
9.2	Future developments	9.2
Acknowledgements		ix
References		x
Appendix 1	Calculation of creep law	A.1
Appendix 2	Stress separation for pressure loaded photoelastic model	A.2
Appendix 3	Etching of lead specimens	A.4
Appendix 4	Program for processing results	A.5
Appendix 5	Bolt load calculation	A.7
Appendix 6	Calculation of stresses to produce test elastic and creep strains	A.9

THE DEVELOPMENT OF MODEL TECHNIQUES FOR PREDICTION OF CREEP STRAINS, APPLIED TO STEAM TURBINE CASINGS

by

R. A. Bellamy

SUMMARY

Because of the long service expected from steam power plant it is not practicable to obtain creep data from prototype installations to assist design against excessive creep. Model techniques, however, allow accelerated creep testing in a laboratory environment, which will produce the required creep information in a period of weeks rather than years.

Models are made of a lead alloy and subjected to the scaled mechanical service loads at room temperature. Similarity conditions, based on the usual stress-strain-time relationships, have been developed which allow the measured strain distribution to be used to predict the strains in the engineering component at any time during its useful service life. This prediction requires only the uniaxial creep characteristics of the model and component materials. At present the technique is limited to constant temperature conditions.

A lead-antimony-arsenic alloy has been selected which can be cast in the laboratory, giving good homogeneity, isotropy and fine grain structure; this material shows sufficient creep strain due to conveniently small stresses at room temperature. The steady load stress-strain-time characteristics have been determined from uniaxial tests.

The model technique has been used to study simplified steam turbine casings subjected to internal pressure. The shapes tested consisted of

axially split, flanged cylinders with domed end closures containing large bossed central bores to simulate the turbine bearings and glands. The loading of the models was due to the bolting forces and due to internal pressure. Strains on the inner and outer surfaces were measured with electric resistance strain gauges.

NOTATION

A	constant
B	constant
C	constant
D	constant
E	Young's Modulus
F(x)	function of x
G(x)	function of x
H(x)	function of x
K	constant
M	general model function
P	general Prototype function
RSIG	stress ratio
T	temperature
b	constant
c	constant
f(x)	function of x
g(x)	function of x
k	elastic stress index
n	creep stress index
p	pressure
q	pseudo-time parameter
r	radius
s	creep time index
t	time
z	axial distance
α	ratio of principal stresses $\frac{\sigma_2}{\sigma_1}$
β	constant
σ	stress
σ^*	flow stress

σ_e	Von Mises equivalent stress
ε	strain
$\dot{\varepsilon}$	strain rate
ε^*	Von Mises equivalent strain
τ	constant
ν	Poisson's ratio
$\phi(x)$	function of x
$\psi(x)$	function of x
η	non-dimensional temperature function
θ	angle
ϕ	angle

Suffices

c	creep
e	elastic
m	model
p	prototype
i	initial
r	radial
θ	hoop
z	axial
1, 2, 3	principal stress and strain directions

Additional notation for Section 2.2

ϕ	time scale ratio
η	strain scale ratio

1. INTRODUCTION

The prediction of the deformations and strains due to creep is of increasing importance due to the increases in efficiency of prime movers (e.g. turbines) associated with higher temperatures.

It is impractical to obtain results simply by direct measurement on components due to the complexity and cost of the actual components, the high operating temperatures and very long service lives required. The calculation of the stress distribution after creep has occurred is extremely complicated and has to be based on uniaxial material characteristics. The latter usually have to be inferred by extrapolation from tests carried out for times much shorter than the required service life at higher temperatures or higher stresses. The model technique is an alternative to the calculation and can therefore also be used as a very necessary check on the latter.

It was intended to satisfy the following requirements;

(i) To develop techniques to obtain model creep data which can be directly applied to predict the creep of steam turbine casings.

(ii) To provide creep data for a simplified three dimensional structure similar to a steam turbine casing. This will allow numerical and finite element techniques being currently developed for creep analysis of casings to be checked against experimental data more comprehensive than that available from turbine installations.

A previous worker, Gill (16), selected an antimony-arsenic alloy of lead in rolled sheet form as suitable for modelling steel structures. On the basis of his work, another antimony-arsenic alloy has been developed which is suitable for casting complicated three-dimensional model shapes to size.

Simplified, scaled down models of a flanged, axially split steam turbine casing were manufactured in this alloy and creep tested under internal pressure at room temperature for periods of up to four weeks. Model correlations were established to enable model creep results to be applied directly to a prototype.

The emphasis of the work reported here was on the development of the techniques and in understanding the problems and limitations involved. The techniques have been established, and on the basis of the experience gained a further series of tests is being carried out.

A parallel finite element analysis for comparison was carried out by Parkes (42), who is extending his work to cover the further tests.

CHAPTER 2

GENERAL THEORETICAL BACKGROUND

2.1 Survey of Literature

2.1.1 Mechanisms of creep in metals

The process of creep deformations in metals is similar to that of plastic deformations. Faults and dislocations in the crystal lattice move under the influence of stress, where there is sufficient energy to dislodge the atoms in the weakend lattice. The large stresses which cause instantaneous plastic deformation provide sufficient energy to move the lattice bodily along its slip planes, but small stresses are inadequate to do this. However, as pointed out by Finnie and Heller (1), a small stress over a large area can build up sufficient energy to move a dislocation through one atom spacing at a time, thus indicating a slow, time dependent drift of vacancies and dislocations through the lattice. Also, if the accumulated energy is large enough, dislocation concentrations can climb out of their original slip planes and spread across the lattice, circumventing obstructions (impurities and barriers) and causing the whole crystal to deform.

Dorn has shown that the activation energy for creep, that is the energy required to move a dislocation across one atom spacing, is very close to that for diffusion in metals. As implied by the need for energy, these processes are more prominent at high temperature; an estimate by Finnie and Heller (1) of the temperature required to produce measurable creep strains at engineering stresses shows that creep becomes significant at about $\frac{1}{2}$ Tm, where Tm is the absolute melting temperature.

It has been demonstrated by Strutt and co-workers and by Maclean (2) that there is also some sliding of grains along grain boundaries during

creep. However, neighbouring grains eventually obstruct translation, and this causes rotation of the slip planes and hence fragmentation of the lattice. The result according to Hoffman (3) is that grain boundary sliding makes up a smaller proportion of the total creep deformation than does slip within the crystal.

The rate of creep strain is therefore initially regulated by the ease of movement of dislocations, the straining itself introducing barriers. As these barriers build up, the strain rate is then governed also by the rate at which thermal recovery overcomes them. Thus secondary, or steady state, creep is seen as a balance between strain hardening and thermal recovery, a description given by Hoffman (3) and Rotherham (4).

2.1.2 Theoretical analysis of uniaxial creep

Finnie and Heller (1), Warren (5) and Hult (6) observe that attempts to derive a macroscopic analysis of creep behaviour from observations of the microscopic processes in creep have not been successful. The most commonly used expressions for representing creep behaviour are therefore derived from curve fitting to uniaxial creep tests, with refinements if required to allow for temperature and load changes, relaxation and recovery.

Surveys of uniaxial creep theories have been presented by Warren and Hult. Hult (6) begins with a general statement that creep strain (ε_c) is a function of stress (σ), temperature (T) and time (t)

i.e. $$\varepsilon_c = F(\sigma, T, t) \qquad (2.1)$$

differentiating, $$\dot{\varepsilon}_c = \frac{d}{dt} F(\sigma, T, t) = G(\sigma, T, t) \qquad (2.2)$$

Since the form of equation (2.1) gives the total creep strain, it assumes that stress and temperature are constant. The incremental strain theory of the form of equation (2.2) is therefore more useful, since it allows for varying stress and temperature.

Eliminating the time variable from (2.1) and (2.2),

$$\dot{\varepsilon}_c = H(\sigma, T, \varepsilon_c) \qquad (2.3)$$

Although for constant stress and temperature equations (2.2) and (2.3) are identical, different creep rates are predicted by each when stress and temperature vary. Equation (2.1) assumes that the state of the material in creep depends on the elapsed time, and is known as the time hardening law. Equation (2.3) assumes that the state of the material in creep depends on the accumulated creep strain, and is known as the strain hardening law.

Rabotnov (7) has pointed out that the idea of time hardening is fundamentally contradicting and inaccurate, since the state of the material should be considered independent of any time origin. Furthermore, Dorn (8) has shown from X-ray evidence that similar creep strains show a similar metallurgical structure, supporting the more acceptable concept of strain hardening, in that the strain rate should depend on the degree of plastic deformation in the structure. Experimental evidence reported by Finnie and Heller (1), Hult (6), Goldhoff (9), Taira and co-workers (10), King and Mackie (11) and Marin and Ohji (12) on the whole supports the strain hardening hypothesis.

Warren (5) replaces the accumulated creep strain in equation (2.3) and the time in equation (2.2) by a more general parameter 'q', to describe the state of the material in creep.

i.e. $$\dot{\varepsilon}_c = H(\sigma, T, q) \qquad (2.4)$$

The time hardening and strain hardening hypotheses are then represented by $q \equiv t$ and $q \equiv \varepsilon_c$ respectively. Warren discusses also the life fraction hypothesis, in which the parameter 'q' is governed by the fraction of material 'life' so far expended. This life can be arbitrarily chosen to be some limiting creep strain ε_c', or alternatively the time to rupture. If tf_1 is

the time taken to reach the limiting creep strain at a stress level of σ_1, the fraction of life used after time t_1 is given by

$$q = \frac{t_1}{tf_1}$$

So under varying conditions, $q = \frac{t_1}{tf_1} + \frac{t_2}{tf_2} + \frac{t_3}{tf_3} + \ldots$ (= 1 at failure)

The objection to this hypothesis is that it depends on the value ε'_c chosen, but since each life fraction is a strain fraction (in spite of the apparent time relation), the results obtained using this hypothesis are shown by Goldhoff (9) and Clarke (13) to be close to those derived from the strain hardening law.

Although the time hardening hypothesis has been discredited on the grounds of accuracy, the analytical expressions based on time hardening are the most simple. Marriott and Leckie (14) have shown, however, that in structures where redistribution takes place, strain and time hardening predictions are very close, because of structural constraints. The use of the time hardening law is therefore common both for developing the equation of state and for subsequent numerical analysis.

The equation of state

Warren begins with a general phenomenological expression suggested by Graham,

$$\varepsilon_c = \sum_i C_i \, \sigma^{\beta i} \, \phi^{Ki} \qquad (2.5)$$

where Ci, βi, Ki are constants. ϕ is the time-temperature parameter or 'pseudo time', given by $\phi_i = \eta_i t$

where $\eta_i = f(T)$, a non-dimensional function of temperature.

Dorn suggested a temperature function $\eta \propto e^{-KT}$ common to all terms of equation (2.5), but the supposed constant 'K' is dependent on both stress and creep strain. The Larson Miller parameter accounts for this, but makes

the subsequent analysis too complicated. Warren adopted the parameter due to Graham,

$$\eta_i \propto (T_i - T)^{20} \qquad (2.6)$$

where T_i in each term is an experimentally determined constant. Equation (2.5) then becomes,

$$\varepsilon_c = \sum_i C_i \sigma^{\beta i} \eta_i^{Ki} t^{Ki} \qquad (2.7)$$

differentiating

$$\dot{\varepsilon}_c = \sum_i C_i K_i \sigma^{\beta i} \eta_i^{Ki} t^{(Ki - 1)} \qquad (2.8)$$

Warren points out that for certain ranges of stress, temperature and time, a few of the terms of equation (2.8) are likely to dominate, and to simplify the analysis the temperature function η can be made common to all terms.

i.e. $$\dot{\varepsilon}_c = \eta \sum_i C_i K_i \sigma^{\beta i} (\eta t)^{(Ki - 1)}$$

hence $$\dot{\varepsilon}_c \eta^{-1} = \sum_i C_i K_i \sigma^{\beta i} \phi^{(Ki - 1)} \qquad (2.9)$$

Further simplification is achieved by separating the functions of stress and time, and reducing equation (2.5) to a Nutting expression,

$$\varepsilon_c = C \sigma^{\beta} \phi^{K} \qquad (2.10)$$

Equation (2.9) then becomes,

$$\dot{\varepsilon}_c \eta^{-1} = C \sigma^{\beta} K \phi^{(K - 1)} \qquad (2.11) \text{ for time hardening}$$

and $$\dot{\varepsilon}_c \eta^{-1} = K C^{\frac{1}{K}} \sigma^{\frac{\beta}{K}} \varepsilon_c^{\frac{K-1}{K}} \qquad (2.12) \text{ for strain hardening,}$$

Substituting for $\phi^{K - 1}$ from equation (2.10).

Rearranging equation (2.12) in terms of stress,

$$\sigma = \left[\frac{1}{K} C^{\frac{-1}{K}}\right]^{\frac{K}{\beta}} \left[\dot{\varepsilon}_c \eta^{-1}\right]^{\frac{K}{\beta}} \left[\varepsilon_c\right]^{\left(\frac{1-K}{\beta}\right)} \qquad (2.13)$$

Here, $\frac{(1-K)}{\beta}$ represents the strain hardening rate. When $\frac{1-K}{\beta} = 0$ (i.e. K = 1) there is no hardening with accumulating strain, and this corresponds to steady state or secondary creep. A measure of the response of strain rate $\dot{\varepsilon}_c$ to a change in the stress σ is given by $\frac{K}{\beta}$, the rate sensitivity.

As $\frac{K}{\beta}$ approaches zero, equation 2.13 reduces to

$$\varepsilon_c = D\,\sigma^{\beta} \qquad \text{where } D = \left[\frac{1}{K} C^{\frac{1}{K}}\right]^{\frac{K}{\beta}}$$

This is the expression for 'instantaneous' plasticity, and was adopted by Lubahn and Felgar (15), who introduce the idea of a flow stress σ^* to describe the strength or condition of the material at a particular stage during creep. The flow stress σ^*, at a particular stage, is defined as that stress which, when applied to the material (at that stage) at some standard temperature, will produce a certain arbitrarily chosen standard creep rate. For convenience, these choices are such that

$$\dot{\varepsilon}_c \eta^{-1} = 1 \qquad \text{for } \sigma = \sigma^*$$

then $$\sigma^* = D\,\varepsilon_c^{\frac{1-K}{\beta}}$$

and from equation (2.12)

$$\dot{\varepsilon}_c \eta^{-1} = \left(\frac{\sigma}{\sigma^*}\right)^{\frac{\beta}{K}} \qquad (2.14)$$

This corresponds exactly with the Bailey, Norton creep law (1929) defined as

$$\dot{\varepsilon}_c = \frac{1}{\tau}\left[\frac{\sigma}{\sigma_n(T)}\right]^{n(T)} \qquad (2.15)$$

The form of equation (2.10) adopted by Gill (16) to represent the creep behaviour of rolled 0.2% Sb 0.02% As lead alloy was

$$\varepsilon_c = A\,\sigma^n\,(t^s + bt) \qquad (2.16)$$

The first term in the time factor represents the primary (hardening) stage of creep, and the second represents the secondary (steady state) stage. A, n, s and b are constants, so equation (2.16) is for constant temperature only.

Stationary creep

Stationary creep is defined as creep during which the strain distribution remains constant.

If $$\varepsilon_c = \phi(\sigma, T)\,\psi(t) \qquad (2.17)$$

then at two points in a structure

$$\varepsilon_{c1} = \phi(\sigma_1, T_1)\,\psi(t)$$

and $$\varepsilon_{c2} = \phi(\sigma_2, T_2)\,\psi(t)$$

For large values of time t, where $\varepsilon_c \gg \varepsilon_{elastic}$, the creep strain will approximately equal the total strain.

i.e. $$\frac{\varepsilon_1}{\varepsilon_2} \simeq \frac{\varepsilon_{c1}}{\varepsilon_{c2}} = \frac{\phi(\sigma_1, T_1)\psi(t)}{\phi(\sigma_2, T_2)\psi(t)} = \frac{\phi(\sigma_1, T_1)}{\phi(\sigma_2, T_2)}$$ i.e. independent of time.

This ratio is therefore constant with time, and of the same form as the elastic strain ratio would be if the material followed the elastic law

$$\varepsilon = C\,\phi(\sigma, T) \qquad \text{where } C = \text{constant.}$$

The stationary creep strain distribution can be obtained, therefore, by an elastic analysis, replacing

$$\varepsilon \propto \sigma \qquad \text{by} \qquad \varepsilon \propto \phi(\sigma, T)$$

An elastic material which follows the creep law given by equation (2.16) will have an elastic strain distribution $\frac{\varepsilon_1}{\varepsilon_2} = \frac{\sigma_1}{\sigma_2}$ and a stationary creep distribution $\frac{\varepsilon_1}{\varepsilon_2} = \left(\frac{\sigma_1}{\sigma_2}\right)^n$ (2.18)

This elastic analogy was rigorously established by Hoff (1954), and Hult (1962) showed that a material undergoing creep according to the power law (equ. (2.5) and equ. (2.16)) will always approach a state of stationary creep.

2.1.3 Theoretical analysis of multiaxial creep

To apply principles developed for uniaxial creep analysis to creep in a multiaxial stress field, the following assumptions are made;

(i) The principal strains ε_1 ε_2 ε_3 coincide with the principal stresses σ_1 σ_2 σ_3 at any point.

(ii) Since creep is seen as a flow of metal, there is no volume change. i.e. $\varepsilon_{1c} + \varepsilon_{2c} + \varepsilon_{3c} = 0$. It follows that Poisson's Ratio in creep, $\nu = 0.5$, and a hydrostatic stress has no effect on the creep behaviour of the material.

(iii) The shear strain rate is proportional to the shear stress

hence $\frac{\dot{\varepsilon}_{1c} - \dot{\varepsilon}_{2c}}{\sigma_1 - \sigma_2} = \frac{\dot{\varepsilon}_{2c} - \dot{\varepsilon}_{3c}}{\sigma_2 - \sigma_3} = \frac{\dot{\varepsilon}_{3c} - \dot{\varepsilon}_{1c}}{\sigma_3 - \sigma_1} = \text{Constant}$ (2.19)

This is St. Venant's principle that there should be zero slide velocity on a plane of zero shear stress, and results in the Mohr's circle of shear strain rates being similar to that of the stresses.

Thus, for an isotropic material,

$$\dot{\varepsilon}_{1c} = \tfrac{3}{2}C\left[\sigma_1 - \tfrac{1}{2}(\sigma_2 + \sigma_3)\right]$$

$$\dot{\varepsilon}_{2c} = \tfrac{3}{2}C\left[\sigma_2 - \tfrac{1}{2}(\sigma_3 + \sigma_1)\right]$$

$$\dot{\varepsilon}_{3c} = \tfrac{3}{2}C\left[\sigma_3 - \tfrac{1}{2}(\sigma_1 + \sigma_2)\right]$$

This replaces Hooke's Law (2.20)

(iv) In order to apply a uniaxial creep law, the multiaxial stress field must be reduced to an "effective" uniaxial stress σ_e, producing an "effective" creep strain rate $\dot{\varepsilon}_c^*$, which can then be expanded back to the multiaxial strain field. The most commonly used criteria for relating effective stress to the multiaxial stress field and effective strain to the multiaxial strain field are those due to Huber, Von Mises and Hencky.

$$\sigma_e = \frac{1}{\sqrt{2}} \left[(\sigma_1 - \sigma_2)^2 + (\sigma_2 - \sigma_3)^2 + (\sigma_3 - \sigma_1)^2 \right]^{\frac{1}{2}} \qquad (2.21)$$

and $$\dot{\varepsilon}_c^* = \frac{\sqrt{2}}{3} \left[(\dot{\varepsilon}_{1c} - \dot{\varepsilon}_{2c})^2 + (\dot{\varepsilon}_{2c} - \dot{\varepsilon}_{3c})^2 + (\dot{\varepsilon}_{3c} - \dot{\varepsilon}_{1c})^2 \right]^{\frac{1}{2}} \qquad (2.22)$$

(v) The effective stress σ_e and the effective creep strain rate $\dot{\varepsilon}_c^*$ are related by the creep law $\dot{\varepsilon}_c^* = f(\sigma_e, T, t)$ for time hardening

or $\dot{\varepsilon}_c^* = f'(\sigma_e, T, \varepsilon_c^*)$ for strain hardening

and for the case of uniaxial creep, these laws reduce to

$\dot{\varepsilon}_c = f(\sigma, T, t)$ for time hardening

$\dot{\varepsilon}_c = f'(\sigma, T, \varepsilon_c)$ for strain hardening.

Finnie and Heller (1) and Hult (6) point out that a result of the assumption that hydrostatic stress has no effect on the creep behaviour is that any three-dimensional stress field can be reduced to a two-dimensional stress field, by adding a hydrostatic stress equal and opposite to one of the three stresses, say σ_3. Then if $\sigma_2 = \alpha \sigma_1 \quad (\sigma_1 > \sigma_2)$

Von Mises equivalent stress becomes $\sigma_e = \sigma_1 \sqrt{1 - \alpha + \alpha^2}$ (2.23)

2.1.4 Use and experimental confirmation of theory

A number of numerical analyses of multiaxial creep have been carried out, based on the Huber-Von Mises-Hencky criteria for relating to uniaxial creep laws. In many cases, experimental evidence is used to check the results.

Taira (10) and Co-workers creep tested tubular specimens of 0.19% carbon steel under internal pressure at 450°C, and calibrated the material uniaxially in creep at the same temperature. By measuring the residual stresses in the deformed cylinders after test, they also obtained the actual stress distribution under creep conditions. Comparison with multiaxial theory showed that the Von Mises criteria gives a good approximation when used with a strain hardening creep law, and the other assumptions given in Section 2.1.3 are confirmed.

Marriott and Leckie (14) propose an analysis of a cylinder undergoing creep, based on the observation that at a "skeletal point" near the mean radius in the cylinder wall, the Von Mises equivalent stress stays virtually constant. Ohnami (17) and co-workers established the validity of this analysis by comparing the results with experiments on a cylindrical tube of SK15C 0.15% Carbon Steel.

Another series of experiments were carried out by Taira and co-workers (18) to test the assumptions of multiaxial creep theory. Thick walled, capped tubes of 0.14% carbon steel were loaded at 500°C under internal pressure, pure tension and a combination of pressure and tension in six different ratios - all to give the same equivalent uniaxial stress according to the Von-Mises criterion. When the change in effective stress due to creep deformations was taken into account, the experimental creep strains agreed closely with those predicted by the Von-Mises analysis.

King and Mackie (11) in a theoretical and experimental study of the creep of thick cylinders, concluded that the time hardening law is inadequate.

Marin and Ohji (12) confirm, with experimental evidence, that the strain hardening law gives good agreement between theory and experiment, but only for small strains with structurally unstable materials such as 12% Cr steel. Johnson (19) confirms the validity of the Von-Mises approach to complex stress systems with experimental torsion and tension tests, and further supports the Von Mises criteria in a review of creep work, both theoretical and experimental, from 1940 to 1960. (20). The application of Von Mises to lead in multiaxial creep was shown to be valid by Hoffmann and Malotki (21) from experiments on lead pipes subjected to internal pressure.

Mackenzie (22), Fairburn and Mackie (23), Smith (24), Ohnami and Motoie (25) and Muakami and Iwatsuki (26) all use the Von Mises criteria in numerical analyses of multiaxial creep in cylinders and shells, but provide no experimental evidence. Muakami and Iwatsuki conclude that where redistribution takes place, differences in strain and deformation predictions by strain hardening and time hardening theories are less than 5% - a similar conclusion to that of Marriott and Leckie (14).

2.1.5 Varying load and temperature

The effects of intermittent and regular variations in load and temperature are discussed by Warren (5) in his survey. The time and strain hardening laws predict no effect from intermittent variations, but thermal stresses resulting from material inhomogeneity and metallurgical changes during the rest period lead to reports of as much as 40% increase in creep in some materials, while other materials remain unaffected.

The evidence involving more regular changes is also inconsistent. However, agreement with the strain hardening law was reported to be good in those tests on alloy materials in which the test time and variations in load and temperature were small. Tests with extended time periods or large stress ranges are made less predictable because of thermal recovery, leading

to creep strains up to 50% greater than predicted. This effect was most marked in tests on materials of an unstable metallurgical structure; and the experiments on pure lead by Morrow and Halford are mentioned, in which a ten-fold increase in creep strain rate was developed after 100 reversals of stress.

The antimony-arsenic alloy of lead developed for the model tests (see Chapters 3 and 5) has been shown to be metallurgically stable (Section 2.1.8). Furthermore, stress changes are limited to redistribution effects and the tests take place at constant temperature. The material is therefore expected to be predictable under the test conditions.

2.1.6 Uniaxial calibration in creep

Specimen alignment

With a creep stress index between 3 and 7 in most engineering materials, a small amount of bending in a supposedly uniaxial, uniformly stressed specimen can lead to significant variation of creep rate on opposite sides of the specimen. Finnie and Heller (1) attribute much of the scatter in creep data to misalignment in uniaxial tests, since bending stresses of 10% or more are common with conventional creep testing machines.

Penny and co-workers (27), describing a button head uniaxial creep test machine of their own design, emphasise the difficulty of achieving true uniaxiality by comparing the bending of less than 5% in their own machine with bending of more than 10% in commercial machines. Where the specimen thickness is less than $\frac{1}{2}$ inch, to achieve much less than 5% bending would require impossible machining tolerances in both machine and specimen.

Dutton (28) points out that while tension creep tests will automatically reduce bending as the specimen strains, slight misalignment in compression creep tests will become worse as the test proceeds.

Penny and Leckie (29) have investigated the effect of bending in supposed uniaxial creep calibration tests on the average strain reading,

which would be used in formulating the uniaxial creep law for the material. Solving numerically equations developed for a time hardening material, the ratio of total strain to elastic strain in a test specimen of circular cross-section was obtained at various times for different ratios of loading eccentricity (δ) to specimen diameter (d). Where the material has a stress index of 5 (see Chapter 3) the total average strain of a specimen for which $\delta/d = 0.08$ soon becomes more than 70% greater than that of a truly uniaxial specimen for which $\delta/d = 0$. This difference in average strain values increases with time, and from the results presented, the difference appears to vary exponentially with δ/d.

It was pointed out that the values of δ/d used are not uncommon in commercial test machines, and the computer variations would easily account for the large scatter usually obtained from creep tests.

Stress dependence of creep

There is some controversy over the behaviour of the creep stress index 'n' in equation (2.16). Uniaxial theory assumes the creep stress index to be constant, independent of stress or strain levels and of time.

Gifkins (30) points out that there is an increasing body of evidence to suggest that at least two stress regimes commonly occur, with n = 1 at low stresses, and n = 5, 6 or 7 at higher stresses. A number of theories, such as Weertman's, predict n = 5, and the results of many workers support this. Gifkins proposes a possible explanation for these regimes and for non-integral values of n that arise from a combination of regimes. Grain boundary sliding and crystal slip are two mechanisms of creep, and each is dominant at a different stress. The transition between regimes produces apparently non-integral values of n.

Gifkins and Snowden (31) in an earlier work had shown that for bicrystals of pure lead at 50°C, n = 1 for stresses less than 250 lbf/in^2,

suggesting that grain boundary sliding predominates. However, above a certain "creep yield point" the value of n rises to 5 or more.

Woodford (32), however, holds a different view. He examined constant load creep results of a Cr-Mo steel at 950°, 1050° and 1100°F, from which previous authors have predicted a low stress regime where n = 1, and makes two criticisms. Firstly, the very low creep rates were interpreted graphically, when only a computer could give reasonable accuracy. Secondly, minimum creep rates should be measured only when the minimum region has been passed. There is no other way of identifying a minimum. When the stresses are very low and the creep rate is very small anyway, it is easy to mistake a decreasing creep rate for a constant one.

He cites as an example the above steel at 1050°F tested at 1400 lbf/in^2. The true minimum creep rate of 2.71×10^{-5}%/hour is obtained after 18,300 hours (2 years +). If the test had been stopped after 5000 hours, the linear creep rate would have appeared to be 4.6×10^{-5}%/hour, leading to an apparent 'n' value of near unity. Further examination of results show that minimum creep rates occur at similar strains for particular materials, which emphasises that creep tests should be given a strain limit rather than a time limit.

More, Betty and Dollins (33) also referred to by Woodford, creep tested lead sheathing materials. They suspected that apparent curvature in their log-creep-rate versus log-stress graphs might be due to a failure to reach the minimum creep rate at low stresses in the test time of 2000 hours. Further tests between 7200 and 9000 hours showed that the minimum creep rates were indeed lower, and apparent n values were higher.

Careker (34) found that the 'n' value for constant stress creep of platinum was identical over a wide temperature range when log-strain-rate was plotted against log-stress at each of four different strains during primary creep. This suggests that the material is strain hardening rather than time

hardening, and that the 'n' value of other strain hardening materials should be determined in the same way. There is evidence that lead behaves in the same way (Finnie and Heller).

Analysis of scatter

A detailed analysis of the scatter of creep data was made by Walles and Graham (35). Based on the general form of the creep law due to Graham in equation (2.5), with the temperature parameter given by equation (2.6), creep and creep-rupture data for a range of steel and aluminium alloys were analysed statistically.

In the analysis, deviations from the 'family' curve were measured in terms of temperature, $\Delta T = T' - T$ from equation (2.6). This parameter was chosen because little difference occurs between relative and absolute deviations (the range of values being very small). However, the value of T' must be determined experimentally, and where it is not available, the next most convenient parameter is Log(stress), provided the deviations are not large. Some results analysed in terms of ΔT revealed multi-model distributions, for which the standard deviation of the scatter is markedly different from that determined from the uninodal distribution obtained from traditional analyses.

2.1.7 The work of Gill (16)

Gill surveyed the available creep data of a number of pressure vessel steels, including cast AA, and then tested a number of tin and lead alloys to find one suitable as a model material for accelerated creep testing at room temperature.

The acceptance criteria adopted were based on correlations due to Frederick (43 and Section 2.2.4), with additional conditions that there should be at least 10 grains across the minimum model dimension; that the creep stress index 'n' should be between 3.5 and 6.0 to be representative of the steels he surveyed; that there should be no age hardening effects; and

that compressive and tensile creep behaviour should be similar.

Tin alloys showed age hardening effects and were rejected. On the basis of published work regarding grain refining and stabilising of lead alloys for extended cable sheathing, lead antimony alloys were tried in both cast and worked form. Cast specimens had coarse grain structure and showed considerably non-uniform straining, and the alloy finally adopted was 0.2% Sb 0.02% As lead alloy in its worked form. This material showed no age hardening effects, strained uniformly and showed similar tensile and compressive behaviour.

The extreme softness of the materials tested presented problems of uniaxial loading and strain measurement. Conventional extensometers such as the Huggenberger extensometers gave trouble due to 'digging in' of the knife edges, and observation of marks on the specimen with a travelling microscope proved both too insensitive to moderate strains and inconvenient for instantaneous strain measurement at the beginning of a test. Strain gauges were rejected from fears of instability during a week of testing.

These difficulties were overcome by loading dumbell specimens between grips and determining the strains from dial gauge measurements of their relative displacements (see Section 3.2). Tests showed that if the parallel section was longer than 1 inch end effects were negligible; and the much larger cross-section area of the dumbell ends, combined with the loading through the faces of the grips rather than through the pins, meant that significant creep strains occurred only in the parallel section.

Uniaxial creep properties were represented by seperable stress and time functions, $\varepsilon_c = F(\sigma)\, G(t)$ (2.24)

Suitable stress functions were either $F(\sigma) = B\sigma^n$ (2.25)

where $B = 3.02 \times 10^{-19}$ lb in h units

and $n = 5.46$

or $F(\sigma) = D \sinh \frac{\sigma}{\sigma_0}$ (2.26)

where $D = 1.335 \times 10^{-5}$ lb in h units

and $\sigma_o = 143$ lbf/in^2

Function (2.26) was found to be a better fit for $\sigma > 1000$ lbf/in^2, and function (2.25) better for $\sigma < 1000$ lbf/in^2.

Suitable time functions were

$$G(t) = t^m \qquad (2.27)$$

where $m = 0.54$

or

$$G(t) = t^s + bt \qquad (2.28)$$

where $s = 0.39$

and $b = 0.106$

Function (2.28) gave a better fit to the data, but function (2.27) is in a form more suited to Frederick's correlations.

Young's modulus was found to be 3.05×10^6 lbf/in^2, and Poisson's ratio 0.43.

2.1.8 Antimony and Arsenic alloys of lead

Rapid recrystallisation and grain growth in pure lead means that small grain size is difficult to achieve and maintain. During creep at room temperature recrystallisation occurs, changing the creep properties according to the rate of plastic deformation.

Greenwood and Warner (36) observed that where recrystallisation took place in pure lead, the original creep properties were restored. However, small additions of alloying elements (Antimony included) dramatically reduced the rate of recrystallisation; and with more than 0.1% Antimony, no recrystallisation was found.

Lead-Antimony is known as hard lead, and is used for pipe, sheet and cable sheathing, where strength is required. Hoffman (3) states that its hardness is due to the decomposition of supersaturated solid solution, resulting in the precipitation of antimony. The lead antimony equilibrium

diagram (Fig. 2.1) shows that although lead can hold up to 3.45% Sb in solid solution at 250°C, most must precipitate out when the alloy is cooled to room temperature. Maximum hardness occurs at 3% Sb.

However, this precipitation of antimony is extremely slow, producing an age hardening effect which is detectable even after five years. The addition of small quantities of arsenic has been shown to speed up the precipitation of antimony from solid solution in lead to such an extent that complete hardening is achieved in a matter of days.

Bluth and Hanemann (37) experimented with lead alloys of 0.5%, 1.0% and 2.0% antimony, quenched from 240°C. For the 2% antimony alloy, the addition of 0.05% Arsenic caused hardening to be completed within 3 days.

This finding was confirmed by Hopkin and Thwaites (38) who conducted creep tests on an alloy of 0.85% Sb age hardened with arsenic, and found that no recrystallisation took place during tests. Williams (39) found that a trace of 0.15% arsenic in lead antimony alloys speeded up the age hardening properties so that nearly all hardening took plate within ten minutes, and no appreciable difference was noted after two years.

Nishikawa and Tsummaya (40) also investigated the speeding up of age hardening of lead-antimony due to arsenic. They concluded that since the mobility of the As atom in the Pb lattice is very high, some clustering of As atoms form stable nuclei for metastable Sb precipitates. Since the As atom is interstitial and expands the Pb lattice, and the Sb atom is substitutional and contracts, the Pb lattice, the presence of As atoms stress relax the lattice and allow precipitation of the antimony.

2.1.9 Chill casting and the solidification of metals

The casting to size of a model in a lead alloy is a major feature of the experimental work (Chapter 5). The grain size, distribution and orientation in the model is largely determined by the conditions under which the alloy solidifies, so certain features of solidification processes in

general are relevant as background. These processes are described by Winegard (41).

Nucleation

When a molten metal cools below the melting temperature, solidification does not automatically take place. In pure metals, solidification depends on the spontaneous formation of solid nuclei around which more solid can form; and the survival of nucleus depends on the balance between the increase of interfacial free energy needed to increase the radius of the nucleus and the energy supplied by the latent heat of the newly attached solid. Since the former increases with the square of the increasing radius and the latter with the cube of the increasing radius, there is a critical radius for a nucleus below which it will disappear, and above which it will grow.

The driving force for the spontaneous formation of nuclei is the degree of undercooling. The greater the degree of undercooling, the more likely it is that a nucleus of the required radius will form and grow. The number of nuclei to act as growth centres determines the grain size.

Heterogeneous nucleation will greatly increase the number of nucleation sites and hence reduce grain size. In this process foreign particles, either impurities or even the container wall, act as ready-made nuclei. If the angle of contact is low between the molten liquid and the particle surface, the interface has low energy and readily allows atoms to deposit. The same degree of undercooling will initiate freezing more readily and in more places in a melt containing impurities than in one without.

Grain Growth

Where there is a positive temperature gradient into the molten metal, the interface of solidifying pure metal advances as a flat, structureless barrier. Where there is a negative temperature gradient, however, dentritic growth takes place. If a spike should solidify, the tip of the spike will be in a region of greater undercooling than the base, encouraging it to grow;

and in the region of the base of the spike the released latent heat raises the melt temperature, inhibiting solidification. In general a negative temperature gradient will always be generated in the region of the interface because of the latent heat release.

Non-equilibrium cooling of a binary alloy leads to 'coring'. This is due to the different freezing temperatures of different compositions of the alloy which leads to successive concentrations of the alloy solidifying one after the other too quickly to allow the diffusion to take place.

Constitutional Undercooling

The non-equilibrium cooling of an alloy can be used to promote nucleation and grain growth ahead of the solid interface. As an alloy of two metals A and B solidifies, the 'coring' effect will mean that the concentration of one alloy, say B, will be less in the initial solidified layers than in the overall melt. This means that there will be a high concentration of rejected alloy near the interface, decaying exponentially into the melt (Fig. 2.2). For each particular concentration, there is its own freezing temperature, leading to a freezing temperature distribution similar to the concentration distribution, but inverted. Then, even with a positive temperature gradient, there could be considerable undercooling for some distance ahead of the solid interface; and the position of maximum undercooling can be well ahead of the interface (Fig. 2.2).

It can be seen that constitutional undercooling in an alloy can produce sufficient undercooling to generate nucleation well in advance of the solid interface and over a wide band. This will assist the development of a large number of randomly orientated grains, a desired feature of the lead alloy castings of Chapter 5.

A disadvantage, however, is that if the nucleation band is wide liquid will find difficulty in flowing through the 'mushy' zone to the solid interface to take up contraction, and porosity may develop.

2.2 Similarity Conditions for Creep

2.2.1 Similarity conditions

The strain history of a prototype component subjected to constant loading is to be predicted from a model made of a different material with accelerated creep properties.

The initial strain distribution is assumed to be elastic. It is determined by the shape of the component and the type of loading. The elastic strain distribution depends also on the material uniaxial stress-strain law, $\varepsilon \propto \sigma^{k}$ where k is the elastic stress index. For most engineering materials, k = 1. As creep takes place, the stresses redistribute until a state of stationary creep has been reached, at which no further stress redistribution occurs as the material strains. When stationary creep has developed, the creep strain distribution is governed by the shape of the component, the type of loading and the material's uniaxial creep law, usually expressed as $\varepsilon \propto \sigma^{n}$ where n is the creep stress index.

If the model behaviour is to represent the prototype behaviour, the distribution of total strains must be similar at all equivalent times. The model must also show the same degree of redistribution, governed by the ratio of creep strain to elastic strain, at equivalent times.

It follows that:

(i) The model must be the same shape as the prototype. i.e. the model must be a scaled version of the prototype.

(ii) The model must be loaded in the same manner as the prototype.

(iii) The model and prototype must have the same elastic stress index. i.e. $k_m = k_p$.

(iv) The model and prototype must have the same creep stress index. i.e. $n_m = n_p$.

(v) At all equivalent times, the ratio of creep strain to elastic strain at any point in the model must be the same as that at the same point in the prototype.

In the usual analysis of three-dimensional creep problems, an effective or equivalent stress σ_e is calculated using the Von Mises expression, where

$$\sigma_e = \frac{1}{\sqrt{2}} \left[(\sigma_1 - \sigma_2)^2 + (\sigma_2 - \sigma_3)^2 + (\sigma_3 - \sigma_1)^2 \right]^{\frac{1}{2}}$$

Uniaxial creep data for the material is then used in conjunction with σ_e to predict the creep behaviour in three dimensions. If this method is valid, similarity of creep behaviour between model and prototype materials in uniaxial tension and compression is sufficient to ensure similarity of creep behaviour in a three-dimensional stress field.

The model material creep behaviour will exactly represent the prototype material creep behaviour if, by applying suitable known scaling factors, the uniaxial creep curve for the model material can be made to fit exactly over the corresponding uniaxial creep curve for the prototype material.

For each material, the whole family of creep curves relating creep strain ε_c with stress σ, temperature T and time t can be represented as a single empirical function.

For the model material $\varepsilon_{mc} = M(\sigma_m, T_m, t_m)$

For the prototype material $\varepsilon_{pc} = P(\sigma_p, T_p, t_p)$

For each material one curve is sketched in Fig. 2.3.

To make the model material creep curve fit exactly over the prototype material creep curve, both the strain scale and the time scale for the model curve must be distorted.

Let the strain scale ratio $= \eta$ such that $\varepsilon_{mc} = \frac{1}{\eta} \varepsilon_{pc}$

Let the time scale ratio $= \phi$ such that $t_m = \frac{1}{\phi} t_p$

It follows that

(vi) To represent the prototype material by the model material in creep

$$P(\sigma_p, T_p, \phi t_m) = \eta \; M(\sigma_m, T_m, t_m) \qquad (2.28)$$

2.2.2 Application to engineering materials

If E_m and E_p are the values of Young's modulus for the model and the prototype respectively, then the strains are:

Strain	Model	Prototype
elastic	$\varepsilon_{me} = \sigma_m/E_m$	$\varepsilon_{pe} = \sigma_p/E_p$
creep	$\varepsilon_{mc} = M(\sigma_m, T_m, t_m)$	$\varepsilon_{pc} = P(\sigma_p, T_p, t_p)$
total	$\varepsilon_m = \frac{\sigma_m}{E_m} + M(\sigma_m, T_m, t_m)$	$\varepsilon_p = \frac{\sigma_p}{E_p} + P(\sigma_p, T_p, t_p)$

For constant temperature creep, the creep strain relationship is usually stated in the form, $\varepsilon_c = A\sigma^n F(t)$ where the creep strain at different temperatures changes the value of the constant A and F(t) is some function of time.

As elastic and creep stress indices have to be the same for both model and prototype, to satisfy conditions (iii) and (iv)

$$\varepsilon_{mc} = A_m \sigma_m^n F_m(t_m) \quad \text{and} \quad \varepsilon_{pc} = A_p \sigma_p^n F_p(t_p)$$

and to satisfy condition (v),

$$\frac{A_m \sigma_m^n F_m(t_m)}{\sigma_m/E_m} = \frac{A_p \sigma_p^n F_p(t_p)}{\sigma_p/E_p} \qquad (2.29)$$

To satisfy condition (vi) substitute creep law into equation (2.28)

$$A_p \sigma_p^n F_p(\phi t_m) = \eta A_m \sigma_m^n F_m(t_m) \qquad (2.30)$$

From (2.29) and (2.30)

$$\frac{A_p \sigma_p^n F_p(\phi t_m)}{A_m \sigma_m^n F_m(t_m)} = \eta = \frac{\sigma_p}{\sigma_m}\frac{E_m}{E_p} \qquad (2.31)$$

i.e.

$$\frac{F_p(\phi t_m)}{F_m(t_m)} = \frac{A_m}{A_p}\frac{E_m}{E_p}\left[\frac{\sigma_m}{\sigma_p}\right]^{(n-1)} \qquad (2.32)$$

The following conclusions can be drawn from the above. Given A, E and F(t) and the (common) value for n for both materials,

1. The solution of equations (2.31) and (2.32) establishes the values of strain scale ratio η and time scale ratio ϕ.

2. From equation (2.31) it can be seen that the strain scale ratio η is a function of the stress ratio σ_p/σ_m only and is therefore constant throughout the test.

3. The stress ratio σ_p/σ_m has the same value at all points in the component; since conditions (i) and (ii) dictate that $(\sigma_1/\sigma_2)_p = (\sigma_1/\sigma_2)_m$ for any two positions 1 and 2, and conditions (iii) and (iv) dictate that this must be true, during the whole of the test. This means that the value of σ_p/σ_m can be calculated at any convenient point where the stresses are easily determined.

If the manner of loading of the prototype changes, or the magnitude varies during the prototype lifetime, the model manner and magnitude of loading must be changed accordingly to preserve σ_p/σ_m = constant and $(\sigma_1/\sigma_2)_p = (\sigma_1/\sigma_2)_m$. The timing of the changes to the model can be determined by calculating ϕ for the prototype changes.

4. From equation (2.32) it can be seen that ϕ is a function of σ_p/σ_m and model time t_m.

5. σ_p/σ_m is a test variable. σ_p is fixed by operational requirements of the prototype, but σ_m can be chosen to be any value suitable for model testing. η and ϕ are then fixed by material properties and test convenience.

It follows that having obtained test results at a single convenient model stress level, the results can be scaled by equations (2.31) and (2.32) to represent behaviour at any test stress level, any prototype operational stress level, and, if the material constants are known, for any prototype material with the same stress indices.

This means that a single test is required to establish the creep

behaviour of a particular shape of component made of any material with a particular stress index.

2.2.3 Application to two particular materials

The following exercise is an illustration of the technique. The data were obtained from Reference (16).

The form of the creep law used is

$$\varepsilon_c = A\sigma^n (t^s + Bt)$$

For extruded 0.2% Antimony 0.02% Arsenic lead alloy at room temperature

$$n = 5.46 \simeq 5.5$$

$$s = 0.39$$

$$A = 3.02 \times 10^{-19} \text{ lbf in h units}$$

$$B = 0.106$$

$$E = 3 \times 10^6 \text{ lbf/in}^2$$

For "cast AA", silicon killed 0.14% carbon, 1.25% manganese steel at 375°C,

$$n = 5.5$$

$$s = 0.325$$

$$A = 2.07 \times 10^{-28} \text{ lbf in h units}$$

$$B = 0.00045$$

$$E = 30 \times 10^6 \text{ lbf/in}^2.$$

N.B. The cast AA values have been derived from only three points of the data for cast AA, so should only be taken for illustration. The n values are not exactly equal, but n for the lead alloy was assumed to be 5.5.

Equation (2.31) becomes

$$\eta = \frac{\sigma_p}{\sigma_m} \quad \frac{3 \times 10^6}{30 \times 10^6} \qquad (2.31)$$

Equation (2.32), in terms of t_m, becomes

$$\frac{(\phi^{0.325}\, t_m^{\,0.325} + 0.00045\, t_m \phi)}{t_m^{\,0.39} + 0.106\, t_m} = \frac{(3.02 \times 10^{-19})(3 \times 10^6)}{(2.07 \times 10^{-27})(30 \times 10^6)} \left(\frac{\sigma_p}{\sigma_m}\right)^{(4.5)} \qquad (2.32)$$

η has been calculated from equation (2.31) for various values of σ_p/σ_m. For each of the latter, equation (2.32) has been solved for a number of selected model times. The results are shown in Fig. 2.4.

Prototype prediction for turbine casings

Some prototype casings are made from Chrome-Moly-Vanadimum steel and operate at around 460°C. The model lead casings are cast from 0.2% Antimony 0.02% Arsenic lead alloy. For illustration it is supposed that cast and extruded lead alloys have identical creep properties, and it is required to predict strains in a steam turbine casing made from cast AA and operating at 350°C.

A survey of seven available drawings of steam turbine casings shows a range of mean hoop stress in the cylindrical sections from 3640 lbf/in^2 to 9750 lbf/in^2 with the average at 5760 lbf/in^2. For this example, assume that the prototype mean hoop stress is 6000 lbf/in^2, and that the total life of the prototype is 20 years (174,840 hours).

Suppose that the most convenient lead model test pressure is 25 lbf/in^2, corresponding to a mean hoop stress in the model of 200 lbf/in^2. With the help of Fig. 2.4, a single test at this pressure can be used (i) to predict prototype behaviour at any stress level, (ii) to predict model behaviour at any other test pressure.

Prototype behaviour at any stress level can be predicted by calculating the particular value of the stress ratio RSIG, and reading off the strain scale ratio and equivalent times from the corresponding line on Fig. 2.4.

Suppose that we wish to predict the behaviour of the model tested at 50 lbf/in^2 (corresponding to a mean hoop stress of 400 lbf/in^2). Both model stress levels could be used to predict prototype behaviour at any given stress level, say 8000 lbf/in^2, according to (i). So converting the 25 lbf/in^2 test results via RSIG = 40, and converting the 50 lbf/in^2 test results via RSIG = 20 should result in identical prototype predictions.

It follows that converting the 25 lbf/in^2 test results via RSIG = 40 to the prototype prediction, and converting back from the prototype prediction via RSIG = 20, should produce a prediction of 50 p.s.i. test results. Thus, model testing at different pressures provides a check on the validity of the above method. The same result can be obtained by selecting any two values of RSIG in the ratio of the model test pressures.

2.2.4 Comparison with Frederick

Frederick (42) has derived model correlations for investigating creep and relaxation in structures. Two structures of similar dimensions and load patterns are shown to obey basically similar differential equations, and expressions are derived which will predict corresponding times and strains. In the proof it is demonstrated that the creep strain distribution in a body is equivalent to the strain distribution due to a system of surface and body forces, which with the linearity of the equations of elasticity means that there is a unique distribution of stress for a given distribution of creep strain. This means that the effect of accumulated creep strain can be included in the total stress equations by means of its equivalent stress system according to the principle of superposition.

The resulting stress equation in its general form will apply equally to both bodies. By defining "equivalent times" as the relationship of the time in one structure to that in the other when the stress equation is similar, a general expression for equivalent times is derived.

Investigating several different forms of the creep law, Frederick concludes that both the time hardening and the strain hardening analysis based in the creep law given by equation

$$\varepsilon_c = A \sigma^n t^s$$

give complete correlation, with equivalent times given by

$$E_1 \sigma_1^{n-1} F_1(t) = E_2 \sigma_2^{n-1} F_2(t)$$ which is identical to

equation (2.32),

and equivalent strains given by,

$$\frac{E_1 \varepsilon_{m1}}{\sigma_1} = \frac{E_2 \varepsilon_{m2}}{\sigma_2}$$ which is identical to equation (2.31).

The similarity analysis of Section 2.2.1 is essentially the same as Frederick's analysis, and comes to the same conclusions. Frederick's fundamental and rigorous approach has an advantage over the more intuitive approach of Section 2.2.1 in that it defines more clearly the limitations in the forms of creep law which are suitable for correlations.

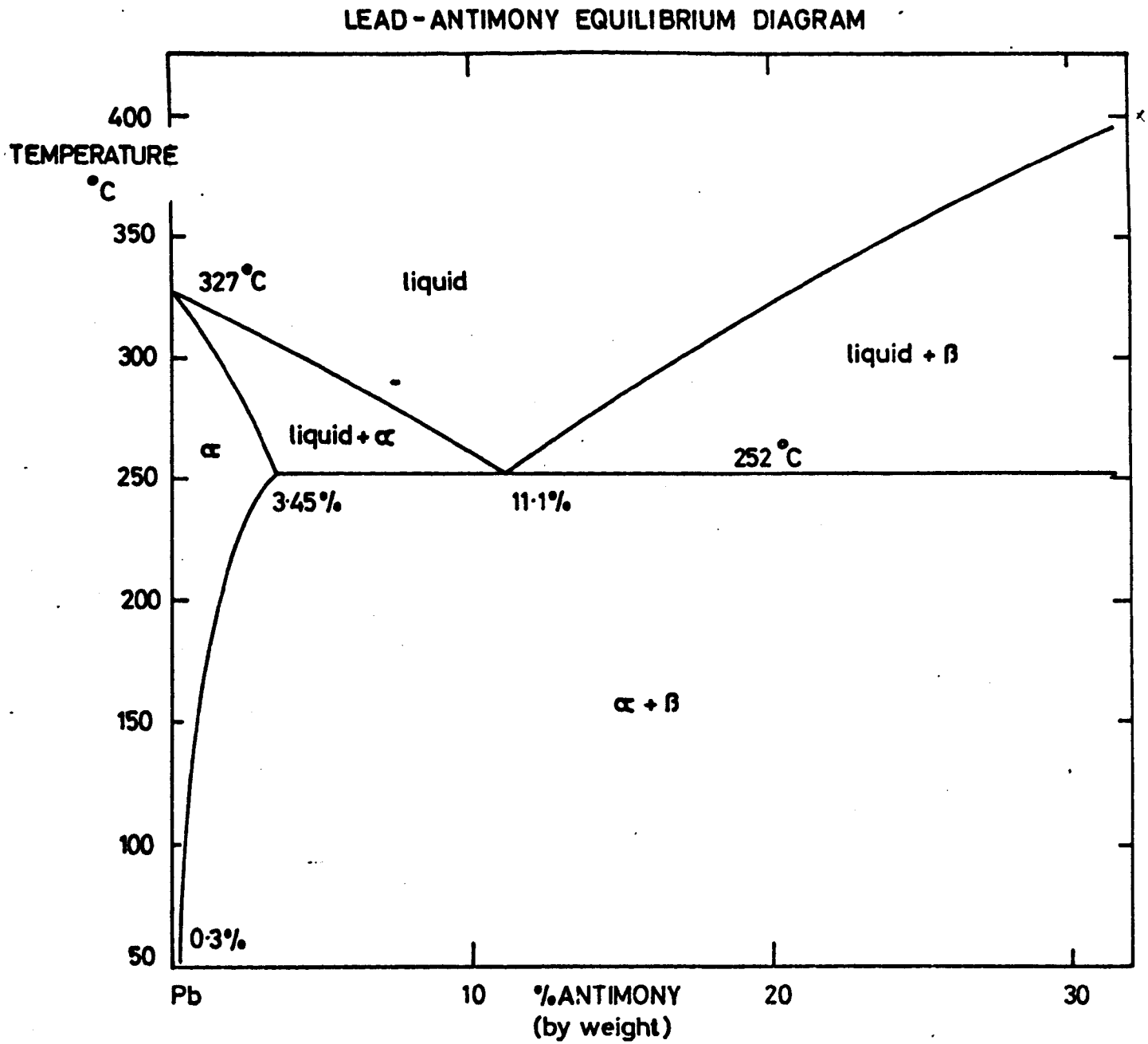

FIG. 2·1

LEAD-ANTIMONY EQUILIBRIUM DIAGRAM

CONSTITUTIONAL UNDERCOOLING FIG. 2·2

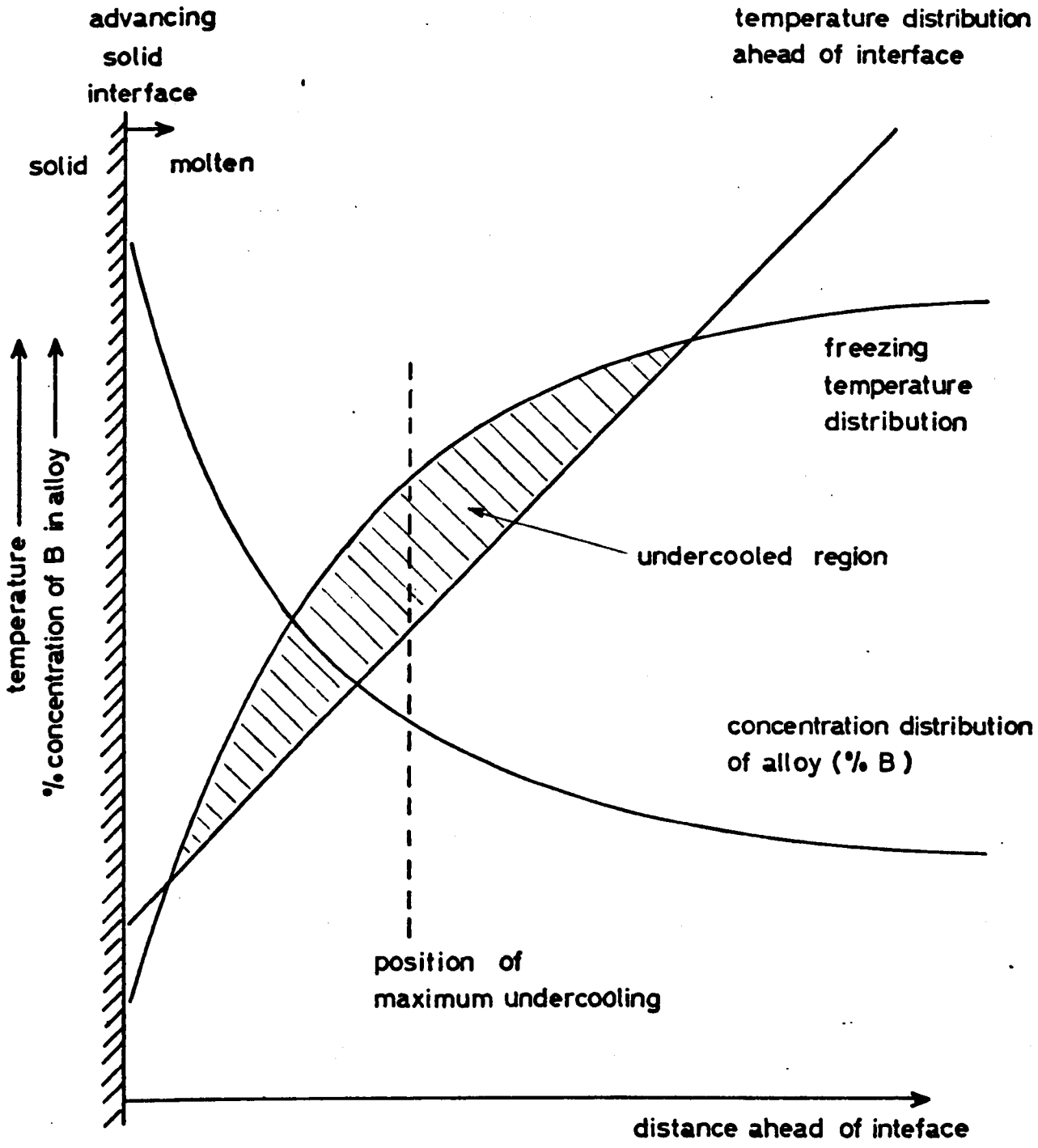

UNIAXIAL CREEP FIG 2·3

A General Creep Curve for each of Model and Prototype Materials

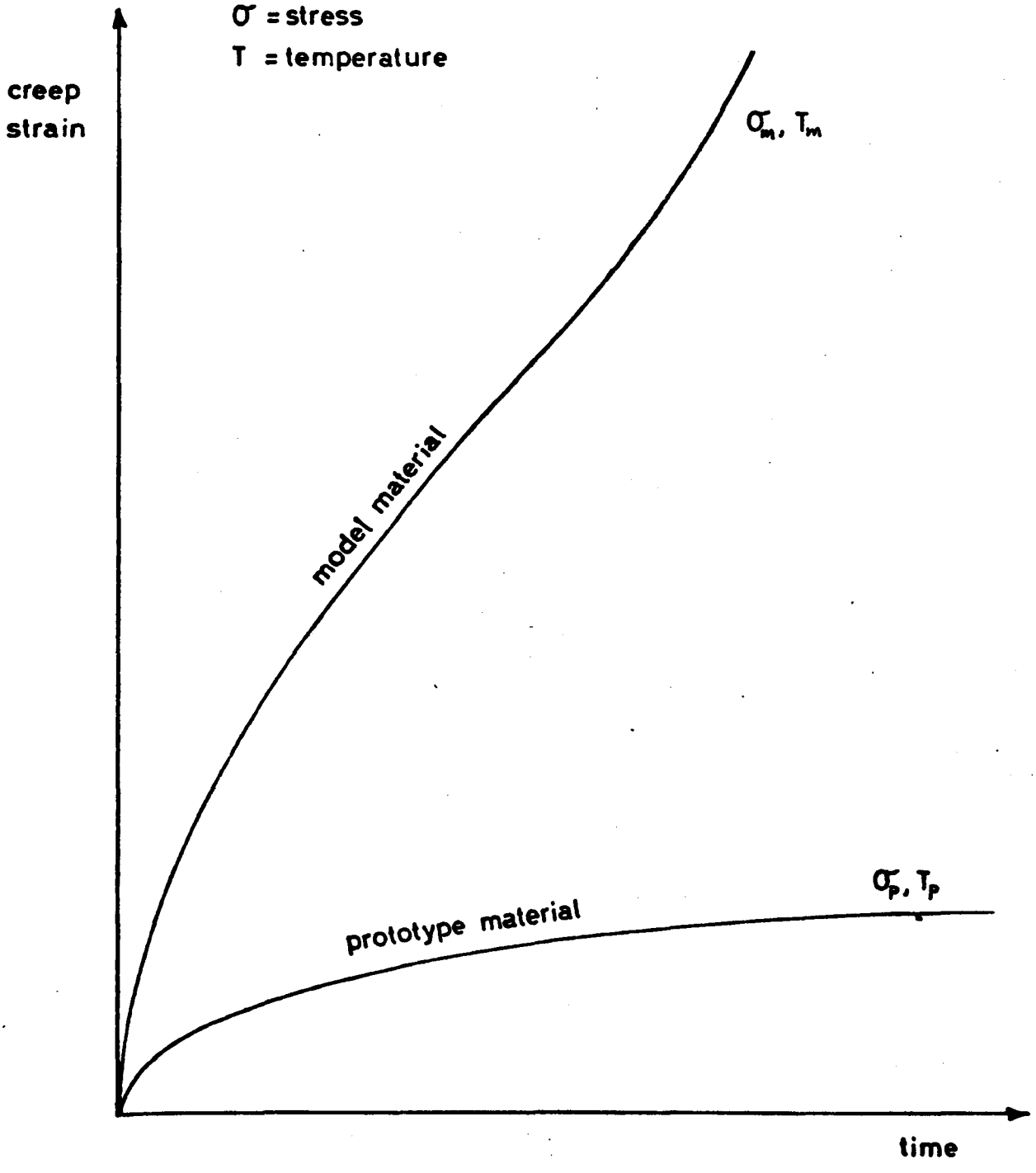

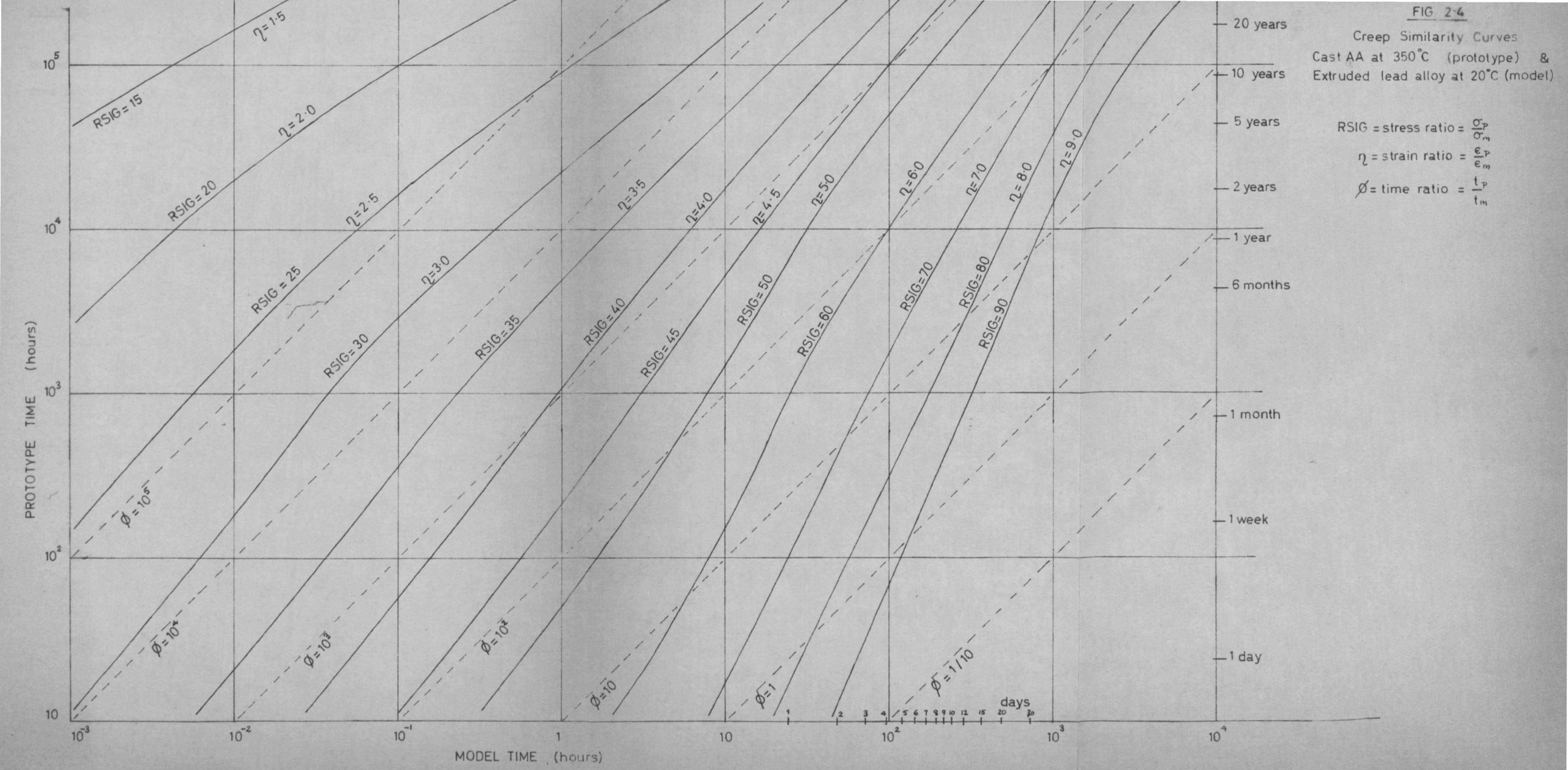

FIG 2·4

Creep Similarity Curves

Cast AA at 350°C (prototype) & Extruded lead alloy at 20°C (model)

RSIG = stress ratio = $\frac{\sigma_p}{\sigma_m}$

η = strain ratio = $\frac{\epsilon_p}{\epsilon_m}$

ϕ = time ratio = $\frac{t_p}{t_m}$

3. THE MODEL MATERIAL

3.1 Selection of Model Material

3.1.1 Requirements of Model Material

In order to represent the creep behaviour of steel structures subjected to large loads at high temperature, the following requirements were sought from the model material.

(i) The elastic behaviour of the material should be similar to that of steel. The model material should therefore be linearly elastic.

(ii) Significant creep strains should result from loads small enough to be easily handled in the laboratory.

(iii) These creep strains should occur when the material is loaded at room temperature.

(iv) These creep strains should be developed in a time convenient for continuous monitoring of the strains. A complete test should take from 100 to 500 hours.

(v) The model material creep stress index, n, should be the same as that of the prototype material. For most engineering materials the creep stress index lies between 3 and 7 (16).

(vi) The material should have a stable, fine grain structure. Its homogeneity and isotropy, should be similar to those of the prototype material.

(vii) Time dependent changes of material structure, such as recrystallisation, grain growth and age hardening, should not occur.

(viii) Manufacture of models from the material should be both simple and repeatable. For complicated shapes, this requires that the material should be easily castable.

3.1.2 Selection of 1.2% Sb 0.12% As Lead Alloy

Gill ('6' selected a lead alloy containing 0.2% Sb and 0.02% As in the form of rolled sheet as a suitable material for modelling steel structures subjected to creep (Section 2.1.9). This material was used as a basis for the development of an antimony-arsenic-lead alloy suitable for casting complicated shapes to size, such as scaled down steam turbine casings.

For the particular shape tested (Section 4.1) it was found to be impossible to produce crack-free castings from the 0.2% Sb 0.02% As lead alloy. This was due to a combination of the large solidification contraction and the low strength of the alloy, aggravated by the differential expansions inherent in the chill casting technique adopted (Section 5.1.1.)

An increase in the proportions of Antimony and Arsenic in the alloy has the effect of both reducing the solidification contraction (Hoffmann, 3) and increasing the strength. The quantities of the alloying elements were increased to 6% Sb 0.6% As, the proportion of Antimony to Arsenic being kept at 10:1 on the recommendation of the Lead Development Association. With this alloy, very good castings were produced, but uniaxial specimens cut from a casing showed no measurable creep under a tensile stress of 2500 lbf/in^2.

Having thus obtained an upper limit for the composition, the antimony and arsenic content of Gill's alloy was increased in stages to 0.4% Sb 0.04% As, 0.8% Sb 0.08% As and 1.2% Sb 0.12% As, using the 6% Sb 0.6% As lead alloy as the "king alloy". At each stage casting and creep properties were tested. The 1.2% Sb 0.12% As lead alloy produced good castings, and still showed significant creep strains at room temperature under reasonable stresses.

The quality of the cast material is discussed in Section 5.1.5.

3.2 Uniaxial Calibration of Model Material

The model material, though harder than the alloy adopted by Gill (16), is still soft enough to present the same problems of loading and strain measurement encountered by him (Section 2.1.9). To calibrate the model material in uniaxial tension, therefore, a modified version of the same uniaxial test machine was used, requiring the same kind of dumbell specimen (Fig. 3.2).

3.2.1 Uniaxial test rig (Fig. 3.1) is a modification of the one used by Gill. Since the 1.2% Sb 0.12% As lead alloy adopted is considerably stronger in creep than Gill's 0.2% Sb 0.02% As lead alloy, the test rig is required to measure very much smaller strains for the lower stress levels. Early tests indicated significant bending in Gill's original rig, so aluminium dumbells were manufactured and mounted with electric resistance strain gauges. These dumbells revealed bending stresses of up to ±40% of the mean stress on a $\frac{3}{8}$ inch section, depending on how well the specimen was aligned before loading. Also, since the machines were mounted in pairs, one at each end of a 3 ft bar which bent under the test loads, the loading up of one machine would induce 20% bending in its pair.

In the modification developed the dumbell is clamped as before (Section 2.1.7) between grips located at each end by the doweled fit of the clamping bolt through the hole (Fig. 3.1). The dumbell holes are drilled in a special jig designed by Gill, which places the holes on the centre line of the parallel section of the specimen.

Pairs of rectangular plates, with edges ground parallel, clamp round the grips at each end, located by the clamping bolt in a hole drilled exactly midway between the edges. Thus the dumbell specimen is aligned with the plates in one plane by assembling loosely, lining up on a face-plate, and clamping up. An accurately ground cylinder with a coned end is located by dowels on the centre line between the plates at each end. Since the plates are identical, clamping up on the dumbell and grips

when attached to a coned cylinder will result in a parallel link mechanism which will align the dumbell midway between the plates in the other plane. At each end, therefore, the point of the coned cylinder will lie on the centre line of the dumbell specimen.

If the specimen assembly is then supported through one cone point, and the loading weights hung from the other, there should be no bending due to loading misalignment. However, since alignment depends on machining accuracy, bending cannot be completely eliminated. Deviation of the cone points from the centre line of the specimen is less than 0.004 in, which, for a prismatic section of the $\frac{3}{8}$ in square, means that initial bending stresses should be less than ±6%.

When an Aluminium dumbell specimen with strain gauges was tested in the modified uniaxial test rig, bending strains were found to be less than ±5%, and remained unchanged when the support frame was shaken, when its pair was also loaded up, and when the weights were swung in a wide arc from the cone pivots.

Because of the small strains, it became necessary to mount the dial gauges from the cone plates themselves, so that free movement of the specimen assembly allowed by the cone pivots does not affect the dial gauge readings. Two dial gauges were mounted in opposition on the top plates of the specimen assembly for balance, and to give some indication of bending during creep.

To assist in loading the specimens, lifting platforms (Fig. 3.3) were used to support the weights before loading, with sufficient travel to allow the weights to be lowered smoothly until supported by the specimen.

3.2.2 Uniaxial Specimens

The specimens used to calibrate the material for the model tests must have the same grain structure and distribution, the same strain and temperature history and the same composition as the model material. This

means that they must be cut from untested models manufactured under the same conditions as the tested models.

The specimens are shown in Fig. 3.4.

Specimen location

Gill showed (Section2.1.7)that uniaxial specimens tested in his design of rig must have a parallel section of more than 1 in to reduce the end effects of the dumbells to insignificance. Because of the curvature of the casings, particularly the toroid end, this means that the specimens can be cut only from the cylindrical section, in the axial direction.

Attempts were made to produce specimens from the toroid end of the model and in the hoop direction by cutting out the parallel section only, and then sticking on dummy dumbell ends with Araldite. However, the Araldite joint failed at stresses higher than 500 lbf/in^2, well below the test stresses; and even where it was possible to include the beginning of the dumbell ends, and hence increase the joint area to reduce the stress, the glued specimens failed below the test stresses.

3.2.3 Uniaxial Tests and Results

The stress levels were selected to produce creep strains measurable by the test rig in fairly short times (0.1 hours), and to give an average length of test of little over 100 hours. Tests were discontinued after their allotted time span, or if the creep strain exceeded 5%. Seven stress levels were chosen in the practicable stress range of 1000 lbf/in^2 to 2500 lbf/in^2 (1000 lbf/in^2, 1200 lbf/in^2, 1400 lbf/in^2, 1600 lbf/in^2, 1900 lbf/in^2, 2200 lbf/in^2 and 2500 lbf/in^2) to establish the stress dependence of the creep response of the material.

The specimens, cut from 5 casings (see Table 3.1), were divided into 4 groups. All the specimens in group 1 came from casing 16, and their positions in that casing were carefully noted (see Fig. 3.5). The specimens in the other groups came from the other casings.

Group 1 specimens were all tested at 1400 lbf/in^2 (Fig. 3.6). These were to establish the scatter in creep behaviour within one casing, and to compare the scatter and creep properties with those of the other casings.

Group 2 specimens were also all tested at 1400 lbf/in^2 (Fig. 3.7). With group 1 these were to establish the scatter between different casings.

Group 3 specimens were tested at the other six stress levels. At least two specimens at each stress level were deemed necessary to establish the creep behaviour at that stress level (Figs. 3.8 to 3.13).

Group 4 includes three extra tests, two at 1000 lbf/in^2 and one at 400 lbf/in^2 to study the creep behaviour at low stresses. Following suspect dial gauge results at low strain levels, and work done in proving electric resistance strain gauges on lead, the strains of these specimens were measured by electric resistance strain gauges. Two long strain gauges on opposite faces of the specimen measured the average strain over the whole of both sides, averaging the small bending strains.

The results at 1000 lbf/in^2 are included in Fig. 3.13. The test at 400 lbf/in^2 showed no measurable creep strains in 320 hours, and is not plotted.

From the results of group 4 tests, the value of Young's modulus for the lead alloy was found to be 2.85×10^6 lbf/in^2.

3.2.4 Analysis of Results

The results are fitted to a single constant temperature creep law of the form:

$$\varepsilon_c = F(\sigma)\, G(t) \qquad (1) \text{ total creep law}$$

or

$$\dot{\varepsilon}_c = F(\sigma)\, G'(t) \qquad (2) \text{ incremental creep law}$$

where F and G are separate functions of stress and time.

For the constant stress tests, $F(\sigma)$ is constant for a particular stress, so equation (1) becomes,

$$\varepsilon_c = K_\sigma \, G(t) \qquad (3)$$

The test results suggest that the time function G(t) takes the form suggested by Gill (Section2.1.7) $G(t) = t^s + bt$, the first term representing primary creep and the second term representing secondary, steady state creep. Since it was found that the steady state term was very small, the constant stress tests were fitted to two functions;

$$\varepsilon_c = K_\sigma \, (t^s + 6t) \qquad (4)$$

and

$$\varepsilon_c = K_\sigma \, t^s \qquad (5)$$

If equation (5) can be fitted satisfactorily, subsequent analysis is simpler.

The equations were fitted using a 'least squares' method, minimising the sum of the squares of the deviations of the test results from the adopted creep law. The choice of Walles and Graham (Section2.1.6) to measure scatter in terms of temperature deviations could not be followed, since the temperature parameters were unknown. It was decided to fit the equation by minimising deviations in Log (strain), but to analyse the scatter in terms of Log (stress).

Finnie and Heller and Penny and Leckie emphasise the importance of stress variations in causing scatter in creep data (Section2.1.6). It is known that the cast material is porous, and that the porosity will lead to variations of stress within the specimens. So by expressing scatter in terms of stress deviations, a combined measure of porosity and specimen misalignment may be obtained.

However, before the stress function $F(\sigma)$ is established curve fitting must be performed in terms of strain.

Selectivity

The purpose is to establish a creep law for the model material as a whole, but in particular for the toroid end of the model which is of greatest interest. It is proposed that since the material in the cylindrical

section of the model, from which the uniaxial specimens are cut, is similar in grain structure, porosity and strain history to the material in the toroid section of the model, the creep behaviour in the two sections will likewise be similar.

However, as discussed in Section 5.1.5, the material in the cylindrical section midway between the flanges contains blow holes that are not likely to be found elsewhere in the model. This is borne out by the results from the specimens in Group 1 (Section 3.2.3) which were cut from this part of the model (Fig. 3.5). These specimens showed both defects and creep rates well above those of the rest of the group (Fig. 3.6). Similarly, specimens with visible defects in groups 2 and 3 (Section 3.2.3) showed creep rates much larger than the others (denoted * in Table 3.I)

To derive a creep law, therefore, which is to apply to the toroid section of the model, those specimens from midway between the flanges, which show visible defects and unusually large strain rates, were excluded. Once a creep law has been derived, however, these specimens may be included in the analysis of scatter in the cylindrical section of the model.

The results of Section 3.2.3 show that the accuracy in measuring strain values less than 100 μs is poor. For strain values above 10,000 μs (1%) the increase in stress due to the change in cross-section becomes significant. The results used for curve fitting were therefore restricted to the range 100 μs $\rightarrow$ 10,000 μs.

Fitted curves at constant stress

The best fit creep laws of the forms given in equations (4) and (5) for particular stress levels are given in Table 3.2. These best fit curves are derived from the results of Group 3 specimens, omitting those denoted '*' in Table 3.1, and are shown in the appropriate graphs as a continuous line. In all cases, for the times involved, the secondary creep term of equation (4) was negligible, and the simpler form of equation (5) was adopted.

Given also in Table 3.2 are the mean and the standard deviation of the experimental points expressed as the ratio (experimental creep strain)/(creep strain predicted by best fit curve), the 'best fit' curve resulting in a mean value of 1.0000 and a minimum standard deviation. Also given is the equivalent standard deviation in terms of stress variations, i.e. assuming that strain variations are due to errors in actual test stress level (as discussed earlier), and assuming a creep law of the form,

$$\varepsilon_c = A\sigma^n t^s \qquad (6)$$

where 'n' is given the value derived for the final creep law.

Final creep law

To give equal weighting to each stress level, seven points were taken directly from the best fit curve at each stress level. A final creep law of the form given in equation (6) was fitted to these points using the same 'least squares' method, finding the values of A, n and s which best fit the list of points. A flow chart of the curve fitting computer program is shown in Fig. 3.14. See also Appendix 1.

The final creep law was,

$$\varepsilon_c = 1.291 \times 10^{-21}\ \sigma^{5.417}\ t^{0.513} \qquad (3.7)$$ lbf in h. units

mean of ratios of experimental to predicted strains = 1.0000.

Standard deviation of ratios of experimental to predicted strains = 1.401

The results from the test at 1000 lbf/in^2 were not included in the determination of the final creep law. Those experimental points available were obviously in error, indicating larger creep strains than those produced by specimens at 1200 lbf/in^2. These and other tests at low stresses are discussed in the next section.

3.2.5 Discussion

Fig. 3.7 shows the scatter in material creep properties to be expected in the toroid section of the lead models. The six D14 specimens did not include any with obvious defects, such as blow holes and, if the scatter is to be attributed largely to variations in stress, as suggested in Section 2.1.6 and Section 3.2.4, Fig. 3.7 shows the effect of porosity on the creep strain levels. The standard deviation in terms of stress variation is given in Table 3.2 as 1.040, which means that the average stress variation from specimen to specimen is 4%. Because of the large 'n' value, this results in a large scatter band in strain in uniaxial tension - more than 20%; although in a structure where the stresses redistribute, the scatter in strain should be less (Section 2.1.6).

Also tested at 1400 lbf/in^2 were the L14 specimens (Fig. 3.6), all from one casing; and the position in that casing from which each was cut is shown in Fig. 3.5. Specimen L14/5 contained a large blow hole, and as a result shows large creep strains. L14/1 and L14/7 also show strain levels above the average, and examination showed bad pitting and surface defects. Fig. 3.5 shows that these specimens were cut from positions near the middle of the cylindrical section of casing 16, midway between the flanges. As discussed earlier and in Section 5.1.5, it is in this region that defects are expected, and so those three specimens are not expected to represent the behaviour of the material in the toroid section.

If specimens L14/1, L14/5 and L14/7 are ignored, the remainder show a fairly close grouping, well within the range of the D14 specimens, although the strains are slightly higher. The final creep law line, however, passes through the middle of the group, and it was concluded that the creep properties of the material of casing 16 are described by the creep law given by equation (7). This creep law was derived from the material of casings 5, 6, 20 and 21 and, since all the casings are of the

same material and cast under the same conditions (Table 5.1), it was concluded that the creep properties of the material in all the lead casings of Table 5.1 are described by equation (7).

The other stress levels (Fig. 3.8 to Fig. 3.13) show the same order of scatter (Table 3.2), apart from the results at 1200 lbf/in^2 (Fig. 3.12).

Low stress levels

Particular problems were encountered with the tests at low stresses. With strain rates less than 10 microstrain per hour, the dial gauges are incapable of showing smooth creep. The initial deflections, which are subtracted from readings to obtain the creep deflections, contain errors and include inevitably the earliest part of the primary creep. The low creep strain levels mean that these errors become significant, and can lead to large apparent shifts in the creep curve.

The tests carried out at 1000 lbf/in^2 (Fig. 3.13) were disbelieved, since strain levels are shown which are in excess of those for stress levels of 1200 lbf/in^2. In view of the work carried out to test the validity of electric resistance strain gauges on lead (Section 6.2.1), two more tests were carried out at 1000 lbf/in^2, but this time measuring the strains with strain gauges (Fig. 3.13).

The strain gauge results show creep strains very much less than those indicated by the dial gauges, and very much closer to those expected. It was concluded, therefore, that the clamping grips of the uniaxial test rig do not hold the dumbell specimens completely firm; and since the creep deflections are almost too small to register on the dial gauges the readings are swamped by slight movement in the grips.

It is likely that the results at 1200 lbf/in^2 were also affected, and possibly even the lower end of the 1400 lbf/in^2 results. Some of the scatter at 1200 lbf/in^2 could be attributed to different degrees of slip.

Stress dependence in creep

If the creep law of the lead alloy is truly of the form of equation (6), then values of Log (creep strain) plotted against Log (stress) for equal times should fall on a straight line whose slope is the creep stress index, 'n'.

i.e. $\text{Log } \varepsilon_c = n \text{ Log } \sigma + \text{Constant}$ (For time t = Constant)

The 'best fit results' are shown plotted thus in Fig. 3.15. Although the upper points are close to the line, the lower points deviate significantly. However, the extra strain gauge results for 1000 lbf/in^2 are marked on after 100 hours, and indicate that the deviation of the lower points is probably due to the large errors in small strain measurements discussed later. Because of the preponderance of the higher stress levels in determining the final creep law, the law given in equation (7) coincides well with the strain gauge results at low stress levels. The results at 400 lbf/in^2 confirm this further.

Much less prone to initial errors is the plot of Log (creep strain rate) against Log(stress) for equal strains (Fig. 3.16). This plot is the one suggested by Woodford (Section 2.1.6) as being more suitable for strain hardening materials. From equation (6)

$$\frac{d\varepsilon_c}{dt} = A\sigma^n st^{s-1} = s\,\varepsilon_c^{1-\frac{1}{s}}\,A^{\frac{1}{s}}\,\sigma^{\frac{n}{s}} \qquad (8)$$

$$\therefore \quad \text{Log } \frac{d\varepsilon_c}{dt} = \frac{n}{s} \text{Log } \sigma + \text{Log}(s\,\varepsilon_c^{1-\frac{1}{s}})$$

Thus for a constant creep strain, $\frac{n}{s}$ is the slope of the lines in Fig. 3.16. The line for the lowest strain level of 100 microstrain is curved; but it is at the low strain levels that the initial errors have most effect, and the lines straighten up at higher strains, keeping more or less parallel as expected. This indicates that the strain hardening form of creep law given in equation (8) is applicable to the model lead alloy.

Examination of experimental results

The experimental points of Fig. 3.8 to Fig. 3.13 appear to lie on straight lines, and the best fit lines at each stress level indicate that any deviation due to secondary creep is small. However, the creep law of the form given in equation (6) assumes a time index independent of stress level, and the 'best fit' laws given in Table 3.2 show a definite trend of increasing time index with increasing stress level.

This might have been because the tests at higher stress levels involve higher strain levels, and the apparent stress dependence of the time index could have been produced indirectly by a strain dependence. To test this, the mean time index of the experimental points was plotted against creep strain for the experimental points of Group 2 and 3 specimens (Fig. 3.17 to Fig. 3.22).

The results are not conclusive. Only the tests at 1900 lbf/in^2 show an upward trend (Fig. 3.20), and both the 1200 lbf/in^2 results (Fig. 3.17) and the 1400 lbf/in^2 results (Fig. 3.18) show a downward trend at higher strains. The 1200 lbf/in^2 results show a great deal of scatter, reflecting the inaccuracies of the dial gauges at very low deflection rates. The overall conclusion, however, is that the time index is dependent on stress level.

A plot of creep strain rate against creep strain level is shown in Fig. 3.23 for the same experimental results. If the strain hardening law of equation (8) is obeyed,

$$\text{Log}\,\frac{d\varepsilon_c}{dt} = \left(1 - \frac{1}{s}\right)\ \text{Log}\,\varepsilon_c + \text{Log}\left(sA^{\frac{1}{s}}\sigma^{\frac{n}{s}}\right)$$

So for each stress level, the points should lie on a straight line whose slope is $\left(1 - \frac{1}{s}\right) = -\left(\frac{1-s}{s}\right)$. The constant which separates the lines involves the stress term $\sigma^{\frac{n}{s}}$, so is very sensitive to slight stress variations, since the value of n/s from the final creep law is 5.417/0.513 = 10.5.

Considering the results with creep strain rates above 10 microstrain per hour, Fig. 3.23 shows quite good straight lines. There is a definite change of slope with changing stress levels, increasing with reducing stress level, reflecting a decrease in time index.

Below strain rates of 10 microstrain per hour the lines are either very steep or become steeper. Comparatively large initial errors in the low strain results would account for a high initial creep strain rates which would not be sustained later on, and any movement in the grips as revealed for low stress results by the tests at 1000 lbf/in^2 (see above) would again result in a steepening line.

The test at 400 lbf/in^2, SG3 in group 4 of Table 3.1, showed no measurable creep strain in 320 hours. This agrees with the final creep law, which predicts only 3 microstrain of creep in 320 hours, which is less than the resolution of the strain measuring equipment.

Comparison with Gill's lead (Section 2.1.7)

For comparison, Table 3.3. sets out the creep constants of the cast lead alloy selected and those of the rolled sheet alloy chosen by Gill. It can be seen that the creep stress indices are nearly equal; and it was mentioned by Gill (16) that for the early part of his calibration tests, the time function without the secondary term 'b' would give a time index s = 0.54, which is again nearly equal to that of the cast alloy. This suggests that for antimony-arsenic alloys of lead, only the constant 'A' varies significantly up to 1.2% Sb, if the Sb:As ratio is kept at 10:1.

Given also in Table 3.3 are the uniaxial creep strains for an arbitrary stress level of 800 lbf/in^2. Clearly, the cast alloy is much stronger in creep than Gill's alloy. The factor between them is about 250 for small times, but increases to nearly 500 after 100 hours. This reflects the continued hardening of the cast alloy after the secondary, steady state phase of creep has become donimant in Gill's alloy.

3.2.6 Conclusions

1. The uniaxial creep law for the 1.2% Sb 0.12% As cast lead alloy is given by equation (3.7) in Section 3.2.4.

2. The material in the middle of the cylindrical section, mid way between the flanges contains blow holes and cannot be represented by the above creep law.

3. Young's Modulus for the material is 2.85×10^6 lbf/in^2.

4. The material appears to be strain hardening, although the scatter of the creep data prevents certainty.

5. Strain gauges should be used in future uniaxial calibrations.

TABLE 3.1

UNIAXIAL SPECIMENS FOR MATERIAL CREEP CALIBRATION

All specimens cut from cylindrical section of Model casings
* denotes specimen NOT used in determination of best fit curves

GROUP NO.	SPECIMEN NO.	CASING	STRESS LEVEL lbf/in^2	TEST TIME hours	REMARKS
1	L 14/1	16	1400	289	
	L 14/2	16		120	Results
	L 14/3	16		289	Fig. 3.6
	L 14/4	16		289	
	L 14/5	16		120	Spec. location
	L 14/6	16		289	Fig. 3.5
	L 14/7	16		289	
	L 14/8	16		120	
	L 14/9	16		289	
2	D 14/1	5/6	1400	340	
	D 14/2	5/6		340	Results
	D 14/3	20/21		118	Fig. 3.7
	D 14/4	20/21		120	
	D 14/5	20/21		168	
	D 14/6	20/21		168	
3	D 10/1	20/21	1000	455	Results
	D 10/2	20/21		455	Fig. 3.13
	D 10/3	20/21		120	* blow holes
	D 10/4	20/21		120	* blow holes
	D 10/5	20/21		120	* blow holes
	D 12/1	5/6	1200	503	
	D 12/2	5/6		503	Results
	D 12/3	20/21		454	Fig. 3.12
	D 12/4	20/21		454	
	D 12/5	20/21		120	* blow holes
	D 12/6	20/21		120	* blow holes

TABLE 3.1 (Cont.)

GROUP NO.	SPECIMEN NO.	CASING	STRESS LEVEL lbf/in^2	TEST TIME hours	REMARKS
3 (cont)	D 16/1	5/6	1600	293	Results
	D 16/2	5/6		294	Fig. 3.11
	D 16/3	20/21		118	
	D 19/1	20/21	1900	120	* cracked
	D 19/2	20/21		120	
	D 19/3	20/21		118	Results
	D 19/4	20/21		168	* Fig. 3.10
	D 19/5	20/21		120	* badly cracked
	D 22/1	20/21	2200	55	* cracked
	D 22/2	20/21		120	Results
	D 22/3	20/21		118	Fig. 3.9
	D 22/4	20/21		120	
	D 25/1	20/21	2500	48	Results
	D 25/2	20/21		120	Fig. 3.8
4	SG 1	5/6	1000		Results
	SG 2	5/6	1000		Fig. 3.13
	SG 3	5/6	400	320	No measurable creep

TABLE 3.2 UNIAXIAL CREEP AT DIFFERENT STRESS LEVELS

STRESS LEVEL lbf/in^2	NO OF SPEC.S	BEST FIT $\varepsilon_c = Kt^S$ lbf in h units		ε_c(exp)/ ε_c(calc)		EQUIV. S.D. RATIO FOR n = 5.417	BEST FIT $\varepsilon_c = K(t^S + bt)$ lbf in h units			ε_c(exp)/ ε_c(calc)		EQUIV. S.D. RATIO FOR n = 5.417
		K	S	MEAN	S.D.		K	S	b	MEAN	S.D.	
1000	2	7.3×10^{-4}	0.513	1.0000	1.117	1.022	7.3×10^{-4}	0.513	0.0	1.0000	1.117	1.022
1200	4	10.6×10^{-4}	0.364	1.0000	1.515	1.095	10.6×10^{-4}	0.364	0.0	1.0000	1.515	1.095
1400	6	14.0×10^{-4}	0.471	1.0000	1.219	1.040	14.0×10^{-4}	0.471	0.0	1.0000	1.219	1.040
1600	3	20.5×10^{-4}	0.500	1.0000	1.148	1.027	20.1×10^{-4}	0.500	0.0038	1.0000	1.147	1.027
1900	2	50.6×10^{-4}	0.571	1.0000	1.159	1.029	45.2×10^{-4}	0.472	0.0876	1.0000	1.135	1.025
2200	3	159.0×10^{-4}	0.599	1.0000	1.232	1.043	159.0×10^{-4}	0.599	0.0	1.0000	1.232	1.043
2500	2	416.9×10^{-4}	0.570	1.0000	1.369	1.068	416.9×10^{-4}	0.570	0.0	1.0000	1.369	1.068

TABLE 3.3

COMPARISON BETWEEN ROLLED 0.2% Sb 0.02% As LEAD ALLOY IN ROLLED SHEET AND CAST 1.2% Sb 0.12% As LEAD ALLOY IN UNIAXIAL CREEP

Creep Law of the form $\varepsilon_c = A\,\sigma^n(t^s + bt)$

LEAD ALLOY		ROLLED SHEET 0.2% Sb 0.02% As	CAST 1.2% Sb 0.12% As	RATIO
CREEP CONSTANTS	A(lbf in h)	3.02×10^{-19}	1.291×10^{-21}	234
	n	5.46	5.417	
	s	0.39	0.513	
	b	0.106	0	
σ = 800 lbf/in^2				
μ Strain	ε_c after 10h	5700	22.4	254
	ε_c after 30h	14950	39.5	378
	ε_c after 100h	35800	73	490

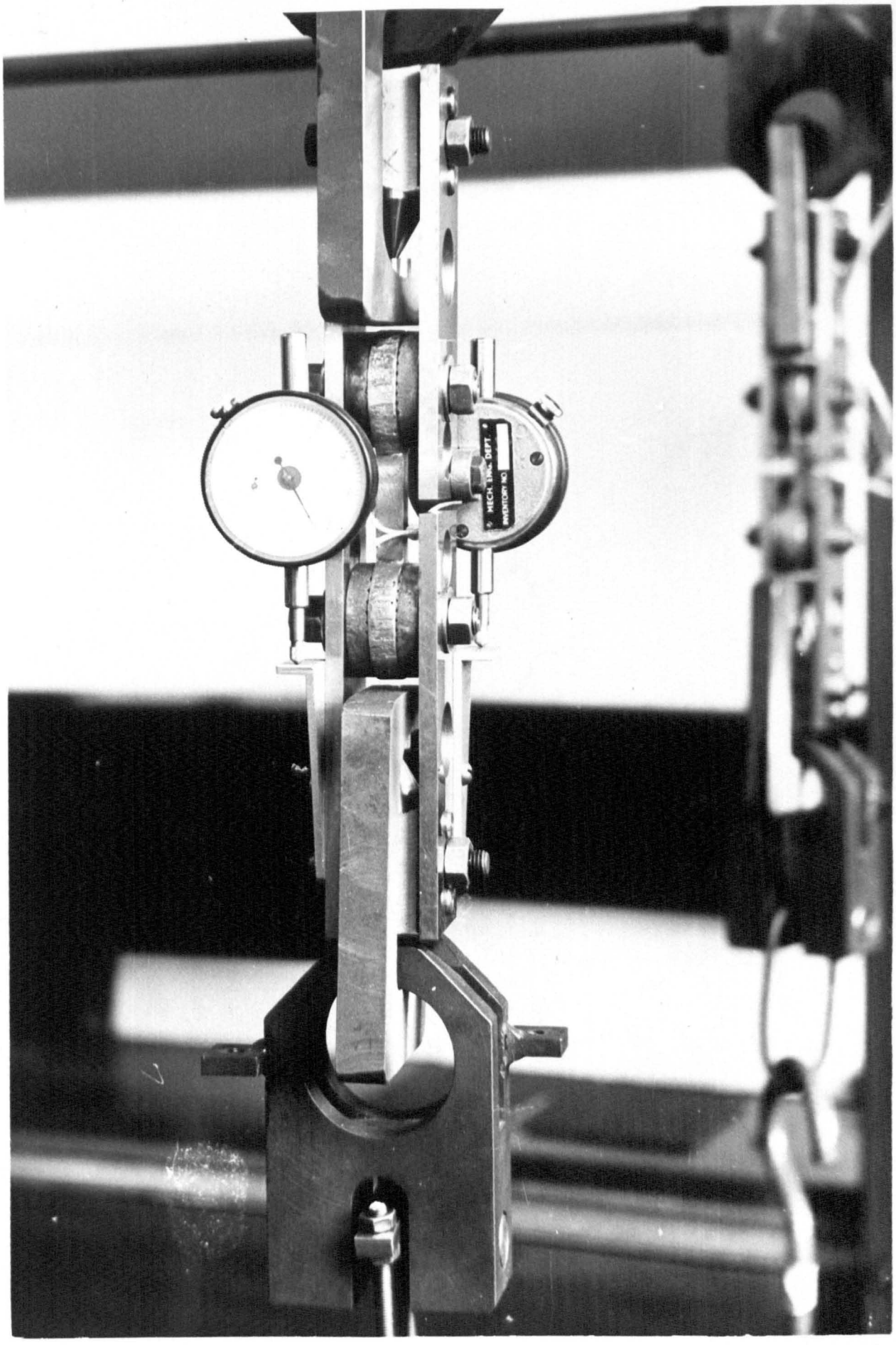

UNIAXIAL TEST MACHINE

FIG. 3·1

UNIAXIAL DUMBELL SPECIMEN FIG. 3·2

dimensions in inches

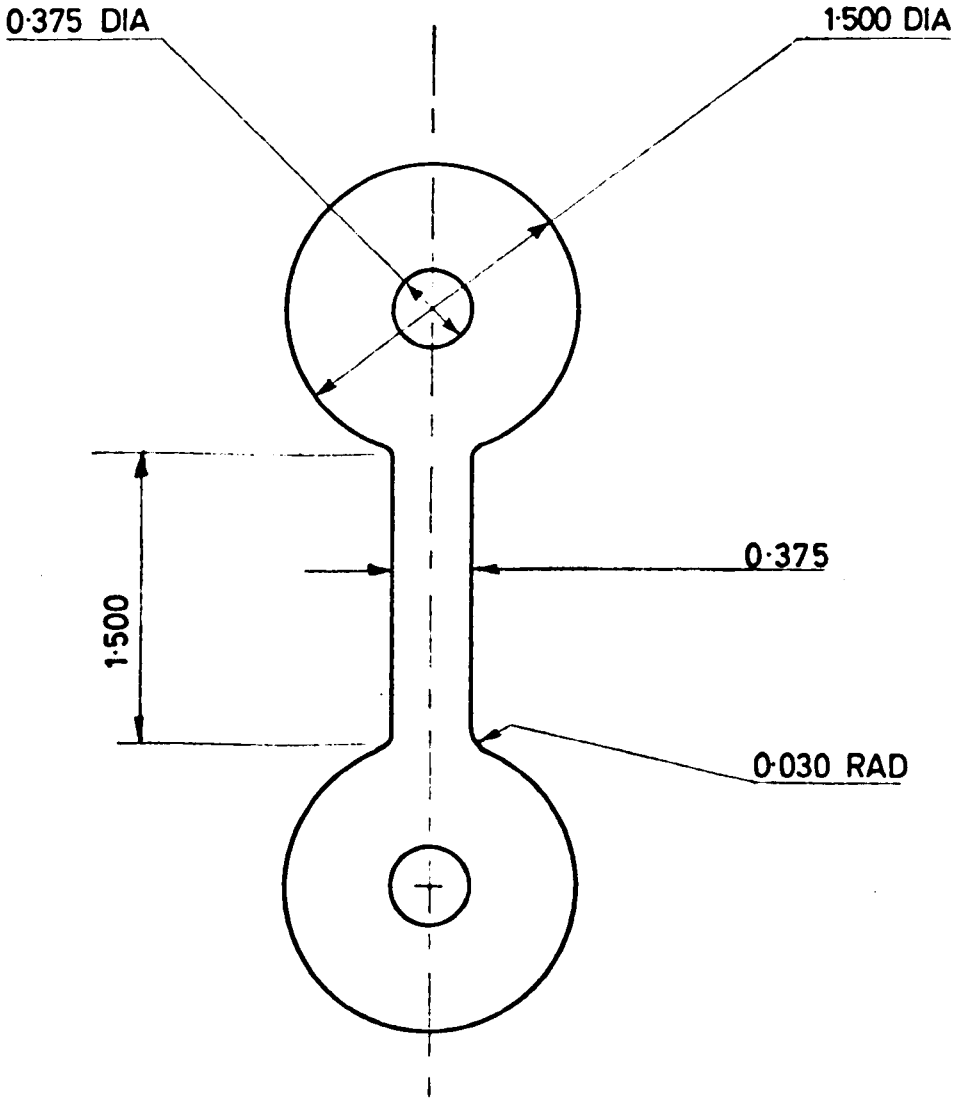

thickness = 0·375

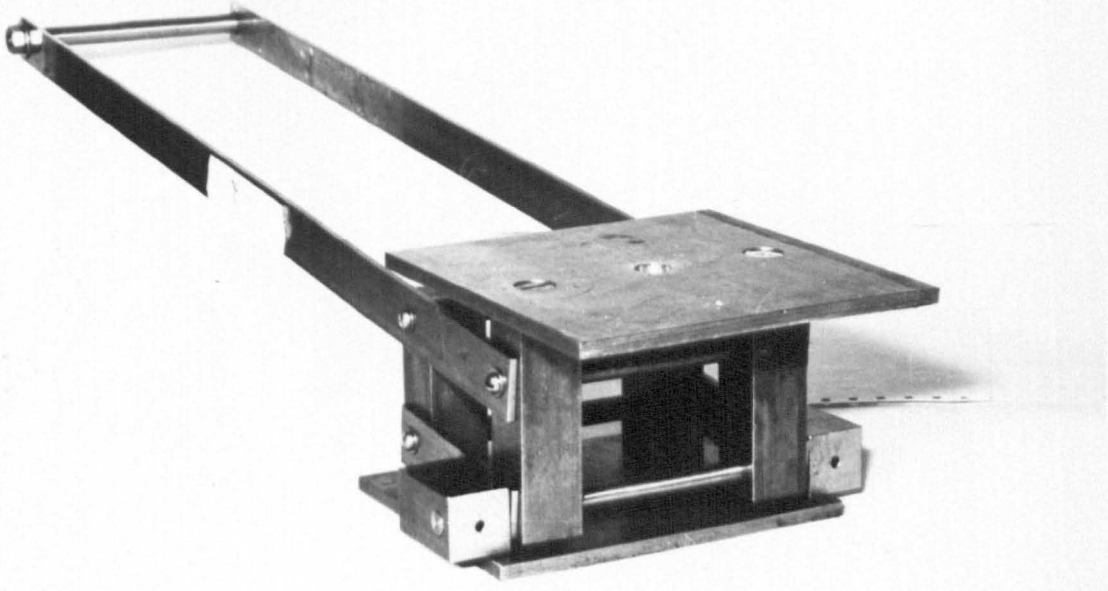

LIFTING PLATFORM FIG. 3·3

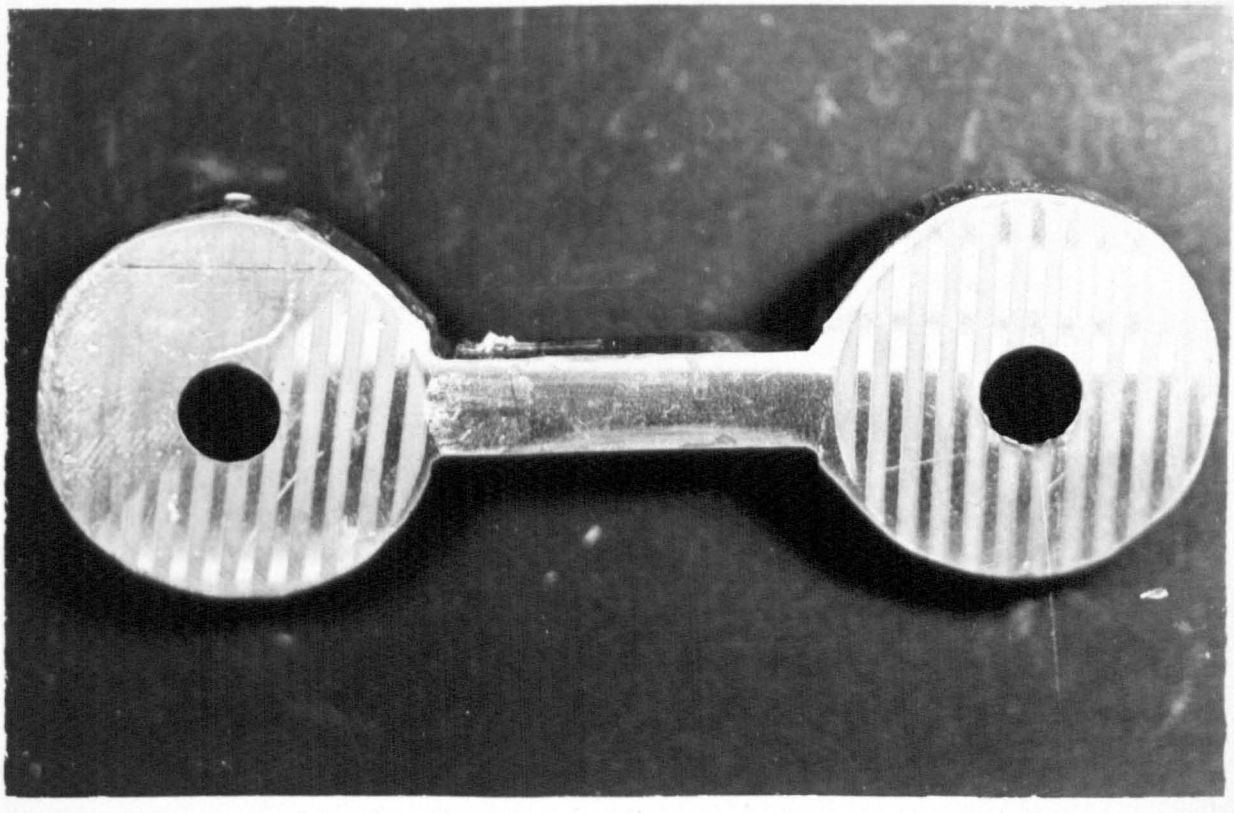

UNIAXIAL DUMBELL SPECIMEN FIG. 3·4

FIG. 3·5

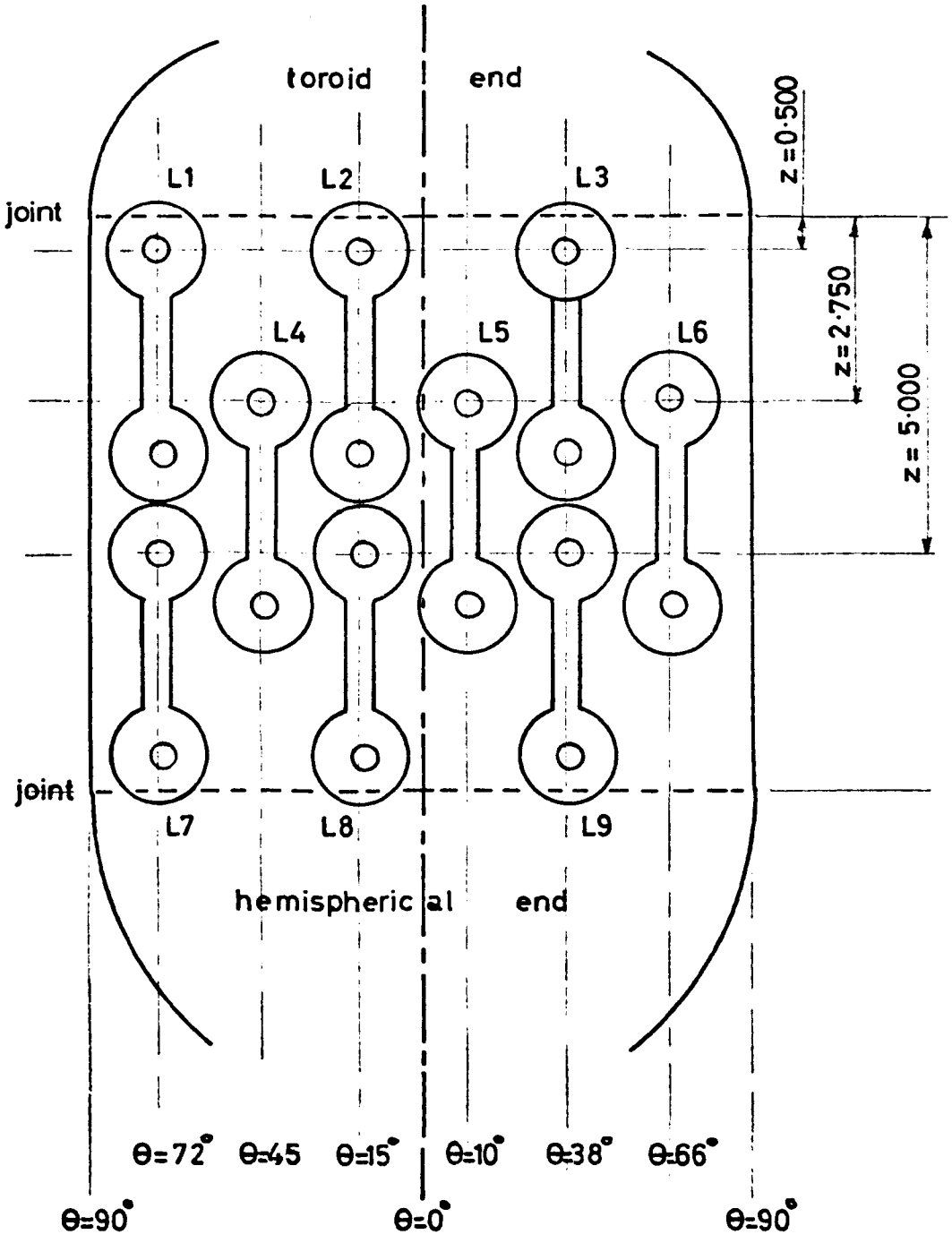

POSITIONS OF UNIAXIAL DUMBELL SPECIMENS

GROUP 1

FIG. 3·6

GROUP 1

UNIAXIAL CREEP CALIBRATION

specimens of known location
all from casing 16

STRESS LEVEL
1400 lbf/in²

○ L14/1
□ L14/2
◕ L14/3
◪ L14/4
⊗ L14/5
× L14/6
△ L14/7
◔ L14/8
◩ L14/9
——— best fit for D14 specimens
·—·—· final creep law

CREEP STRAIN (microstrain)

50 000
10 000 (1 %)
5000
1000 (0·1 %)
500
100 (0·01 %)
50

·0·1
0·5
1
5
10
50
100
500

TIME (hours)

FIG.3·7

GROUP 2

UNIAXIAL CREEP CALIBRATION

specimens from different casings

STRESS LEVEL

1400 lbf/in²

○ – – – D14/1
△ – – – D14/2
□ – – – D14/3
◕ – – – D14/4
◪ – – – D14/5
× – – – D14/6

——— best fit at 1400 lbf/in²

·——·——· final creep law

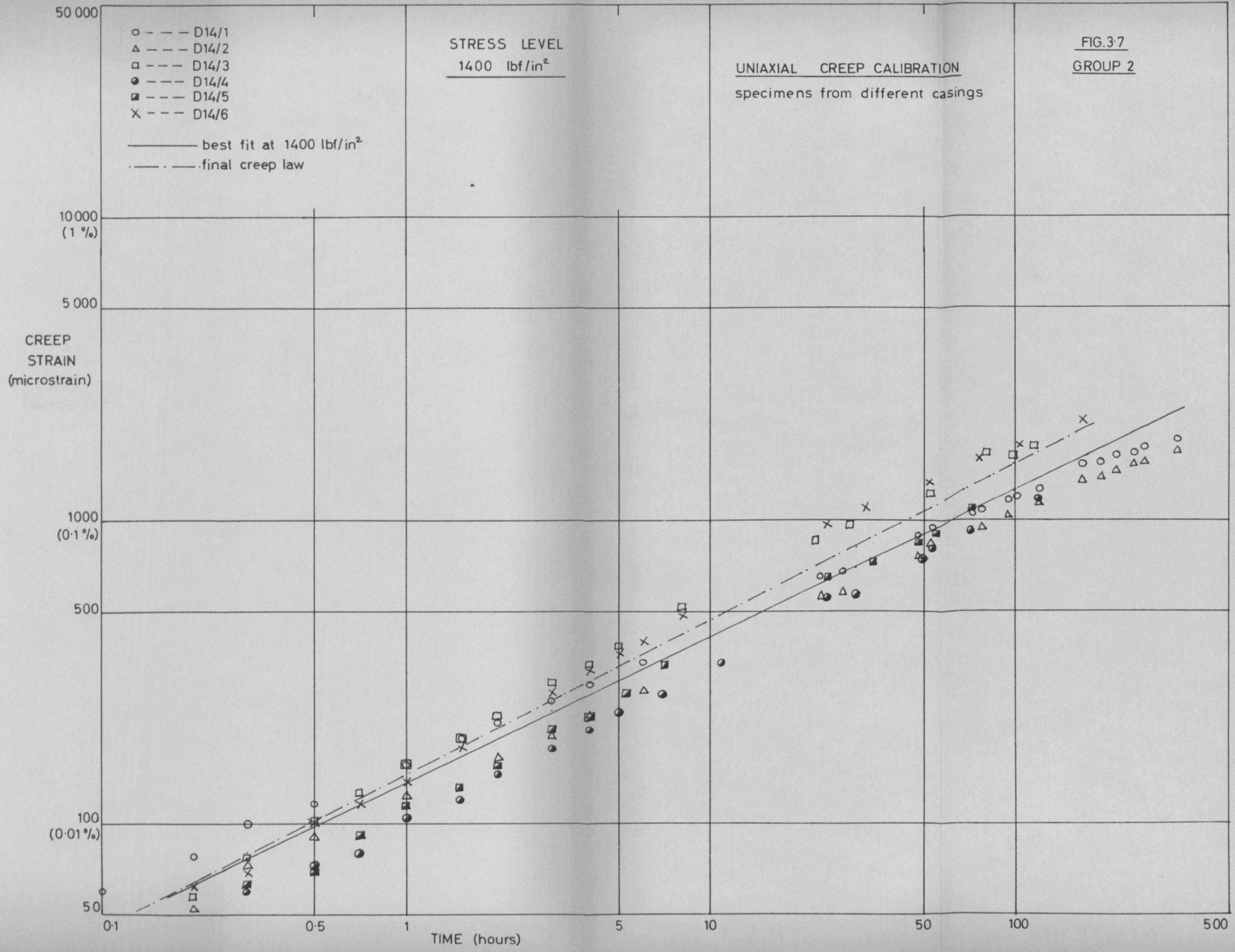

FIG. 3·8
GROUP 3

o – – – D 25/1
Δ – – – D 25/2
——— best fit at 2500 lbf/in²
·—·—· final creep law

50 000
10000 (1 %)
5000
1000 (0·1%)
500
100 (0·01%)
50

CREEP STRAIN (microstrain)

0·1
0·5
1
5
10
50
100
500

TIME (hours)

STRESS LEVEL
2500 lbf/in

UNIAXIAL CREEP CALIBRATION

FIG. 3·9

GROUP 3

□ – – – D 22/1

△ – – – D 22/2

○ – – – D 22/3

◪ – – – D 22/4

——— best fit at 2200 lbf/in²

·—·—· final creep law

50000

10 000
(1 %)

5 000

CREEP
STRAIN
(microstrain)

1 000
(0·1%)

500

100
(0·01%)

50

0·1

0·5

1

5

10

50

100

500

TIME (hours)

STRESS LEVEL

2200 lbf/in²

UNIAXIAL CREEP CALIBRATION

FIG. 3·10

GROUP 3

UNIAXIAL CREEP CALIBRATION

STRESS LEVEL

1900 lbf/in²

□ - - - D19/1

○ - - - D19/2

● - - - D19/3

——— best fit at 1900 lbf/in²

·— · —· final creep law

STRAIN (microstrain)

50 000

10 000 (1 %)

5 000

1 000 (0·1 %)

500

100 (0·01 %)

50

0·1

0·5

1

5

10

50

100

500

TIME (hours)

FIG. 3·11

GROUP 3

UNIAXIAL CREEP CALIBRATION

STRESS LEVEL
1600 lbf/in

△ – – – D16/1
□ – – – D16/2
○ – – – D16/3
——— best fit at 1600 lbf/in
·—·—· final creep law

STRAIN
(microstrain)

50 000
10 000 (1%)
5 000
1000 (0·1%)
500
100 (0·01%)
50

0·1
0·5
1
5
10
50
100
500

TIME (hours)

STRESS LEVEL
1200 lbf/in²

UNIAXIAL CREEP CALIBRATION

FIG. 3·12
GROUP 3

△ — — — D12/1
○ — — — D12/2
● — — — D12/3
□ — — — D12/4
◪ — — — D12/5
× — — — D12/6
——— best fit at 1200 lbf/in²
·— · —· final creep law

CREEP STRAIN (microstrain)

50 000
10 000 (1 %)
5 000
1 000 (0·1%)
500
100 (0·01%)
50

0·1
0·5
1
5
10
50
100
500

TIME (hours)

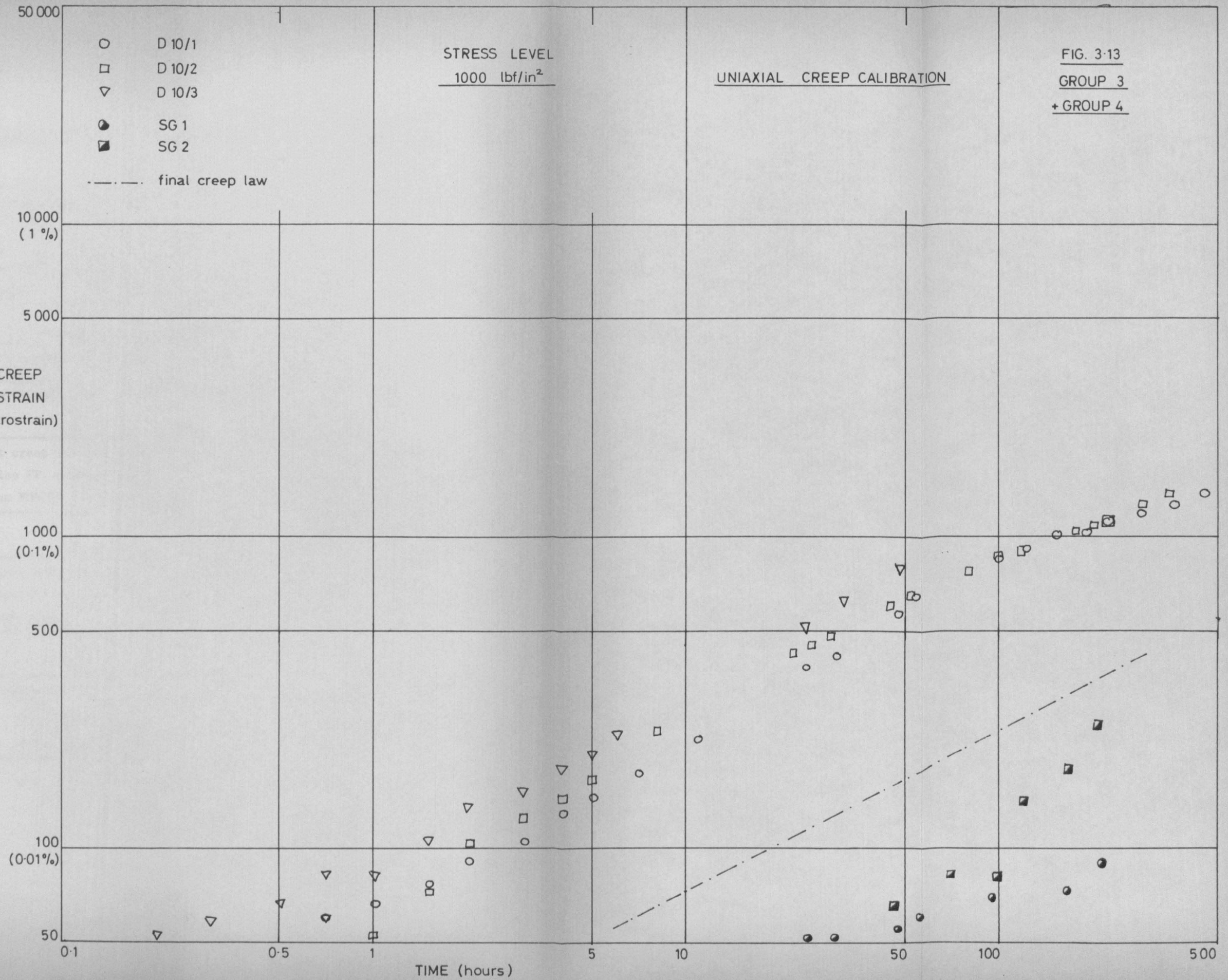
50 000
10 000
(1 %)
5 000
1 000
(0·1%)
500
100
(0·01%)
50
CREEP
STRAIN
(microstrain)
D 10/1
D 10/2
D 10/3
SG 1
SG 2
final creep law
STRESS LEVEL
1000 lbf/in²
UNIAXIAL CREEP CALIBRATION
FIG. 3·13
GROUP 3
+ GROUP 4
0·1
0·5
1
5
10
50
100
500
TIME (hours)

FLOW DIAGRAM OF CREEP LAW CALCULATION

FIG. 3.14

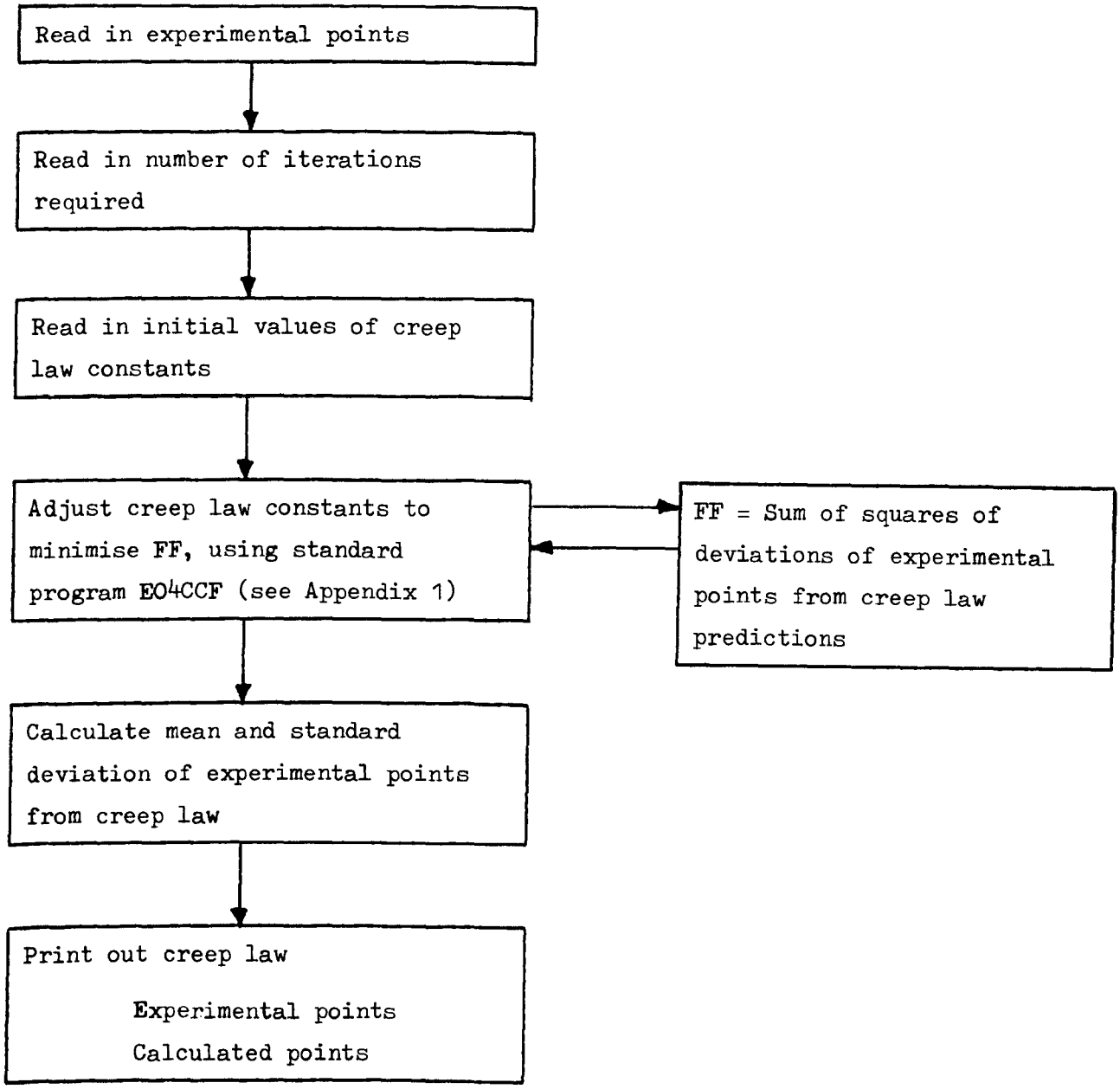

UNIAXIAL CREEP CALIBRATION

FIG. 3·15

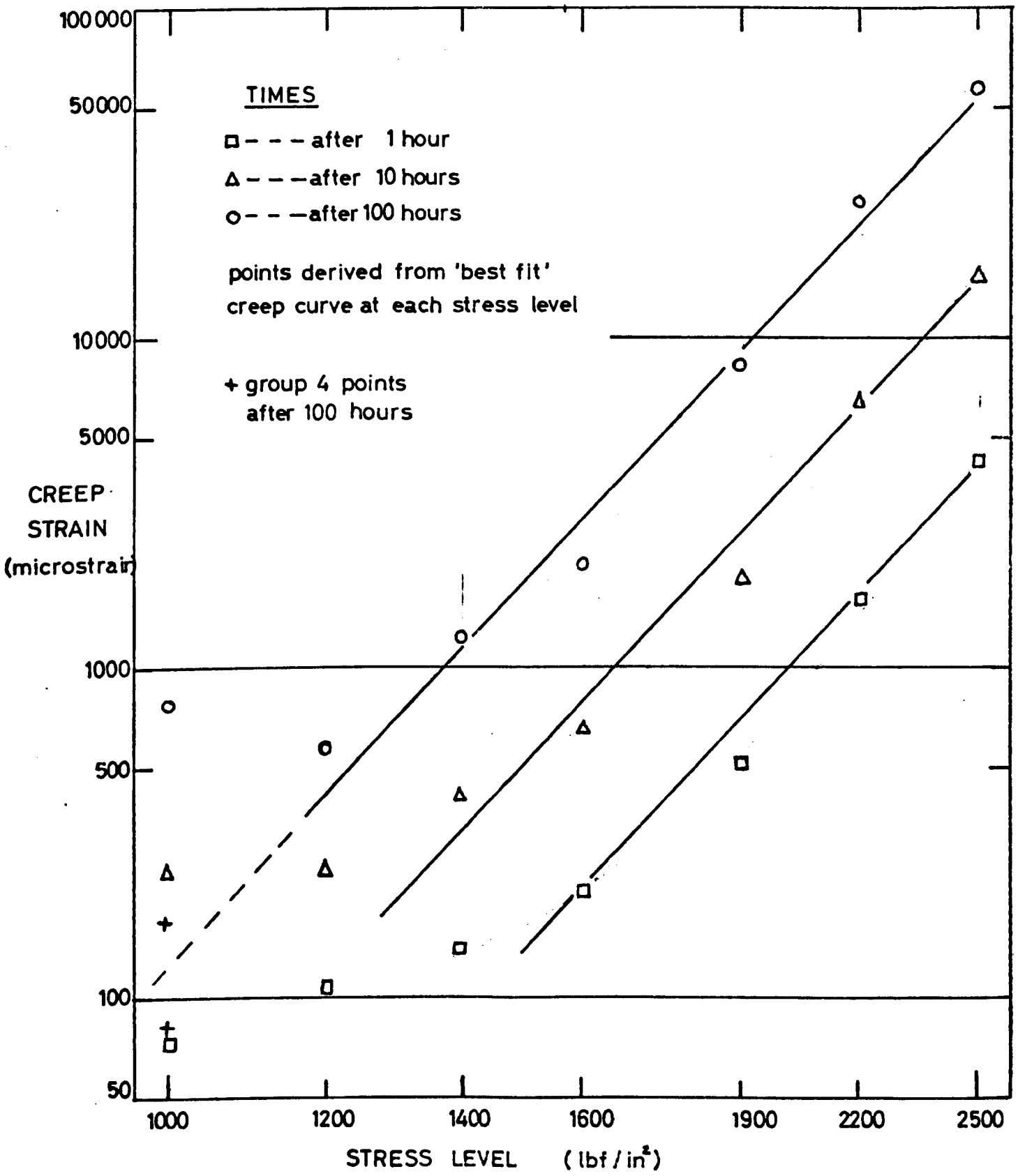

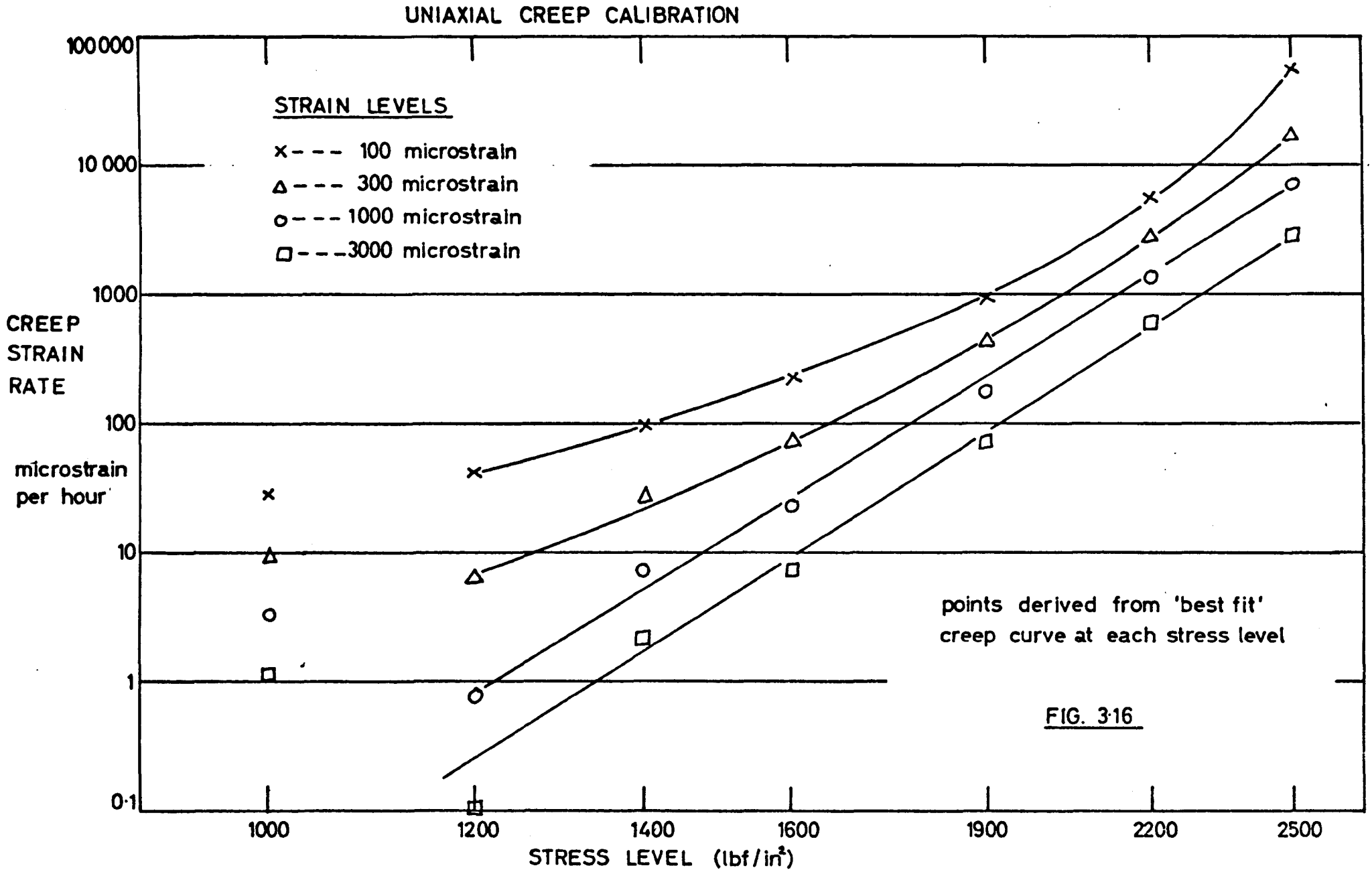
UNIAXIAL CREEP CALIBRATION
STRAIN LEVELS
× - - - 100 microstrain
△ - - - 300 microstrain
○ - - - 1000 microstrain
□ - - - 3000 microstrain
CREEP STRAIN RATE
microstrain per hour
100 000
10 000
1000
100
10
1
0·1
1000
1200
1400
1600
1900
2200
2500
STRESS LEVEL (lbf/in²)
points derived from 'best fit' creep curve at each stress level

FIG. 3·16

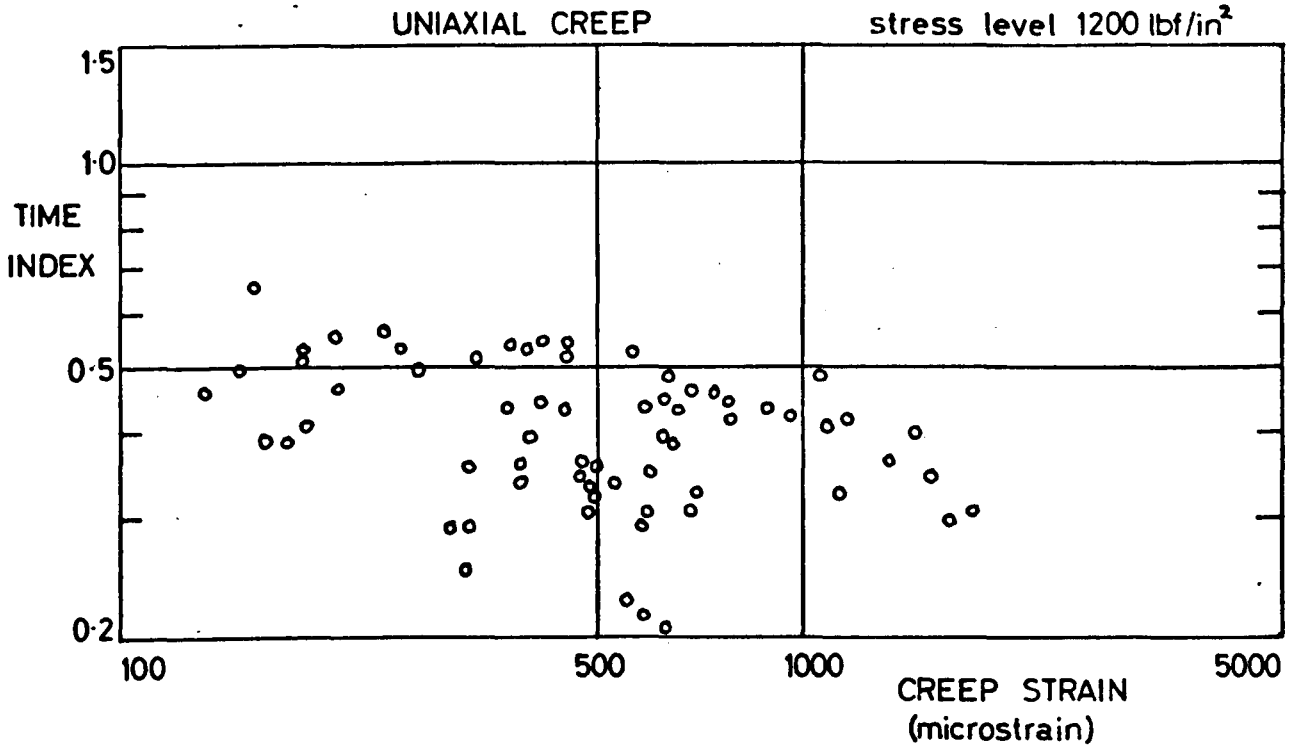

FIG. 3·17

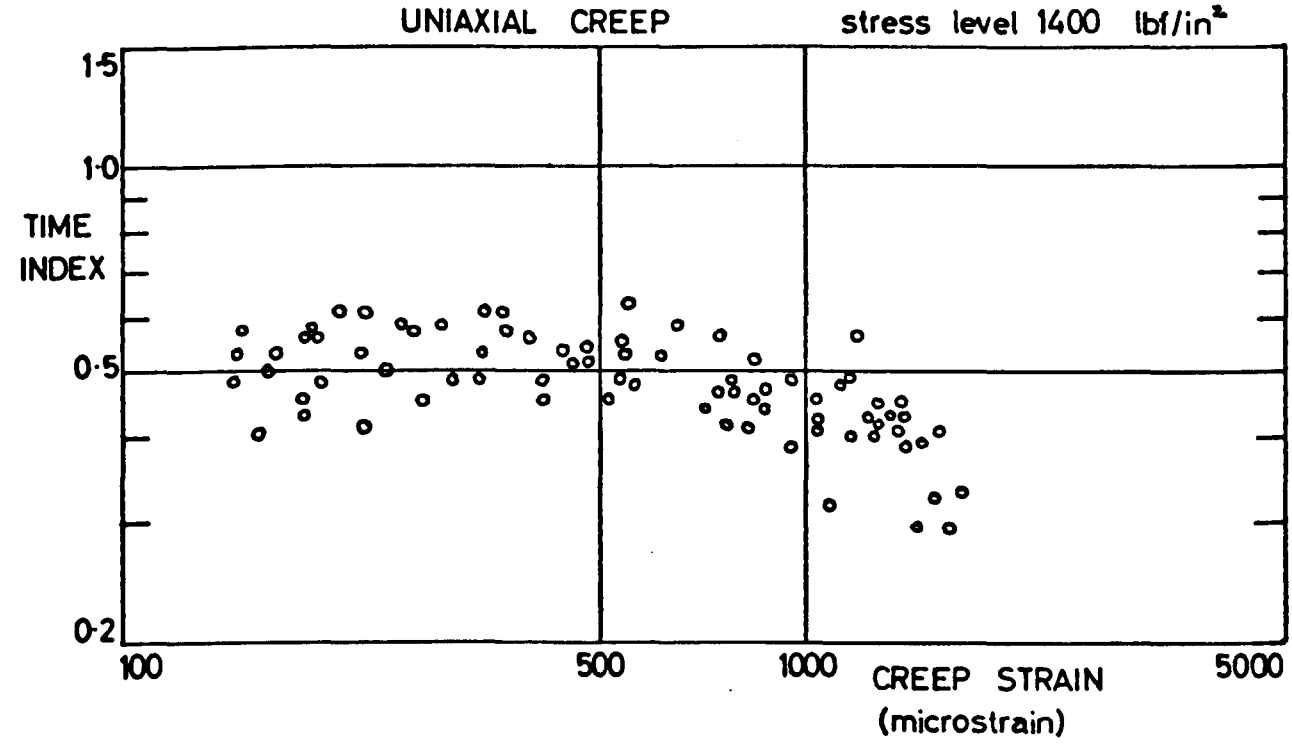

FIG. 3·18

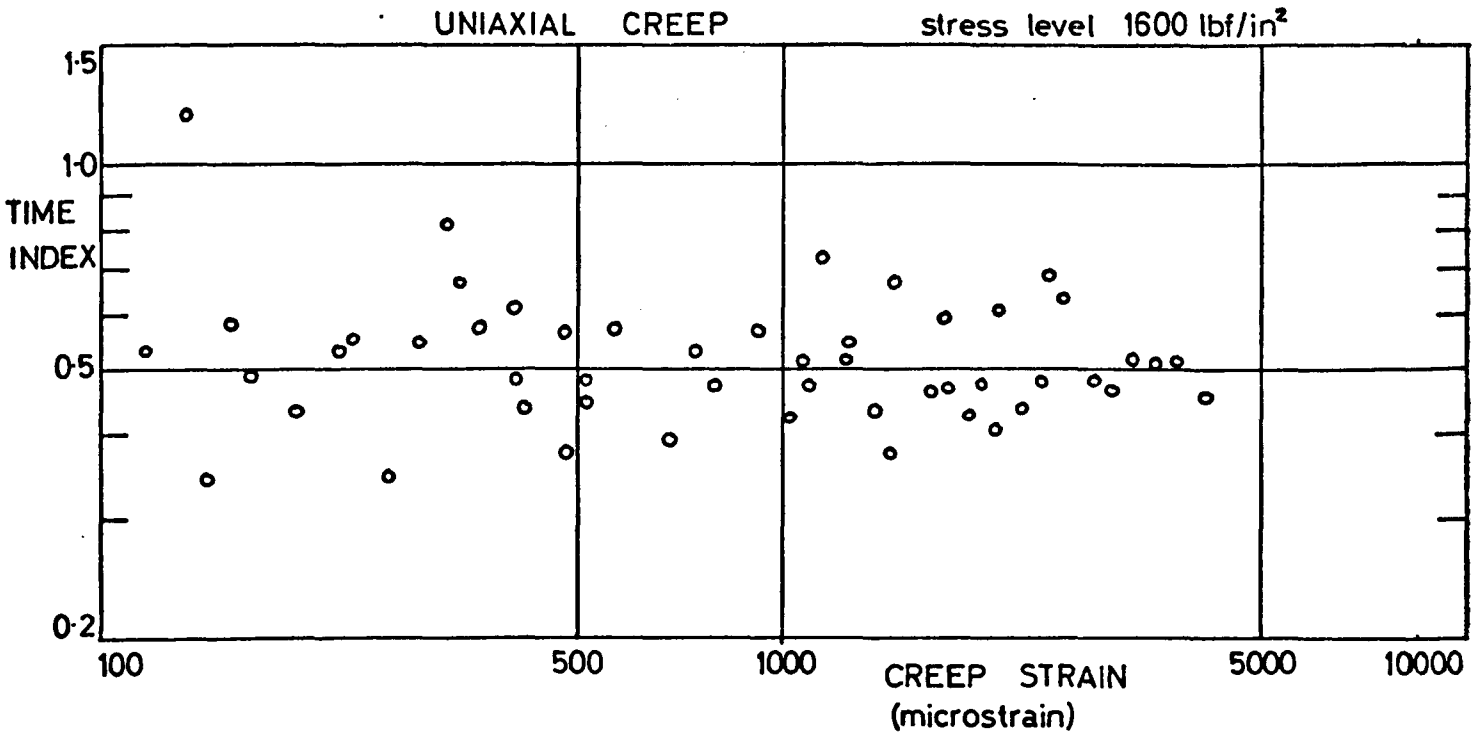

FIG. 3·19

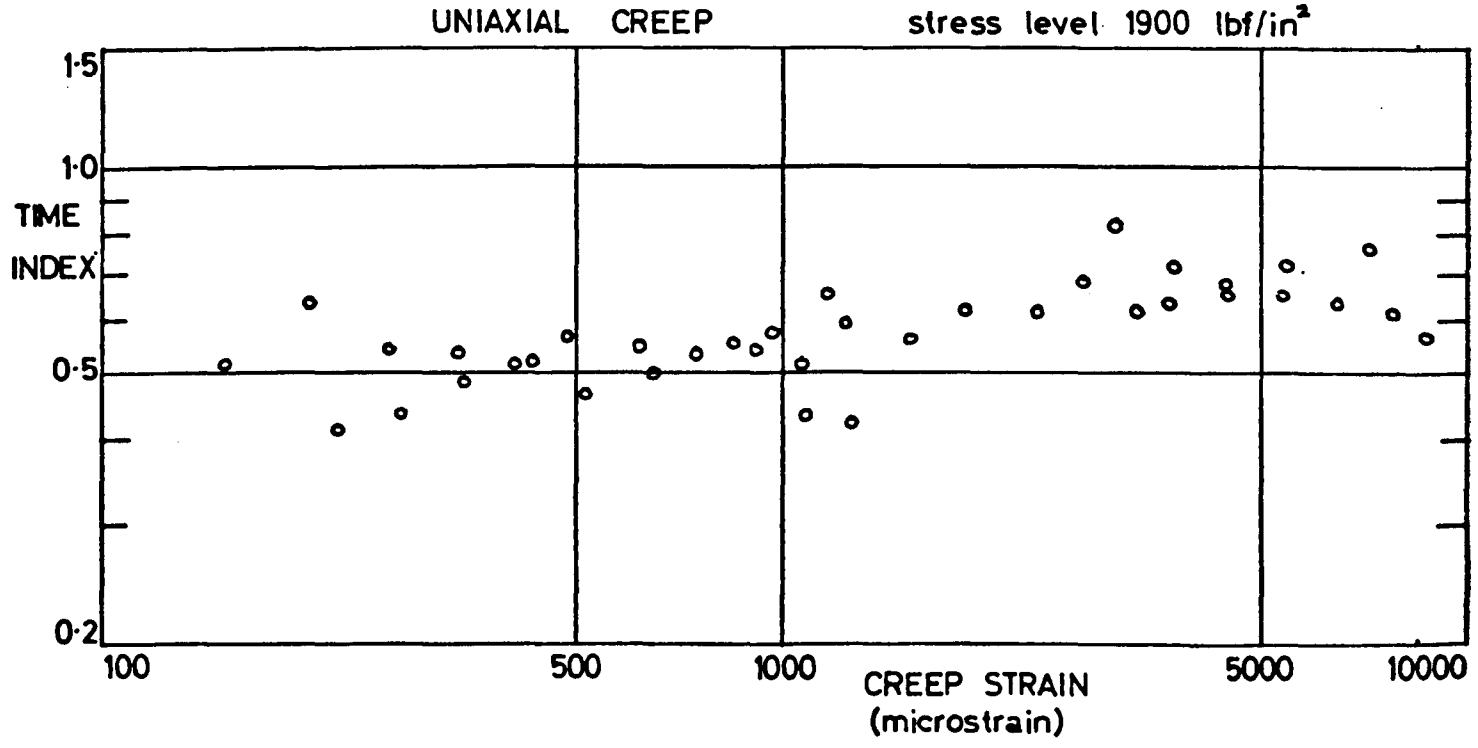

FIG. 3·20

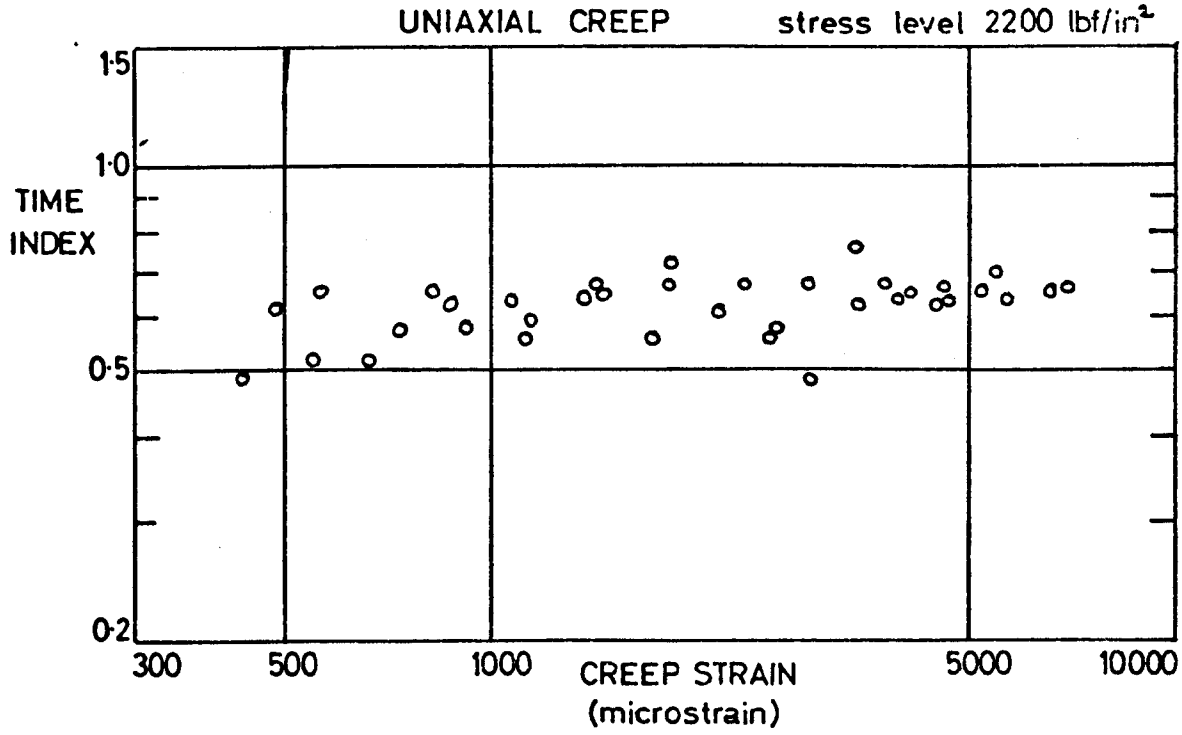

FIG. 3·21

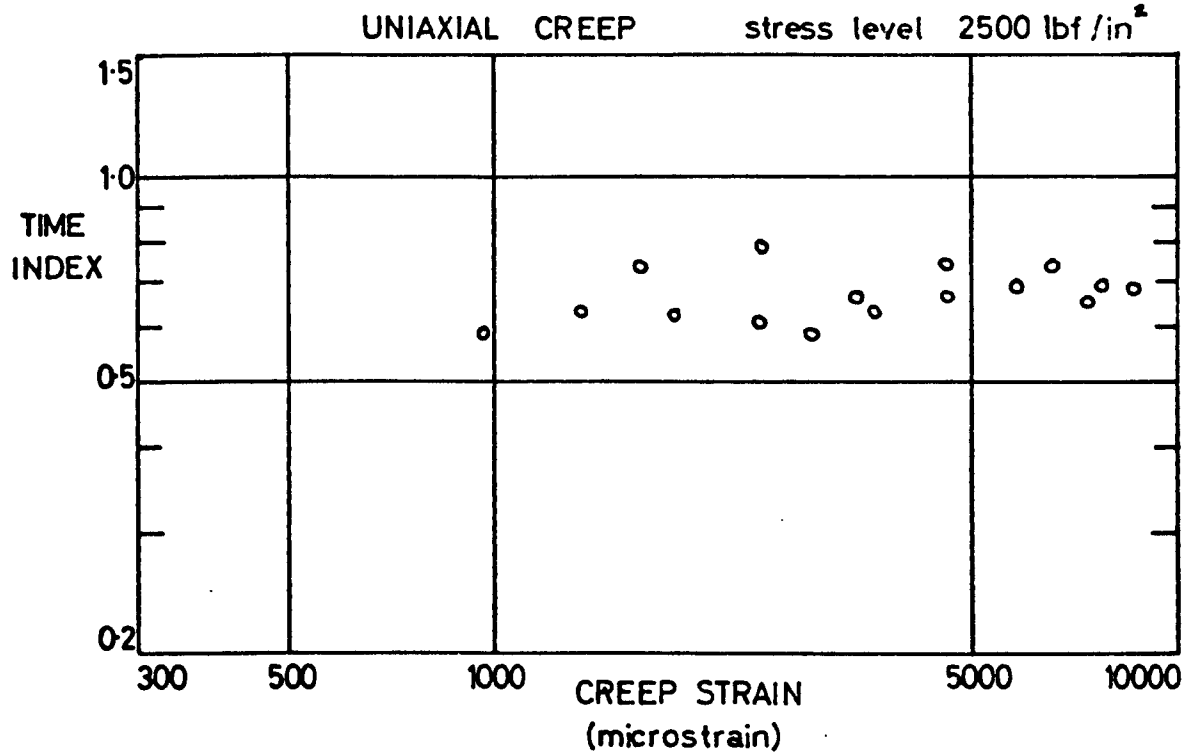

FIG. 3·22

UNIAXIAL CREEP CALIBRATION

GEOMETRIC MEAN CREEP STRAIN RATES AT GEOMETRIC MEAN STRAINS

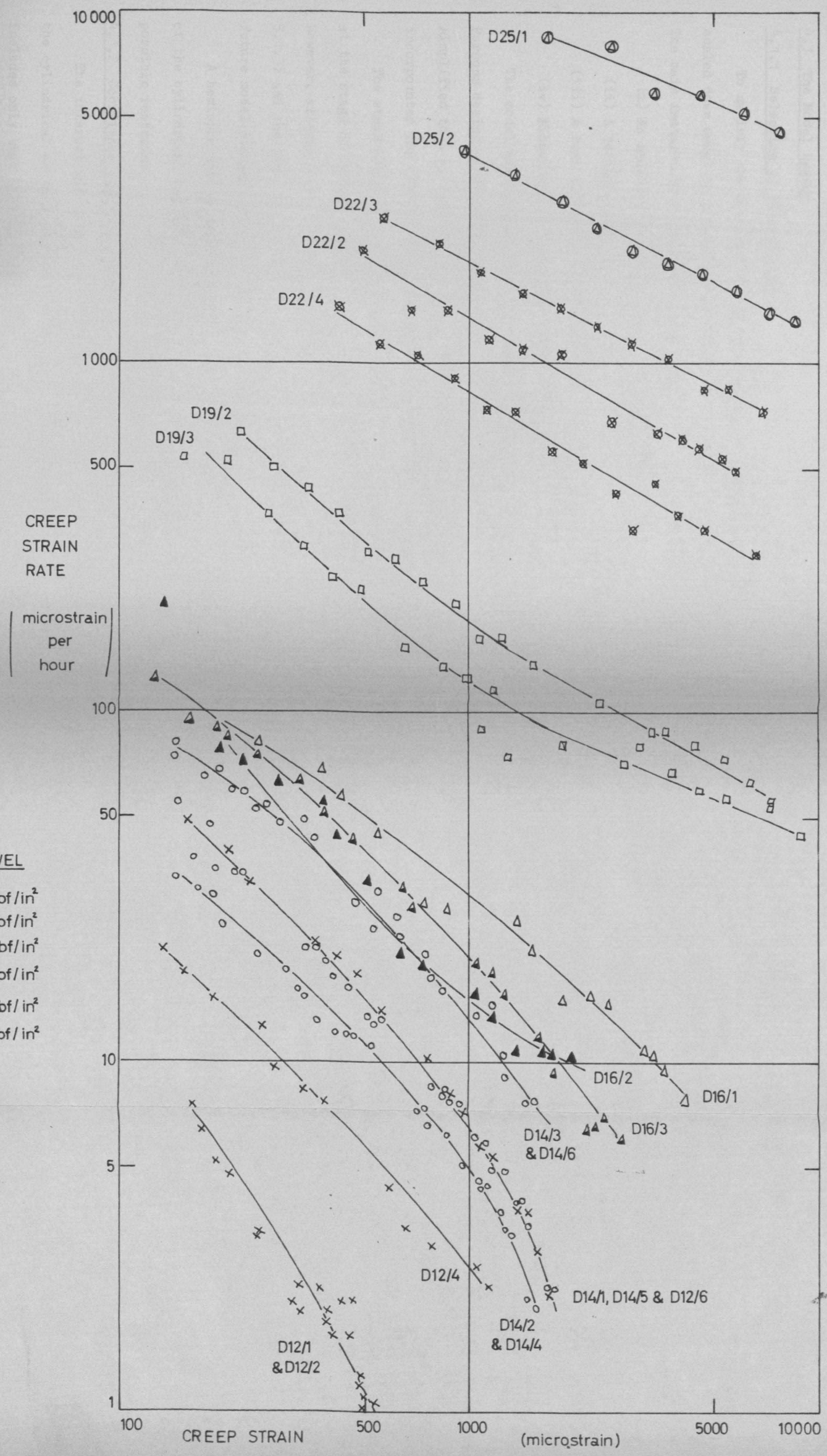

FIG. 3·23

CHAPTER 4

The Model

4.1 The Model Design

4.1.1 Selection of model design

To satisfy the similarity conditions described in Section 2.2, a scaled down model of the prototype steam turbine casing must be used. The main features to be modelled were:

(i) An axially split casing with a bolted flanged joint.

(ii) A torispherical end closure.

(iii) A boss surrounding the shaft holes.

(iv) Either one or two steam entry nozzles in each half casing.

The model was scaled from the Intermediate Pressure casing of a Parsons design of steam turbine to 1/12 full size. The shape was simplified to a cylinder joined to a torispherical end closure and incorporated the first three features listed above (Fig. 4.1 and 4.2).

The steam inlet nozzles were features too complicated to incorporate at the stage of the development of the techniques, so they were omitted. However, allowance was made in the design of the casting mould (Section 5.1.3) and the test rig (Section 6.1.3) to incorporate these features in future model designs, when the techniques have been proved.

A hemispherical end closure with a boss was joined to the other end of the cylindrical section. This was to close the model with the least possible restraint of or disturbance to the cylinder.

4.1.2 Coordinate system for model

The interest was in the torispherical end closure, and its effect on the cylindrical section, so the coordinate system shown in Fig. 4.3 includes only that part of the model.

Positions on the casing are located on meridional planes through the axis of the model inclined at an angle 'Θ' to the plane perpendicular to the flange joint. In the cylindrical section the position along this plane is given as the axial distance 'z' from the toroid/cylinder joint, and in the toroid the position is given as the angle 'Ø' subtended at the centre of curvature with the toroid/cylinder joint.

The bolt holes are numbered, beginning with the one adjacent to the toroid boss. Bolt hole No. 5 has its centre line in the plane of the toroid/cylinder joint.

4.2 Elastic Analysis

The elastic analysis of the model shape under internal pressure and bolt loading was carried out using the frozen stress Photoelastic technique.

4.2.1 Production of Araldite models

Because of the complicated shape of the flanged casing, models in Araldite CT200 must be cast to size and machining kept to a minimum. An attempt was made at first to cast the Araldite half-casings in the metal mould, but contraction due to curing split the casing round the steel core. Lifting the core slightly after the resin had gelled also failed, since the material still could not support its shape, and sagged.

Using a lead model as a pattern, a mould was then fabricated out of silicone rubber and Araldite, and six half casings made. However, the overall size of the castings in relation to the wall thickness allowed mould flexibility and thermal distortion to produce irregular section thicknesses in those models.

Three more pairs were then cast to size, using a new technique developed by Dr. M. Perla and Mr. B. Mynett for exact casting to size of complicated shapes. Again, using a lead model as a pattern, a very thin coating of silicone rubber is backed up by a $\frac{1}{8}$ in wall of a mixture of plaster and cold setting Araldite. This mould casing is strengthened if necessary by the inclusion of beams and cross pieces made of the same plaster and Araldite mixture. The silicone rubber lining is stuck to the plaster and Araldite mould case by sticking filter papers onto the rubber before applying the Araldite mixture. This mould, Fig. 4.4, therefore, has a thin lining which does not stick to the Araldite casing, and yields slightly to accommodate casting contraction, but has a casing which has nearly the same coefficient of thermal expansion and density as the casting material itself.

Since the Araldite castings were the same shape as the lead models, they were machined in exactly the same way, using the same jigs.

4.2.2 Loading of Araldite models

For the pressure loading of an Araldite model, the first pair of half casings were stuck together at the flange joint (Fig. 4.5). A shaft, of Araldite for the same thermal expansion coefficient as the model, was fitted with end plates in the bores to carry the end pressure load. Sticking silicone rubber (Silcoset 151) provided a flexible seal between the plates and the bores.

Considerable difficulty was experienced in loading and stress-freezing the Araldite models under internal pressure. The great flexibility of the Araldite above the stress freezing temperature aggravates the tendency of the flange joint to tear open under internal pressure; and the flange itself, while providing the cause and the pivot for this tearing action, is unfortunately too thin to provide any support or rigidity against rotation.

The dimensions and shape of the model dictate that at least 1 lbf/in^2 of pressure is required to produce reasonable fringe orders in the Araldite casings from the frozen stress technique. This is a large pressure for photoelastic work, and because of the end closures and the small bore holes, it is not possible to guarantee a perfect joint of the flange faces on the inside edge by patching from the inside.

The result is that while the model may hold pressure when cold, as soon as the freezing temperature is reached ($125^{\circ}C$), a crack starts in the flange joint from the inside and runs immediately through to release the pressure. Attempts were made to stick the joint with cold setting Araldite, sticking silicone rubber (Silcoset 151), and finally with hot setting Araldite. All failed.

The alternative was to load the model under a negative internal pressure, or suction. This overcomes the problem of sealing, since the tendency for the flange to open is reversed, and leaks can be easily sealed from the outside. For this method of loading the flange was stuck with sticking silicone rubber, and no sealing problems were encountered in the model.

However, loading the casing in compression with a necessarily large negative pressure can lead to buckling of the cylindrical section. One model was loaded and stress-frozen in oil with a suction of 2 lbf/in^2 (Fig. 4.6). Although the oil supports 75% of the model self weight, the remainder is significant. This means that the model must be loaded horizontally, supported under the flanges, so that the self weight effects are reversed for the top and bottom halves of the casing, and can be eliminated by averaging the stresses of the two halves.

When the model was removed after the stress freezing cycle, it was found that while the bottom half-casing had an inward deflection of 3/16 in in the middle of the cylindrical section, mid way between the flanges, the top half-casing had an outward deflection of 0.025 in in the same position (Fig. 4.7). Meridional slices taken from the top and bottom casings mid way between the flanges, showed an average tensile meridional stress in that plane of the cylindrical section. Clearly, the model had buckled.

When supported under the flanges, the self weight of the model tends to rotate the flanges as shown in Fig. 4.7. This will by itself cause centre plane deflections inwards at the bottom and outwards at the top. Thus, the self weight effect reduces the chance of buckling in the top half casing and increases the chance of buckling in the bottom half casing when the model is loaded in suction.

The second model was sealed in the same manner as the first and loaded under suction to obtain the stress distribution due to internal pressure. This time, to avoid any twisting of the flanges due to self weight and the consequent encouragement of buckling, the model was loaded in the vertical position (Fig. 4.8). However, any self weight loads would now cause bending in the domed ends which could not be averaged out, so to eliminate all self-weight effects, the model was loaded in Glycerine.

At 125°C, Glycerine and Araldite have virtually the same density so the self-weight of the model is completely eliminated. Glycerine was previously avoided because its use in earlier photoelastic work had caused a compressive surface stress to develop in the models con erned, similar to that caused by water absorption, but not removable. This makes surface fringe orders difficult to read, since they have to be inferred by extrapolation to the edge of the slice. The experience of some workers, however, was that this might be avoided if the surfaces of the model were smeared with silicone grease, and if new, clean Glycerine was used.

The second model, therefore, was smeared with silicone grease and immersed in new Glycerine. A device with a scissors action and a dial gauge (Fig. 4.8) was made so that the diameter of the cylinder could be measured while it was loaded. When the stress freezing temperature (125°C) was reached, the vacuum was increased in stages, the diameter being measured half an hour after each increase. Buckling of the model would be shown both by a large diameter change in the middle of the cylinder and by a large change in the glycerine level in the main reservoir, allowing immediate recovery by reducing pressure while the model was still above 125°C. In this way the model was loaded without buckling at about 1.5 lbf/in^2.

The third model was to have been used to obtain the stress distribution due to the bolt loading. However, it was found that the hole positions in the machined model were wrong, displaced 1/16 in outside the mid point of the flange. The model was loaded in spite of this, since although no correct detailed stress distribution was possible, some useful indications of the effect of bolt loading on the stresses in the casing and flange could be obtained.

The load was applied by 'soft' compression springs, previously calibrated, held down by long bolts through the bolt holes to a predetermined length. This guarantees a known bolt load which will not change significantly with small dimension changes in the flange (Fig. 4.9). The model, coated with silicone grease, was supported on blocks under the bolts, and totally immersed in Glycerine when undergoing the stress freezing cycle. Thus, the weight of the bolts and the springs was taken by the supporting blocks, while the self-weight of the model was taken hydrostatically by the Glycerine.

Because of the low Young's modulus of Araldite above 125°C, the spring load was applied through Araldite washers. This gives the bolt load stress distribution of a steel bolt clamping a steel flange. However, for the creep tests on the lead models, steel dummy bolts were used; so some of the flexibility of the Araldite washers was removed by making them thin and backing them with steel washers.

4.2.3 Photoelastic Results

When the model was removed from the oven after loading under suction, it was found that one casing contained a series of longitudinal cracks in the middle of the cylindrical section. These cracks, probably due to a material fault, did not penetrate the shell and the model had maintained pressure during the loading cycle, so the stresses due to pressure were obtained from the other casing.

The slicing plan of the pressure model for meridional slices is shown in Fig. 4.10, and for hoop slices in Fig. 4.11. Hoop slices in the toroid section were obtained by subslicing meridional slices as shown. The slices cut on a slitting machine, were 0.200 in thick to give adequate fringe orders from the low stresses.

A test strip was cut from the model and reloaded under uniaxial tension through the stress freezing cycle to determine the material fringe value; and an equilibrium stress separation was performed on a small section from the $\theta = 0^{\circ}$ meridional slice, in the middle of the cylinder, to determine the exact test pressure (see Appendix 2).

Material Fringe Value = 1.41 lbf/in^2/fringes per inch

Test pressure = -1.531 lbf/in^2

The stresses, divided by the test pressure, are presented as stress indices, and are plotted along the line of the mean casing thickness.

The measurement positions in a meridional section are shown for the casing in Fig. 4.12, and for the flange ($\theta = 90^{\circ}$) in Fig. 4.13. The measurement positions in a hoop section are shown in Fig. 4.14.

The meridional stress distributions are shown in Fig. 4.15 to 4.18, and the hoop stress distributions are shown in Fig. 4.19 to Fig. 4.35. These stresses are due to internal pressure only.

The bolt loading model, whose flanges had been glued together with hot-setting Araldite, showed tensile stresses on the inside surface at the flange joint, so no results are plotted. However, a meridional slice at the $\theta = 0^{\circ}$ section showed zero meridional stresses along the whole section; and hoop slices in the cylinder showed that the influence of the bolt loading in the casing diminished rapidly away from the flange.

4.2.4 Discussion of results

The finite element analysis of Parkes (41) showed that the principal stress directions remained hoop and meridional over most of the casing. Only near the flange and the end boss did the directions deviate slightly.

The results from the bolt loading model show that the stress distribution in the casing is very little affected by the bolt loading, a conclusion which is supported by Parkes, whose meridional stress distribution for combined pressure and bolt loading in the $\theta = 0^{o}$ meridional section is compared in Fig. 4.15 with the photoelastic result for pressure only.

The conclusion from this is that the stress distribution in the casing due to combined pressure and bolt loading is close enough to that from pressure loading alone, to allow the positioning of strain gauges at stress peaks and the calculation of approximate elastic strains for the lead model tests to be based on the photoelastic result for pressure loading alone.

In the toroid section, the photoelastic pressure results agree closely with Parkes' analysis (Fig. 4.15). However, in the cylinder, while the bending dies rapidly away according to the finite element analysis, the photoelastic results show a uniform bending along the length of the cylinder. The deformed photoelastic casing showed a deflection of nearly $\frac{1}{8}$ in at position 'w'. This large deflection in the cylinder leads to similar differences in the hoop stress distribution. Fig. 4.35 compares the hoop stresses along the $\theta = 0^{o}$ meridional section for the photoelastic and finite element analyses. Again, the photoelastic casing shows large bending in the cylinder, while the finite element analysis shows virtually none. In the toroid, there is reasonable agreement, and the mean stress levels are close in both the toroid and the cylinder.

Two reasons are suggested for the large amount of bending in the cylindrical section of the photoelastic model.

Firstly, in order to obtain fringe orders large enough to read, a large pressure was used to load the model. This leads to large deflections, particularly in the cylinder. The meridional bending in the cylinder arises from being restrained by the much stiffer toroid end section, so the greater the difference in movement between the cylinder and the toroid end section, the greater and more extensive will be the meridional bending in the cylinder. A similar effect results from the other end of the cylinder being attached to the spherical end section, and in this case the deflection of the cylinder is so great that the meridional bending from each end has run together and prevented any decay along the length.

Secondly, it is possible that the flange faces did not remain completely flat under load. Although the cracks in the other casing (Section 4.2.3) did not affect the pressure, since they did not penetrate the wall, they would prevent the development of any significant bending in that casing to completely react the moment at the flange face generated by the other half. This would allow the flange to rotate slightly, relieving the bending at the flange fillet radius, but aggravating the outward bulge in the casing adjacent to the flange and the inward movement at the $\Theta = 0^{\circ}$ position (ih in Fig. 4.14). This would tend to reproduce the kind of condition of the collapsed model (Section 4.2.2 and Fig. 4.7), and thus lead to greatly increased bending in the hoop direction in the middle of the cylindrical section. It would appear, therefore, that the middle of the cylinder of the photoelastic casing from which the results were taken was close to the buckling condition under the suction applied and that as a result of this, the photoelastic results in that region show much more bending than would be expected for the same model under internal pressure.

The results from the faulty bolt loading photoelastic test emphasise the difficulties arising from a thin flange. Although displaced only 1/16 in outside the mid point of the flange the positioning of the bolt holes resulted in a net tension at the flange interface on the inside surface from a compressive bolt clamping load. Although not a true 'point load', the bolt forces had not spread to the inside edge of the flange before the flange interface was reached. This is in addition to the bolt holes being forced away from the inside edge because of interference with the casing wall.

The main interest is in the toroid end section. Here, the hoop stresses are relatively low, except in the region of the boss (Fig. 4.19 to Fig. 4.28). The meridional stresses, however, (Fig. 4.15 to Fig. 4.17) show the expected bending peaks near the middle of the toroid curve, from the axial movement of the boss under the end pressure load. This peak is greatest in the $\theta = 0^{\circ}$ meridional plane, and reduces round towards the flange.

In the $\theta = 60^{\circ}$ meridional plane (Fig. 4.17), the mean value of the surface meridional stresses starts to drop off before reaching the cylindrical section, and the sense of the bending changes near to position 'r' in the cylinder. This plane is approximately in the middle of the bulge adjacent to the flange in the cylindrical section where the large hoop bending has reversed the camber of the cylinder wall, reversing the sense of the meridional bending and pulling down the mean value. So although the shape of the meridional stress distribution in the toroid section represents the expected pattern in the lead model, the peak value shown in Fig. 4.17 is probably too low.

4.2.5 Conclusions

The photoelastic analysis had two purposes. Firstly, from the elastic distribution of surface stresses in the model due to pressure and bolt loading, positions of interest could be selected for the mounting of strain gauges on the lead models undergoing the creep tests. Secondly, the expected elastic strains in these positions on the lead models could be calculated.

The conclusions of the photoelastic analysis, and comparison with the finite element analysis of Parkes (41) are:-

1. The meridional stress distribution in the toroid section is as shown in Fig. 4.15 to 4.18. The true value of the mid-toroid peak in the $\theta = 60^{\circ}$ plane, however, is probably higher than that shown in Fig. 4.17.
2. The hoop stress distribution in the toroid section is as shown in Fig. 4.19 to Fig. 4.28, and in Fig. 4.35.
3. The meridional stresses dominate in the toroid section, the peak values occurring at position 'ℓ' (Fig. 4.12) on the inside and outside surfaces.
4. The hoop stresses dominate in the cylindrical section, but reach their greatest magnitude away from the end closures.
5. In the toroid boss, both hoop and meridional stresses are large in the fillet radius.
6. Future photoelastic analyses on similar casing should be carried out on models made in one piece (without the axial split along the flange) and loaded under internal pressure.

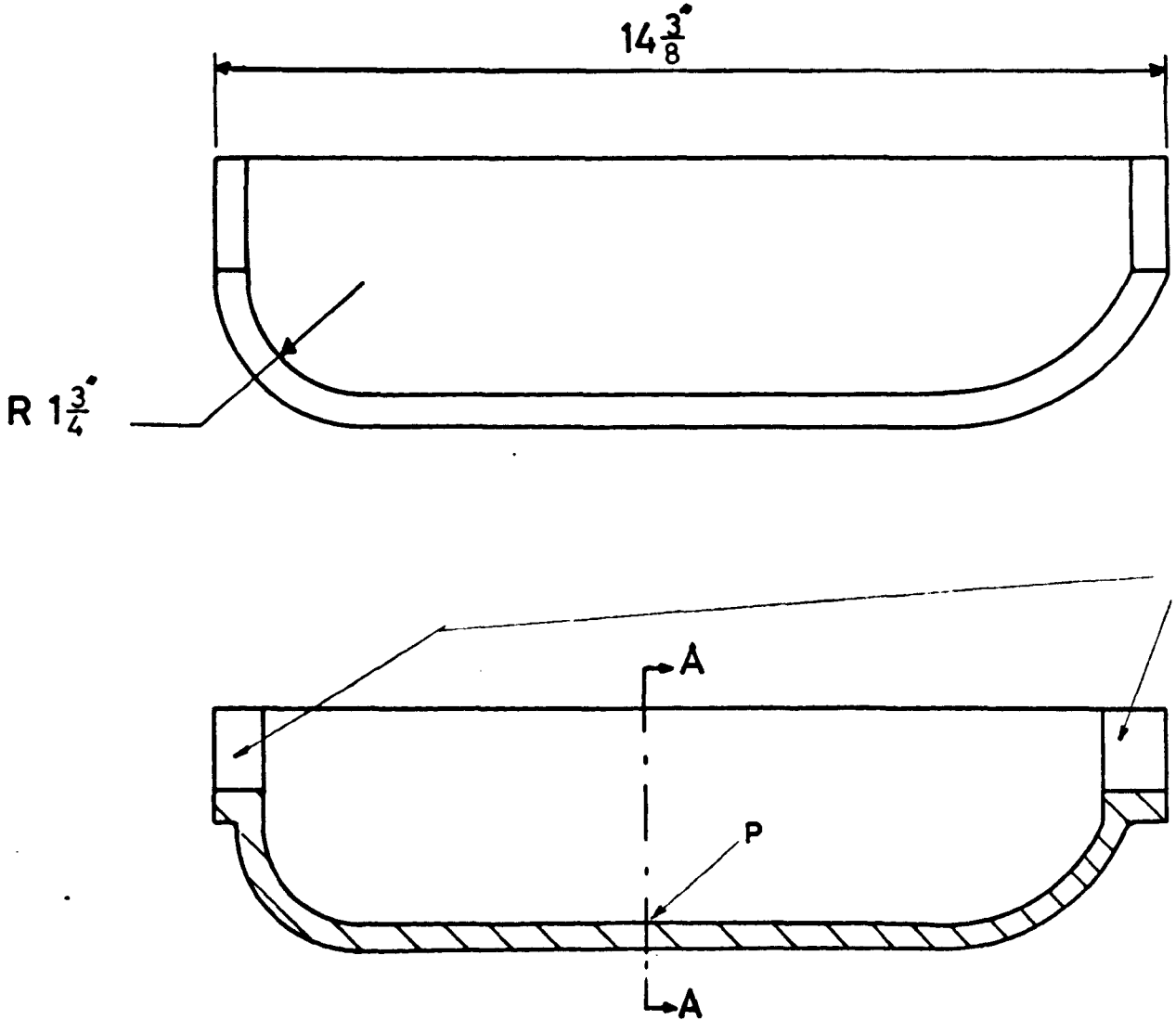

FIG. 4.1 LEAD MODEL

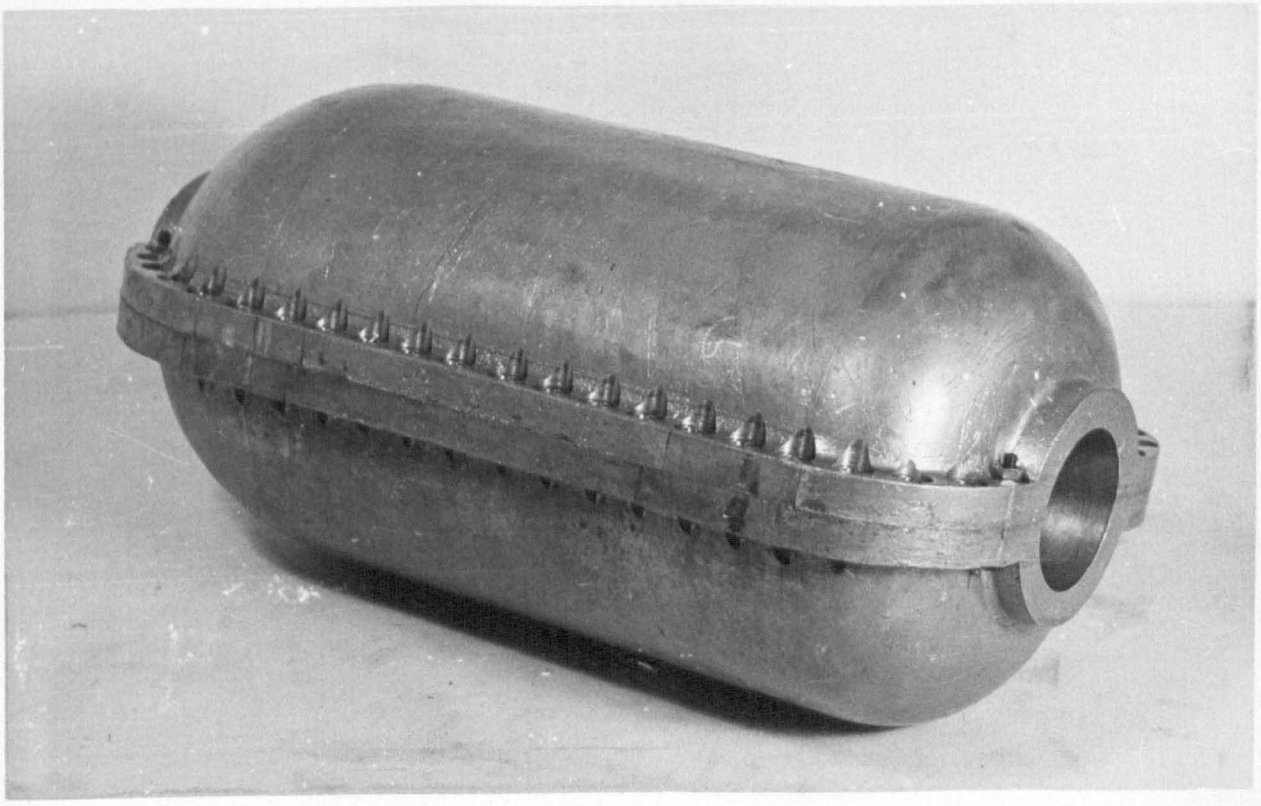

LEAD MODEL

FIG. 4·2

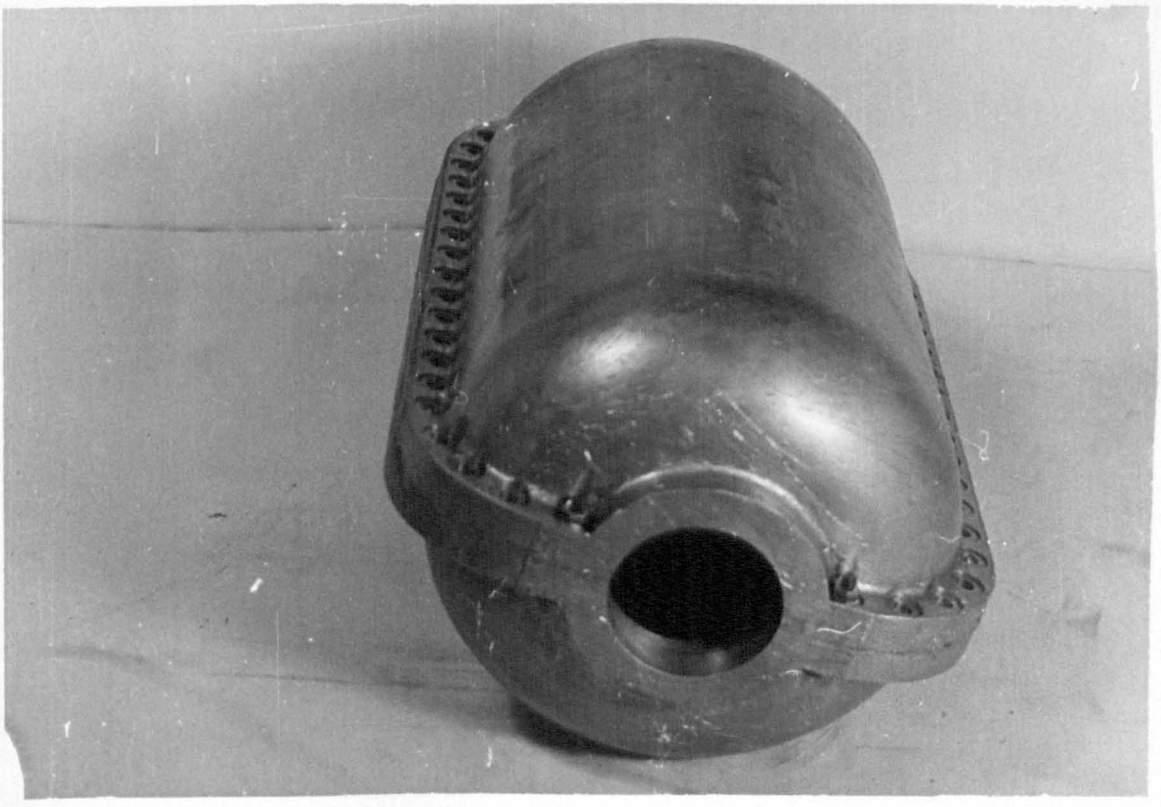

COORDINATE SYSTEM FOR MODEL

FIG. 4·3

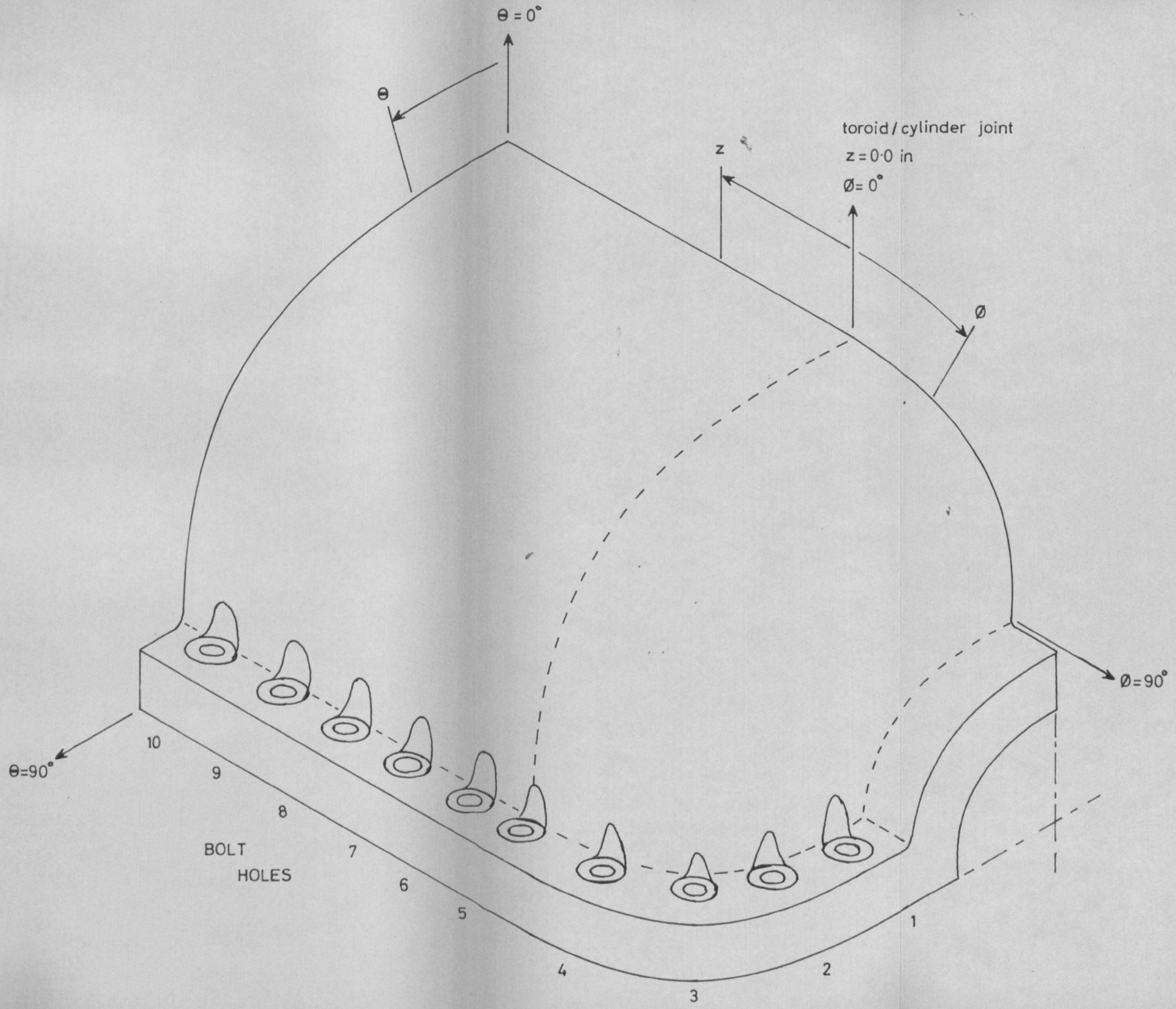

ARALDITE MOULD

FIG. 4·4

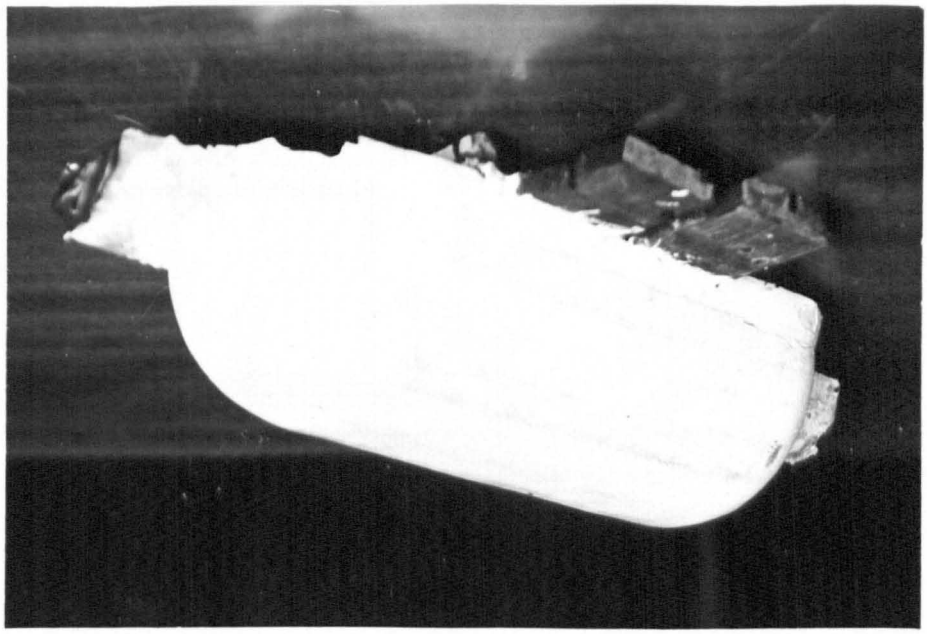

CORE

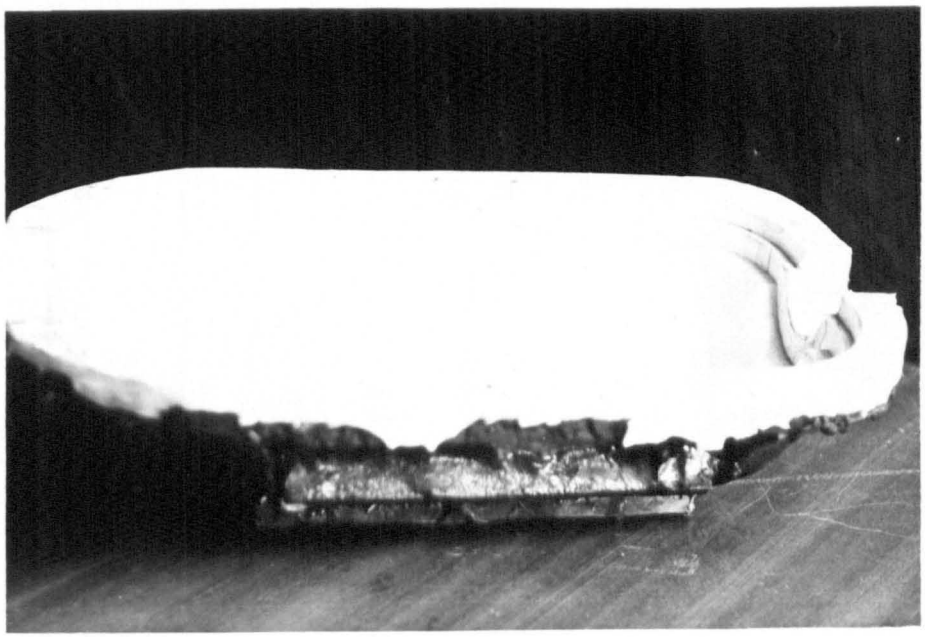

BASE

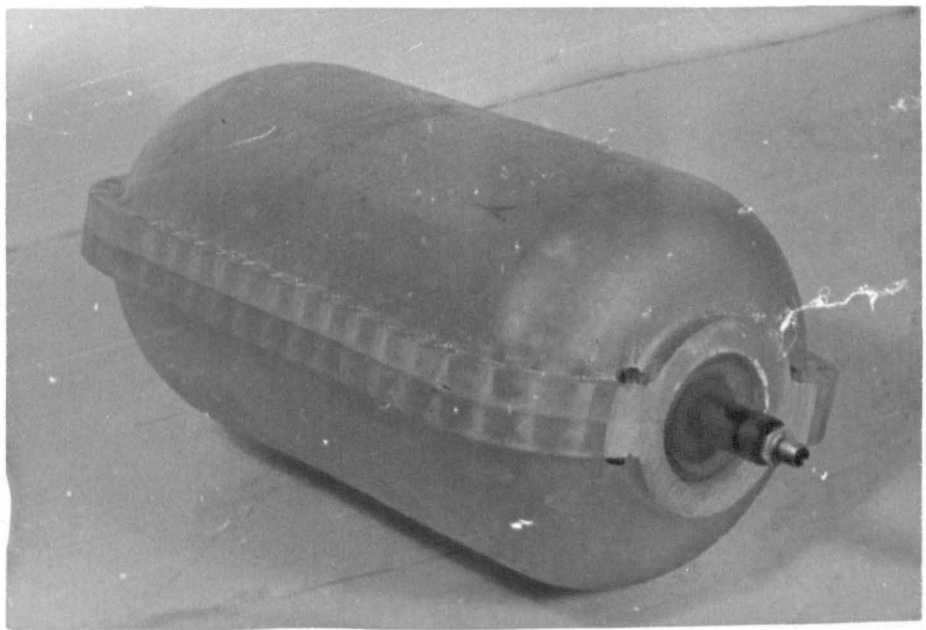

FIG. 4·5

ARALDITE MODEL

ARALDITE MODEL - 1 st. PRESSURE LOADING

FIG. 4·6

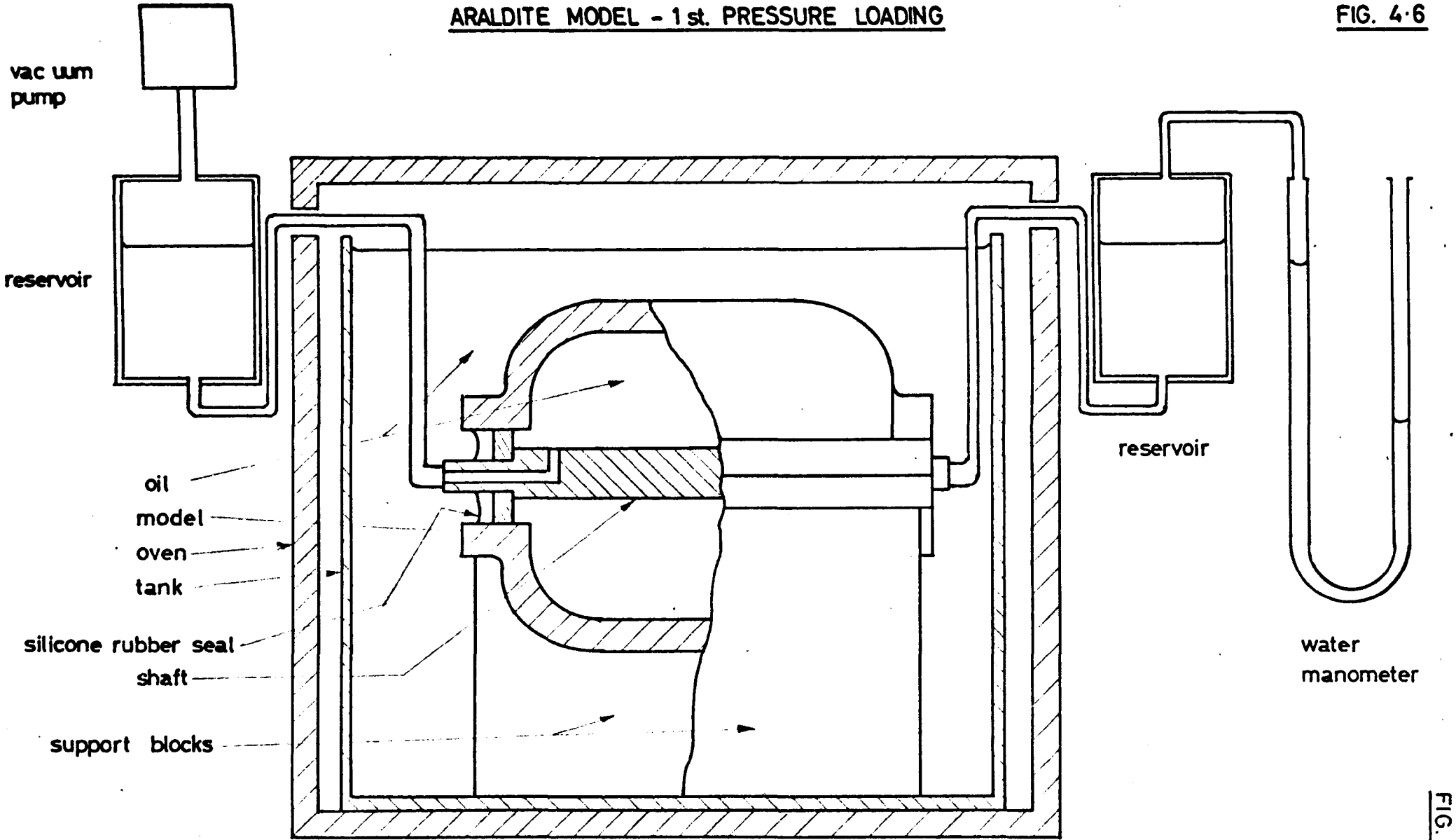

FIG. 4·6

1* PRESSURE LOADING

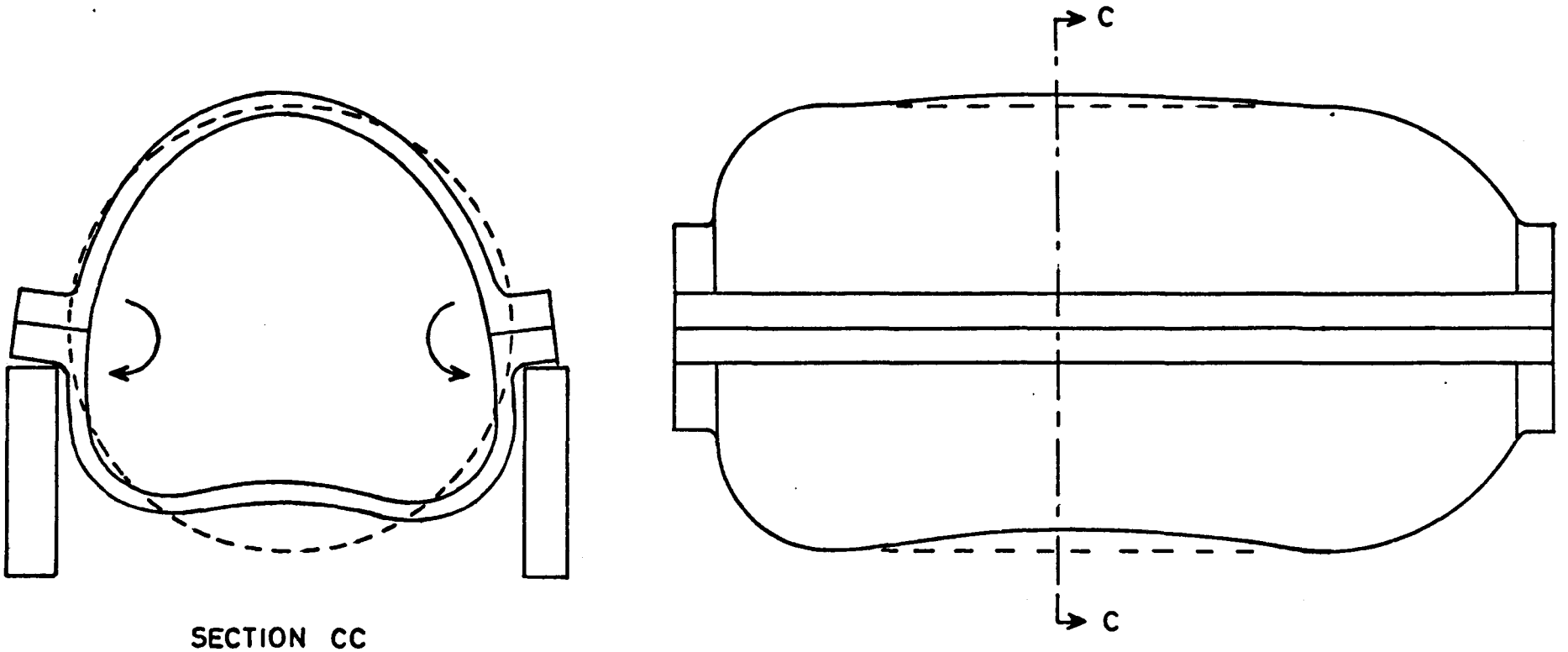

SECTION CC

FIG. 4·7

FIG. 4·7 THE COLLAPSED MODEL - effect of flange rotation and negative internal pressure

ARALDITE MODEL - 2d PRESSURE LOADING

FIG. 4·8

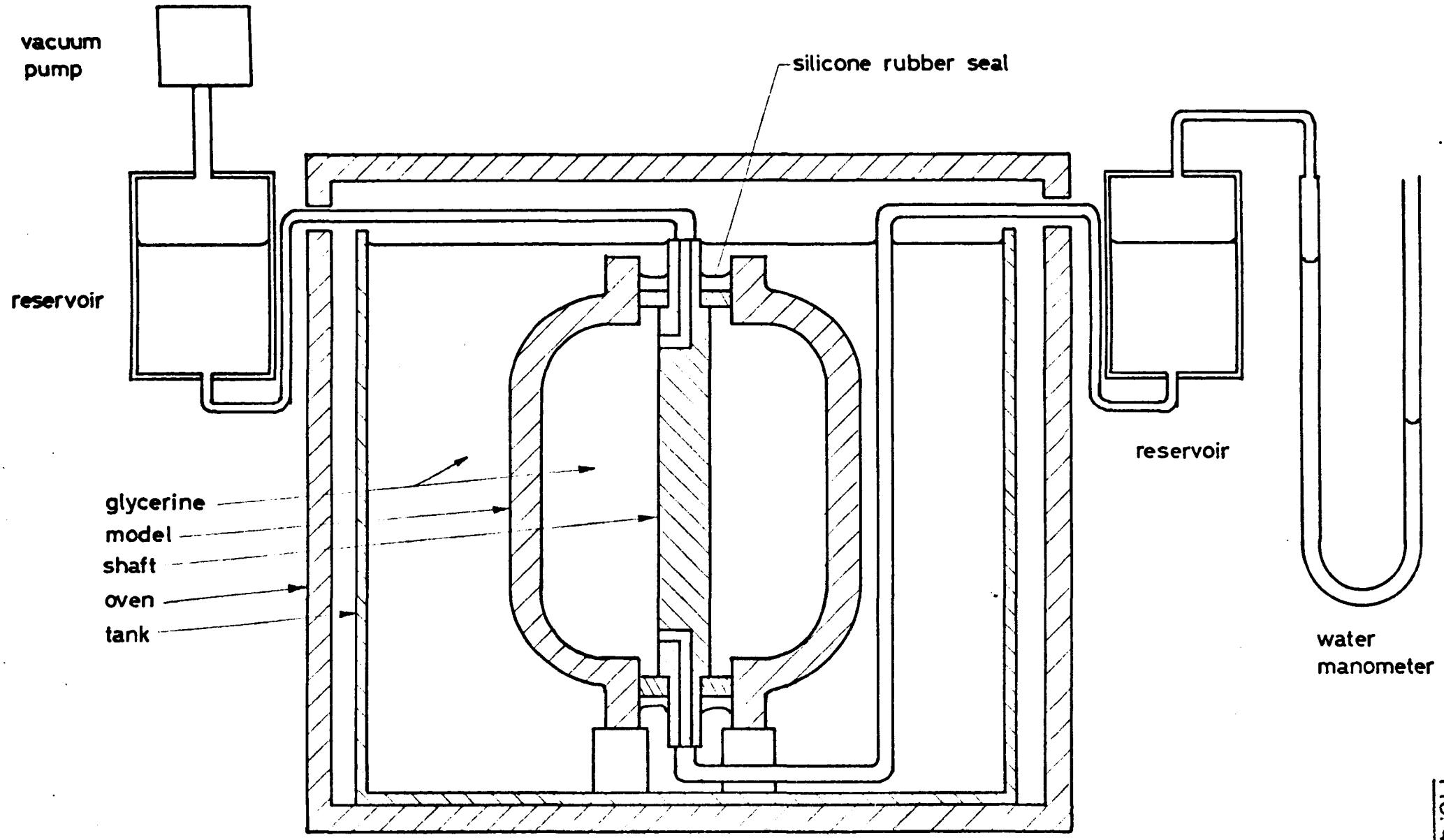

FIG. 4·8

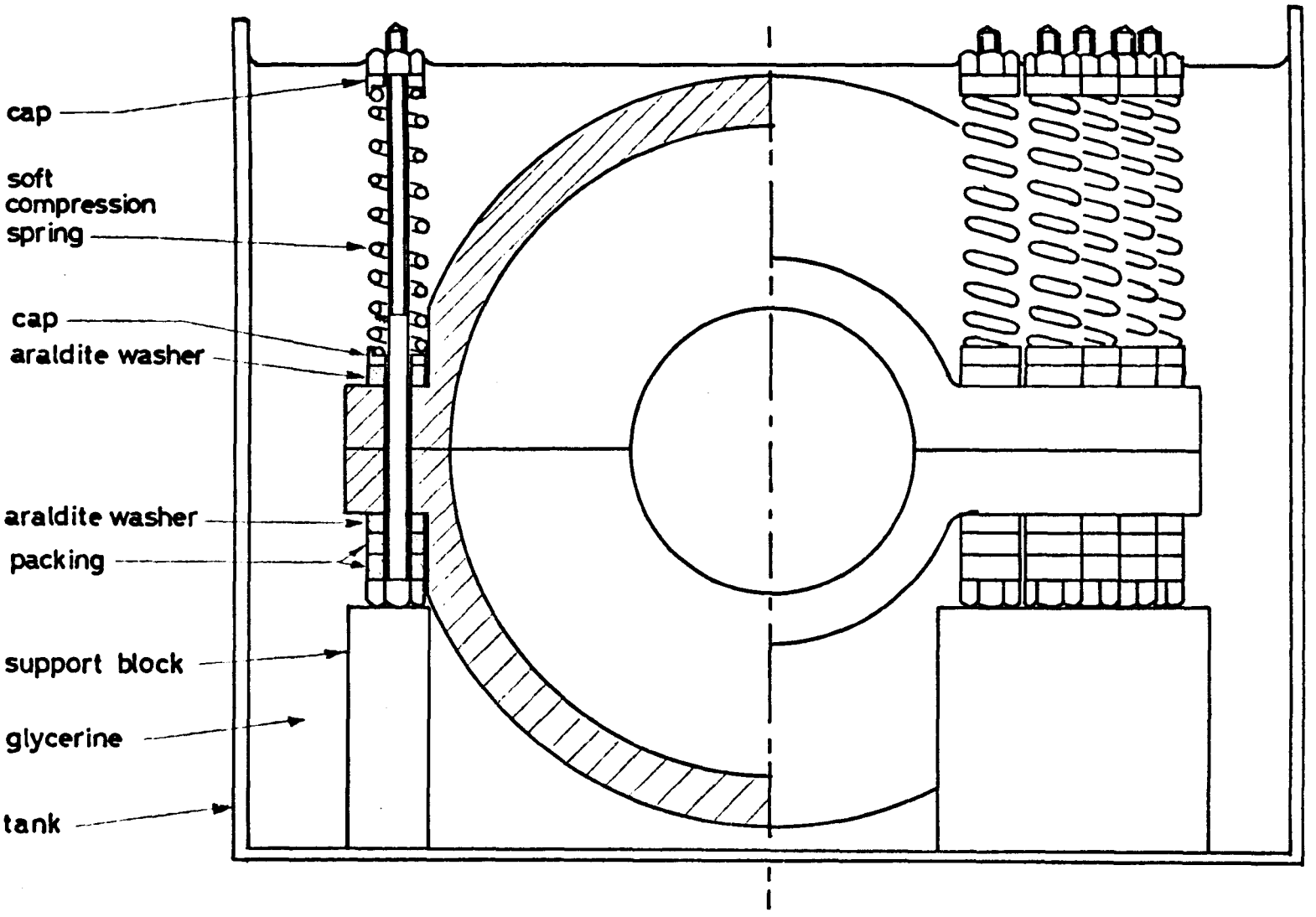

FIG. 4·9 BOLT LOADING ARRANGEMENT FOR ARALDITE MODEL (part section)

FIG. 4·9

FIG. 4·10

ARALDITE MODEL SLICING PLAN

MERIDIONAL SLICES

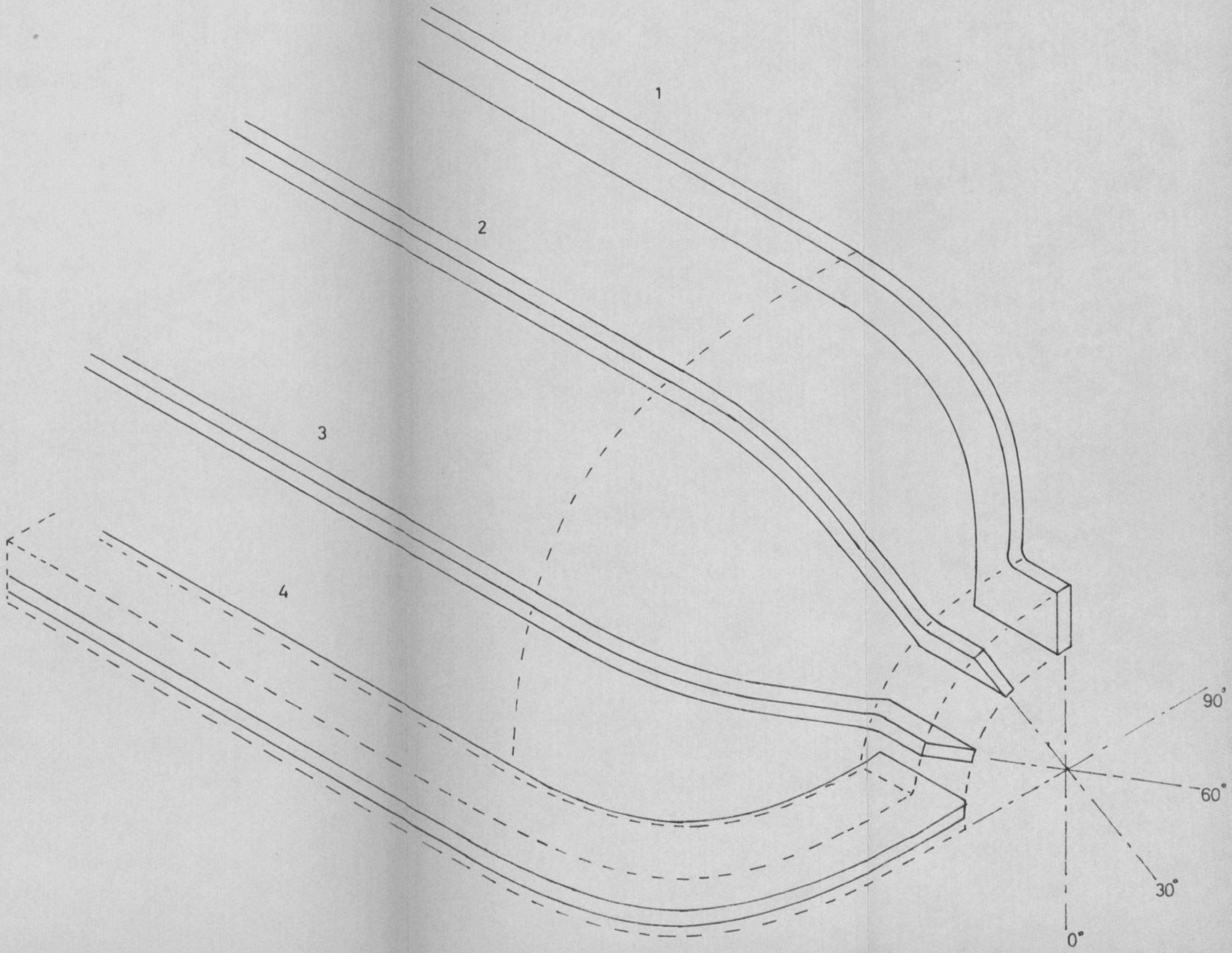

FIG. 4·11

ARALDITE MODEL SLICING PLAN

HOOP SLICES

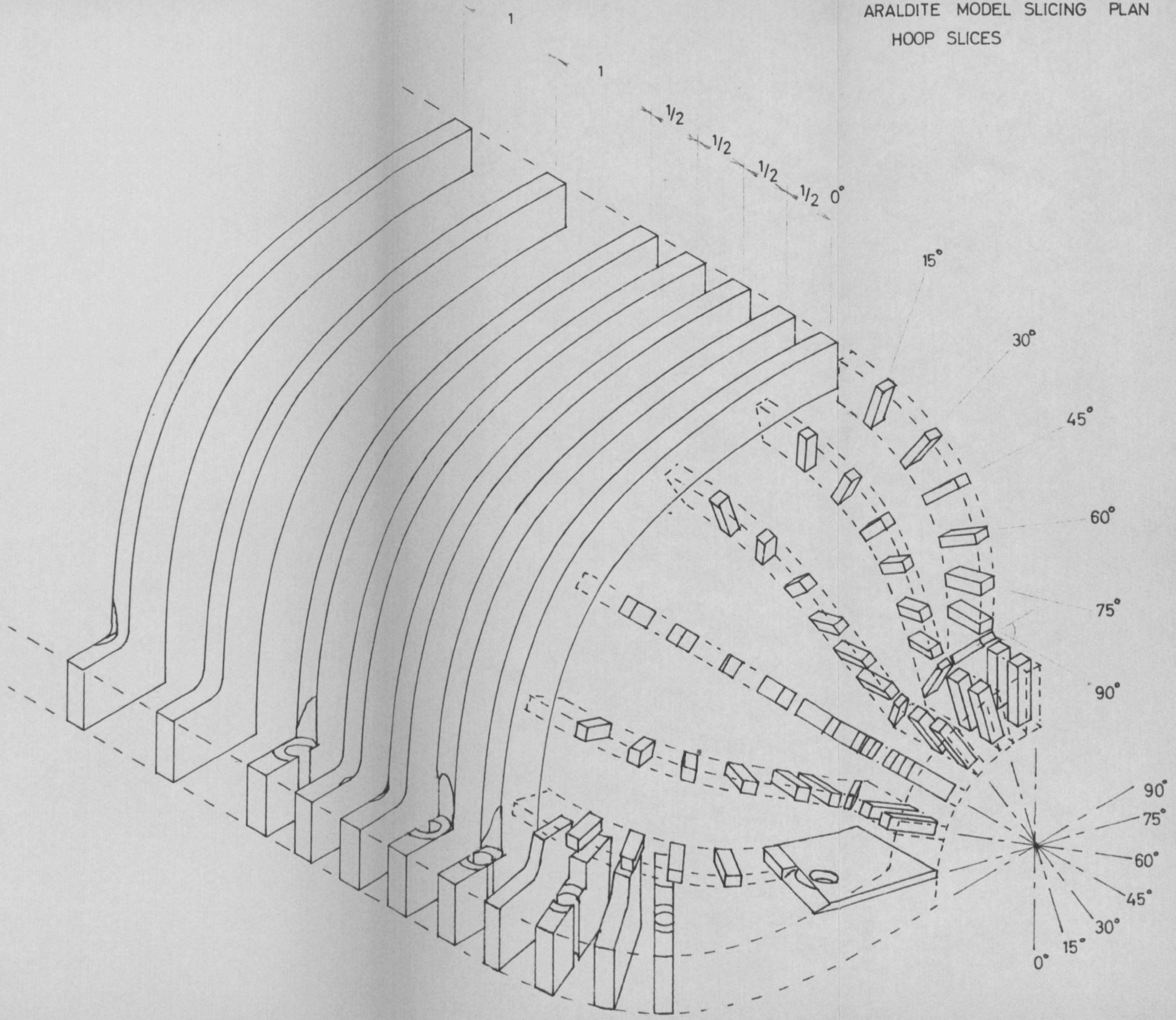

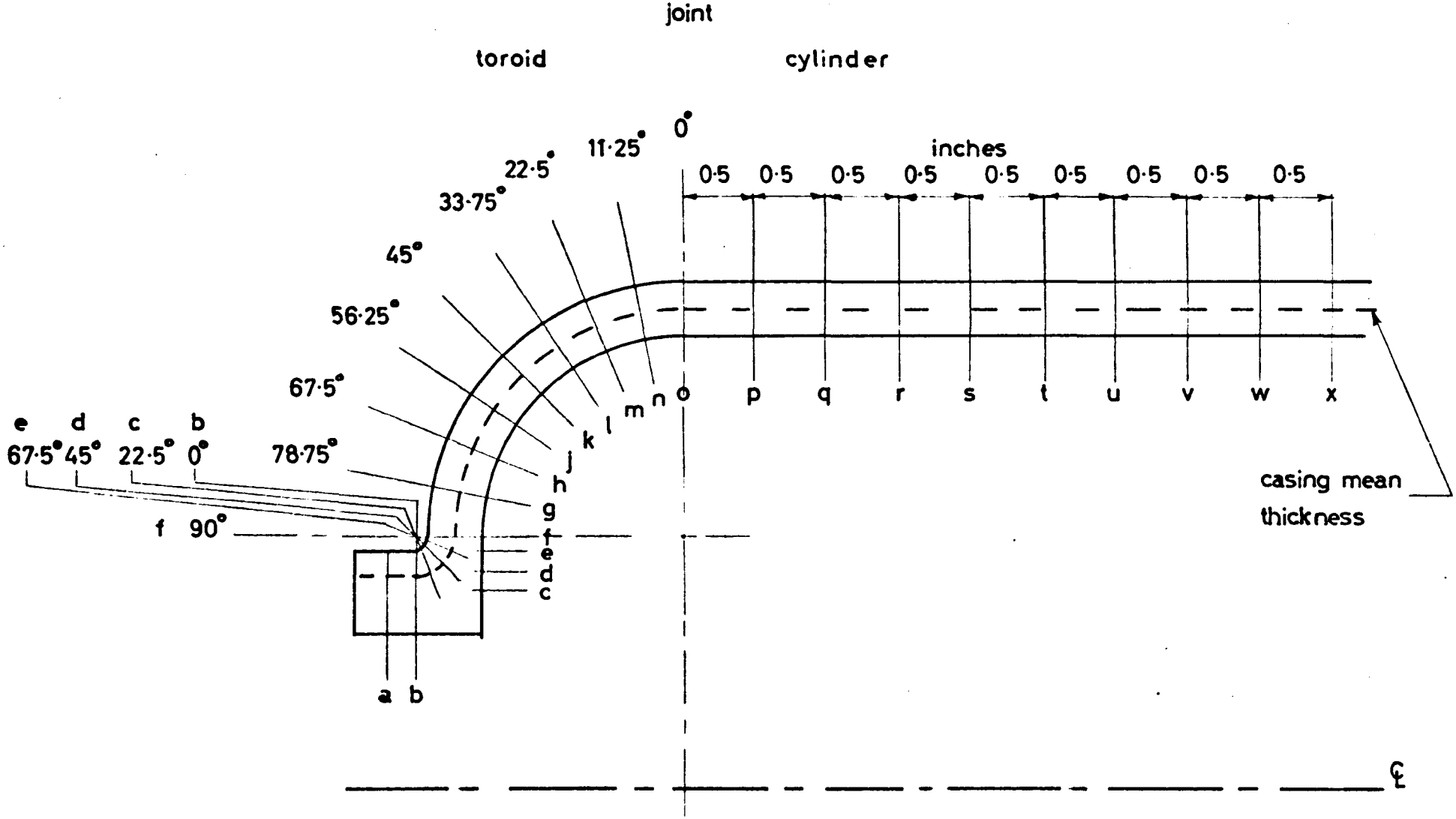

MEASUREMENT POSITIONS - MERIDIONAL SECTION — CASING

FIG. 4·12

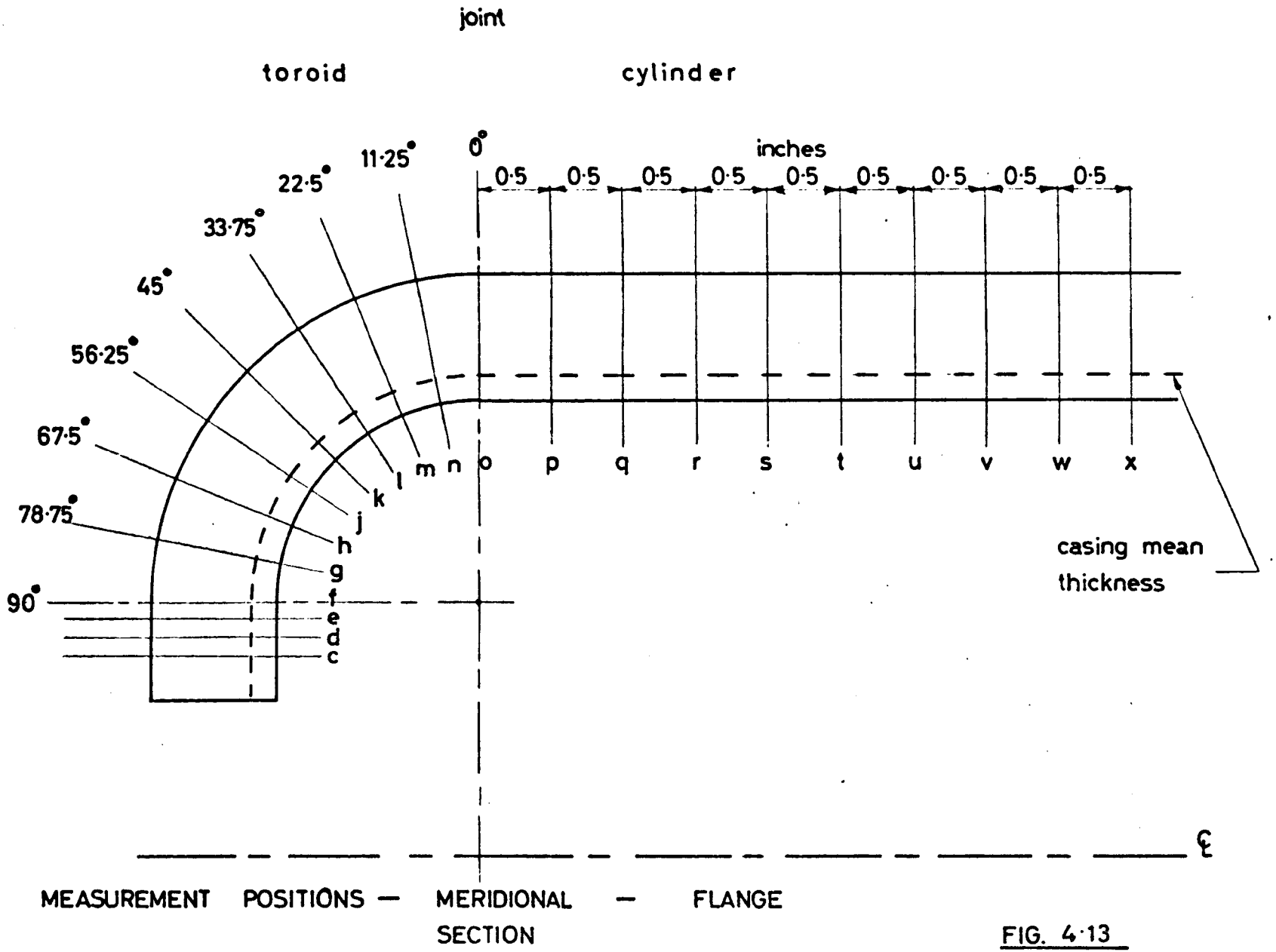

MEASUREMENT POSITIONS — MERIDIONAL SECTION — FLANGE

FIG. 4·13

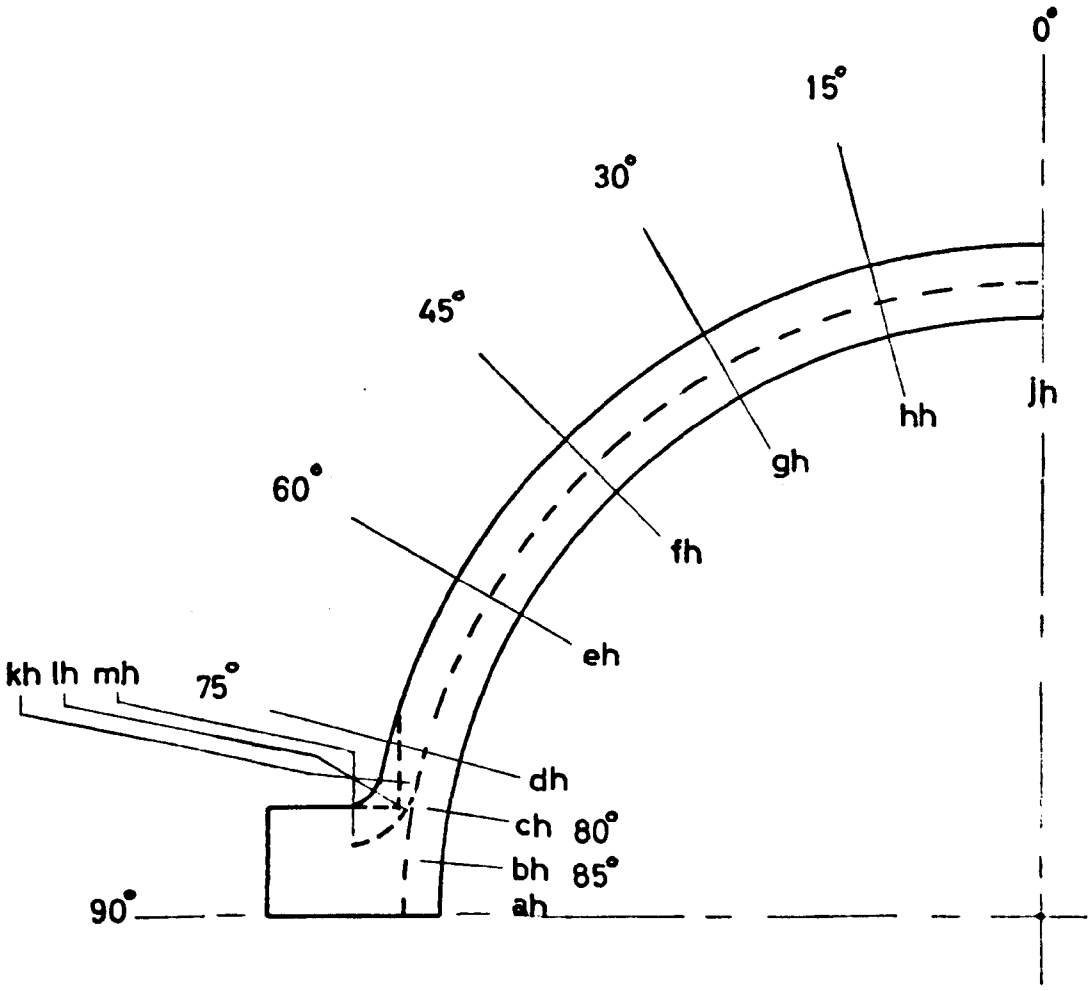

MEASUREMENT POSITIONS HOOP SECTION

FIG. 4·14

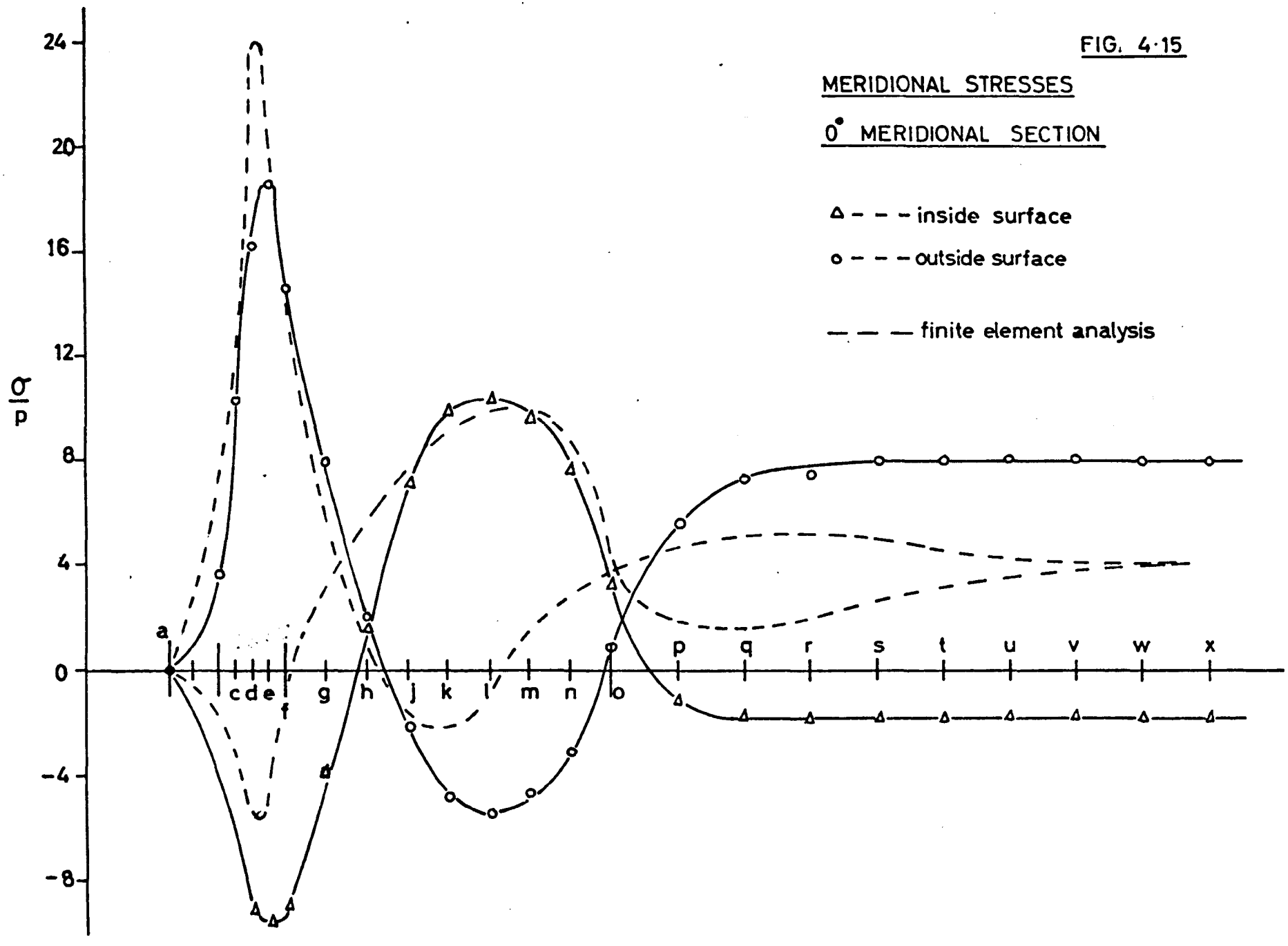
FIG. 4·15
MERIDIONAL STRESSES
0° MERIDIONAL SECTION
inside surface
outside surface
finite element analysis
σ/p
24
20
16
12
8
4
0
-4
-8
a
c d e
f
g
h
j
k
l
m
n
o
p
q
r
s
t
u
v
w
x

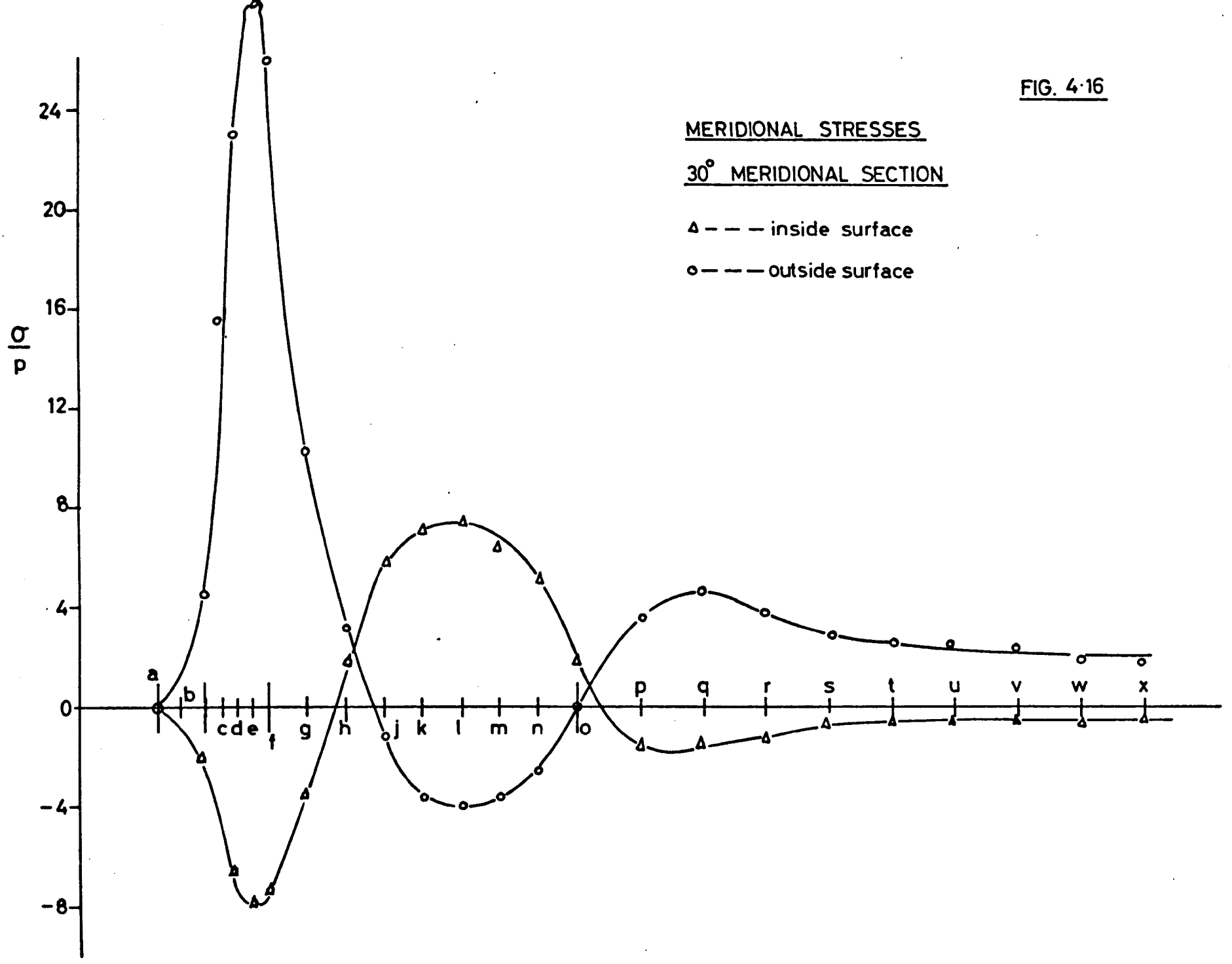
FIG. 4·16
MERIDIONAL STRESSES
30° MERIDIONAL SECTION
Δ – – – inside surface
o – – – outside surface
σ/p
24
20
16
12
8
4
0
-4
-8
a
b
c
d
e
f
g
h
j
k
l
m
n
o
p
q
r
s
t
u
v
w
x

FIG. 4·17

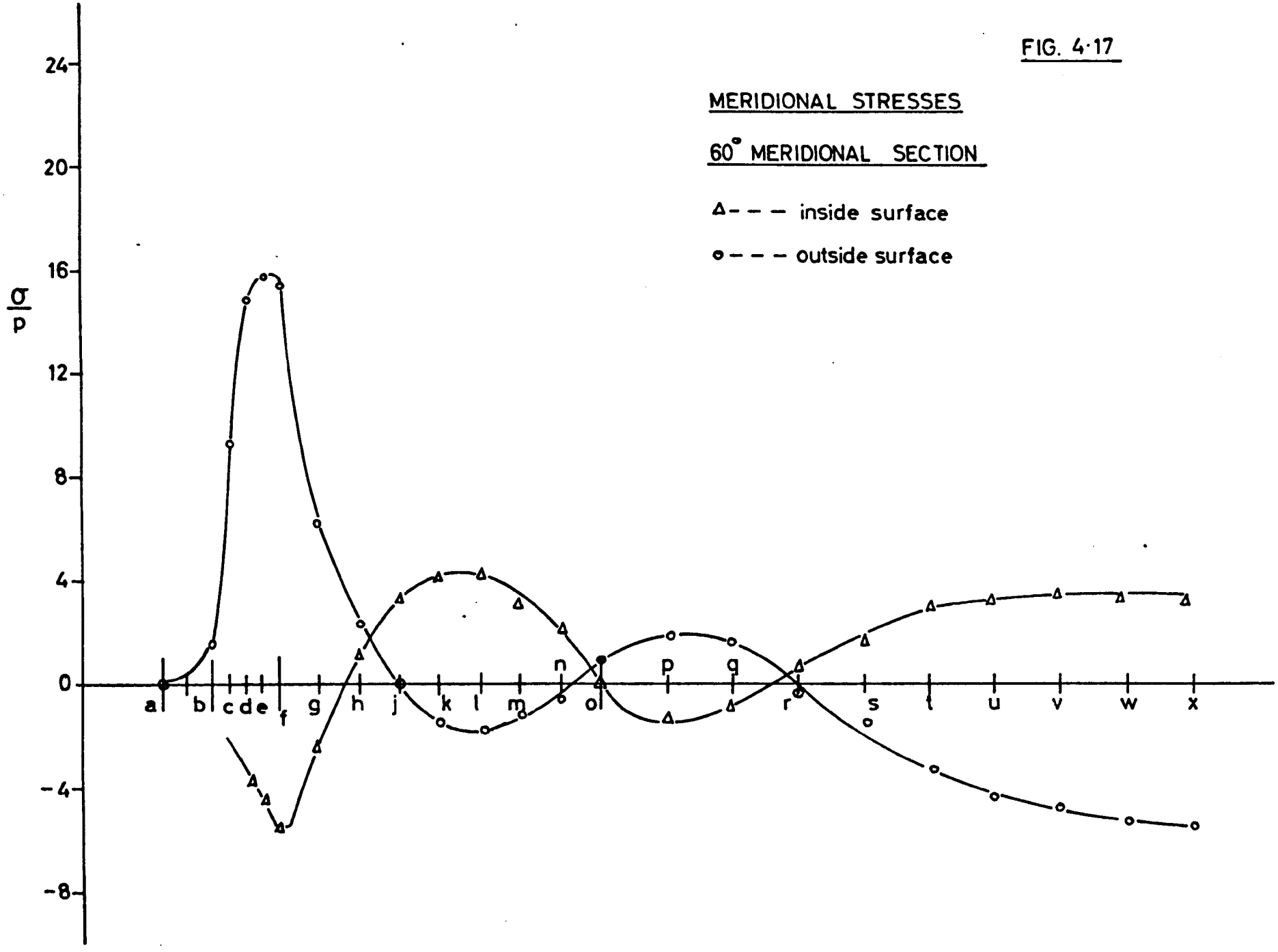
MERIDIONAL STRESSES
60° MERIDIONAL SECTION
Δ- - - inside surface
o- - - outside surface
σ/p
24
20
16
12
8
4
0
-4
-8
a
b
c
d
e
f
g
h
j
k
l
m
n
o
p
q
r
s
t
u
v
w
x

FIG. 4·18

MERIDIONAL STRESSES

90° MERIDIONAL SECTION (FLANGE)

Δ– – – inside surface

o– – – outside surface

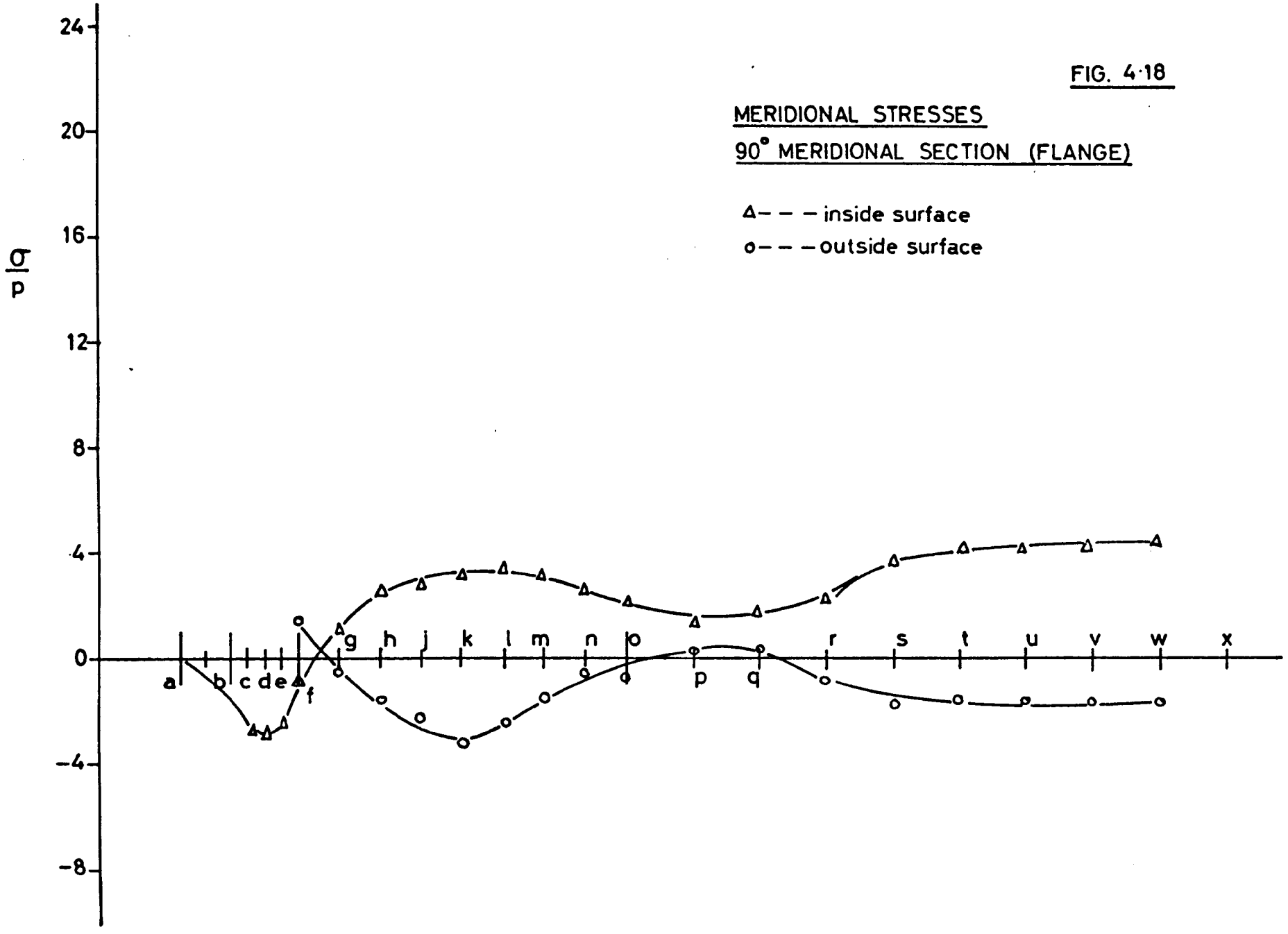

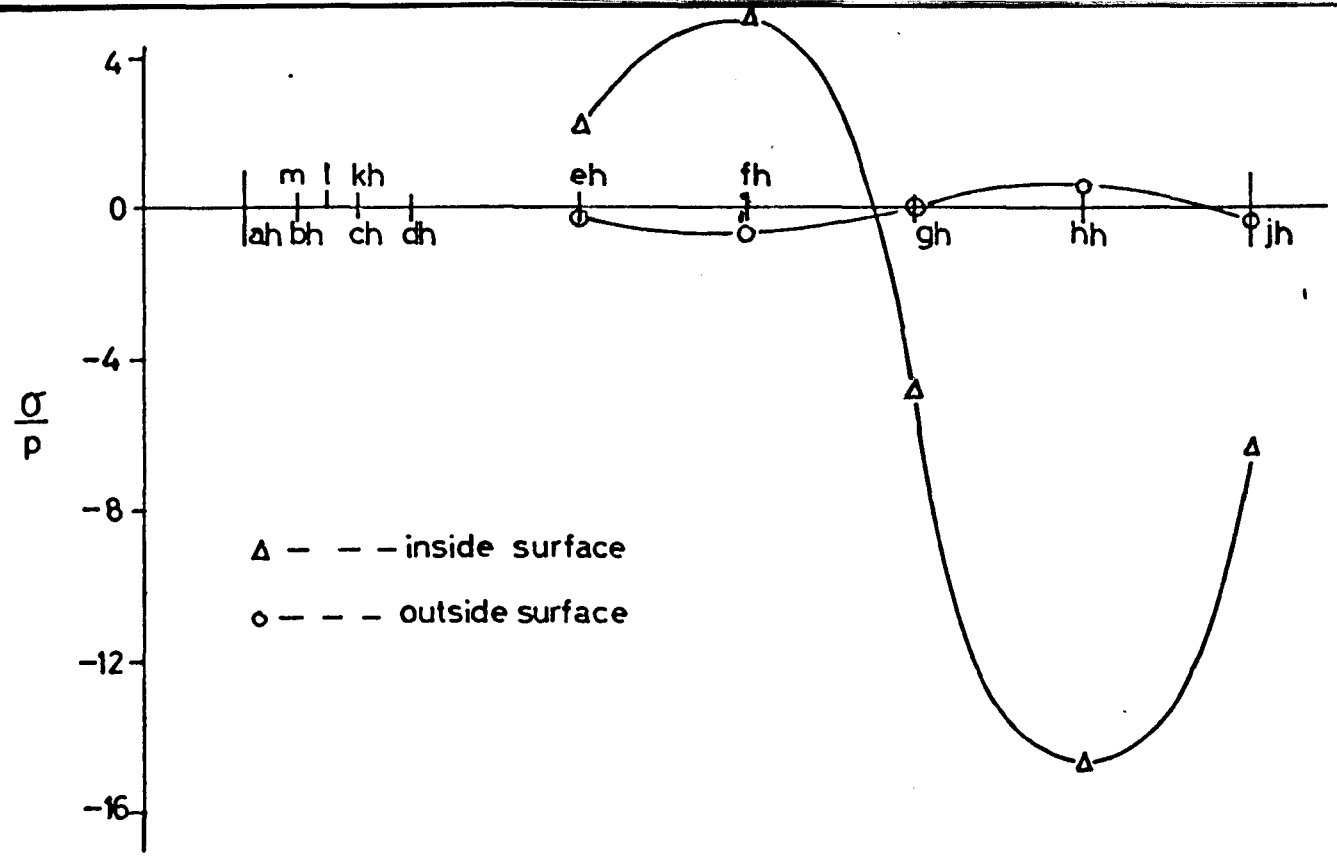

HOOP STRESSES

BOSS END HOOP SECTION

FIG. 4·19

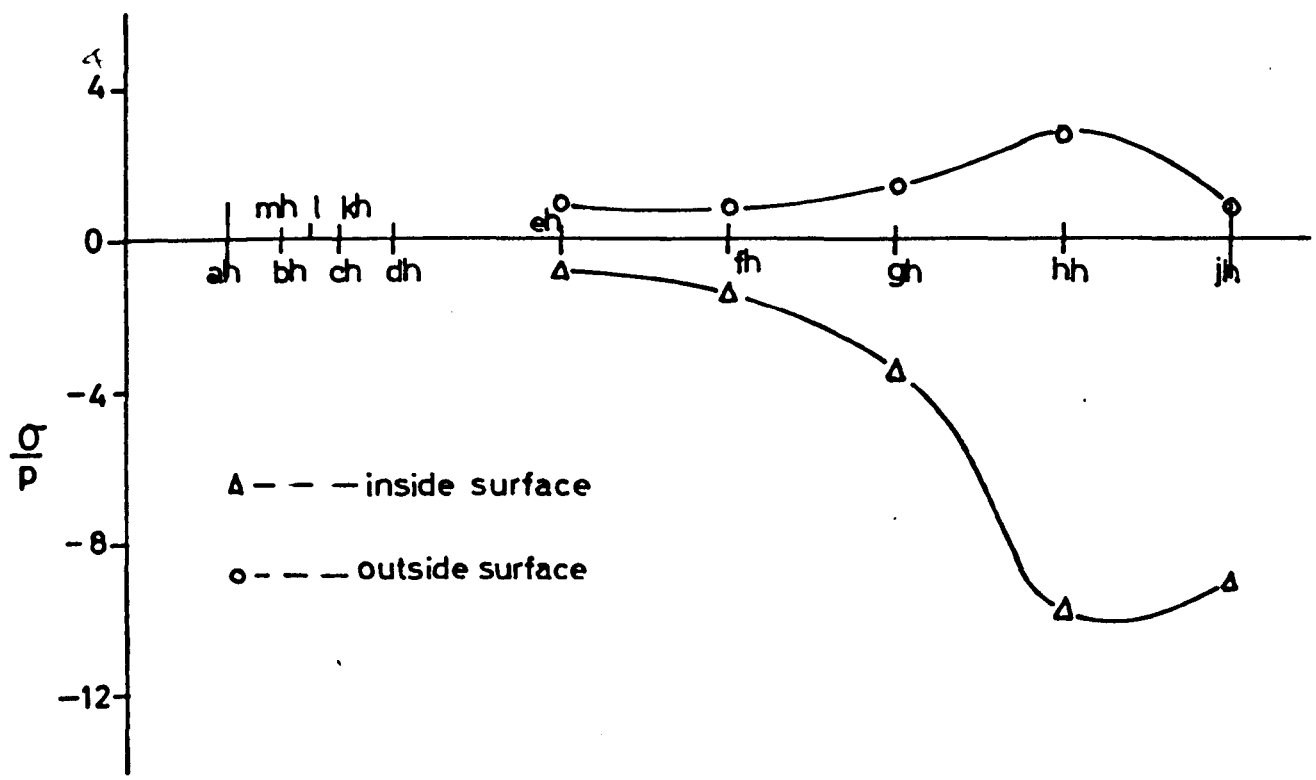

HOOP STRESSES

MID BOSS HOOP SECTION

FIG. 4·20

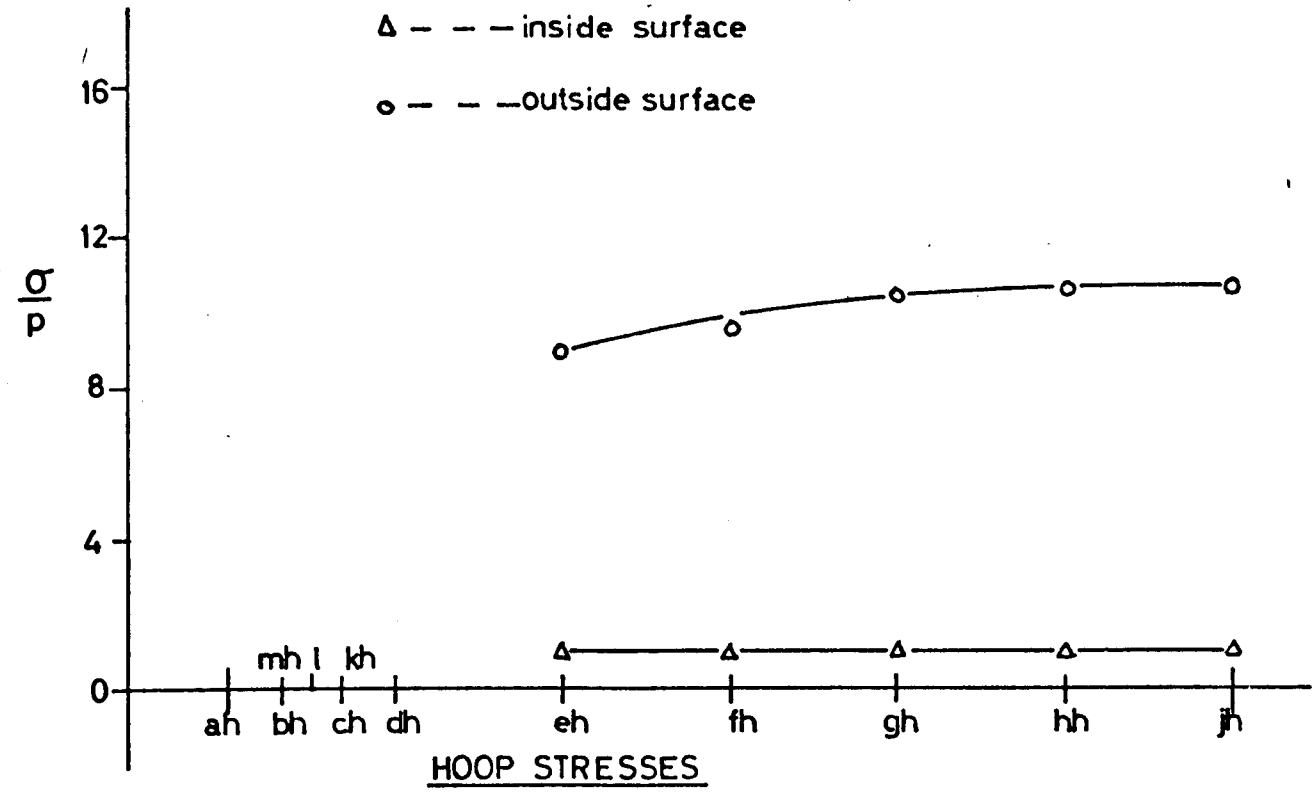

HOOP STRESSES

BOSS FILLET RAD. HOOP SECTION

FIG. 4·21

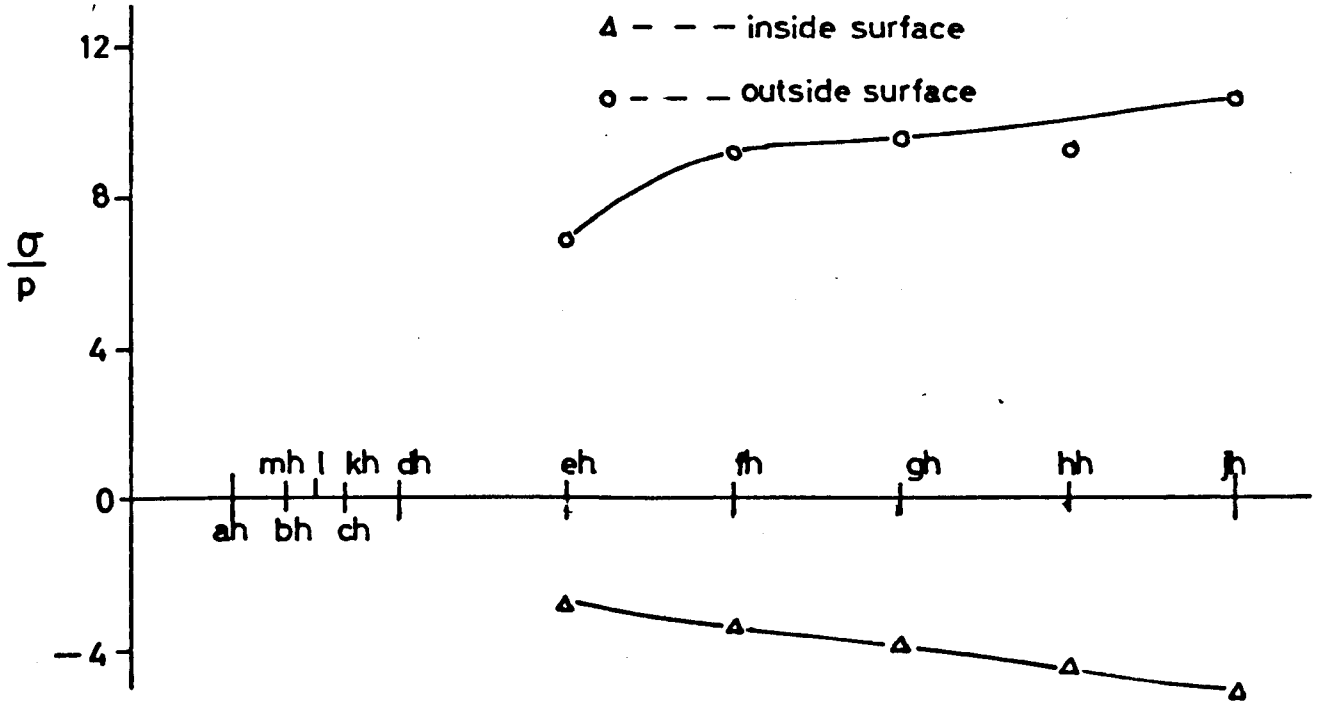

HOOP STRESSES

TOROID 90° HOOP SECTION

FIG. 4·22

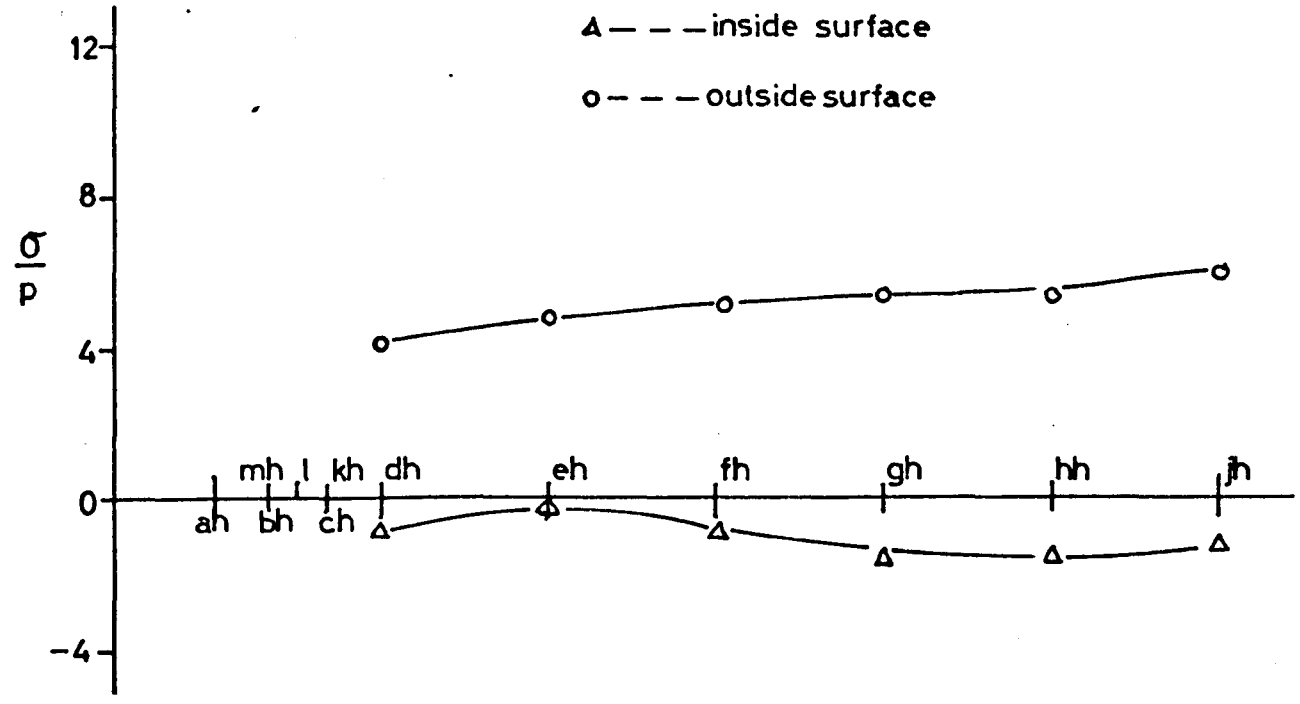

HOOP STRESSES
TOROID 75° HOOP SECTION

FIG. 4·23

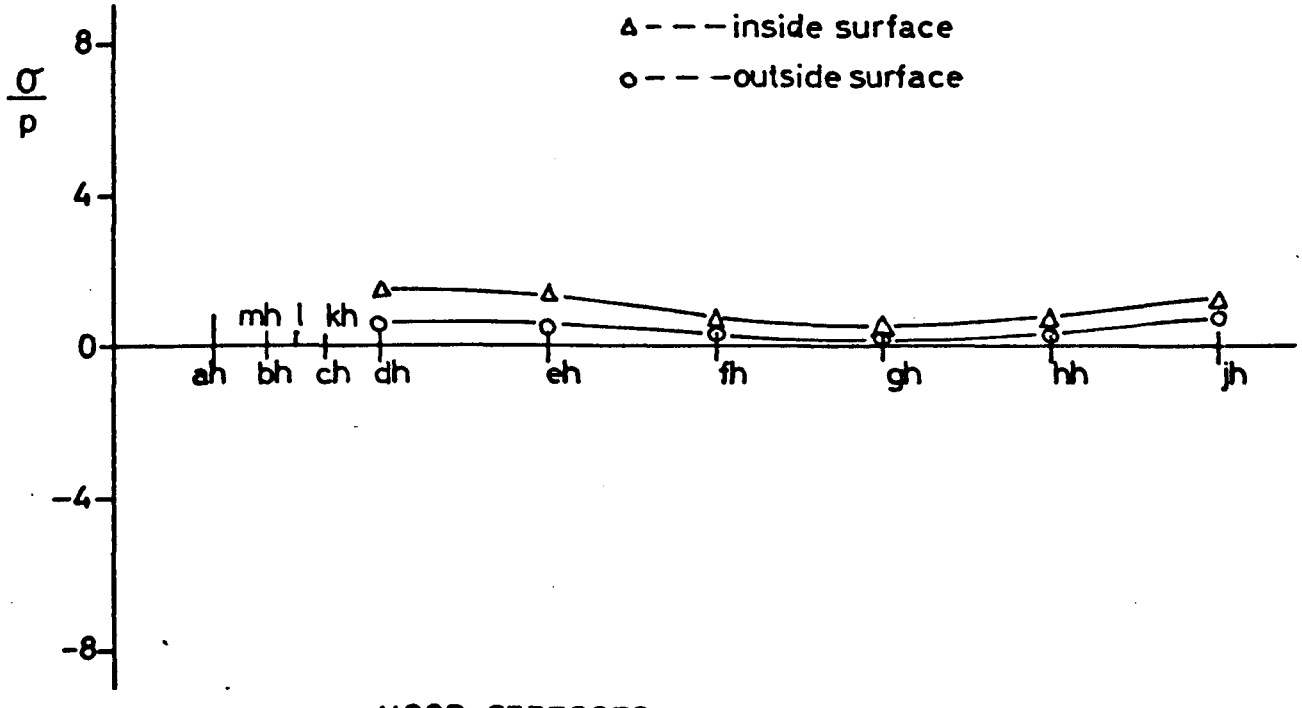

HOOP STRESSES
TOROID 60° HOOP SECTION

FIG. 4·24

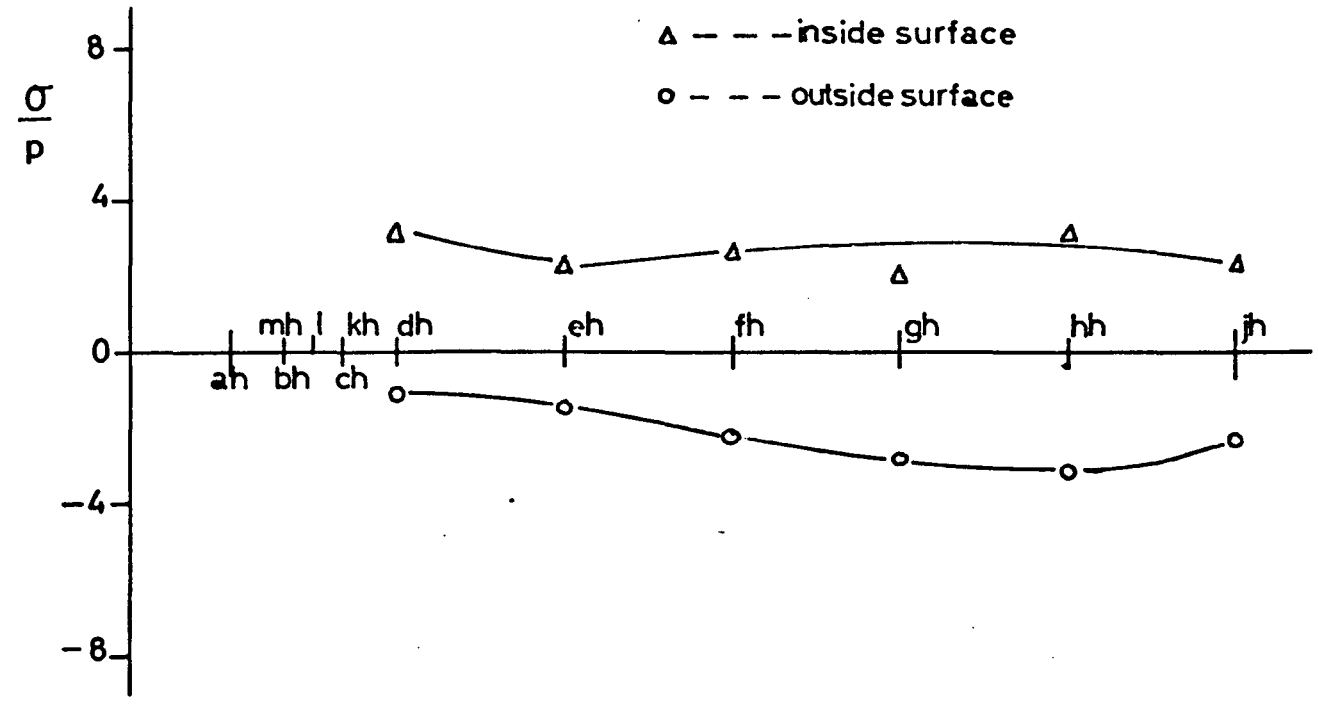

HOOP STRESSES
TOROID 45° HOOP SECTION

FIG. 4·25

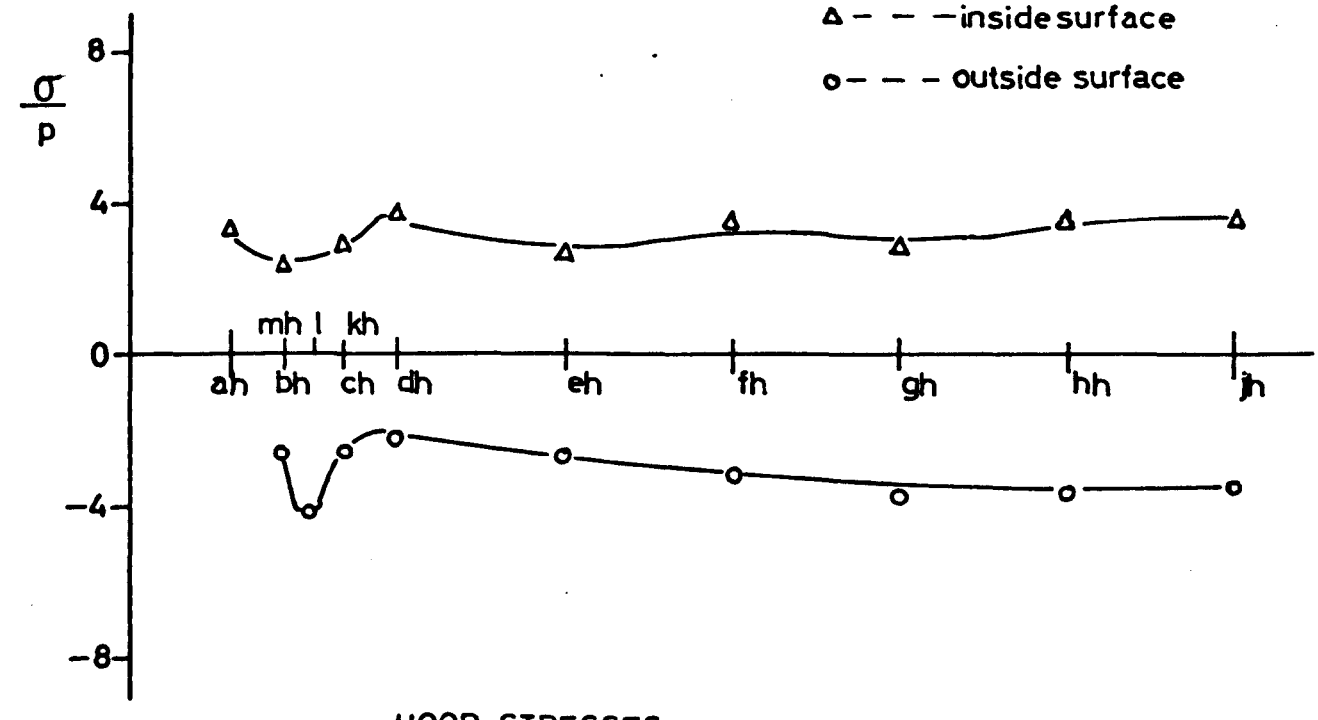

HOOP STRESSES
TOROID 30° HOOP SECTION

FIG. 4·26

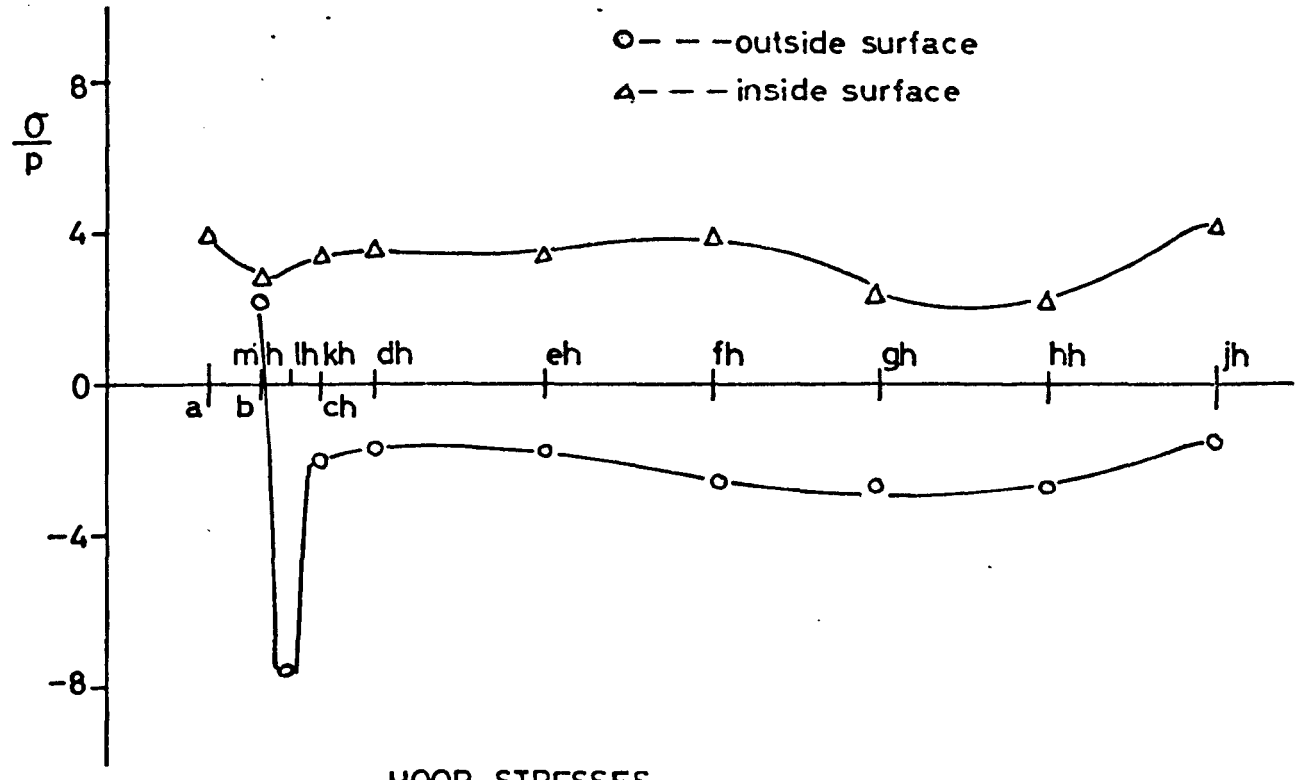

HOOP STRESSES
TOROID 15° HOOP SECTION

FIG.4·27

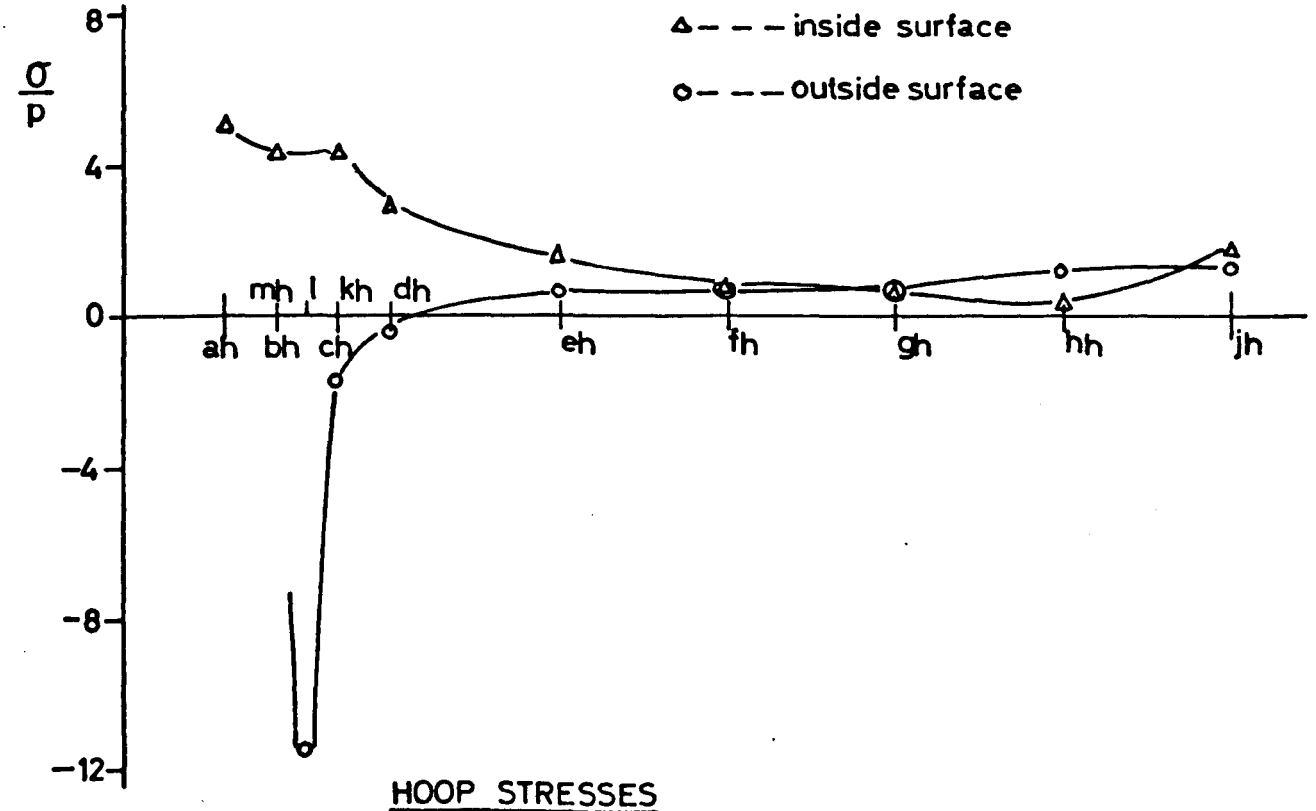

HOOP STRESSES
TOROID 0°/CYLINDER JOINT HOOP SECTION

FIG. 4·28

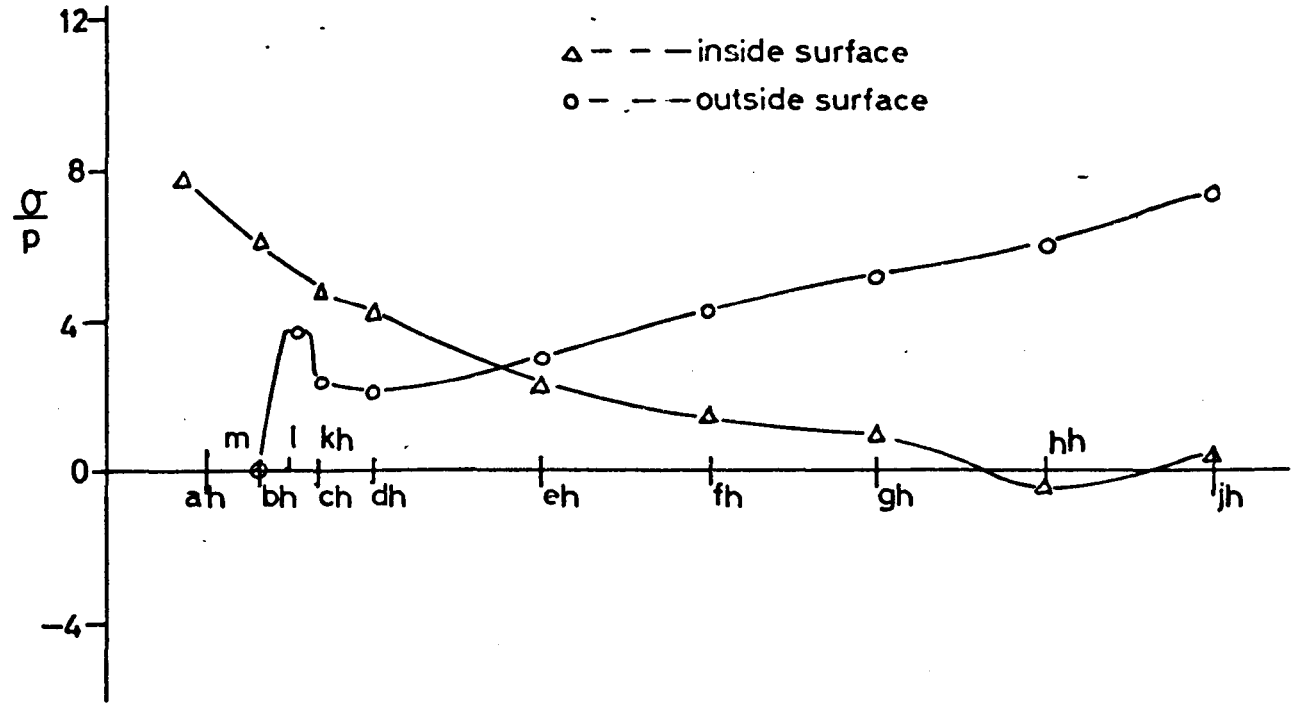

HOOP STRESSES

CYLINDER JOINT + 0·5 in HOOP SECTION

FIG. 4·29

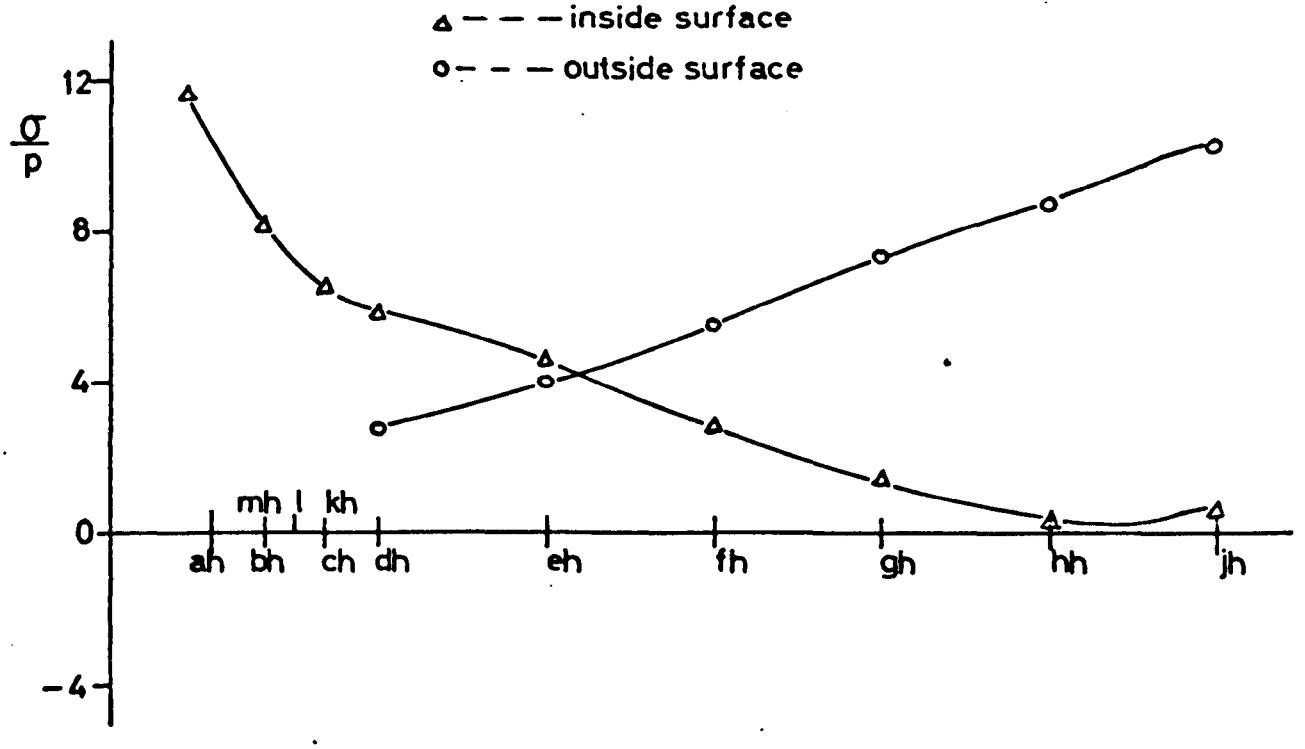

HOOP STRESSES

CYLINDER JOINT + 1·0 in HOOP SECTION

FIG. 4·30

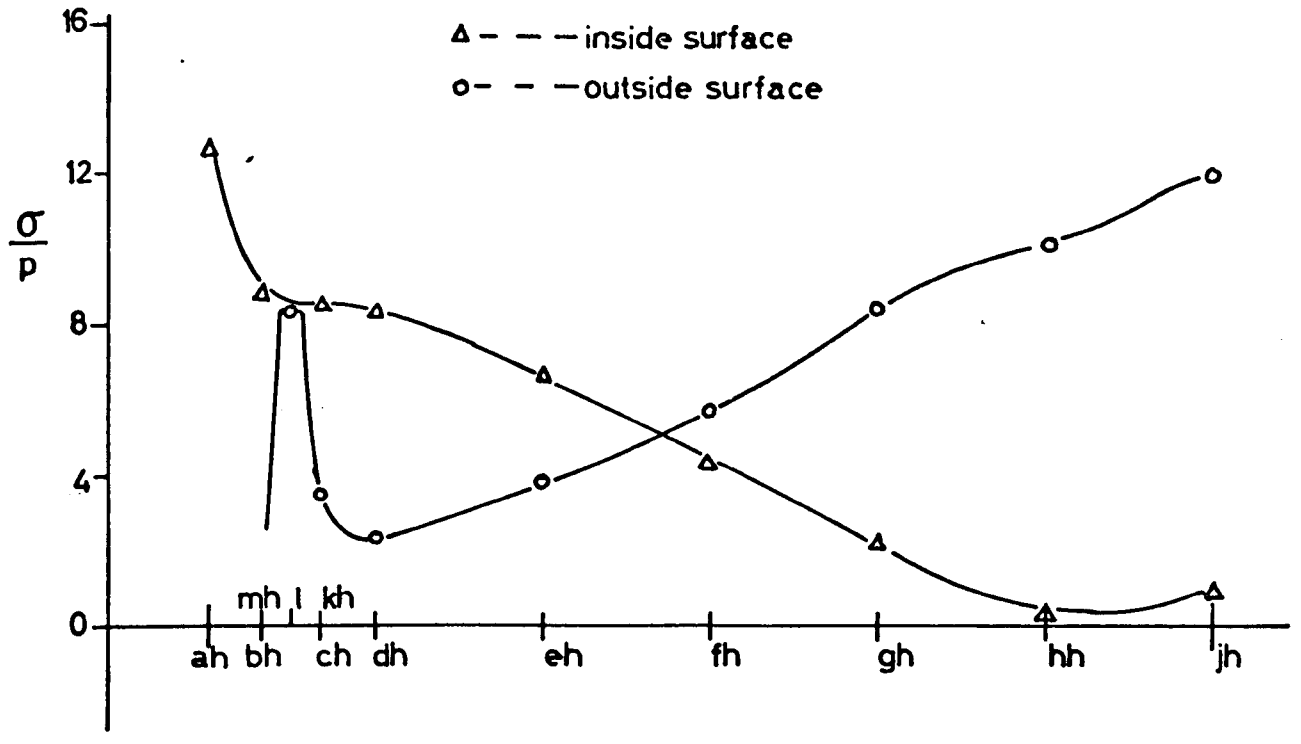

HOOP STRESSES

CYLINDER JOINT + 1·5 in HOOP SECTION

FIG. 4·31

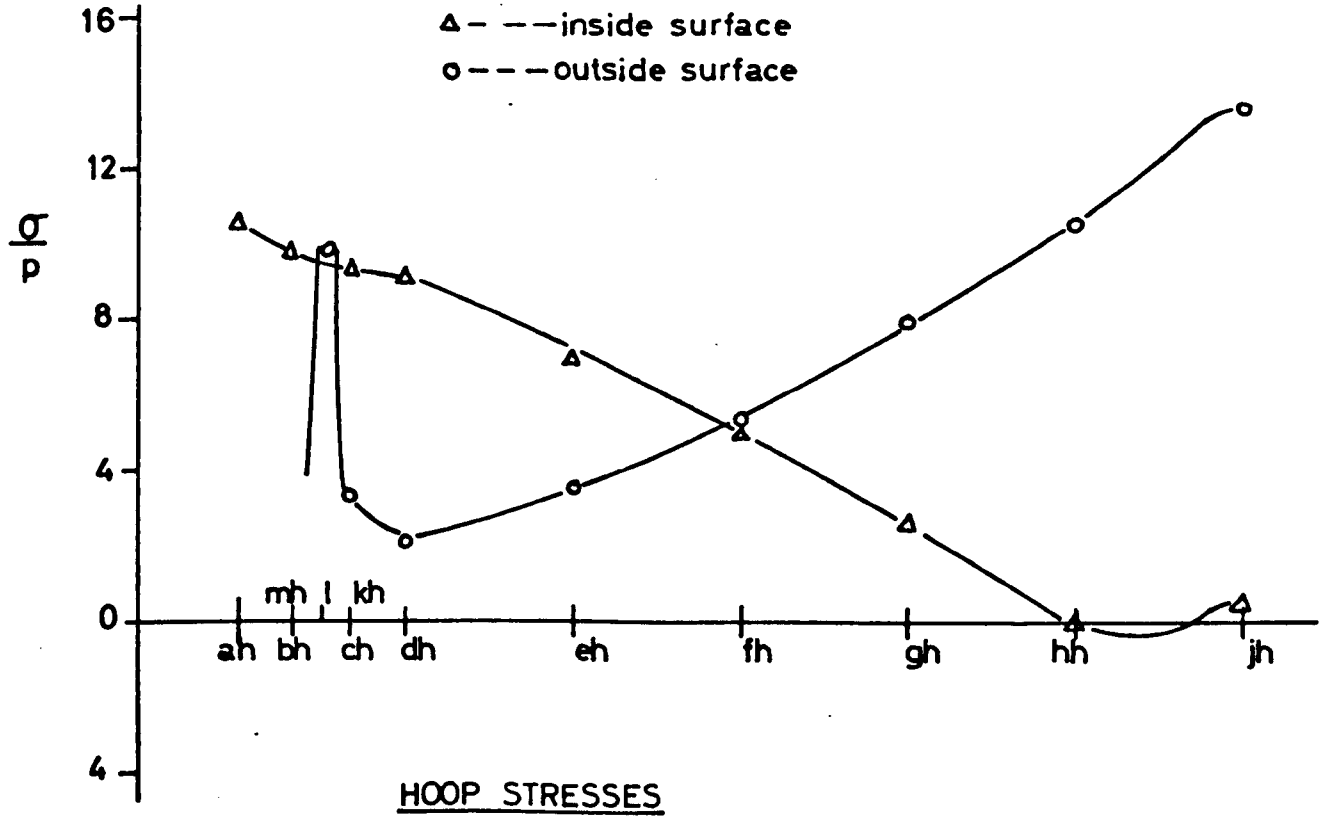

HOOP STRESSES

CYLINDER JOINT + 2·0 in HOOP SECTION

FIG. 4·32

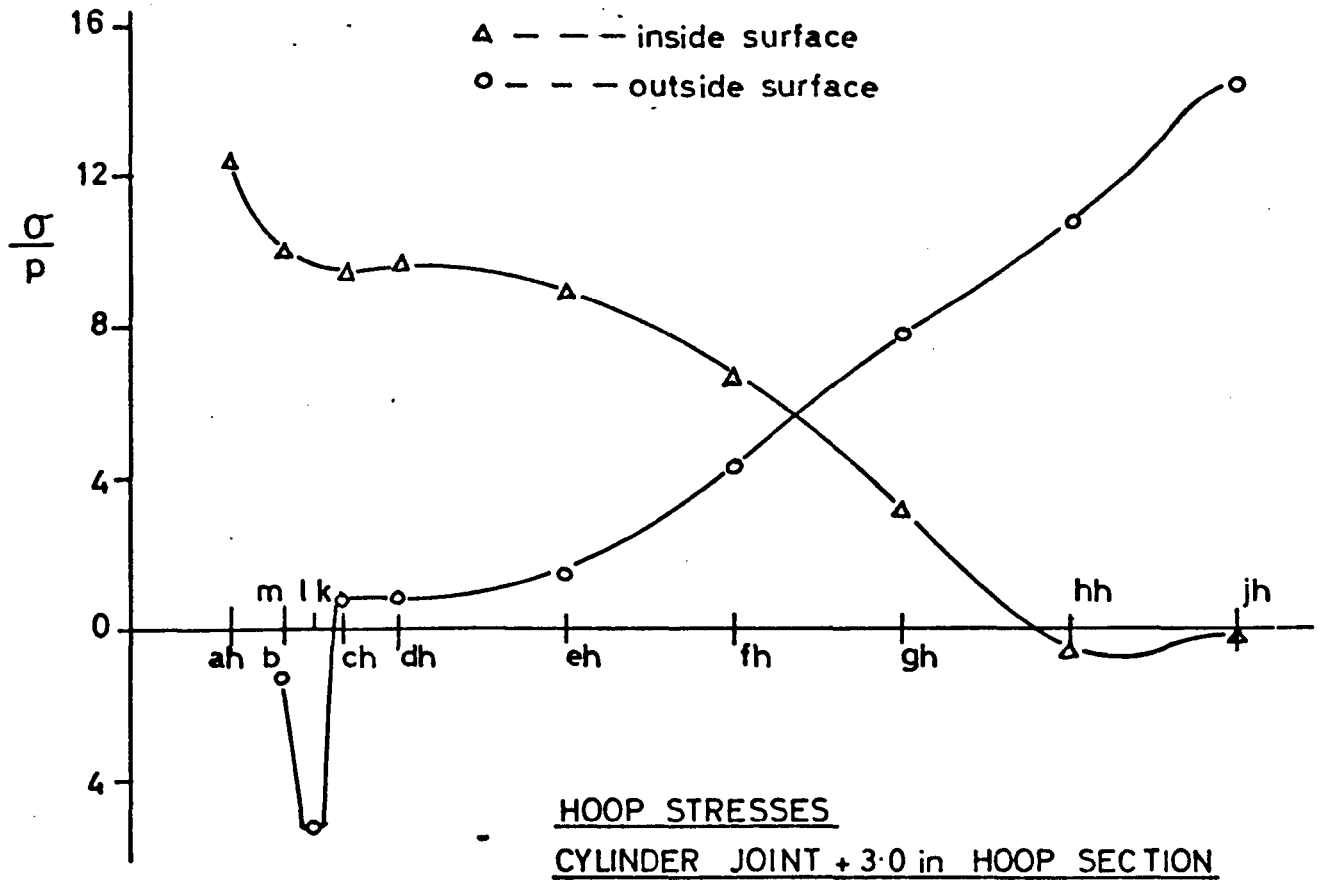

HOOP STRESSES

CYLINDER JOINT + 3·0 in HOOP SECTION

FIG. 4·33

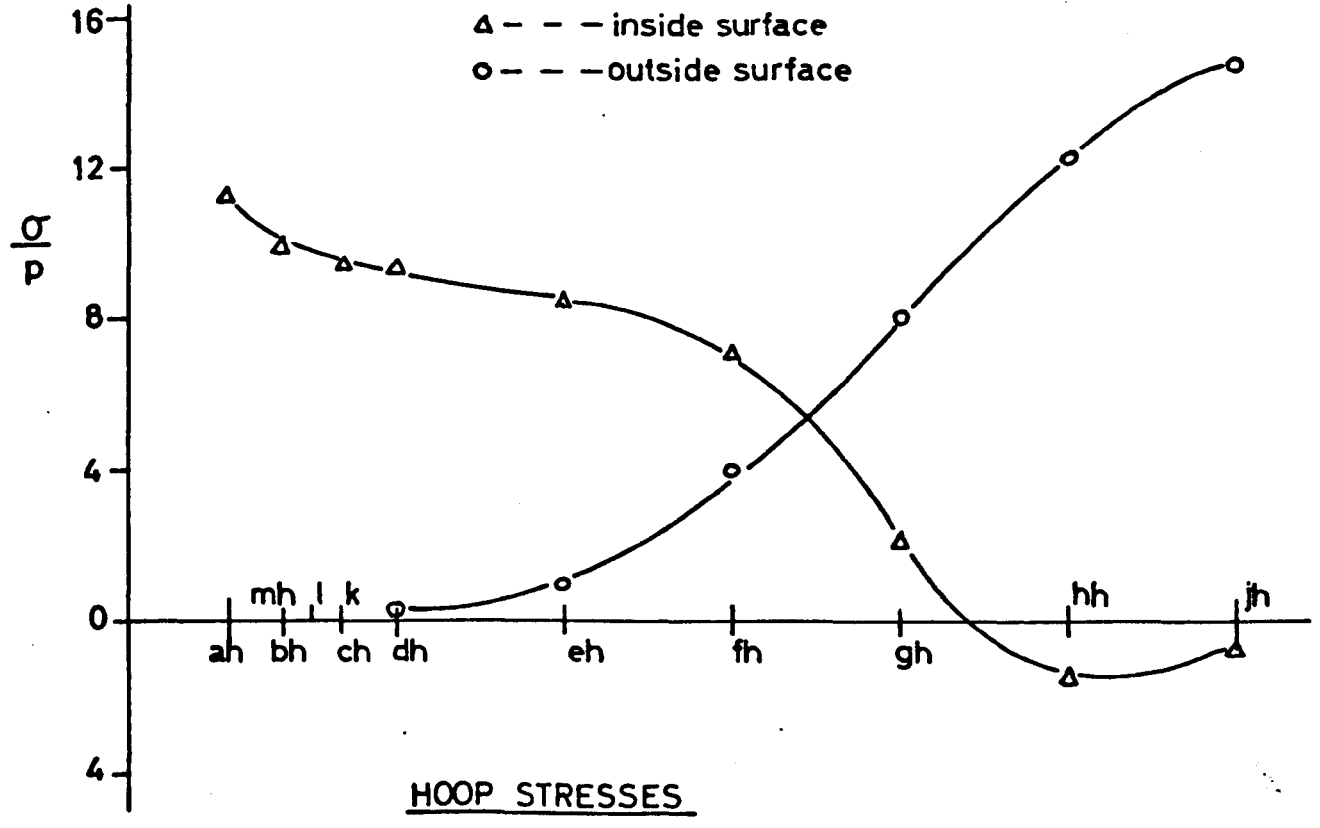

HOOP STRESSES

CYLINDER JOINT + 4·0 in HOOP SECTION

FIG. 4·34

FIG 4·35

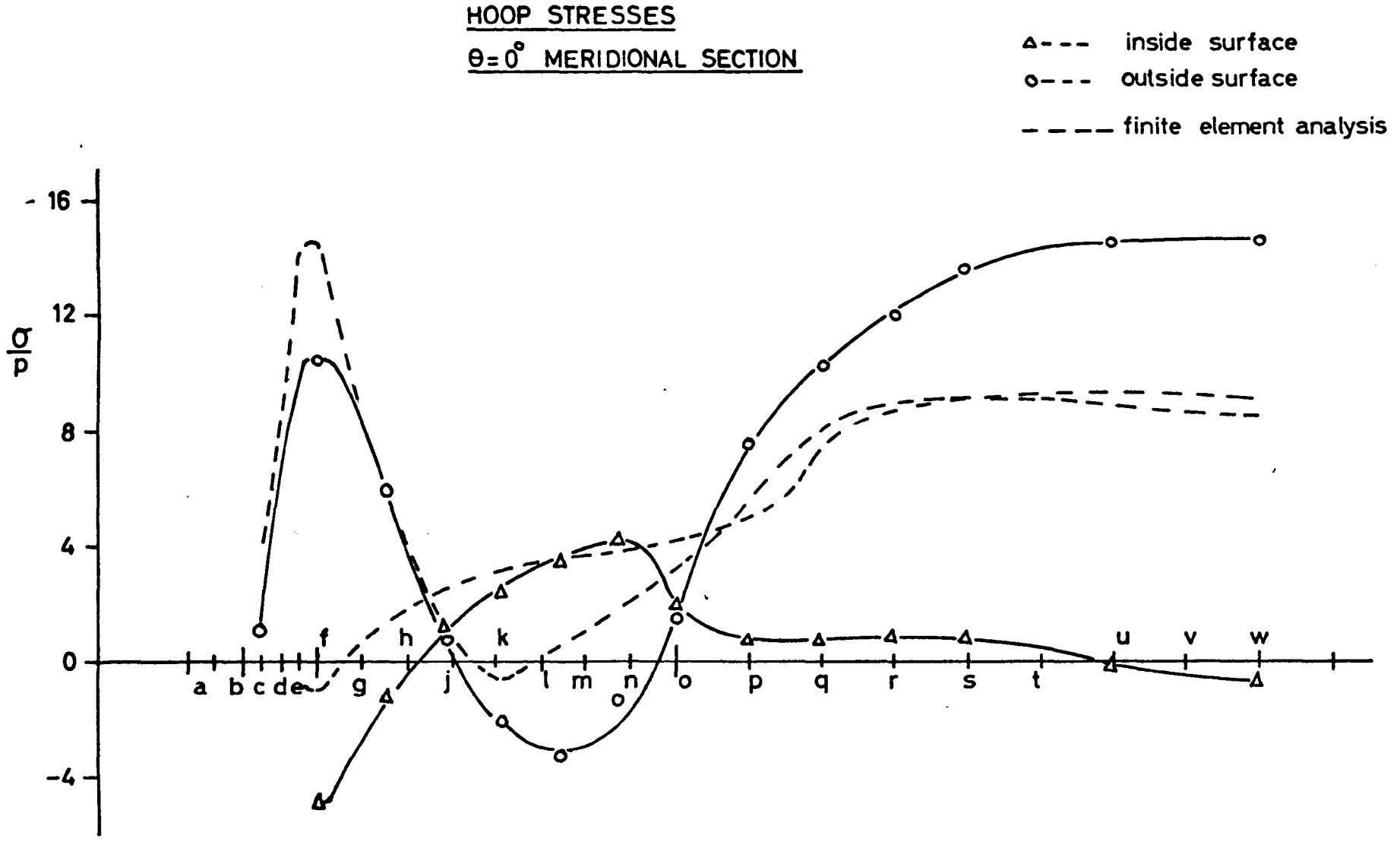
HOOP STRESSES
θ=0° MERIDIONAL SECTION
inside surface
outside surface
finite element analysis
σ/p
16
12
8
4
0
-4
a
b
c
d
e
f
g
h
j
k
l
m
n
o
p
q
r
s
t
u
v
w

CHAPTER 5

MODEL MANUFACTURE

5.1 Production of castings

5.1.1 Chill casting

Since the grain structure of the lead alloy cannot be refined by subsequent heat treatment and cold working would give the structure directional properties not present in the prototype, grain refinement in the model casing must be achieved by rapid cooling. The only way of achieving sufficiently rapid cooling of the molten lead is the chill casting technique adopted, where molten lead is poured into a 'cold' steel mould. The combination of low specific heat, low latent heat of fusion and high conductivity of lead with the high specific heat and high conductivity of steel makes this technique effective.

Advice in casting technique was obtained from Dr. J. E. Bowers of the British Non-Ferrous Metals Research Association. He recommended the use of a large all round header and circumferential feeder, and the exclusion of oxygen from the pouring process.

5.1.2 The crucible

The steel crucible (Figs. 5.1 and 5.2) contains 380 lb of lead when full and is heated by a concentric gas burner at the bottom. The hot gas is guided by spiral fins up the annular passage between the crucible and a hollow outer cylinder, which is insulated with vermiculite. The complete crucible assembly is mounted in a fume cupboard to extract the gas exhaust, lead vapour from the melt and lead oxide dust.

To prevent the scum, which forms on the top of the melt, from entering the mould, a bottom pouring arrangement is used. The valve in the base is

pulled open against the static head of liquid lead and a spring by a solenoid operating through a lever system, which also allows emergency manual operation. The mould is placed under the fume cupboard, and the molten lead falls freely from the valve through a hole in the concrete shelf into a funnel set in the mould inlet. A large steel tube surrounds the lead stream, and a sleeve sliding onto the funnel completely encloses the flow from crucible to mould, allowing casting to be performed in an inert atmosphere such as nitrogen.

Automatic control of the valve, necessitated by the rapid filling of the mould, is achieved by a 'hold on' relay in the solenoid circuit, which is broken when the level of molten lead in the mould rises to touch a contact.

5.1.3 The mould

The steel mould is shown in Fig. 5.3 and Fig. 5.4. The main points are:-

(i) The end sections are detachable to allow for different end shapes and the addition of inlet nozzles. Some provision is also made for thickening the flanges.

(ii) It was found that circumferential feeders were unnecessary, and caused cracking at the joint with the cylindrical section and local grain size variation because of the thick section. Furthermore, circumferential chills were added to the cylindrical section, since the end sections were machined from heavier solid blocks.

(iii) Initially, 'D' pieces were fixed in the mould to give a rough casting of the bore holes. However, on machining, these revealed blow holes caused by trapped air bubbles, which apart from being defects in the casing, seriously hindered sealing in the bores under test. These 'D' pieces were therefore filed

into 'V' pieces, which allowed air bubbles to float to the surface, and subsequent castings showed no blow holes in the bores.

(iv) The rapid filling of a mould of thin section through a single inlet necessitates high velocities of lead flow and much splashing. Considerable difficulties were experienced in locating and protecting the automatic shut off contact for the solenoid, so that splashing would not switch off the solenoid too early and yet the rising lead level would have easy access to switch off at the right time. The shut off contact was finally located next to the boss of the hemispherical end on the opposite side from the inlet, and sheathed in some plastic wire covering.

(v) The core was initially made hollow to allow cooling by boiling water, but was filled instead with lead to increase the heat capacity.

(vi) To prevent the lead from sticking to the mould, its surfaces were coated with graphite. After some use, a certain amount of this graphite became absorbed into the surface of the steel, making further coating unnecessary, and eliminating the cast impression of the graphite smears initially obtained.

(vii) In the chill casting technique, rapid solidification and cooling contraction of the lead is coupled with heating and expansion of the mould. This makes it necessary to lift the core as soon as possible to prevent it from tearing the casting apart. However, the core cannot be extracted until the lead has solidified sufficiently to hold together, so extraction must be very quick when the time comes. To this end, four bolts were tapped through the beams that support the core, bearing down on steel plates which cover the all-round feeder head.

During casting, the core is held down to the main body of the mould be two small bolts to prevent the steel core from floating up on the molten lead. The cover plates, held down by the extraction bolts, serve to enclose the molten lead and prevent splashing out of the mould. On solidification, the two small bolts are quickly released, and by winding down the extraction bolts the core is lifted clear, supported on the cover plates via the extraction bolts.

(viii) In order to prevent too rapid cooling of the lead, causing contraction cracking, the mould must be preheated (Section 5.1.4). A heating box (Fig. 5.5) totally encloses the mould, made of asbestos panels, lined inside with reflective aluminium sheet, and insulated outside by fibreglass wool. Mounted on the sides of the box are four 1 KW firebars.

In the lid there is a hole to allow a pipe to be inserted into the mould to fill it with nitrogen, and another to allow the funnel to be fitted. This means that the mould remains totally enclosed until after casting. Both holes are covered during mould heating.

(ix) The mould and its heating box are mounted on a trolley. This allows the heavy mould to be quickly and easily manoeuvred under the crucible for casting, and out again for core extraction. The base of the trolley forms a wide tray to contain the molten lead in case of disaster.

5.1.4 Development of casting technique

Mould temperature

The capacity of the mould is 38 lb of lead, which must be poured through a single inlet whose maximum width is $\frac{7}{8}$ in, and must then flow to all parts of the mould. The mould must therefore not be so cold as to freeze the

lead before the mould has filled, and the molten stream of lead must have sufficient spare heat capacity to remelt and merge separate flows which meet again.

Because the centre of the casting wall must freeze from cooling through a thickness of lead, the temperature of the lead stream must be kept as low as possible to ensure rapid solidification. This means that mould filling and the remelting of separate flows must be ensured by raising the mould temperature. The mould and melt temperatures were adjusted to reduce the grain size, but at the same time avoid cracking, pitting and flow lines caused by too rapid cooling.

It is important that the mould surface should be at a uniform temperature before casting, to ensure uniform surface grain size. Thermocouples were attached just behind the casting surface of the mould, through fine holes from the outside, in several places, including the core. This way the temperature distribution of the mould during heating up and cooling down was monitored. It was found that the core, which due to its position, has to be heated by the rest of the mould largely across the casting gap ($\frac{3}{8}$ in of air) lagged 80°C behind the mould on heating up. Furthermore, during heating up all the temperature gradients are pumping heat into the centre of the mould, and casting should take place only when these temperature gradients are reversed.

It was found that a uniform mould temperature with the correct temperature gradients could be achieved by over-heating the main body of the mould, switching off the heaters and allowing it to cool. From tests conducted with the thermocouples connected to the Ultra Violet Recorder, Fig. 5.6 was obtained, so that the correct mould conditions can be arrived at at the correct time.

A thermocouple located in the crucible provided accurate temperature control of the melt. After the results shown in Fig. 5.6 were obtained

in terms of a particular thermocouple in the mould, that thermocouple and the one in the crucible were wired up to standard temperature gauges mounted on the fume cabinet.

Mould filling

The impracticable ideal would be to pour lead at just above melting point into a mould at the same temperature, so that the temperature is uniform throughout the melt and the mould, and then instantaneously to drop the temperature of the filled mould uniformly by several hundred degrees. The same effect could be achieved by filling a cold mould with just-molten lead instantaneously. Neither of these two alternatives is practicable, but the latter can be approached by filling the mould in the shortest possible time.

Originally, the mould was filled in 25-30 seconds, which meant that some parts of the mould, under a steady stream of hot lead, became appreciably hotter than others before solidification began. This caused large and varied grain structure. Also, since some parts solidified and contracted while the mould was still filling and the core was already expanding, cracks had already appeared before the core could be extracted.

On the basis of this analysis, the valve of the crucible was redesigned with the help of Dr. A. Lichtarowicz (Fig. 5.7) to give an effective pouring diameter of $1\frac{1}{4}$ in instead of $\frac{1}{2}$ in. The mould filling time is now 1.2 seconds under a full head of lead in the crucible. In theory it would be possible to speed up the filling still further, but the small casting section ($\frac{3}{8}$ in) into which the lead flows and difficulties of control make this impracticable.

The rapid filling of the mould, combined with rapid extraction of the core means that the core can be freed within 10 seconds of the lead entering the mould. This allows the mould temperature to be reduced, with consequent improvement in grain size, and still avoid cracking. Flow lines are also improved, since separate streams of molten lead do not have time to lose much heat before meeting and blending.

Inert gases

During the development of the casting technique it was found that casting in an atmosphere of Nitrogen to avoid oxidation of the lead was unnecessary at the melt temperatures used (430°C). Casting in air produced bright surfaces on which grain structure could be seen directly when magnified. A day or two after casting, the model surface would form an oxide film and become dull, but the average time of less than ½ second spent in transit from the bottom of the crucible, and the time of approximately 1½ seconds to fill the mould, and hence exclude the air from all except the feeder head surface, was too short for much oxide to form, even at 430°C. It was found, however, that oxide did form when the lead temperature was greater than 600°C.

Gravity segregation

Because of the difference in density between Antimony and Lead, there is a degree of gravity segregation in the alloy when molten. Before casting, the crucible would be stirred, and since segregation is a slow process in comparison with casting and freezing times, this was considered sufficient.

Casting parameters

While the lead is heating up, the base of the crucible and the valve are hotter than the molten lead. This condition is preferred for casting to be sure of free outlet flow of the lead, so casting should take place as soon as possible after heating up. The large mass of lead to be melted means that the lowest melt temperature after complete melting and mixing is about 420°C. This was found to be the most convenient melt temperature for casting.

The optimum mould temperature, the lowest that would produce crack-free castings, was found to be 215°C. To achieve the shortest filling time the level of melt in the crucible must be maintained as high as possible (16¾ in), and the valve travel must be at least 1¼ in.

Casting procedure

After completion of the development work, the following procedure was used:-

(i) Clean out mould and insert the core. Check with feeler gauges that the beams that support the core are properly sealed to ensure the correct casting wall thickness. Check the automatic shut off contact for operation and height. This sets the thickness of feeder head. Put the lid in the heater box and cover with fibreglass.

(ii) At casting time minus 3 hours switch on the mould heaters.

(iii) At casting time minus 1 hour 40 minutes switch off the mould heaters. The mould temperature gauge should now show 260°C.

(iv) At casting time minus 25 minutes light the crucible burner to melt the lead. Switch on the extractor fan in the fume cupboard.

(v) At casting time minus 5 minutes switch off the crucible burner. The melt temperature gauge should now show about 450°C. (The thermocouple is near the valve), and the mould temperature gauge should now show 220°C.

(vi) At casting time minus 2 minutes stir the lead in the crucible. The melt temperature should now be about 430°C.

(vii) Take the fibre glass cover off the heating box, and fit the funnel through the hole in the lid into the mould inlet.

(viii) Push the mould under the fume cupboard and position it so that the sleeve round the pouring tube drops onto the funnel rim.

(ix) Press the button to operate the solenoid and open the valve.

(x) As soon as the solenoid switches off and the valve closes, pull the mould out from under the fume cabinet, take out the funnel, take the lid off the heater box, undo the two bolts securing the core.

(xi) Check through the inlet hole that the lead has gone solid, then wind down quickly on the extraction bolts, taking care to keep the core horizontal as it lifts.

(xii) When the core is just lifted clear, replace the lid of the heater box and cover again with fibreglass insulation. The mould temperature should be about 240°C.

(xiii) Leave the mould and casting to slow cool to about 50°C (about 18 hours) before removing the casting from the mould.

Heat treatment

Leaving the casting in the mould to slow cool overnight serves two purposes. Firstly, it prevents cracking and further plastic straining from large thermal stresses due to too rapid cooling. It was found during development that if the core was removed as soon as it was lifted, the inside surface, exposed to cold air, cracked due to differential contraction. Secondly, this long "soak" at above 100°C acts as a normalisation process.

5.1.5 Quality of castings

The castings should have the same composition, a good surface finish without cracks, flow lines, pitting, thickness variations or porosity. The grain structure should be small, randomly orientated and uniform over the surface and through the thickness. There should also be no variations from casting to casting.

Surface defects

Over most of the casing the surface finish is as good as that of the mould (Fig. 5.8). Machining marks and the joints between the three sections of the mould are reproduced exactly by the castings, but there are no flow lines or cracks. There are, however, some local pitting and folds where a small air bubble has become trapped, but these are concentrated in the middle of the cylindrical section on the inside surface mid-way between

the flanges, where the large radius of the core has formed a local "horizontal roof" and prevented the bubble's escape. These defects are very much less at the ends, where the interest lies, and it is felt that the overall behaviour in creep, with stress redistribution taking place, will not be much affected by these local blemishes (see Section 2.1.4).

Porosity and blow holes

A disadvantage of the chill casting technique is the difficulty of avoiding porosity. Although the addition of Antimony reduces the effect, lead alloys contract on freezing, and prevention of porosity depends on good feeding with still-molten alloy. To achieve small grain size and isotropy, the melt has to freeze as quickly as possible, everywhere at the same time, which would impede feeding. It follows that a good grain structure can only be achieved with some porosity.

In addition to the general porosity, sectioning of castings (e.g. cutting dumbell specimens) shows occasional 'blow holes' under the surface. These appear to be due to the same kind of air bubble trapping as gave rise to the surface pitting, and again are concentrated in the middle of the cylindrical section, mid-way between the flanges.

Grain size, distribution and direction

The surface grains appear small, randomly orientated and uniform throughout the casting, except adjacent to the inlet hole in the middle of the cylindrical section (well away from the points of interest) Fig. 5.9. However, in the radial direction through the wall thickness, the grains have grown inward in a dendrite fashion, Fig. 5.10. So, although the material properties should be the same in the hoop and meridional directions, they will probably be different in the radial direction.

Since the casting must be cooled from the outside inwards, the only way to prevent this directional dendrite growth is to provoke spontaneous nucleation ahead of the solid interface through constitutional undercooling. This requires the kind of rapid cooling possible only by means of chill

casting, so the same technique would have to be used, but with a much colder mould. However, it has been shown that a colder mould would lead to cracking, and would further aggravate porosity, pitting, flow lines and blow holes.

In the casing the radial stresses are small, making them unimportant, particularly in creep, but in the flange and the boss ends this anisotropy may lead to significant differences between the behaviour of lead model and steel prototype.

To show the grain pattern in a typical casting (No. 21), a hoop slice was cut and divided into sections (Fig. 5.9). These sections were polished and etched electrolytically (Appendix 3) to show the grain structure through the wall thickness (Fig. 5.10).

The grain structure shown in Fig. 5.10 is of the expected pattern. The layer of fine grains at the surface are the result of the initial shock cooling of the molten lead coming into contact with the relatively cold mould. Momentarily insulated by this layer from the mould, the gap was filled with molten lead of an approximately uniform temperature. Then the remelting of the inner edge of the frozen layer and the rapid loss of heat through to the mould developed the negative temperature gradient inwards from both the inside and outside surfaces, causing inward dendritic growth from the initial surface layer. When this temperature gradient had reached the centre of the molten liquid, constitutional undercooling caused spontaneous nucleation uniformly throughout the remaining molten metal, leading to uniform, randomly orientated grains (see Section 2.1.9).

It can be seen that in the flange (Fig. 5.10 (g) and (h)) the grains are larger than those in the casing. This is because of the greater mass of lead in the flange and the header which slowed down the cooling in that region. Also, the inevitable time delay before filling that section of the

mould allowed the temperature of the surrounding steel to rise before the cooling could begin.

Fig. 5.10 (j) shows a blow hole caused by a trapped air bubble.

5.2 Machining of castings

For machining the lead models it has been found essential to use extremely sharp cutting tools, at the fastest possible cutting speed, taking very light cuts. Otherwise, the lead catches and tears, burnishes over or locally melts, giving poor dimensional accuracy and a bad surface finish.

The moulds as cast require the following machining operations;

(i) removal of the header

(ii) facing of the flange

(iii) drilling and countersinking of the bolt holes

(iv) boring of the shaft hole.

The castings are fixed in the machining jig (Fig. 5.11), a frame locating on the back of the joint flange. This enables the header to be bandsawn off for re-use, and the flange to be faced to within 0.020 in of final thickness.

The bolt holes are then drilled and countersunk. This was initially done in a drilling jig (Fig. 5.12), where the model is located on the flange face on a flat plate, and the drill is located by a bush through positioned holes in a plate held parallel over the back of the flange. However, the introduction into the workshop of a numerical controlled drilling machine greatly improved the drilling and countersinking of the bolt holes, and facilitates the changing of hole positions since no jig is required.

The drilling ruins the faced surface, and the model is remounted in the facing jig, and the flange refaced to the correct thickness.

At this stage the models are paired. They are bolted together and the shaft hole bored on a horizontal borer.

A list of the castings manufactured and their subsequent use is given in Table 5.1.

TABLE 5.1 LEAD CASTINGS OF MODEL TURBINE CASINGS

CASING NO.	CASTING TEMPERATURES (°C)		CRACKS	USE
	CRUCIBLE	MOULD		
1	420	210	none	Model Test 4 (Top)
2	420	214	none	Model Test 4 (Base)
3	415	212	none	Model Test 5 (Top)
4	420	210	none	Model Test 5 (Base)
5	420	214	slight	Uniaxial Specimens
6	420	215	slight	Uniaxial Specimens
7	420	212	none	Shelf
8	420	212	bad	Return to Crucible
9	420	217	none	Model Test 7 (Base)
10	420	220	none	Model Test 7 (Top)
11	420	210	bad	Return to Crucible
12	420	217	none	Model Test 9 (Top)
13	430	220	none	Model Test 6 (Base)
14	430	220	none	Model Test 6 (Top)
15	430	220	none	Model Test 9 (Base)
16	430	220	none	Uniaxial Specimens
17	420	225	none	Model Test 8 (Top)
18	425	225	none	Shelf
19	420	218	none	Model Test 8 (Base)
20	440	221	none	Uniaxial Specimens
21	420	225	none	Uniaxial Specimens

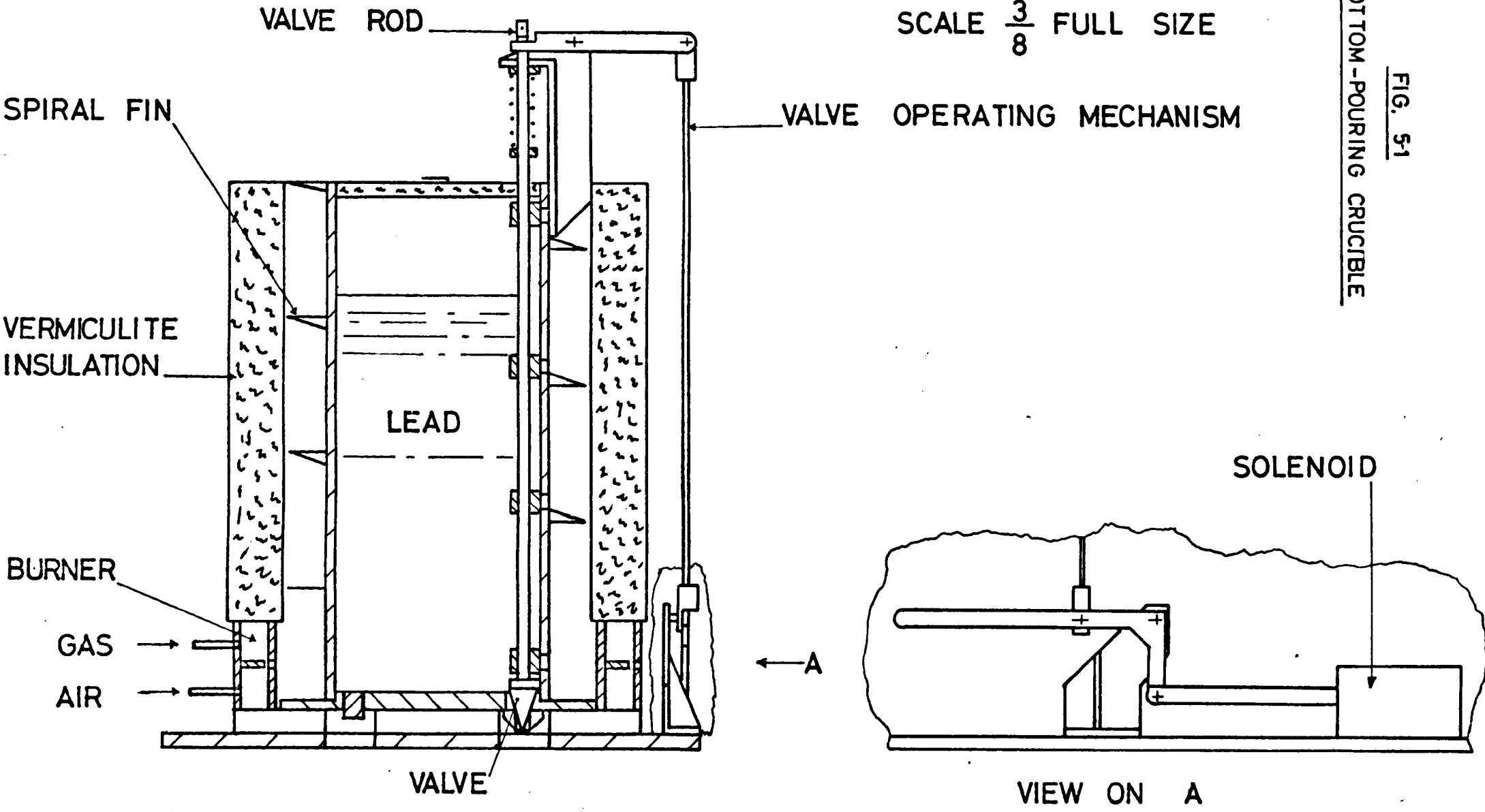

SCALE $\frac{3}{8}$ FULL SIZE

FIG. 5-1
BOTTOM-POURING CRUCIBLE

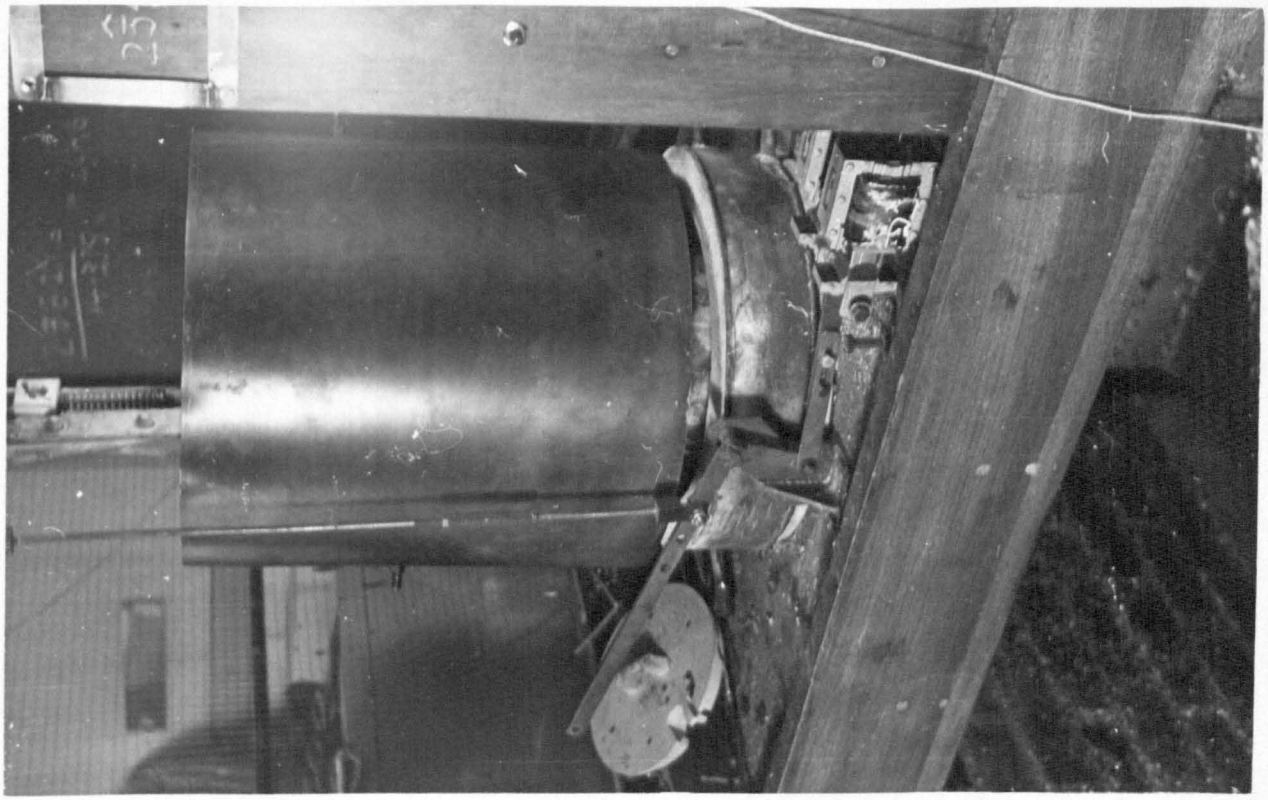

THE CRUCIBLE FIG. 5·2

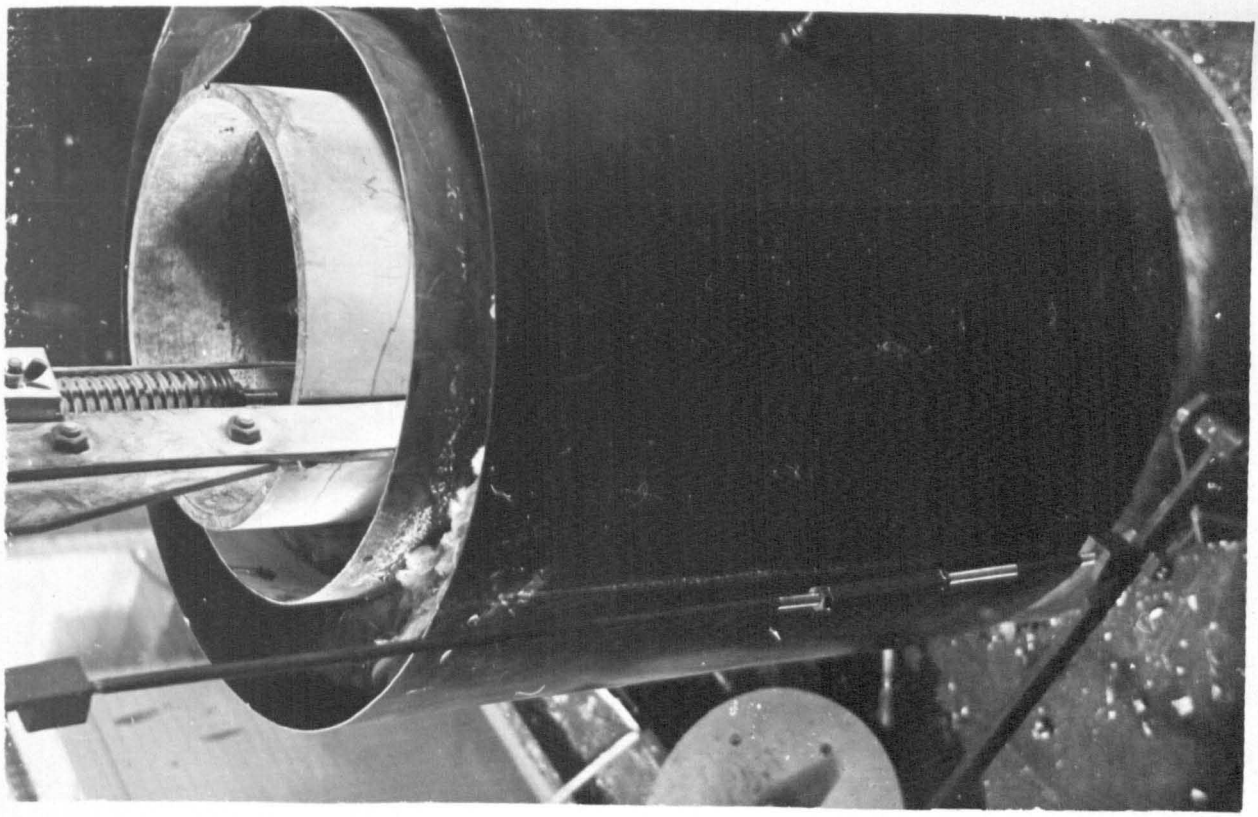

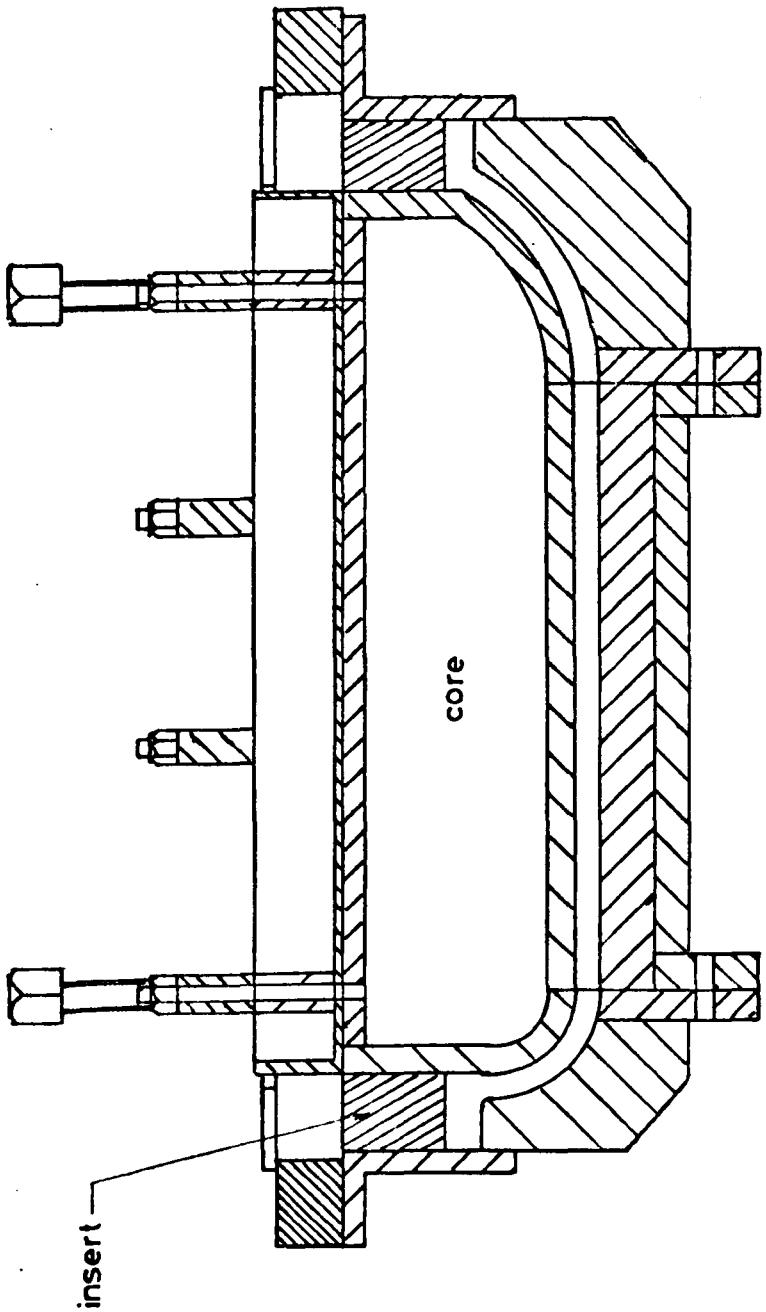

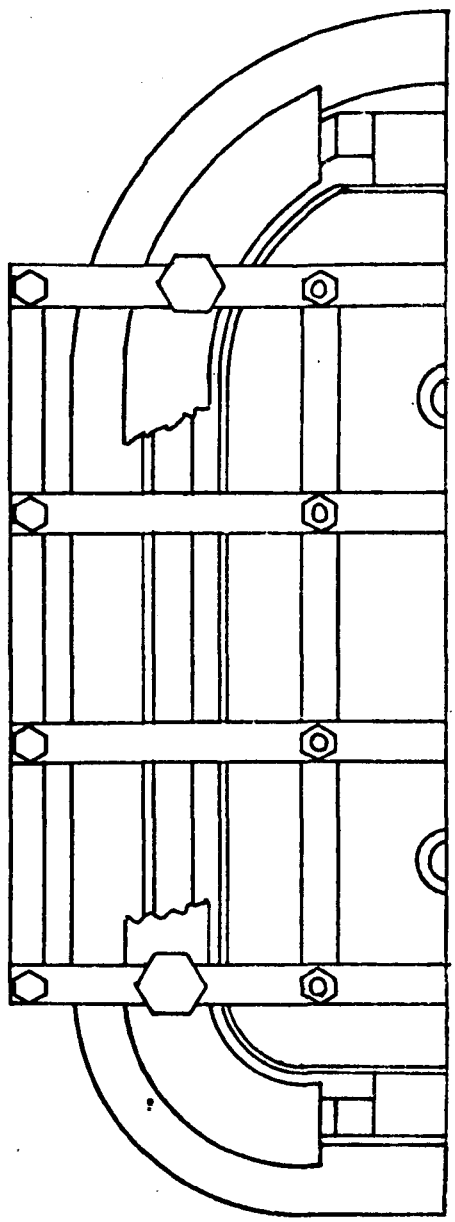

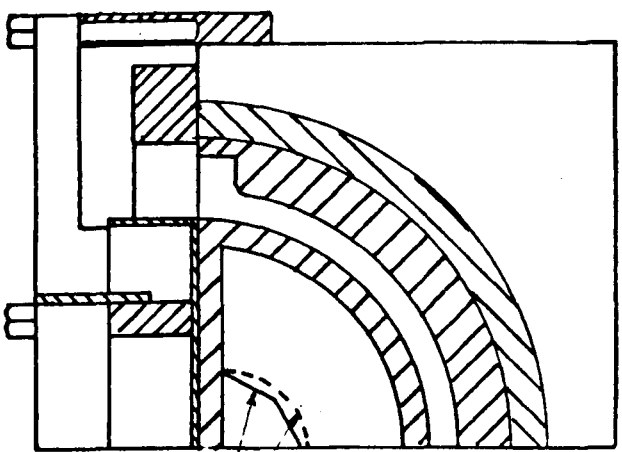

FIG. 5·3

MOULD FOR LEAD MODELS

THE MOULD FIG. 5·4

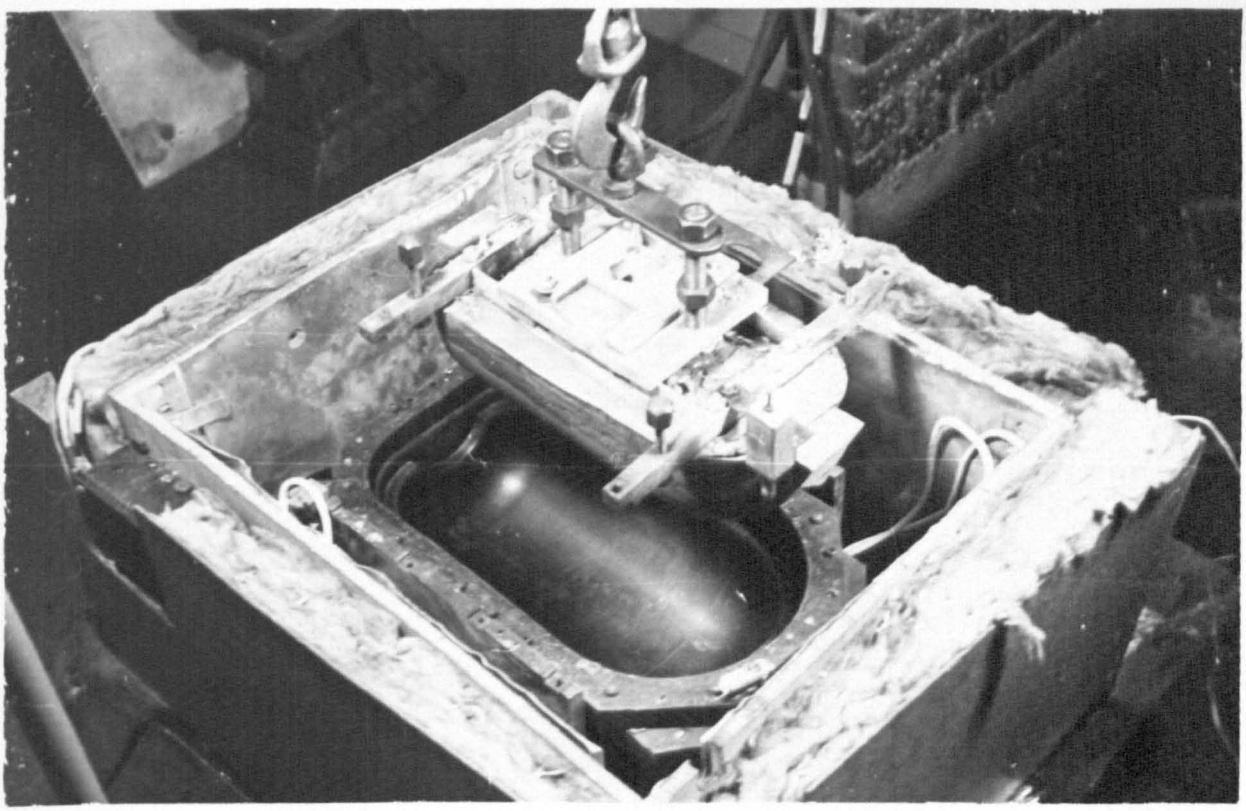

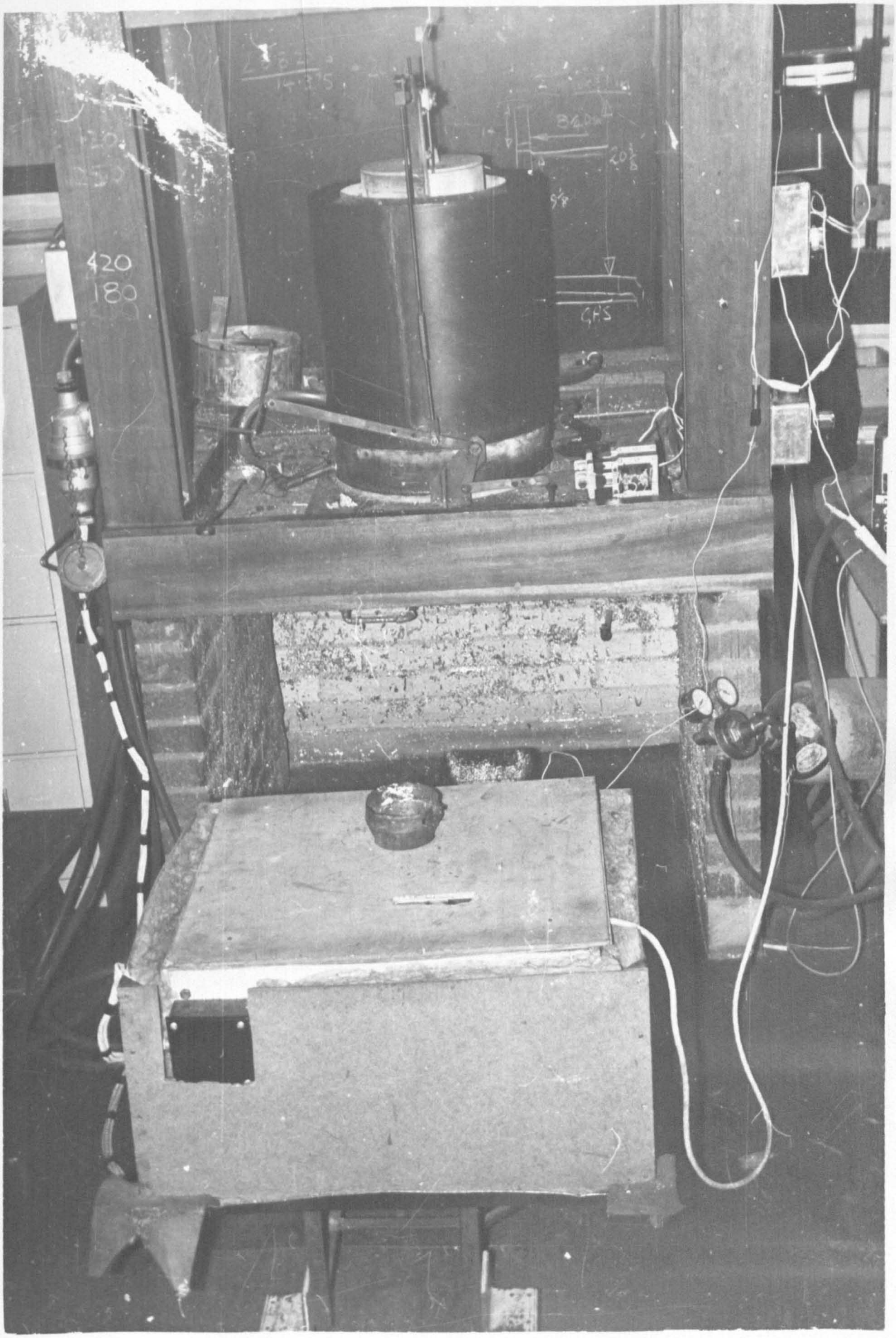

MOULD IN HEATING BOX

FIG.5·5

MOULD HEATING CHARACTERISTICS FIG. 5·6

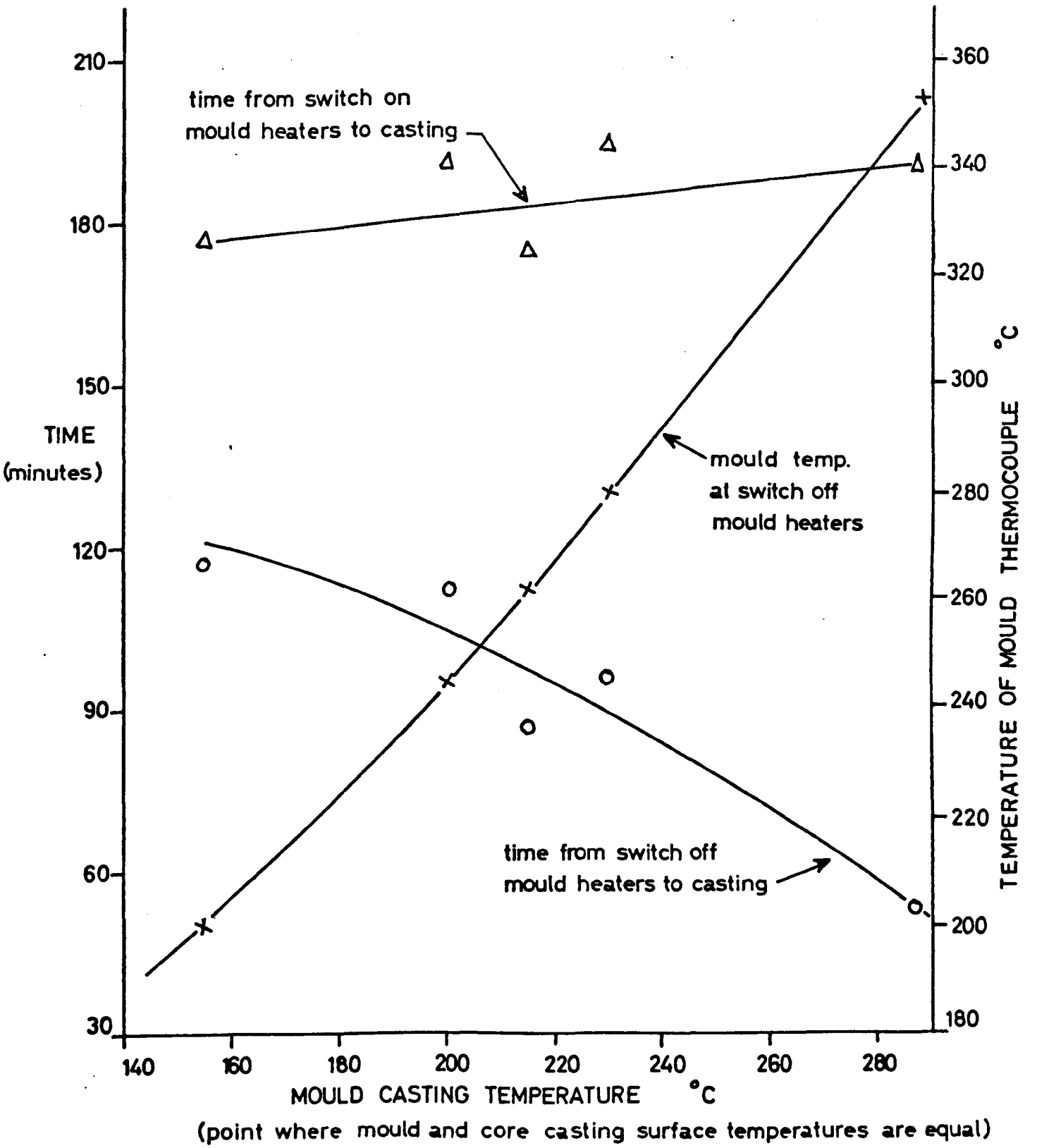

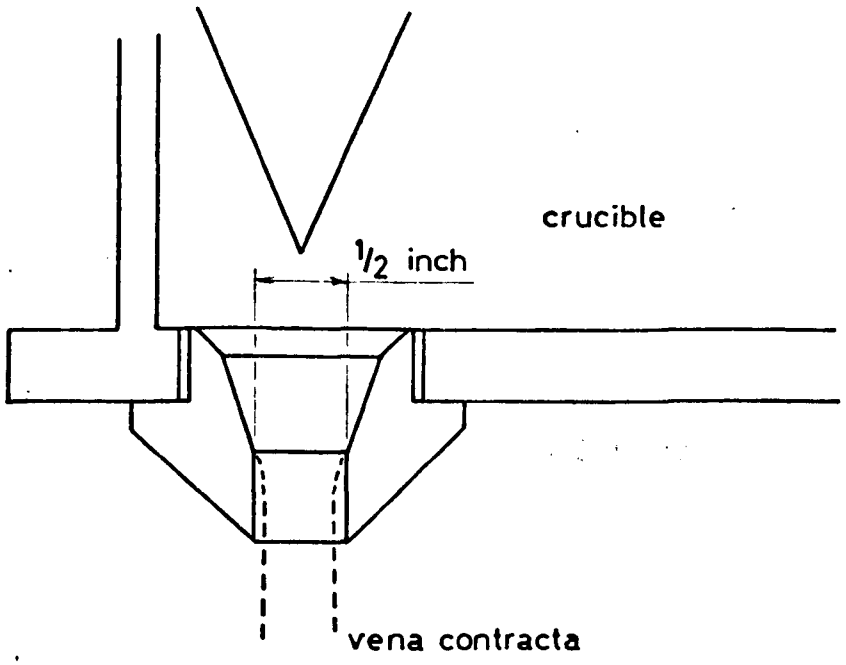

Original Nozzle

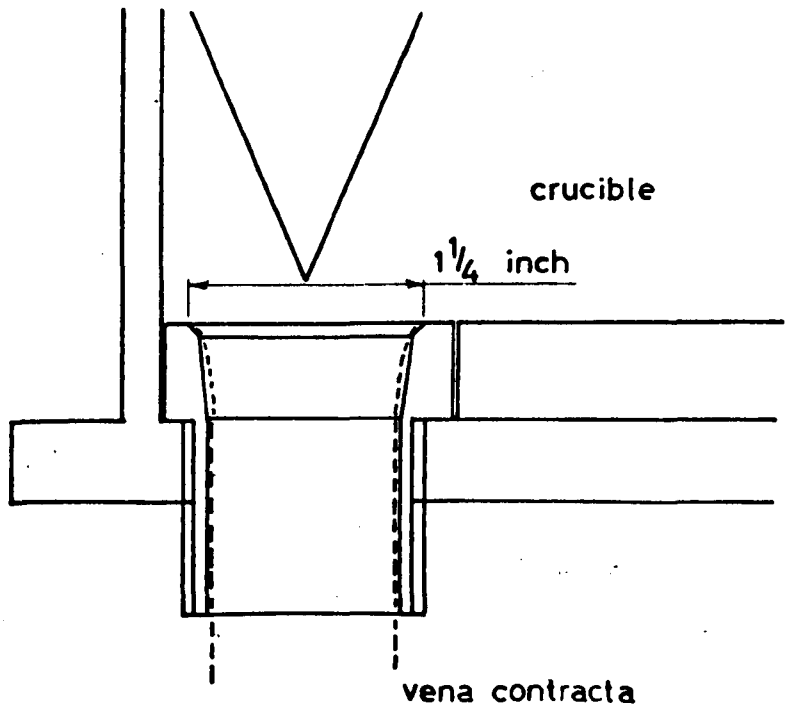

Modified Nozzle

FIG 5·7

CASTING SURFACE FINISH

FIG. 5·8

FIG. 5·9

LOCATION OF ETCHED SPECIMENS

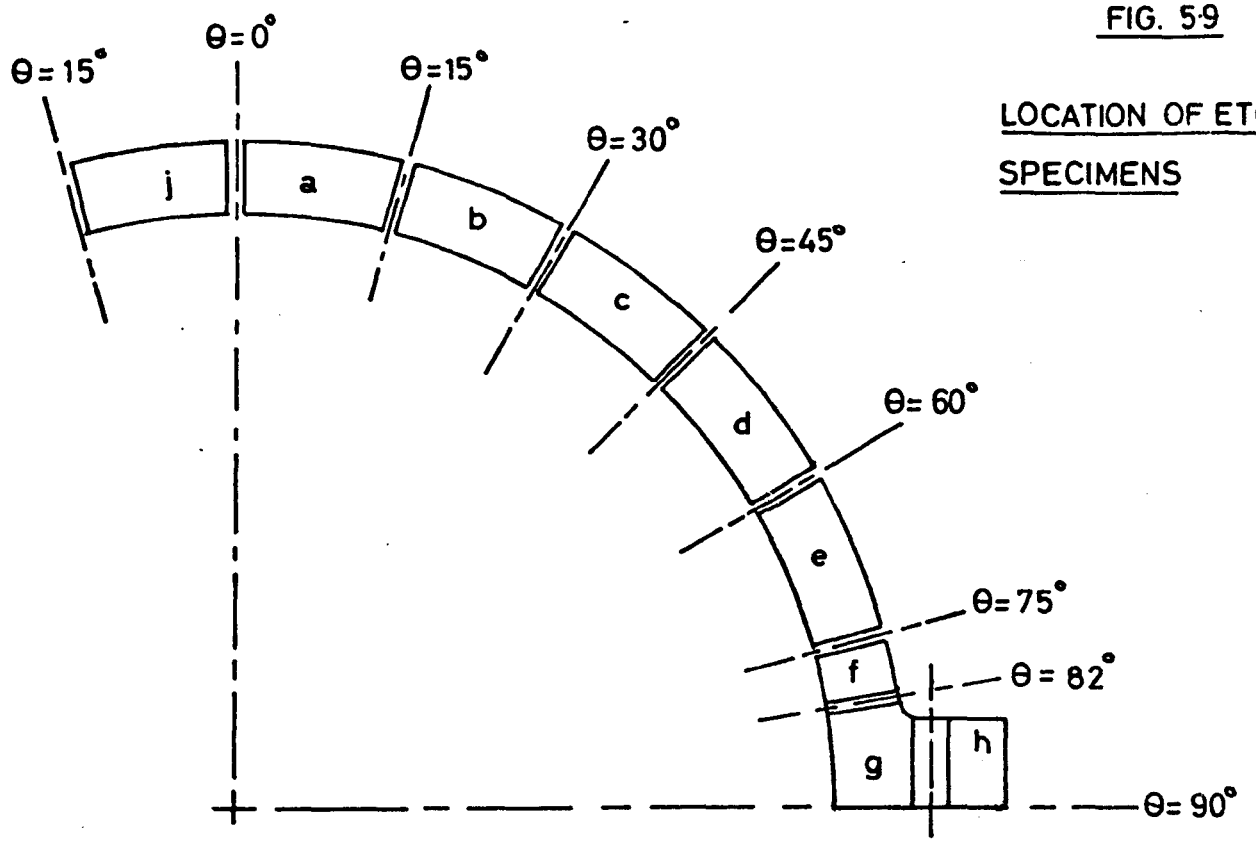

section at toroid/cylinder joint

FIG 5·11

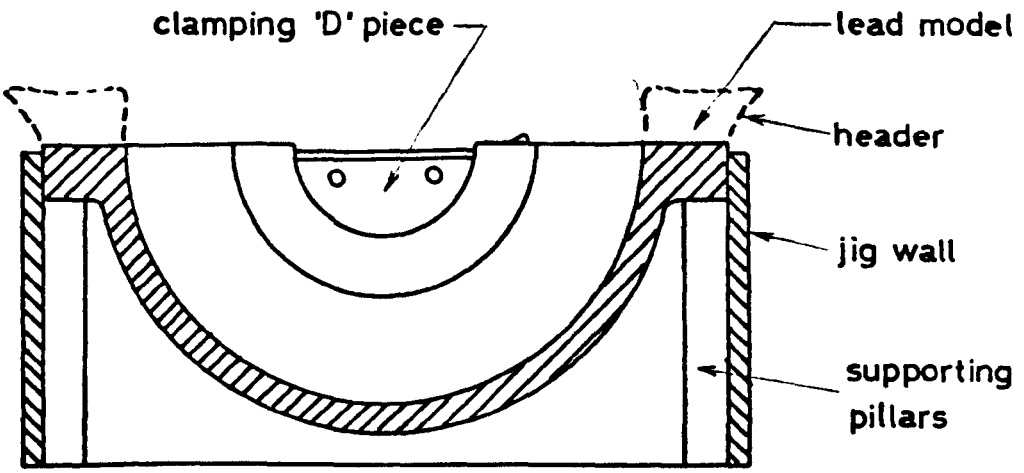

SECTION THROUGH MACHINING JIG

GRAIN STRUCTURE IN CASTING

FIG. 5·10

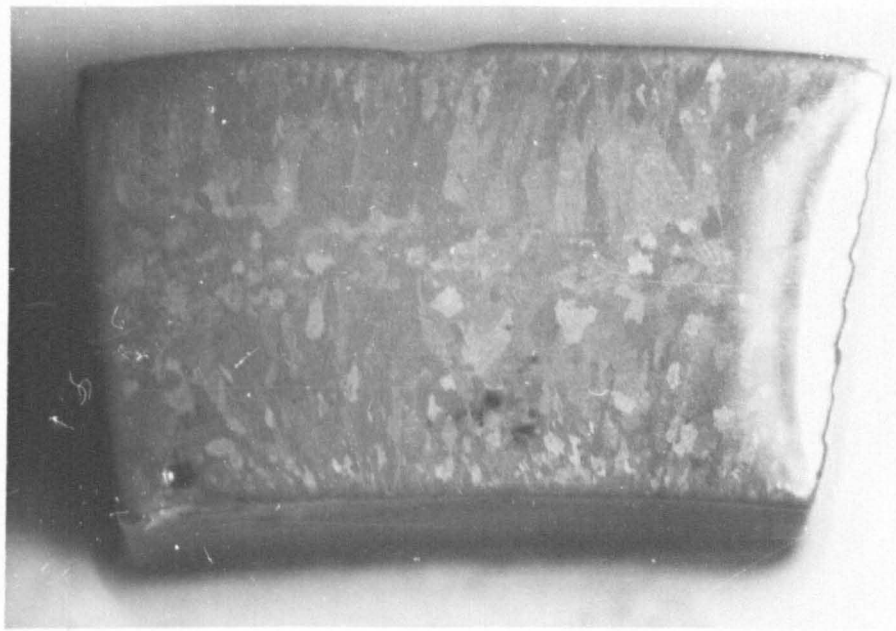

(a)

(b)

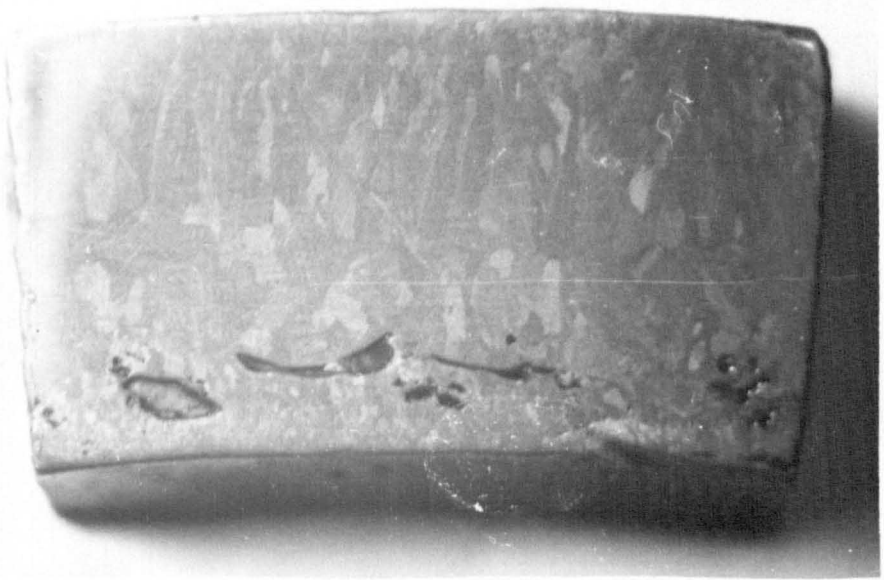

(c)

FIG. 5·10 (cont.)

(d)

(e)

(f)

FIG. 5·10 (cont.)

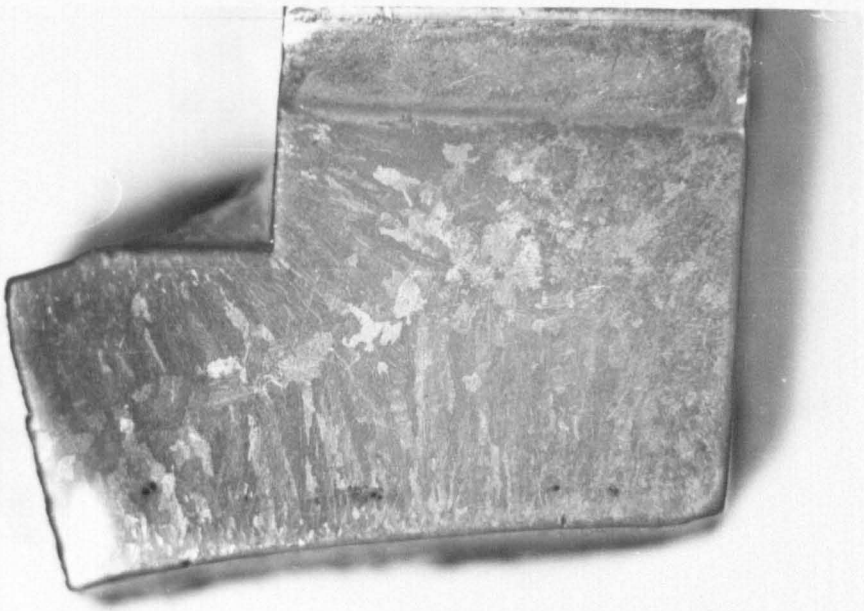

(g)

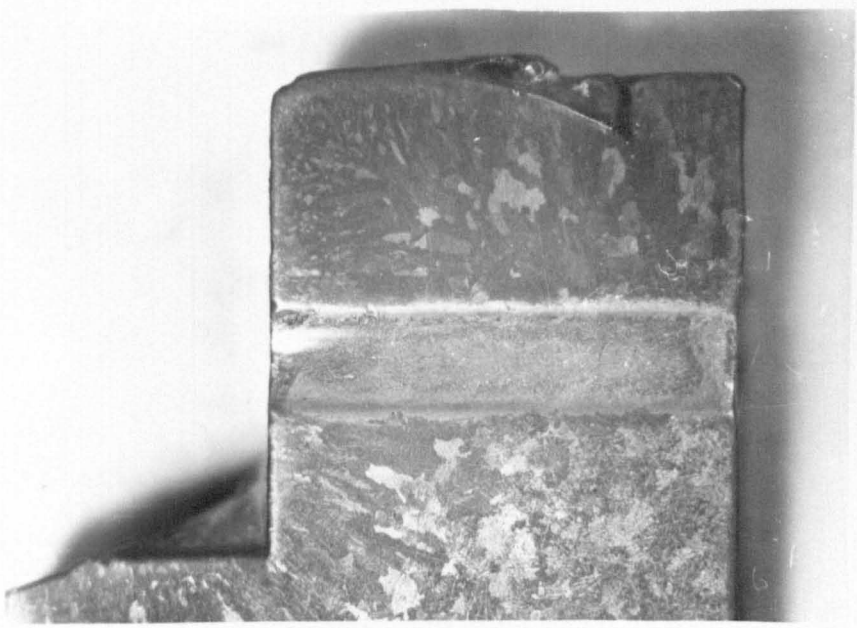

(h)

(j)

FIG. 5·12

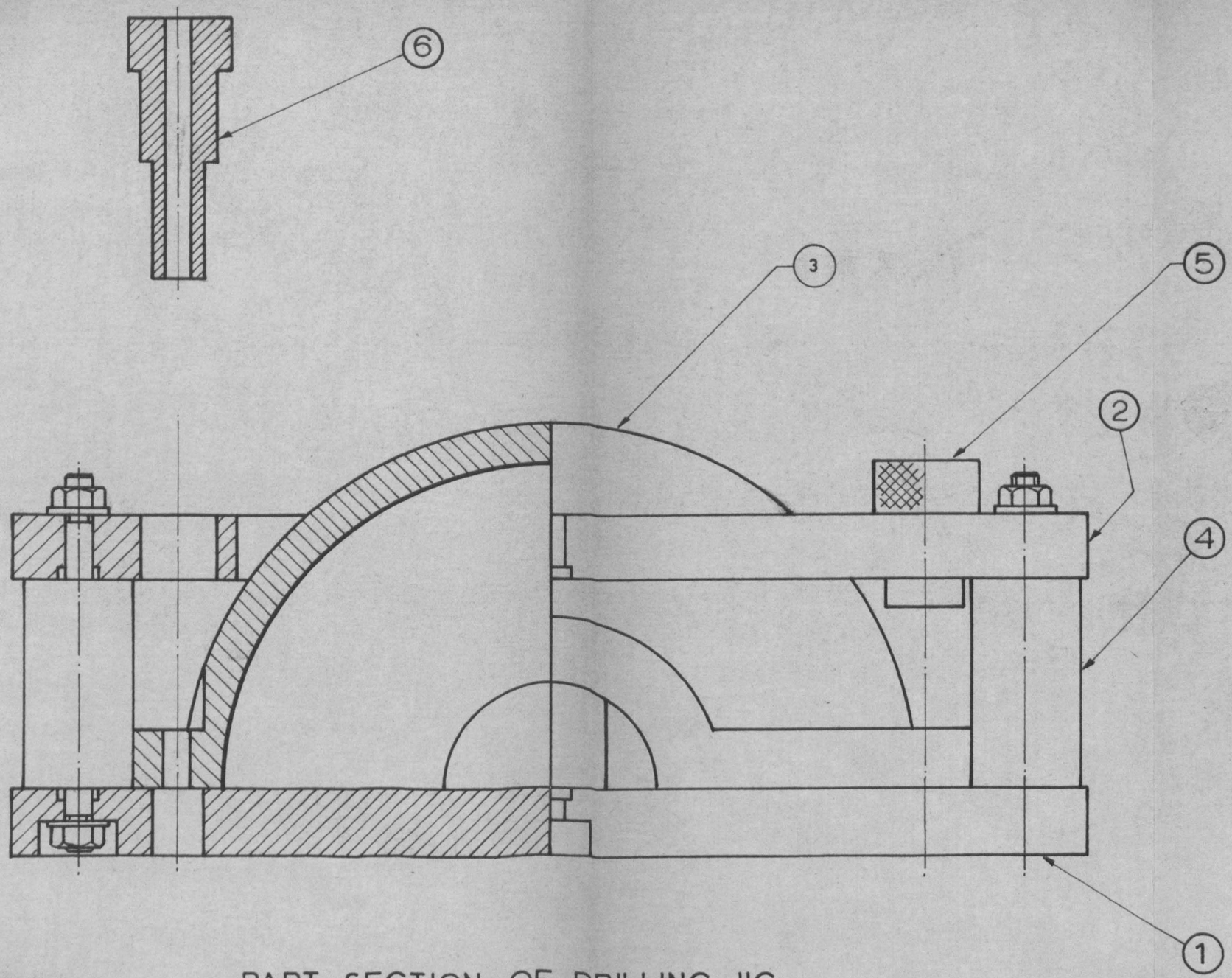

KEY	DESCRIPTION
1	BOTTOM PLATE
2	TOP PLATE
3	LEAD MODEL
4	LOCATING SPACER
5	COUNTERBORE BUSH
6	BOLT HOLE BUSH

PART SECTION OF DRILLING JIG

CHAPTER 6

MODEL TEST EQUIPMENT

6.1 Model loading equipment

6.1.1 Design parameters

The model loading equipment was designed not only for the models that have so far been tested, but also to accommodate design changes such as thicker flanges and the addition of inlet branches in the toroid end (See Section 5

6.1.2 The sealing shaft

The shaft is to perform the following functions:

(i) seal the bores at the ends of the models;

(ii) prevent the models from carrying any end load due to internal pressure acting on the area of the bores;

(iii) reduce the quantity of oil necessary to pressurise the model;

(iv) provide access for pressure application and measurement;

(v) provide access for internal instrumentation leads.

The sealing shaft is shown in Fig. 6.1. A proprietary 'U' packing seal is mounted on a sleeve in a hollow shaft through each of the bored end holes of the model. To avoid seal damage, the sleeve slides forward to clear the 'U' packing while the model halves are put together. The sleeve is then pulled back against an 'O' ring on the shaft stop, drawing the 'U' packing backwards into the bored hole, and can be clamped in this position by the screw-in clamp, which also gives the 'O' ring its initial nip.

In the forward position, the back of the sleeve locates in the bored hole and allows the shaft to rotate freely. However, when clamped in the sealing position, while still locating in the bored hole, friction at the 'O' ring prevents the shaft from rotating.

One of the stub shafts has a longer threaded section and a clamp nut. This allows the axial distance between the 'U' packings to be increased to ensure they are completely within the bore when extended.

The two hollow shafts are connected by a large hollow drum with end plates, which occupies $\frac{2}{3}$ of the inside volume. All pressure and electrical tappings are fed through the hollow shaft into this drum and pass to the inside of the model through the end plates. To form a sealed electrical connection, copper wires are set in Araldite in small holes through the end plates. Leads can then be soldered to each side of the insulated, leak-tight copper wires.

6.1.3 The clamping rig

The models are supported and clamped in the clamping rig. It is necessary to ensure that

(i) the model is supported under the flanges,

(ii) the clamping represents the bolt action of the actual turbine casing,

(iii) the clamping load of 12000 lbf to retain an internal pressure of 100 lbf/in^2 can be applied,

(iv) the clamping load must be put on rapidly to avoid creep in the flanges before pressure loading,

(v) the clamping load remains more or less constant during the test (i.e. while flanges creep),

(vi) light clamping is possible for filling the model with oil,

(vii) there is good access to the model, both before and after clamping.

The model is both loaded and supported by pillars representing the bolts (Fig. 6.2). These pillars, of the same diameter as scaled down bolt heads or nuts, are located by stub pins in the bolt holes. Four of the 88 pins are longer than the flange thickness of one half model, and

therefore locate one half model to another. The gap between two opposing stub pins is sufficient to allow for creep of the flange.

The pillars on each side are loaded through a rubber pad by a distribution bar (Fig. 6.3) to spread the load evenly among the pillars, despite variations in pillar height.

In each of the four corners, the sandwich of flanges, pillars, rubber pads and distribution bars is mounted on a frame (Fig. 6.4). Part of each mounting is a strong spring (1 tonf/in stiffness) trapped between two plates. The top plate bears up against the bottom of the frame; two T-bolts, hooking onto the frame and passing down through the top plate and the inside of the spring, support the bottom plate on nuts, which can be tightened up to pre-compress the spring to the required load, up to 1.5 tonf.

When pressed down from the top, the sandwich assembly bears down in each corner through a column onto the top plate, pushing it clear of the frame, and so transferring the spring load of $1\frac{1}{4}$ tonf through the sandwich. The displacement of the top plate need only be $\frac{1}{4}$ in to ensure that the full clamping acts throughout the test. The clamping force remains effectively constant because the pre-compression of the springs is much larger than the anticipated creep deformation. When all four corners are pressed down, clear of the frame, a clamping load of up to 6 tonf can be produced.

Each clamping displacement is applied through a pivot arm mounted on the frame next to the loading column by means of an expanding toggle linkage on the other side of the pivot as shown in Fig. 6.5. This linkage, mounted on the frame and driven by a hydraulic piston, has two toggle actions. In the fully contracted position (on the left) the top link and the support link form a toggle, so that the initial movement of the piston causes the support link to swing rapidly under the pivot arm. Further movement of

the piston straightens the top and bottom links, and the pivot arm is lifted, pressing down on the sandwich on the other side of the pivot. As the top and bottom links come "into line" they form a toggle, and the piston force required drops rapidly to zero in the straight line, fully expanded position.

For each linkage fully expanded, it is arranged that the pivot arms are horizontal. The deflection of the top spring plates in this condition can be adjusted by inserting packing between the top distribution bar and the pivot arms. Each linkage is locked in this position by sliding a collar over the joint of the top and bottom links to prevent them from being knocked out of line. The pressure on the pistons can then be released.

The expanding linkages are arranged "back to back" in pairs, each pair operating the clamping on one side of the model. Thus, all the horizontal forces which arise during the straightening of the linkages are carried by the linkage unit and not in the frame. All the vertical forces at each clamping point are confined to a very short load path, allowing the use of a very light frame. This separation of function of units allows two features to improve access to the model:

(i) The linkage unit and pivot arm supports on each side themselves form a parallel linkage, allowing all the clamping equipment to be swung away from the model on the frame when it is not in use.

(ii) The frame which carries the model and clamping devise is itself mounted on a shaft on a trolley; this allows the clamping assembly to be tilted at any angle up to 180° and makes the whole apparatus mobile. In particular, being able to clamp the model lightly (by only partial pumping up of the hydraulic cylinders) and to tilt it through 90° so that its axis is vertical, allows the model to be filled with oil and "bled" through the bored hole at one end before any creep occurs.

There is sufficient room in the existing rig, at present taken up by spacers, to accommodate models with twice the existing flange thickness, no changes are necessary when models are produced with inlet nozzles at the toroid end. If larger design changes are to be accommodated, the modular construction of the clamping rig means that only certain parts need to be replaced. Greater clamping loads could be achieved by mounting stronger springs or by adding smaller springs to fit inside the existing ones.

6.1.4 The pressure rig

Transformer oil was used as the pressurising fluid because an incompressible electrical insulation was required. To keep the pressure constant inspite of leakage and expansion of the model, the oil is fed to the model from a chamber pressurised by a seal-less piston under dead weight loading (Fig. 6.6). This chamber is itself supplied from a 2-gallon reservoir tank by a pump driven by an electric motor (Fig. 6.8). Microswitches, mounted on the piston, start the pump when the piston reaches the bottom of its travel and switch off again when the piston reaches the top. A spring loaded bypass valve controls the flow rate from the pump.

The pressurised oil is fed into the model by a pipe through the inside of the sealing shaft drum. Another pipe from the other end of the sealing shaft drum feeds the model pressure back to a pressure switch, which is set to switch off power to the pump motor if the pressure should fall below a set level after the test has begun, indicating failure of the test. Sockets to supply the recording equipment with electric power are also connected through the pressure switch to switch off if a failure occurs.

The reservoir, pump, seal-less piston, control equipment and pressure switch are mounted on a trolley (Fig. 6.7). The seal-less piston hangs

freely and must be vertical both before and after the weights are applied. This ensures that there are no side faces on the piston which could cause sticking and thereby prevent the intended pressure being exerted by the oil in the chamber.

6.1.5 Performance of loading equipment

The metal to metal flange joint sealed completely; but in the bore, where the flange joint meets the sealing face of the 'U' packing, oil leakage was too fast. The rapid fall of the seal-less piston in the pressure rig caused the pump to be switched on and off so frequently (once every 10 seconds) that the pump motor overheated. Application of Red Hermatite to the flange joint and the bore failed to slow down the leakage sufficiently, but silicone rubber was found to seal the model completely.

Four drops of Hardener 'D' curing agent were mixed with 75 grams of Silcoset 151. The mixture was quickly applied to the flange faces and bores, the shaft inserted, and the two halves put together and lightly clamped. Within 1½ hours the rubber was completely cured and the models ready to be pressurised. Since the rubber was still liquid when the flange faces were pressed together, only a very thin gasket is formed (about 0.001 in, Fig. 6.9), but any gaps at the 'U' packing are filled completely.

Repeated soldering to the copper pins through the end plates of the sealing shaft caused the Araldite, in which they are set, to crack due to the rapid heating. This allowed the pressurising oil to leak into the hollow shaft. However, this slight leakage was considered beneficial to the operation of the pressure rig. The leakage rate was too slow to cause a significant pressure drop in the oil delivery pipes, and because the seal-less piston was continually moving, there was no danger of it sticking.

A drip tray (Fig. 6.18) was inserted in the trolley under the clamping rig to collect the oil from any leaks, and pipe it back to the oil reservoir on the pressure rig.

6.2 Instrumentation and recording equipment

6.2.1 Strain gauges on lead

It is necessary to measure strains with the greatest possible accuracy at several positions at various times over periods of at least 100 hours on the inside and outside surfaces of the pressurised lead model. Potentially, the most convenient and accurate means for doing this is by using electric resistance strain gauges.

The Moire grid technique used by Gill (16) has the advantage of giving a field coverage of strain. Although it has been adapted for surfaces with single curvature, this technique is clearly out of the question for monitoring strains inside the lead models, or on any surfaces of a complicated shape. Also, the Moire technique cannot measure accurately strains less than about 0.1%.

However, before using electric resistance strain gauges, the following questions must be answered:

(i) Will the gauge adhere properly to the lead surface?

(ii) Will the gauge cause general reinforcement of the model? i.e. will the gauge carry a significant fraction of the force acting on the section where it is attached?

(iii) Will the gauge cause local reinforcement of the lead? i.e. will the surface of the lead be restrained in the immediate vicinity of the gauge?

Because the thickness of the models is at least $\frac{3}{8}$ in and foil gauges are 0.0001 in thick, general reinforcement in direct loading and in bending is negligible. The epoxy resin insulation under the gauge is thin and relatively weak, and the polythene covering of the gauges is not firm.

To answer the other questions, two experiments were carried out. Firstly, a Moire grid was printed on a flat plate, and then a strain gauge was stuck on to an area cleaned to exactly the right size (Fig. 6.10). The

plate was then loaded in uniaxial tension, taking strain readings at regular intervals from both the strain gauge and the Moire grid. The soldered connections on the strain gauge prevented placing the Moire master grid over the gauge, but Moire fringes could be measured right up to the edge of the strain gauge on both sides, and were observed to be straight and continuous. The results (Fig. 6.11), up to 2.2% strain when the gauge failed, show that the strain in the plate measured by the strain gauge is at all times identical to that measured by the Moire grid, which can exert no restraint on the plate material.

In the second experiment a strain gauge was again stuck onto a flat plate. This time, a Moire grid was printed over the whole area, including the gauge, which was left unconnected to keep the protrusion as small as possible. The plate was loaded in uniaxial tension for five days up to a creep strain of 5%. Initially, and at regular intervals afterwards, the Moire fringes were observed on the plate, care being taken to avoid parallax. The fringes were continuous across the gauge and showed no distortion in the vicinity of the gauge.

Detailed measurement of the residual moire pattern immediately after unloading and after a period of recovery showed no disturbance due to the strain gauge.

From these tests it was concluded that strain gauges follow exactly the behaviour of the lead surface to which they are attached, and produce no local or general elastic or creep reinforcement, i.e. they do not affect plastic and creep strains.

It should be pointed out that a tag strip, which was also stuck on the plate, near the gauge, showed a very sharp discontinuity of fringes at its edges, though no distortion of the surrounding fringes. This indicates that the tag strip either was not properly adhering to the lead or caused considerable local reinforcement.

The strain gauges used for the models were TML and Micro-Measurement gauges, bonded with Eastman 910 thin film curing adhesive. The lead surface was initially prepared by polishing with trichlorethylene or inhibisol, though a neutralising agent was found unnecessary. A standardised gauge length of 5 mm was adopted to ensure strain measurement over a large number of lead grains, and although initially provision was made for using post yield gauges, elastic gauges with linearity up to 2% strain were found to be adequate for the strains measured.

6.2.2 Instrumentation and Recording

The use of electric resistance strain gauges for measuring strain, and the need to take a large number of readings in quick succession at various times over a period of several days has led to the use of a digital voltmeter coupled to a punched paper tape output, fed by a scanner and timing unit (Fig. 6.12). To simplify the recording, the clamping force, pressure and scan time readings have also been arranged to give voltage signals.

Up to 100 input channels can be automatically scanned, each fed in turn through an amplifier to a Digital Voltmeter (D.V.M.). The D.V.M. reading is visually displayed and punched on tape, together with the channel number. The device is set to scan 80 channels at the rate of 4 channels per second, and each scan can be triggered either manually or by a timing unit, which triggers at pre-determined regular intervals between 5 min and 75 min.

At each scan during a test, the following readings must be taken;

(i) the strains in the model

(ii) the clamping load

(iii) the pressure

(iv) the time of the scan and supply voltage.

Independently of the above system, a continuous record of 12 quantities can be obtained by a U.V. Recorder. This is used at the beginning of the tests.

6.2.3 The model strains

All model strain gauges use a multi-half-bridge system shown in Fig. 6.13. Each active gauge has its own balance resistor and an apex potentiometer to obtain initial balance (or near balance) with the apex of two standard resistances called the common base pair (Fig. 6.13). A common base pair of resistances can be used since, at any time during a scan, only one active gauge is being measured, and the apex tappings of all the others are disconnected from the D.V.M.

All strain gauges are standard 120 Ω wire or foil gauges, with a tolerance of $\pm 0.3\ \Omega$. The gauge length of all gauges is 5 mm, being the smallest deemed advisable with the expected grain size of the material. "Post yield" gauges are used where large strains are anticipated.

The balance resistors and base resistors are strain gauges of the same type, mounted on aluminium plates. 10 balance gauges (all elastic or all post yield) are mounted on each aluminium plate (Fig. 6.14), easily changed for a plate of 10 gauges of a different kind if different active gauges should be required.

The balance gauges, base gauges and apex potentiometers are mounted in a screened box and are connected with the active gauges on the model by screened cables running either to a connecting box mounted on the clamping rig (for the outside gauges), or to the shaft, which acts also as a connecting box for the inside gauges. The connections through the shaft are made to each side of copper pins set in Araldite in holes in the shaft end plates (see Section 6.1.2).

Each active gauge must have a wire to connect it with its apex potentiometer in the balancing box, but the other ends of all the active gauges are connected to ground (Fig. 6.13). It is convenient, therefore, for all the gauges to have common earth wires, and the screening of the cables is used for this purpose. Because of difficulties experienced during the

first model test there are no common wires within the strain bridges. In the original circuit (Fig. 6.15), the base gauge connection with the active gauges was in the balancing box, so the common earth wire along the screening of the cables was within the bridge. This meant that any change in current through this common wire due to a gauge failure affected the voltage readout of all the other gauges. To exclude the common ground wire from the bridge, the ground sides of the base gauge pairs have been brought along the cable to complete the bridge in either the connecting box or the shaft; i.e. two base gauge pairs are needed. (Fig. 6.13).

To follow any temperature or other zero shift effects, there are four reference gauges, two inside the model and two outside. Each pair of reference gauges (one elastic and one post yield) is mounted on an aluminium plate which is mounted either close to the model on the clamping rig or on the shaft inside the model. They are connected as active gauges in the usual way, but, since they are not strained, they provide a zero check at each scan for the strain measuring.

One of the reference gauges has a socket connected in parallel at the tagstrip. At the beginning of each test a standard 120,000 Ω resistor is plugged in parallel with this reference gauge, reducing the resistance between the strain gauge terminals by 0.1%. The change in the D.V.M. reading of the reference gauge channel thus represents an electrical strain of 0.1% and, together with the supply voltage reading which is also taken at every scan, is used to relate voltage readings to proportional change in resistance.

To prevent large errors due to subtracting the initial reading from a reading to obtain the true value, the initial reading should not be larger than the true value. It is necessary to have apex potentiometers to obtain small initial values when measuring small strains.

A stabilised 5 volt D.C. supply to the strain bridges is provided by a mains powered Farnel unit having a maximum output of 3 amps.

6.2.4 Clamping load

The clamping load is measured by strain gauging the four columns which carry the spring force from the spring top plates to the distribution bars of the clamping rig (see Section 6.1.3 and Fig. 6.4). On opposite sides of each column flats are machined for mounting 120Ω gauges. The pair of gauges on each column is wired in series to measure compressive stress without bending. The balance gauges and base gauges are mounted on a steel plate in the balancing box, and are linked to the column gauges through the connecting box in the usual way to form 240Ω bridges, which are included in each scan.

The columns are calibrated on a Denison machine and are then used to pretension the clamping springs by clamping up on some dummy blocks.

6.2.5 Pressure measurement

The pressure is measured by a pressure transducer. A complete 120Ω strain bridge is mounted on a thin disc which forms one integral end of a short hollow cylinder. The supply and tapping wires pass through a hole in the cylinder wall, sealed with Araldite; the cylinder is closed by a bolted lid, and sealed with an O ring.

The transducer is suspended inside the model, the supply and tapping points are connected via the shaft pins and cable to the balancing box. The tapping wires are carried straight through to the scanning unit.

To calibrate the rig, some pressure gauges were first calibrated in a dead-weight standard calibrating unit. These pressure gauges were then connected to the output of the pressure rig to calibrate the seal-less piston. The pressure transducer was then calibrated in the model at the beginning of the test when the leakage was very small and the pressure drop along the connecting pipe negligible.

6.2.6 Scan starting time and voltage check

An additional unit is mounted adjacent to the Farnel unit on the back of the balancing box to measure scan starting time and supply voltage (Fig. 6.16).

Because the range setting of the D.V.M. for strain measurement prevents the direct reading of supply voltage, two high-stability resistors are used as a voltage divider to produce 8000 μV. across BC (see Fig. 6.16) when the supply is 5 V across AC.

To measure time, three continuous track, linear potentiometers are connected in parallel across BC, each driven by a synchronous motor. The motor speeds are 1/30 R.P.S., 1/30 R.P.M., 1/24 rev/hour. The voltage of the tapping points, DC, EC and FC as a proportion of the scaled down supply voltage BC gives the rotational position of each timing potentiometer at every scan, allowing the starting time of the scan to be calculated.

The scaled down supply voltage reading is also used to correct all strain gauge readings to a constant voltage, since each strain bridge output is proportional to supply voltage.

6.2.7 Ultra-violet recorder

To obtain a continuous strain record of the model during the application of the internal pressure and the first half hour of constant loading, a 12 channel Ultra Violet Recorder will be used.

Six strain gauges from the outside of the model, five from the inside and another pressure transducer are connected through the balancing unit to the U.V. Recorder (instead of to the D.V.M.). Except for the supply, these strain bridges are electrically independent of the scanned gauges and from each other, each having its own separate base gauge pair mounted on the aluminium plate with its balance gauge. Thus, there is no inter-connection during continuous recording and scanning.

6.3 Test arrangement and processing of results

6.3.1 Test arrangement

The arrangement of the rigs for a model test is shown in Fig. 6.17 and in Fig. 6.18.

Since all the electrical connections within the strain bridges are soldered, it is convenient to mount the clamping rig and the balancing box on the same trolley (see Section 6.2.3). The sealing shaft is permanently linked to the balancing box by cables (for the strain gauges on the inside of the model), and is mounted on the balancing box until the bottom half of the model is placed in the clamping rig. When the bottom half is wired in and checked by the D.V.M., the top half is rested on a platform over the balancing box, and the lead wires from the inside are connected to the pins in the shaft, and the top half inside gauges checked.

In this position the silicone rubber sealing is applied (see Section 6.1.5), and the top half placed onto the bottom half resting in the clamping rig, taking care that the lead wires to the shaft do not get caught between the flanges. The pillars, rubber pads and distribution bar are assembled on the top half, the clamping linkage swung up into position (section 6.1.3), the required amount of packing inserted under the pivot arm, and the whole assembly lightly nipped while the silicone rubber sets.

When the top half outside gauges are wired in and checked, the model is ready to be tested.

It is important before assembling the model to relate the strain gauge positions to the lead wires (by colour), and after wiring in to relate the lead wires to the D.V.M. channel numbers; and hence relate strain gauge locations to channel numbers on the paper tape output.

The tests are carried out in the creep laboratory which is temperature controlled to 20°C ±1°C. The D.V.M. and the D.C. supply to the strain

gauges are switched on at least 24 hours before a test to allow the D.V.M. amplifier and the strain gauges to attain constant temperature. The power is on continuously until a test finishes.

6.3.2 Test procedure

The following procedure was adopted for testing the lead models once they have been assembled and connected up in the clamping rig.

(i) At least 1½ hours before a test, the 24 hour timing potentiometer is adjusted to near the beginning of its track. This ensures that a long time elapses before the 'dead spot' on the track is reached (see Section 6.3.3). All the timing potentiometer synchronous motors are then switched on to guarantee that all the backlash in their gear boxes is taken up before the test begins.

(ii) The strain gauges are checked on the D.V.M.

(iii) The seal-less piston on the pressure rig is checked to ensure that it is hanging vertically, and weights are added to produce the correct pressure.

(iv) The clamping rig is rotated through 90°, so that the model is vertical for filling.

(v) The model is filled by switching on the pump (bypassing the pressure switch). The pipe from the model to the pressure switch is disconnected to act as a bleed for the displaced air. When oil emerges from this pipe, the model is full, and the pump is stopped.

(vi) The pipe is reconnected to the pressure switch and the clamping rig and model are rotated back to the horizontal position.

(vii) The drip tray is inserted under the model and its outlet pipe fed to the reservoir of the pressure rig.

(viii) The strain gauges are checked on the D.V.M., and are adjusted to near zero by the apex potentiometers (Section 6.2.3).

(ix) Two zero readings are taken (i.e. two scans).

(x) The model is clamped (see Section 6.1.3)

(xi) A reading is taken.

(xii) The scanning unit is set to scan continuously. This is the time zero. t = 0.

(xiii) After the first scan, the pump is started on the pressure rig, bypassing the pressure switch. When the pressure in the model reaches the test pressure, the seal-less piston will rise, and the bypass switch can be released. Pressure will now be maintained automatically (Section 6.1.4).

(xiv) At t = 3 minutes, continuous scanning is stopped, and scans taken at intervals of one minute.

(xv) At t = 7 minutes, the scan interval is increased to 3 minutes.

(xvi) At t = 16 minutes, the scan interval is increased to 6 minutes.

(xvii) At t = 34 minutes, the scan interval is increased to 20 minutes.

(xviii) At t = 74 minutes, the scan interval is increased to 1 hour. This continues overnight.

(xix) On the second day (t ≃ 20 hours), the scan timer unit is switched off and all further scans triggered manually; three scans on the second day; two on the third; two on the fourth; one on the fifth and on every other succeeding day.

6.3.3 Processing of readings

The output of the recording equipment is a sequence of numbers separated by spaces on punched tape. As each channel is scanned the channel number is followed by the Digital Voltmeter reading. These readings must be corrected, converted and arranged in a convenient form for inspection and subsequent plotting and analysis.

A computer program was written in FORTRAN and ALGOL to do this on the Nottingham University KDF9 digital computer (See Appendix 4). A dummy tape sample of 5 scans, was produced to develop and check this program.

The program gives the following instructions:-

(a) Read in the data from the tape

(b) Print out the data in a more convenient form

(c) Process the strain readings

(i) correct for D.V.M. amplifier zero drift

(ii) correct for supply voltage variation

(iii) correct for zero shift

(iv) convert to mechanical strain

(v) subtract initial values

(d) Calculate the scan start time from the timing potentiometers

(e) Print out processed results in some array as before

(f) Punch out processed results on cards (for use with plotting program)

(a) Tape input

Although the main program has been written in FORTRAN, the Nottingham University EGDON system requires the paper tape read in instructions to be written in ALGOL, so an ALGOL subroutine has been written to read in the tape.

(b) and (c) Print out

A FORTRAN subroutine has been written to print out the results from one array and the calculated scan start time from another array. It prints out the values of each channel in columns, together with scan number and calculated scan start time in hours.

All readings are related to a reference scan and processed in the following way:-

(i) Correction for D.V.M. amplifier zero drift. The D.V.M. used involved an amplifier whose zero could not be relied upon to remain constant over a long period. One channel was therefore short circuited to give a true zero reading for every scan. For every scan, therefore, this zero reading must be subtracted from all other readings. Any variation in amplifier gain, however, will be reflected in the supply voltage reading, and so will be corrected by the supply voltage correction.

(ii) Correction for supply voltage variation. All readings are proportional to supply voltage and one channel takes a direct, scaled down reading of supply voltage. All readings of a particular scan, therefore, are adjusted in the inverse ratio of scan voltage reading to reference scan voltage reading, to produce the effect of a constant supply voltage throughout the test.

(iii) Correction for zero shift. All model strain gauges are expected to behave exactly like their corresponding reference gauges (See section 3), except for their strain history. So if a reference gauge reading shows (after voltage correction) a change of value from the reference scan value, this change must be reflected in all the corresponding active gauges. So for a particular scan, the change of reference gauge value from the reference scan must be subtracted from all the corresponding active gauge values, to produce the effect of no zero shift of the active gauge readings throughout the test.

(iv) Conversion to mechanical strain. The calibration reading taken at the beginning of a test is described in Section 6.2.3. This provides a conversion factor to mechanical strain for all model gauges, since the gauge factors are known.

(v) Subtraction of initial values. Since the strain bridges are not necessarily initially zeroed, when all gauge readings are corrected and converted, the strain reference scan value of each gauge channel is subtracted from all scans of that channel, so that the initial calculated strain at every point is zero.

(vi) Calculation of scan start time. Section 6.2.6 describes the timing potentiometers circuit and how the voltage reading gives the rotational position. By subtracting the initial position (given by the time reference scan) and relating the change of position with the speed of the synchronous driving motor, the time interval between a particular scan and the reference scan is calculated.

If the n^{th} scan starting time t_n is greater than 5 hours, it is calculated from the 24 hour potentiometer only. The interval between scans is always less than 24 hours, so to allow for several turns of the 24 hour potentiometer, if t_n is less than t_{n-1}, then t_n becomes $t_n + 24$. This process is repeated until t_n is greater than t_{n-1}.

If t_n is between 30 minutes and 5 hours, it is calculated up to the nearest whole number of 30 minutes by the 24 hour potentiometer, and the remaining fraction of 30 minutes is calculated more accurately from the 30 minute potentiometer and added on.

If t_n is between 10 minutes and 30 minutes, it is calculated from the 30 minute potentiometer only.

If t_n is between 30 seconds and 10 minutes, it is calculated up to the nearest whole number of 30 seconds by the 30 minutes potentiometer, and the remaining fraction of 30 seconds is calculated more accurately from the 30 second potentiometer and added on.

If t_n is less than 30 seconds, it is calculated from the 30 second potentiometer only.

It was found that the voltage reading of the potentiometers was not linear over a complete revolution, due to a 'dead spot' as it reached the supply voltage and jumped down to zero again. A correction was included in the computer program to linearise the readings.

A complete scan of 80 channels takes 20 seconds, a significant time at the beginning of a test. So where necessary, additional time should be added to the calculated scan time, calculated at 0.25 sec for every channel separating the relevant channel from the channel monitoring the 30 second potentiometer. The maximum time difference is 17 seconds, so the correction is not significant after 30 minutes of test time.

FIG. 6·1

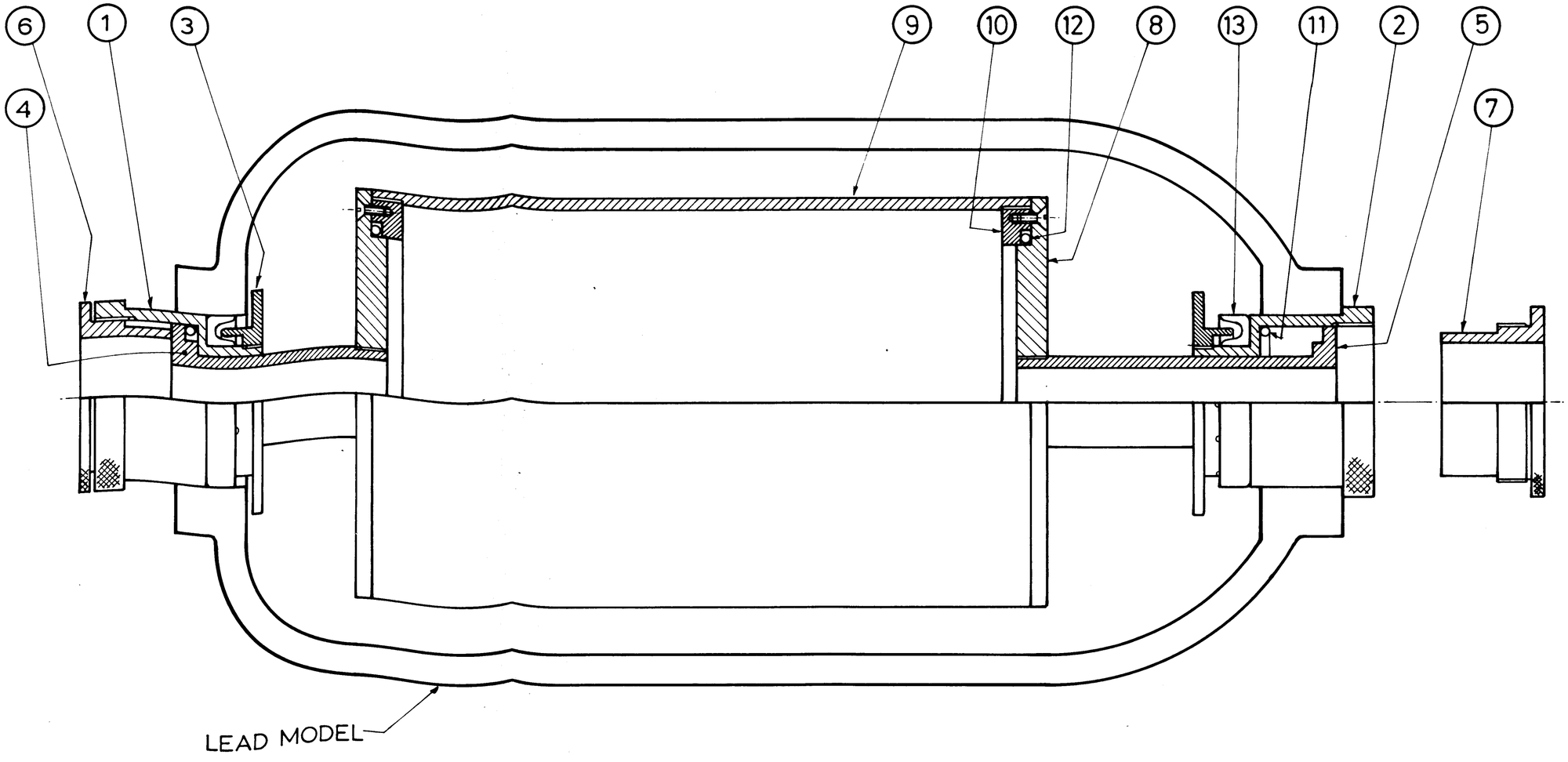

KEY	DESCRIPTION
1	SLEEVE (toroid end)
2	SLEEVE (spherical end)
3	LANTERN RING
4	SHAFT (toroid end)
5	SHAFT (spherical end)
6	CLAMP (toroid end)
7	CLAMP (spherical end)
8	PLATE
9	DRUM
10	INSERT
11	'O' RING
12	'O' RING
13	'U' PACKING

THE SEALING SHAFT

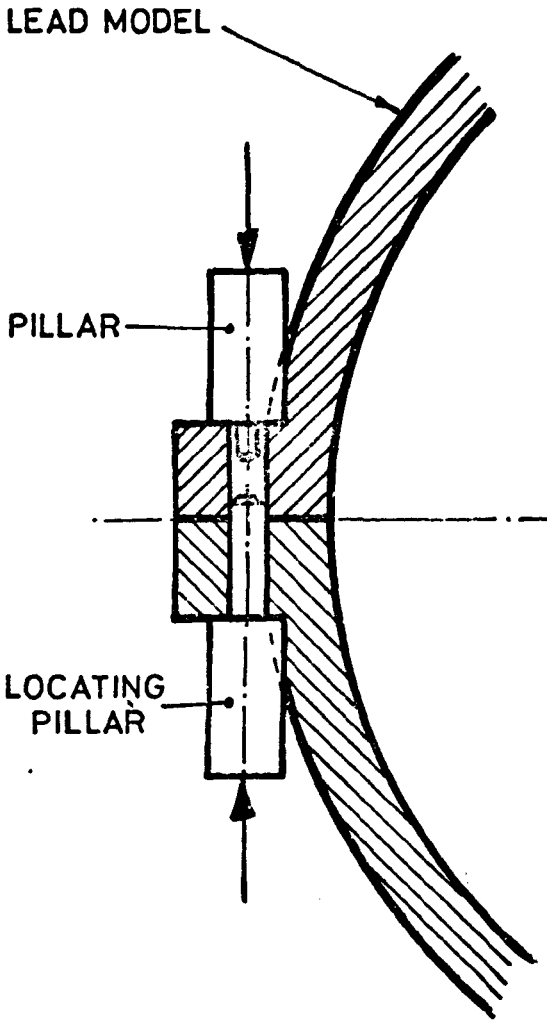
LEAD MODEL
PILLAR
LOCATING PILLAR

FIG.6·2

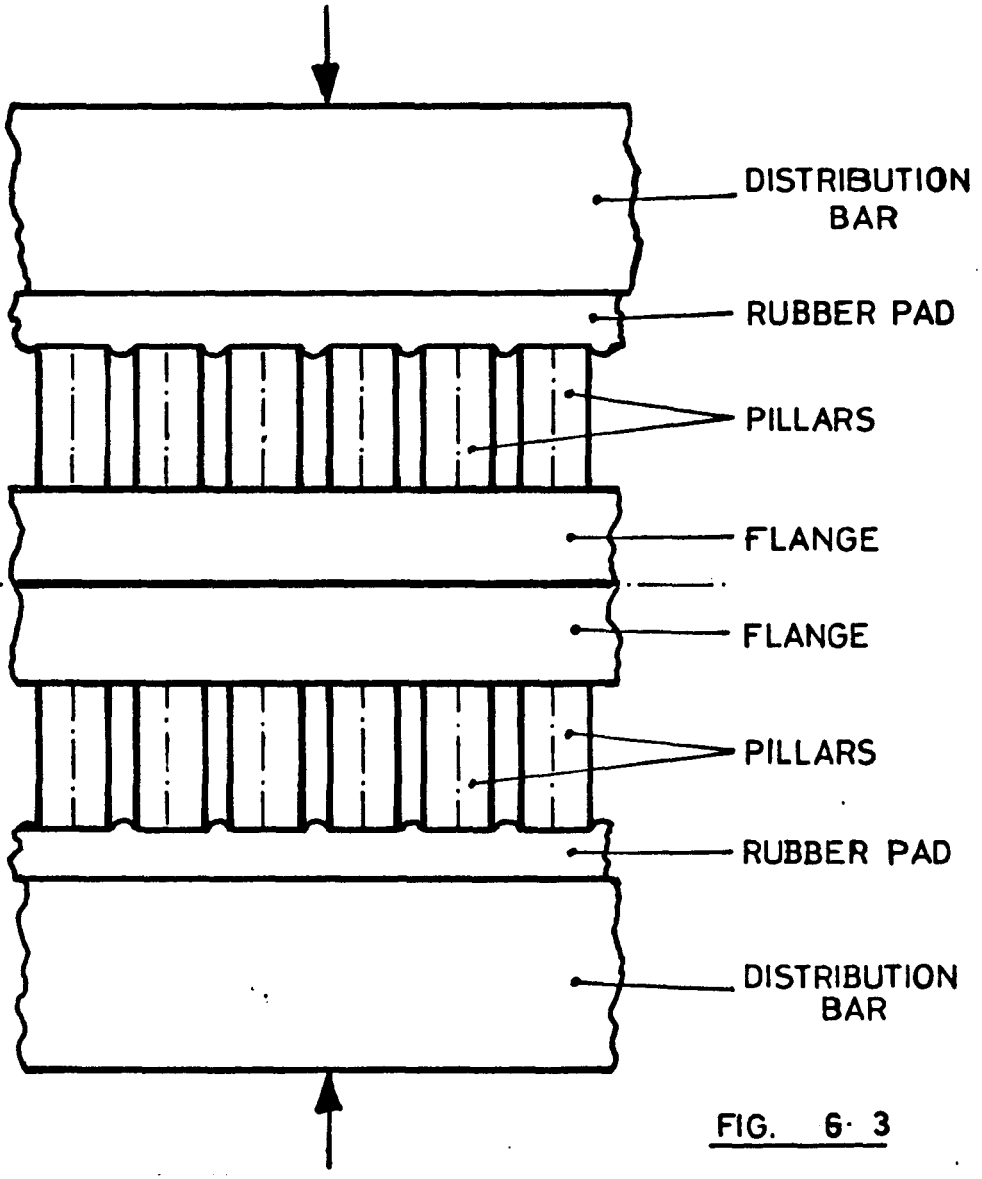
DISTRIBUTION BAR
RUBBER PAD
PILLARS
FLANGE
FLANGE
PILLARS
RUBBER PAD
DISTRIBUTION BAR

FIG. 6·3

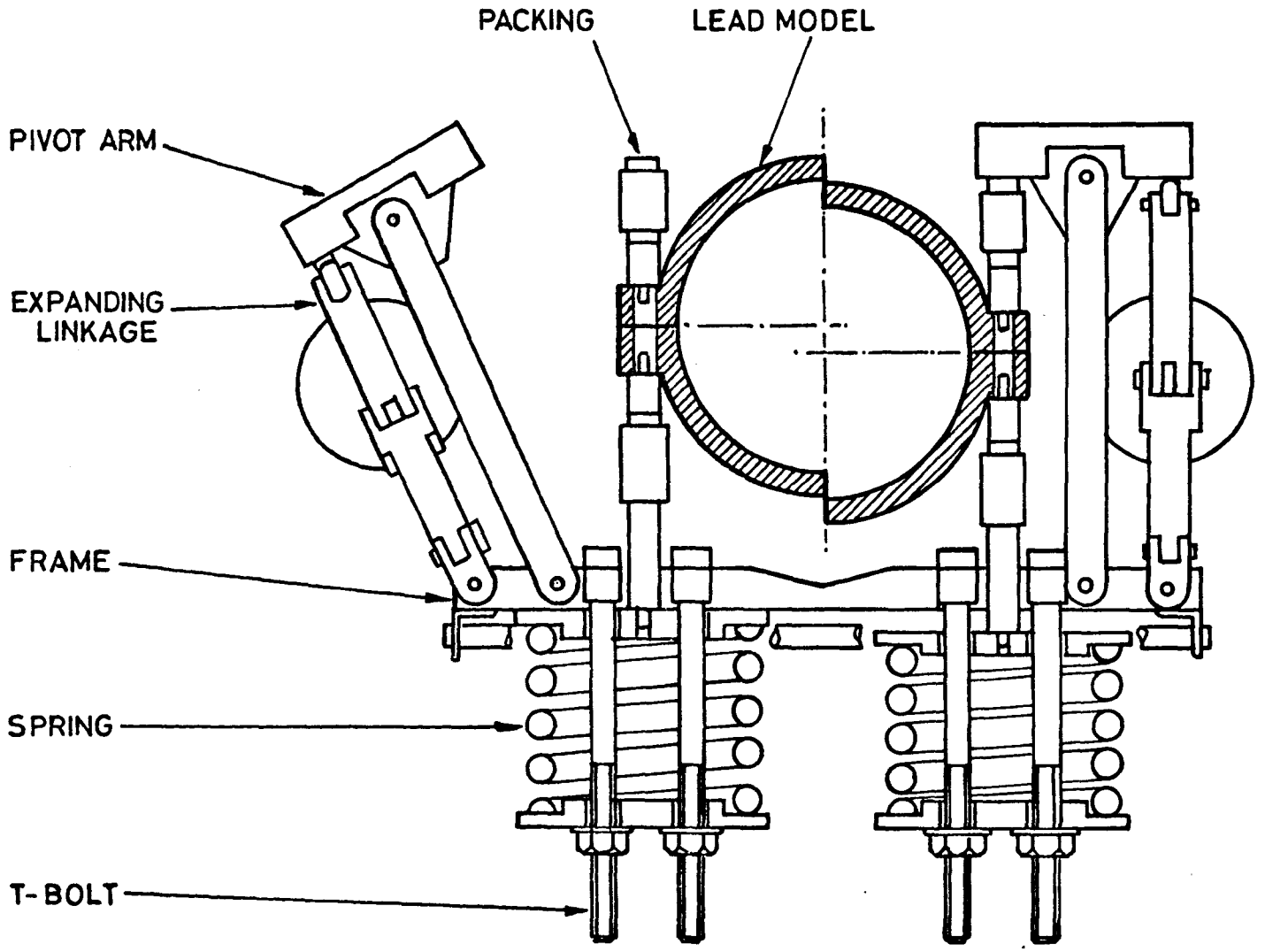

THE CLAMPING RIG

FIG 6·4

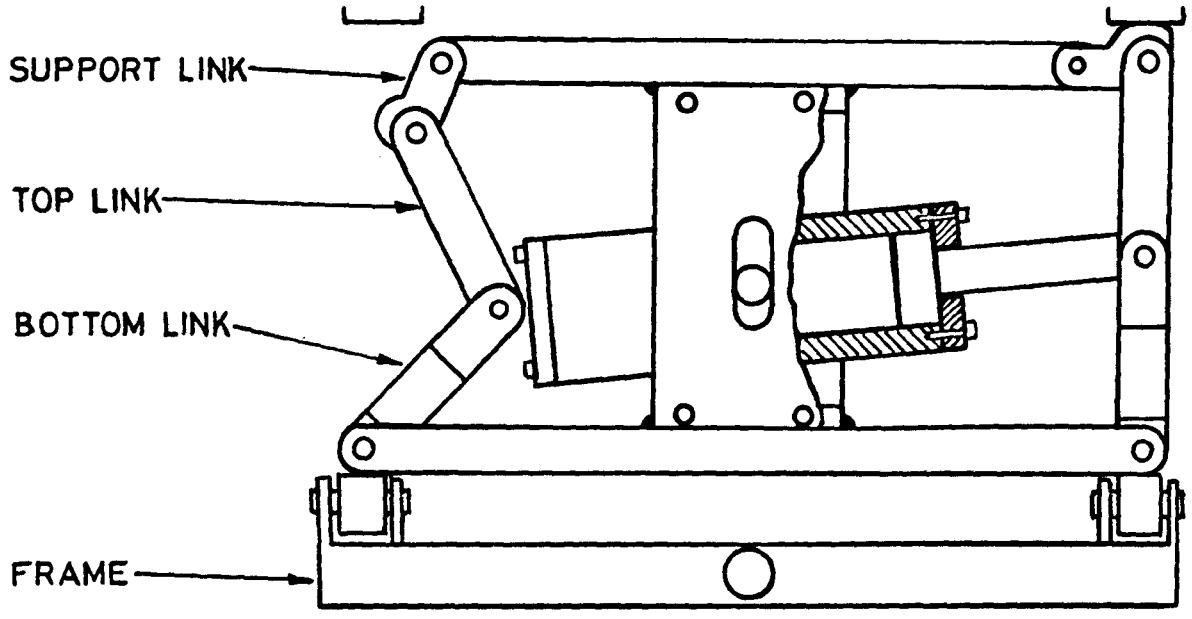

TOGGLE LINKAGE

FIG. 6·5

SEAL-LESS PISTON ASSEMBLY FIG. 6·6

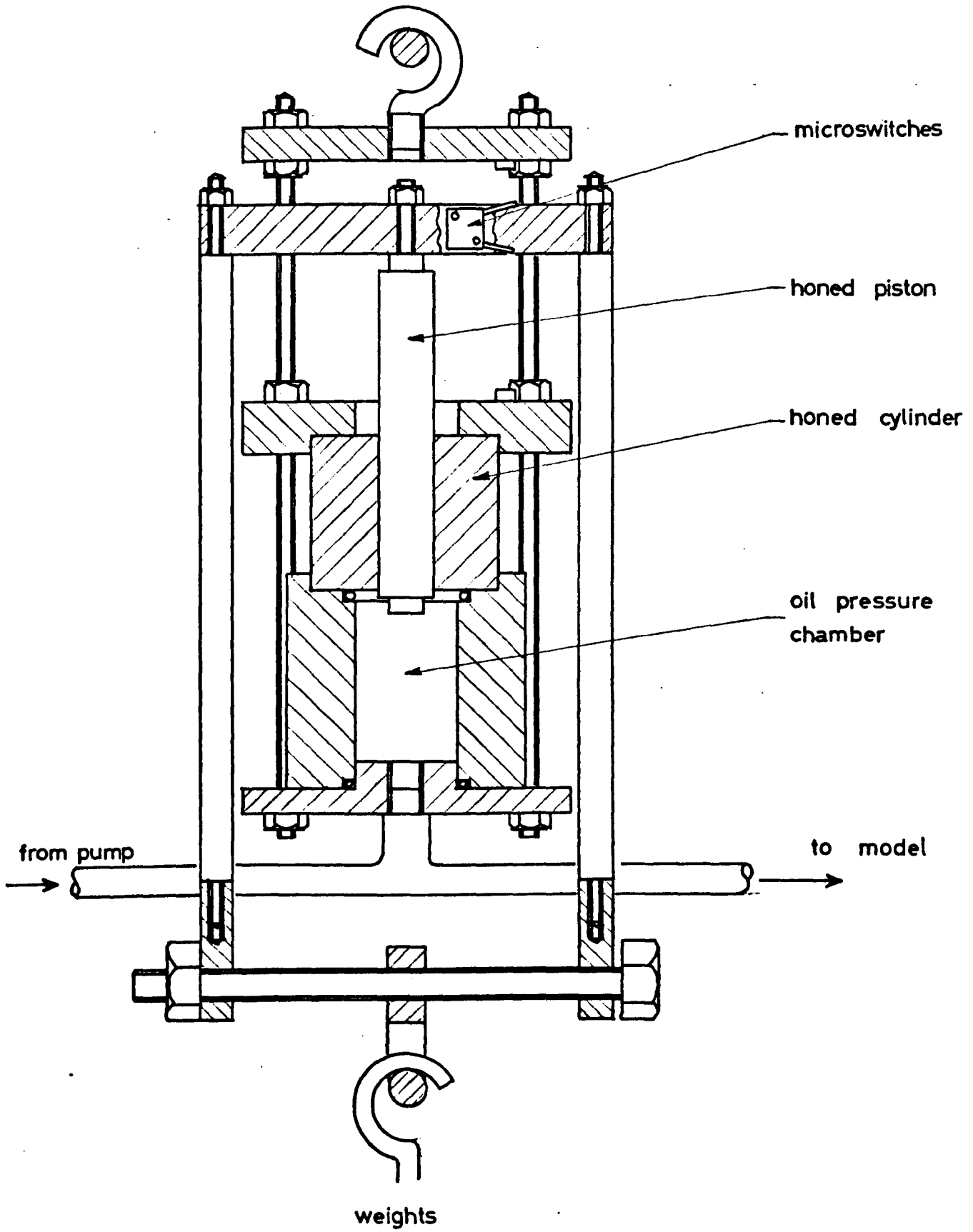

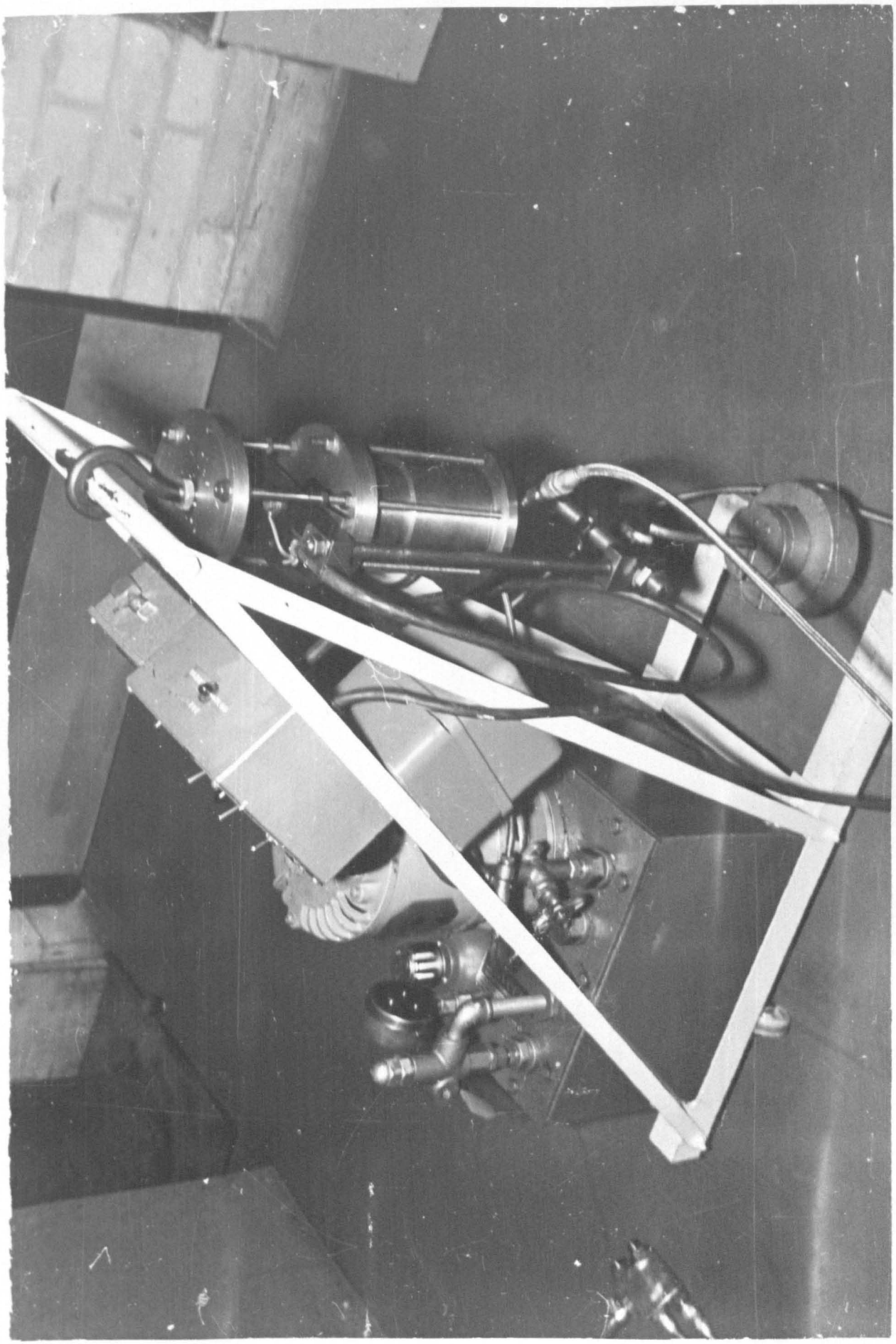

THE PRESSURE RIG

FIG. 6·7

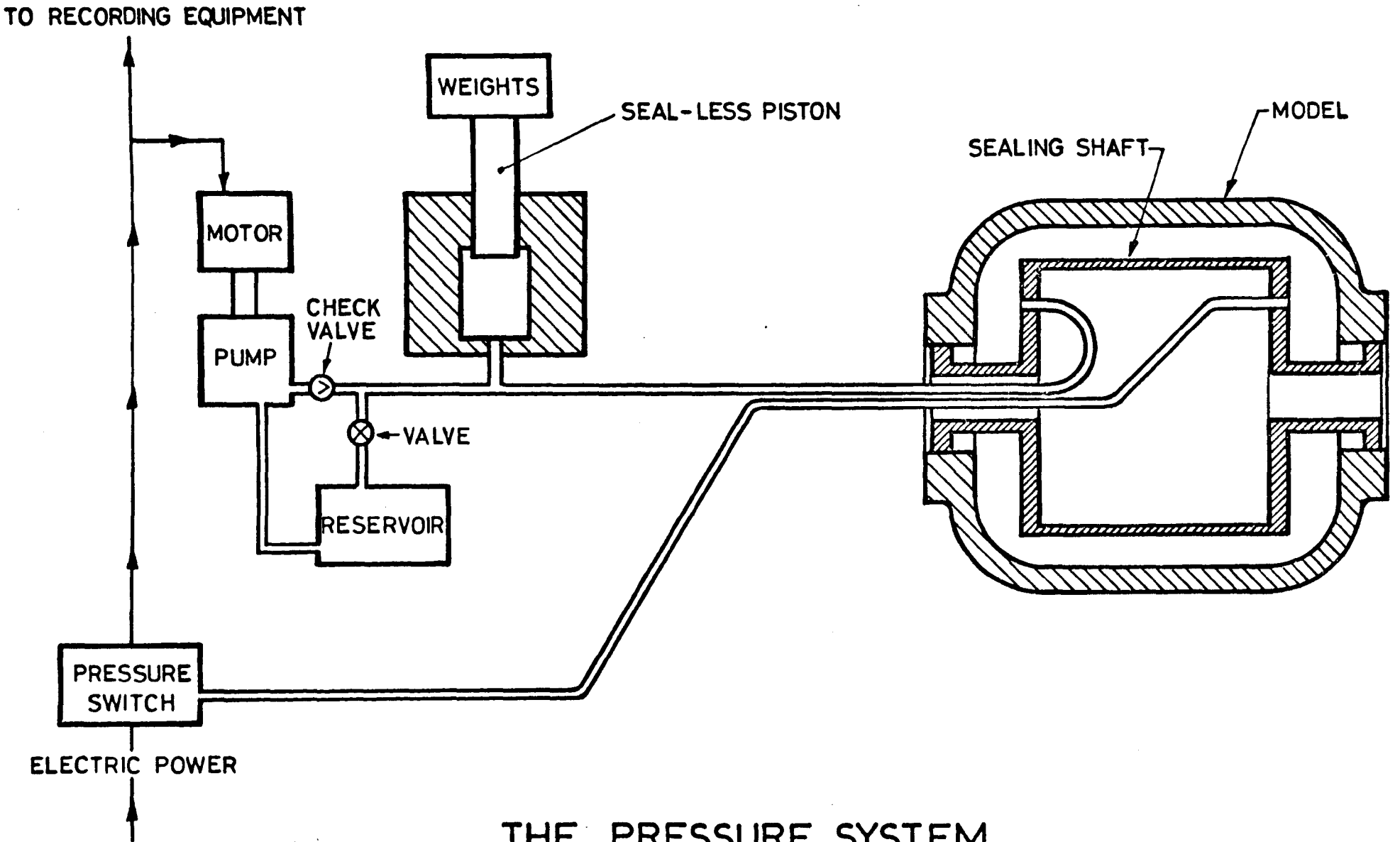

THE PRESSURE SYSTEM

FIG. 6·8

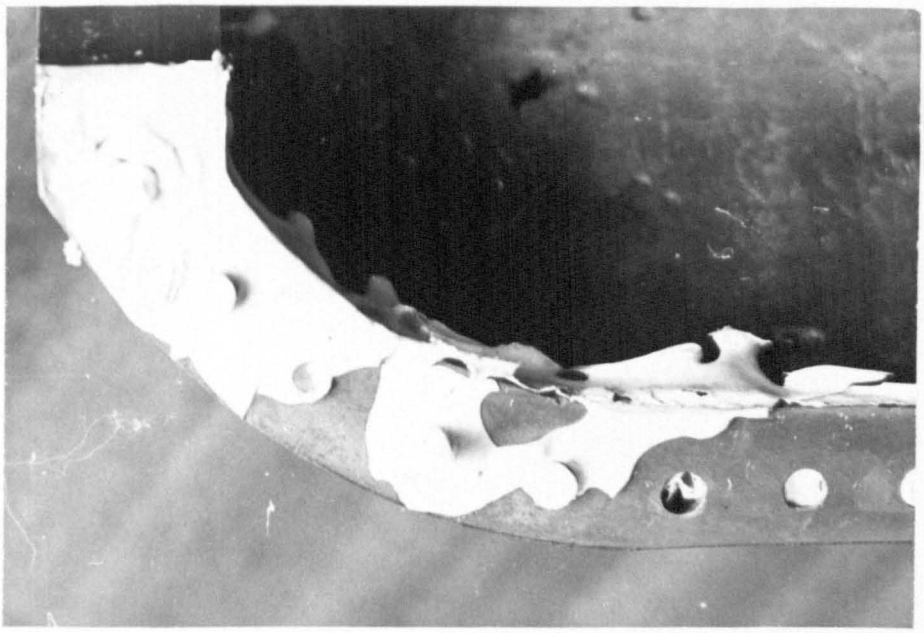

FIG. 6·9

SILICONE RUBBER SEAL

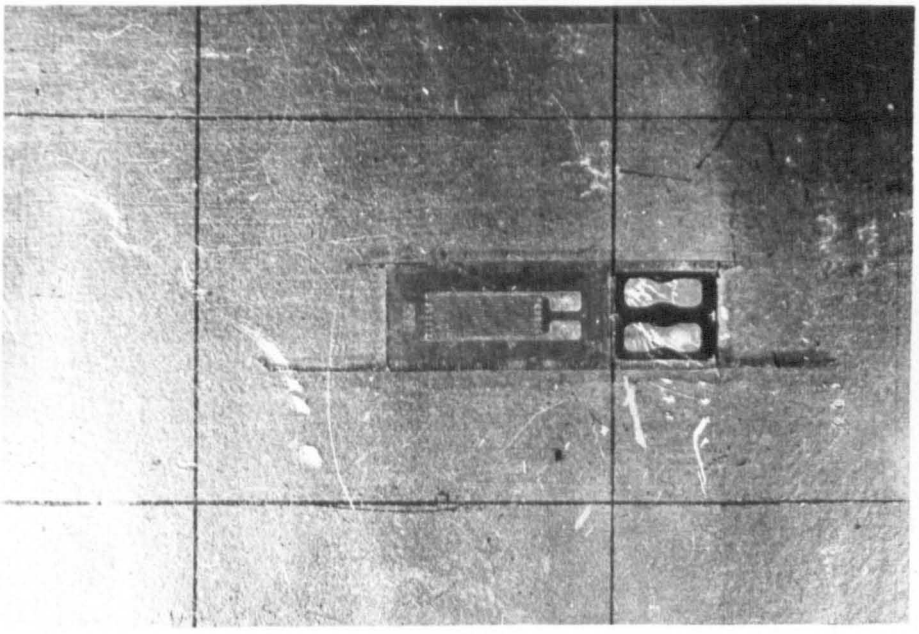

FIG. 6·10

GAUGED LEAD PLATE

with moiré grid

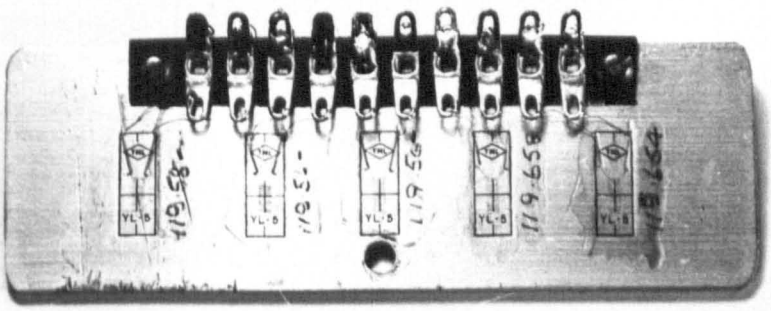

FIG. 6·14

ALUMINIUM PLATE

with mounted strain gauges

FIG. 6·11

COMPARISON OF STRAINS OF ELECTRIC RESISTANCE STRAIN GAUGE AND OF MOIRE GRID - ON LEAD

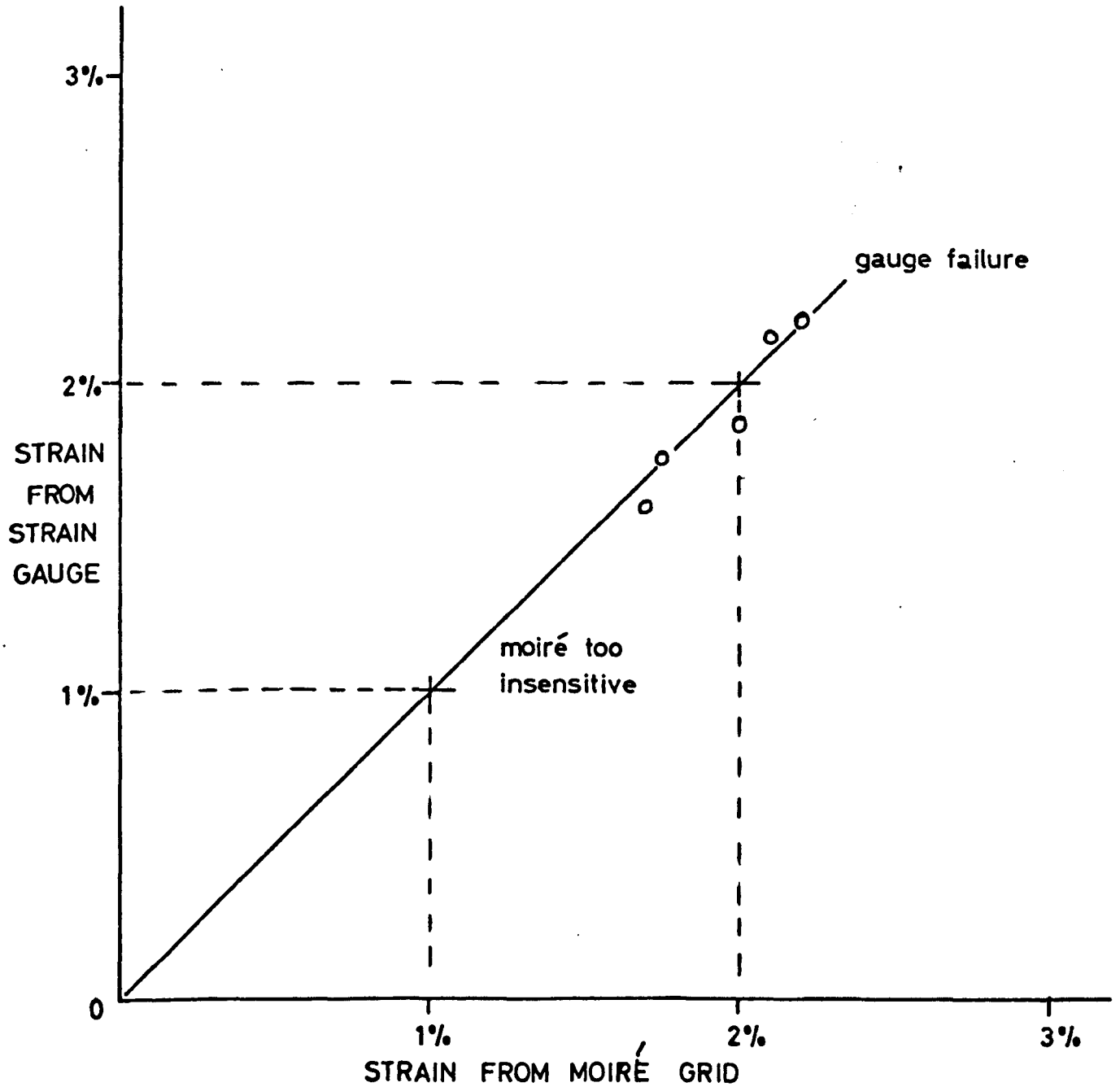

FIG. 6·12

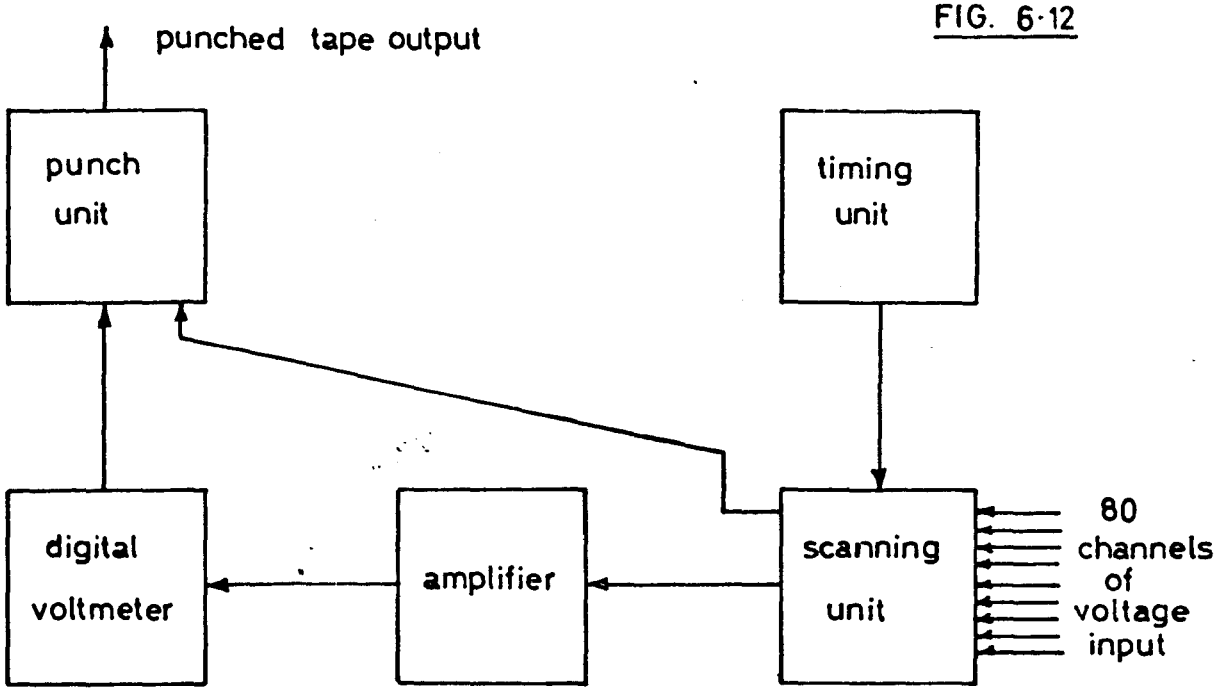

FIG 6·13

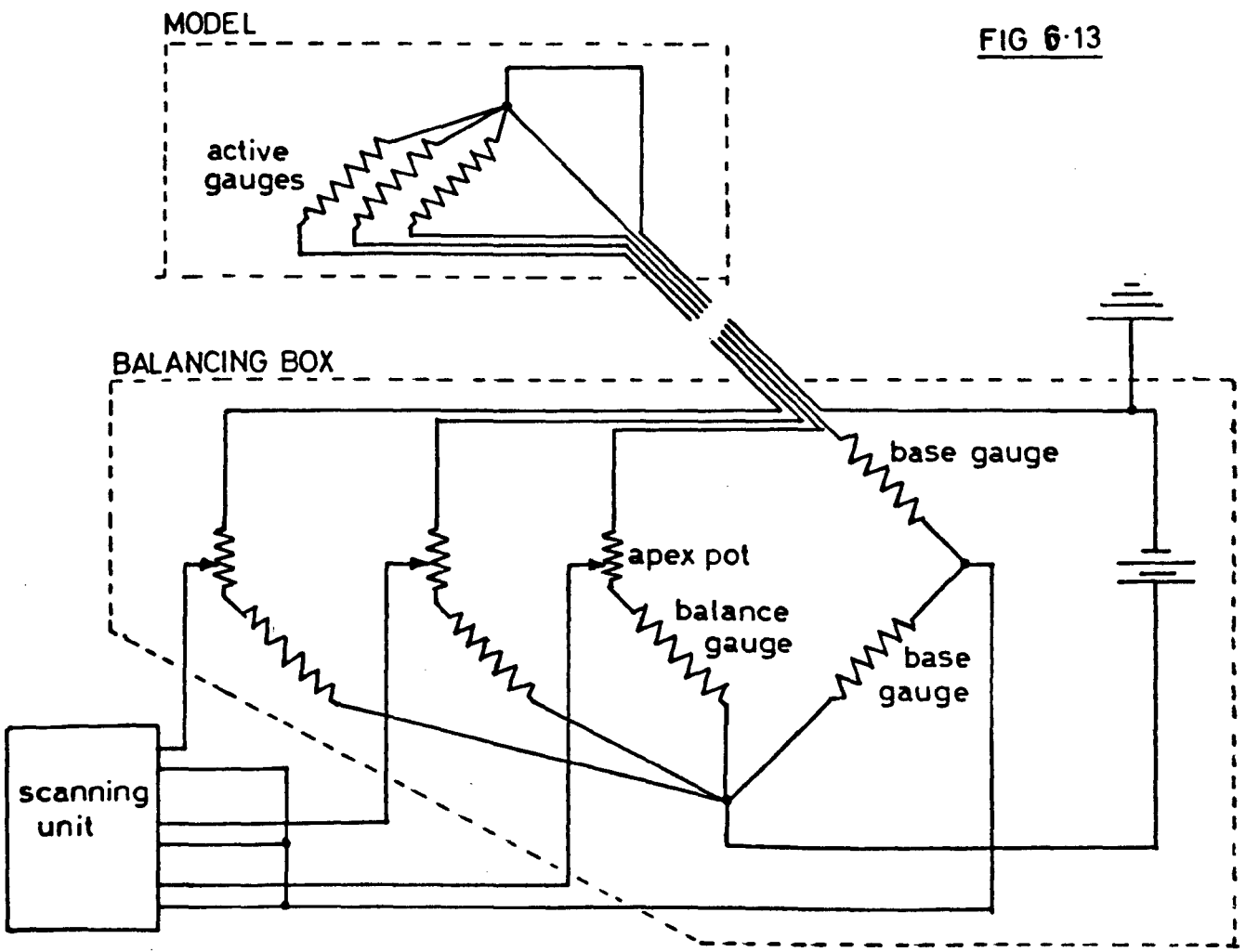

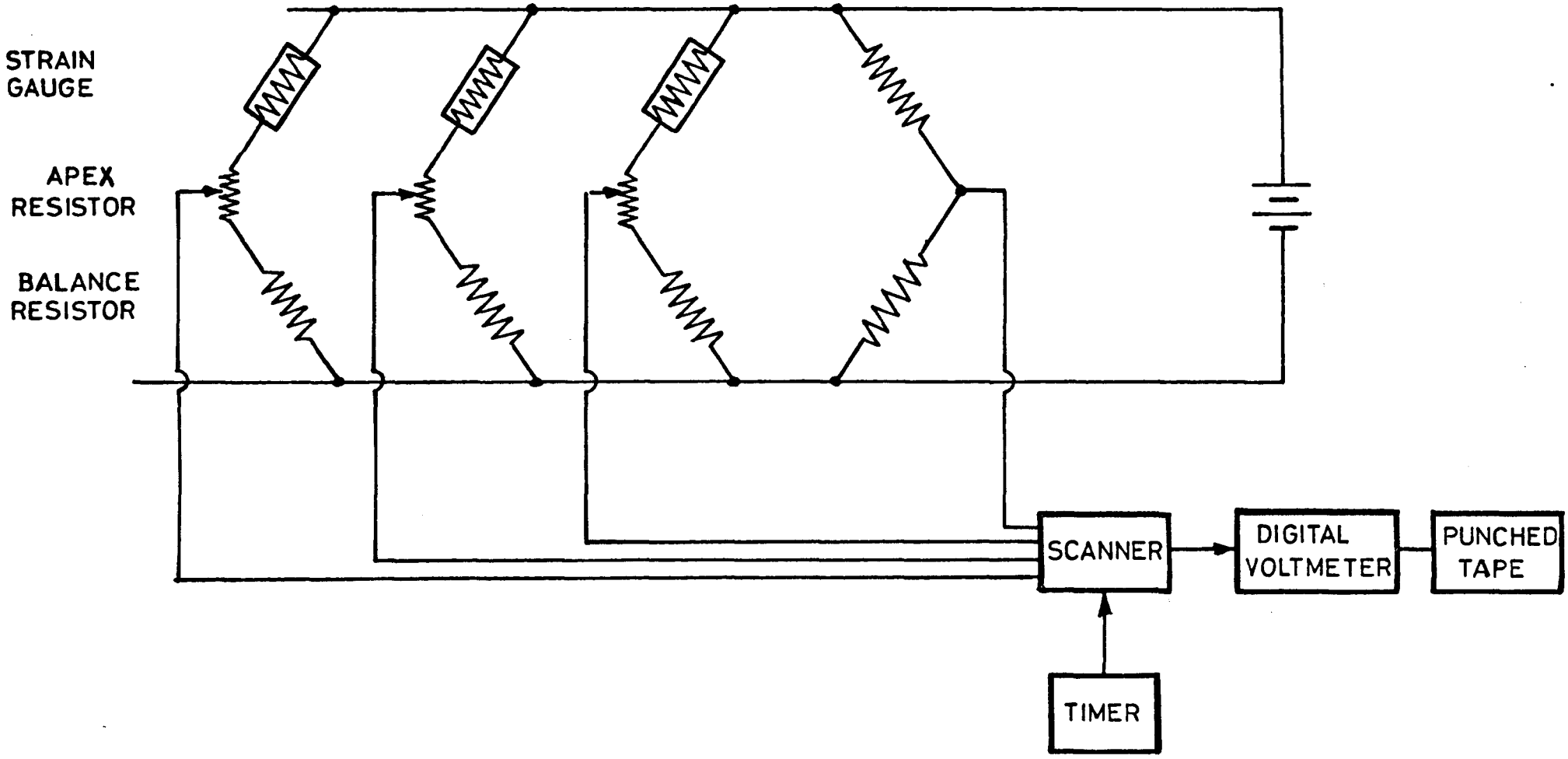

STRAIN MEASUREMENT and RECORDER

FIG. 6·15

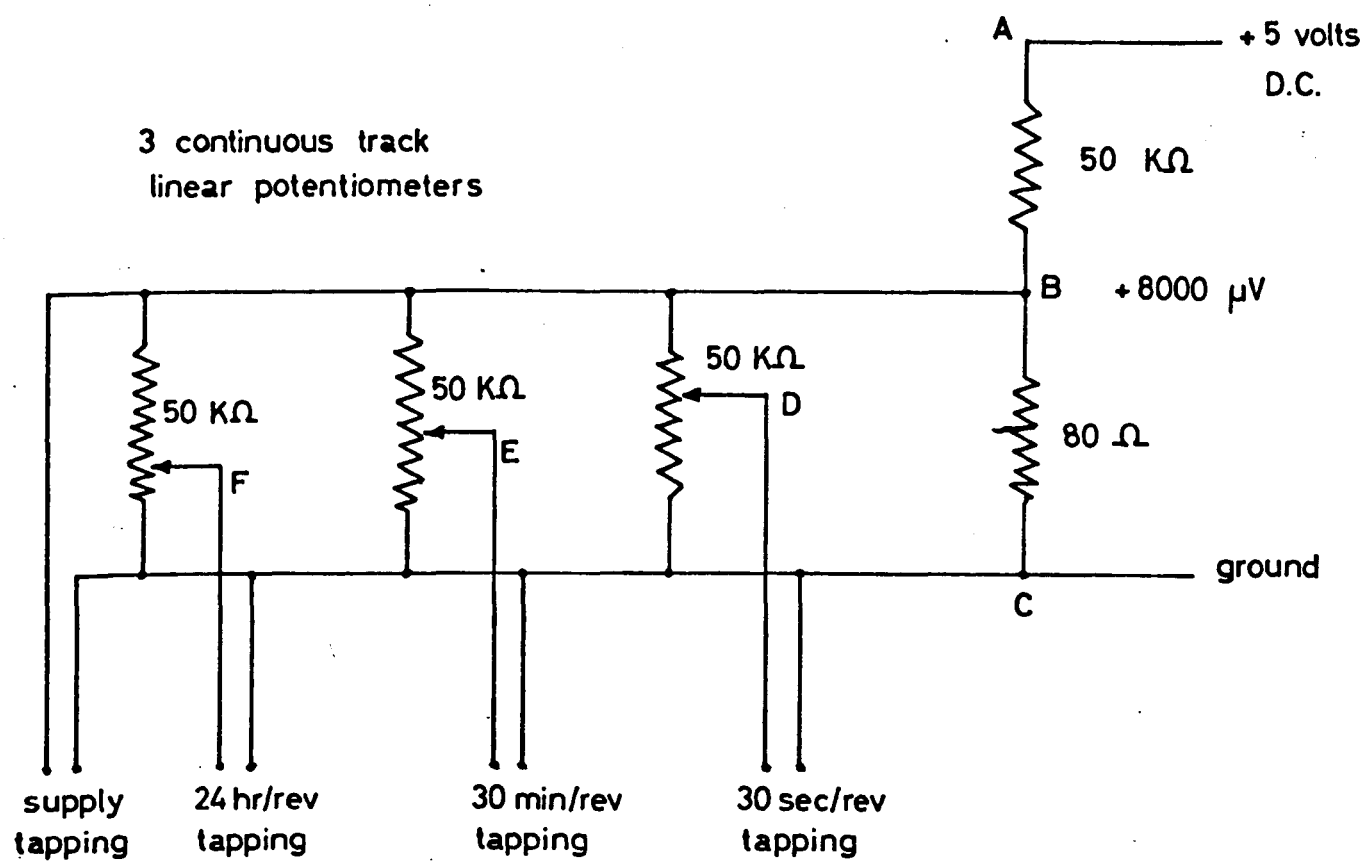
A
+5 volts
D.C.
3 continuous track
linear potentiometers
50 KΩ
B
+8000 μV
50 KΩ
50 KΩ
50 KΩ
D
E
F
80 Ω
ground
C
supply
tapping
24 hr/rev
tapping
30 min/rev
tapping
30 sec/rev
tapping

FIG 6·16

FIG 6·17 General Arrangement for Model Testing

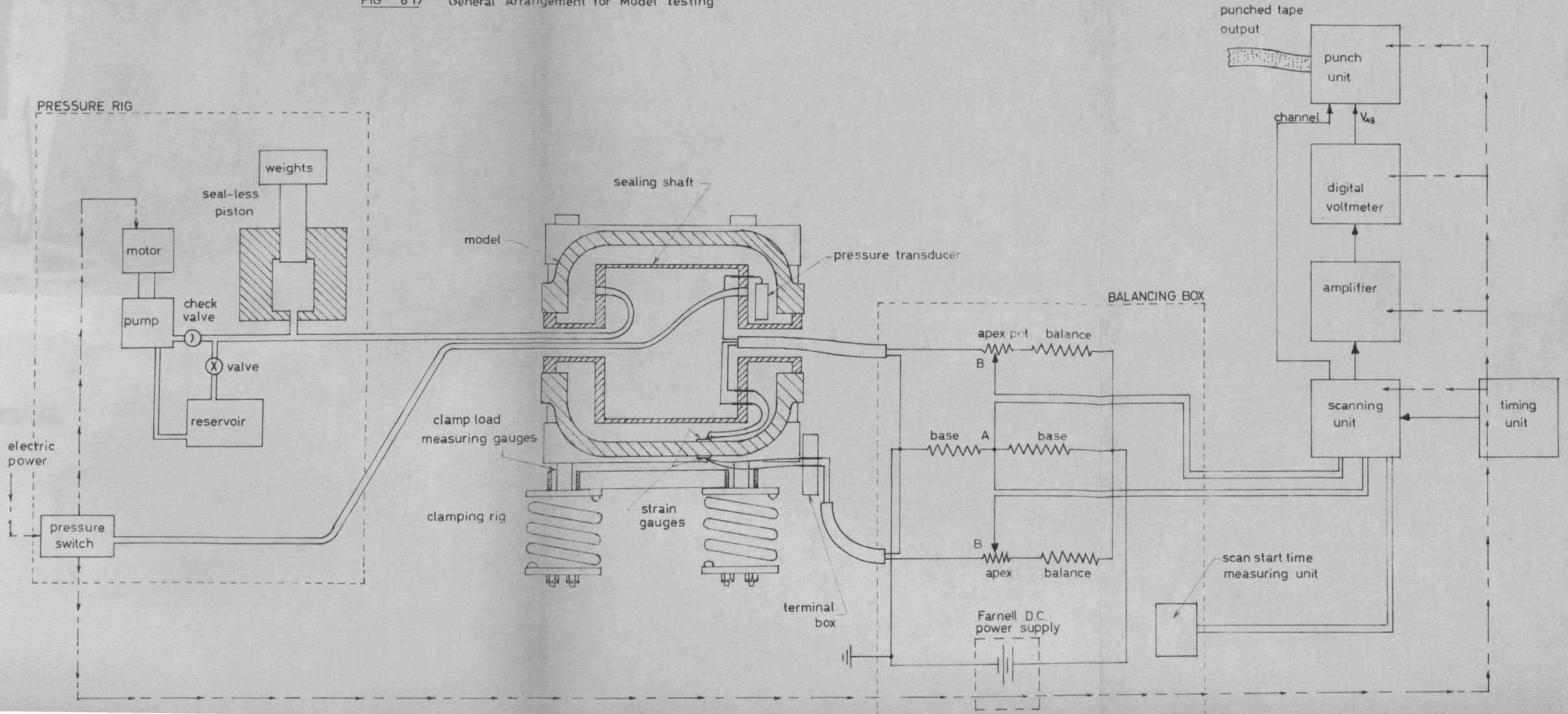

TEST ARRANGEMENT

FIG. 6·18

CHAPTER 7

THE MODEL CREEP TESTS

7.1 Test Parameters

7.1.1 Pressure and bolt loading

The analysis of similarity conditions discussed in Section 2.2, for relating a model creep test to the prototype casing, shows that the pressure of the model creep test can be chosen on the basis of test convenience, provided that sufficiently large creep strains are produced in reasonable time. The bolt loading is then dictated as that which will produce a resultant compressive stress equal to the internal pressure at the inside edge of the flange face in the cylindrical section. This is the minimum condition to ensure that the flange face will remain closed under pressure.

A survey was carried out of steam turbine casings from drawings supplied by three manufacturers, and Table 7.1 was drawn up to show the pressures which would be required to produce the same elastic mean hoop stresses in 1/12 scale lead models. Because of the creep acceleration properties of the lead alloy, it was felt that the elastic strains in the prototypes would represent the upper limit for the model tests, and from Table 7.1 it was decided that 100 lbf/in^2 would be the maximum pressure required.

This maximum pressure applies to the high pressure, thick flanged casings and using the calculation of the bolt loading described in Appendix 5, the maximum clamping force required from the clamping rig was determined as 6 tonf. For the thin flanged casing that was tested (Section 4.1), the poor mechanical advantage, which resulted from the positioning of the bolt holes necessarily further from the inside edge

edge of the flange, meant that even with the maximum clamping load, the limit of allowed pressure was reduced to about 40 lbf/in^2.

The flange was already heavily loaded, and it was felt that 25 lbf/in^2 would be an adequate pressure for this casing if it were made of the lead alloy developed by P.A.T. Gill (Section 2.1.7). However, as discussed in Chapter 5, a new, stronger alloy had to be developed in order to produce acceptable castings, and in 100 hours of uniaxial creep at 1000 lbf/in^2 the creep strain of the 1.2% Sb alloy is 1/300 times that of the 0.2% Sb alloy. To completely compensate for this, the stress level, and hence pressure, would have to be raised by a factor of 2.8, bringing the pressure up to 70 lbf/in^2.

For the development of the technique, and in view of the proposed future increase in flange thickness which would allow pressures of up to 100 lbf/in^2, the policy adopted was to test the model with the current flange design at the maximum pressure allowed by the capacity of the clamping rig.

This pressure, allowing a small margin of safety, was 35 lbf/in^2, for which each bolt load was 233 lbf, giving a total clamping load of 10,230 lbf (4.6 tonf). Test 9 was conducted at these conditions.

Further tests at higher and lower pressures were carried out to provide a range of experimental results for comparison. The bolt loading, however, was not changed, so the higher pressures would be expected to separate the flange faces at the inside edge.

7.1.2 Measurement positions

The greatest interest was in the behaviour of the toroid end closure of the casing, including the boss, and in the junction of the casing with the flange. For comparison between top and bottom casings, the adopted practice was to cover the positions of interest on one casing (the bottom

casing for convenience of assembly in the clamping rig), and to allow sufficient channels to duplicate the most important positions on the other casing. The positions of the strain gauges are given in terms of the coordinate system described in Section 4.1 and Figs. 4.3, 4.12, 4.13 and 4.14.

The elastic analysis of Chapter 4 shows peak meridional stresses in the toroid section at position '1' in the $\Theta = 0^{\circ}$ (Fig. 4.15), the $\Theta = 30^{\circ}$ (Fig. 4.16) and the $\Theta = 60^{\circ}$ (Fig. 4.17) meridional planes. Strain gauges on the models were therefore located at these positions in the meridional direction on the inside and outside surfaces. In order to show the effects of creep stress redistribution, strain gauges were also located in the meridional direction in these planes at positions 'j' and 'n' to show the strain distribution across the peak. Meridional strain gauges were also located at position 'e', in and behind the boss fillet radius, to study the peaks shown by the elastic analysis.

Hoop strains in the flange fillet radius can only be measured between the bolt holes, since the counterbores cut into the casing. Strain gauges were positioned in the fillet between the holes round the toroid section and in the middle of the cylindrical section.

In some tests a pair of strain gauges, inside and outside, were positioned along the $\Theta = 0^{\circ}$ meridional plane in the hoop direction to provide a reference in the cylindrical section of the casing.

A strain gauged model is shown in Fig. 7.1.

Difficulties in obtaining the elastic analysis (Section 4.2) meant that the correct distribution of strain gauges was only available from test 6 onwards. The positioning of gauges for the earlier tests, therefore, had to be guessed. A consequence of this was that these earlier tests concentrated more on the hoop and meridional strains in the cylinder, and the peak meridional strains in the toroid were missed.

7.1.3 Measurement intervals and test times in relation to creep rates

Since the creep strain rates reduce as the test progresses, it is necessary to take strain readings frequently at the beginning of a test, and convenient to increase the interval between measurements as the test progresses. At the start of a test the recording equipment was set to scan continuously, which with 80 channels means an interval of 20 sec between readings. The intervals were increased until after 100 hours of testing, one reading was taken each day; and after ten days, one reading was taken every two days.

For the low pressure tests the frequency of readings was reduced and the test time had to be extended to 3 or 4 weeks to obtain sufficient creep strains. For high pressure tests the frequency of readings was increased and the test time could be reduced, although these tests were usually extended to two weeks. In general, about 50 readings were taken in each test.

After switching on the pump of the pressure rig, it takes about 20 seconds for the pressure to build up to its test value. Most of the tests showed little creep in the early stages, but it is possible that there is some very rapid redistribution as the pressure comes on, which is not detectable even with continuous scanning. To check this, a group of 20 gauges located in peak strain positions were scanned continuously alone with the pressure transducer at the beginning of Test 9. This reduction for a short while of the number of channels reduced the scanning time to 5 seconds, and enabled the onset of the pressure load to be more clearly distinguished. No rapid redistribution, however, was detected.

7.1.4 Summary of Tests

Table 7.2 lists the model tests and the test parameters.

Tests 1, 2 and 3 were carried out on the same pair of casings cast from 6% Sb 0.6% As lead alloy. This material, while having similar elastic properties to those of the creep alloy, is very strong in creep (see Section 3.1.2) and makes the casings very suitable to test the elastic behaviour of the models and the test equipment.

Test 1 was simply a trial of the rigs and the instrumentation. In this test it was shown that the plain flange joint was inadequate to prevent leakage under pressure at the junction with the 'U' packing seal in the bores (see Chapter 6) and Red Hermatite was adopted as a seal.

Test 2 was an elastic test. The pressure was increased in stages until leakage was caused by the two halves of the model separating. Readings were taken at each stage to study the linearity of the response and to give some indication of the opening of the inside edge of the flanges. The separation pressure was 90 lbf/in^2.

Test 3 was in two parts. The first part was a drift test on the unloaded model. Readings taken at intervals over a period of two days and nights showed drift strain readings of not more than 7 microstrain. The temperature of the room in which the tests took place was controlled at $20^{\circ}C \pm 1^{\circ}C$. The second part was a creep test for 200 hours at 75 lbf/in^2. No significant creep strains were measured in the casing, although the fillet radii in the boss and flange showed some creep.

Tests 4 to 9 were the model creep tests, for which the casings were made of the 1.2% Sb 0.12% As lead alloy described in Chapter 3. Test 9 was the reference test, the pressure being the maximum to produce creep without separation of the inside edge of the flange joint. The other tests were designed to provide a range of results at higher and lower pressures for comparison.

In test 4, to provide an upper limit, the pressure was set at the highest value thought feasible on the basis of test 2. However, the leakage proved too great to continue the test beyond $1\frac{1}{2}$ hours, although the high pressure produced large creep strains even in this time. This model was then used to develop the sealing with silicone rubber (Section 6.1.5).

7.2 Test 2 (elastic casings)

7.2.1 Results

Two positions on the elastic casings of Test 2, both with strain gauges on the inside and outside surfaces in the hoop direction, were chosen to illustrate the elastic response to pressure of the model. Both positions were in the $\theta = 0^{o}$ meridional plane in the cylindrical section; position A at $Z = 2.50$ in, and position B at $Z = 3.35$ in. The hoop strain response to pressure at position A is shown in Fig. 7.2, and that at position B is shown in Fig. 7.3. Fig. 7.4 and Fig. 7.5 show the same response at positions A and B respectively in terms of the ratio of hoop strain to model pressure, and these ratios are divided into mean and bending components. Also given in these graphs are the values of the hoop strain/pressure ratios predicted by the elastic analysis of Chapter 4 and the finite element elastic analysis of Parkes (42), again divided into mean and bending components.

7.2.2 Discussion

Fig. 7.2 and 7.3 show how the hoop strains on the inside and outside surfaces at first increased together with pressure as expected. At about 40 lbf/in^2 the cylinder wall began to bend, separating the inside and outside hoop stresses. At this point the inside edge of the flange joint has begun to open, rotating the casing wall as shown in Fig. 7.6 and causing bending at positions A and B in the sense shown in Figs. 7.2 and 7.3. The proportion of bending strain increases with further pressure increase (Fig. 7.4 and Fig. 7.5) until the pressure reaches about 55 lbf/in^2, after which the proportion of bending component remains constant. At all pressures the ratio of mean hoop strain to pressure remains constant. This indicates that the sealing surface in the flange moves out from the inside edge at about 40 lbf/in^2 to a stable position at about 55 lbf/in^2. The outer position of the sealing surface is probably the outer edge of the flange.

The finite element elastic analysis of Parkes (42) predicts little bending and a mean value of hoop strain ratio with pressure slightly higher than that of the lead casings. The photoelastic analysis predicts a mean value much closer to that of the lead casings, although the large bending of the photoelastic model is considered unrealistic (see Section 4.2.4). The higher mean value predicted by the finite element analysis may be due to the low pressure and hence the small deformations involved in the calculation.

7.3 Model Creep Results (Test 4 to Test 9)

For discussion the results are grouped as meridional strains in the casing, hoop strains in the casing and hoop strains in the flange fillet radius. Within each group the results are presented in test order, keeping the results from each casing together.

In the distribution graphs the horizontal axis gives the strain gauge location according to the coordinate system described in Section 4.1. The strain distribution is given at various test times near 0.1, 1, 10 and 100 hours and at the end of the test.

7.3.1 Meridional strains in the casing

From Test 4, casing 2, the measured strain distribution in the $\theta = 0^{\circ}$ meridional plane is given in Fig. 7.7.

From Test 5, casing 4, the distribution in the $\theta = 0^{\circ}$ meridional plane is given in Fig. 7.8.

From Test 6, the distribution in the $\theta = 0^{\circ}$, $\theta = 30^{\circ}$ and $\theta = 60^{\circ}$ meridional planes of casing 13 are given in Figs. 7.9, 7.10 and 7.11 respectively. The distribution in the $\theta = 0^{\circ}$ and $\theta = 30^{\circ}$ meridional planes of casing 14 are given in Figs. 7.12 and 7.13 respectively. This was the first test for which the positions of peak stresses were known, so the gauges are concentrated in the toroid section.

From Test 7, the distribution in the $\theta = 0^{\circ}$, $\theta = 30^{\circ}$ and $\theta = 60^{\circ}$ meridional planes of casing 9 are given in Figs. 7.14, 7.15 and 7.16 respectively. The distribution in the $\theta = 0^{\circ}$, $\theta = 30^{\circ}$ and $\theta = 60^{\circ}$ meridional planes of casing 10 are given in Figs. 7.17, 7.18 and 7.19 respectively.

From Test 8, the distribution in the $\theta = 0^{\circ}$, $\theta = 30^{\circ}$ and $\theta = 60^{\circ}$ meridional planes of casing 19 are given in Figs. 7.20, 7.21 and 7.22 respectively. The distribution in the $\theta = 0^{\circ}$, $\theta = 30^{\circ}$ and $\theta = 60^{\circ}$ meridional planes of casing 17 are given in Figs. 7.23, 7.24 and 7.25 respectively.

From Test 9, the distribution in the $\theta = 0^{\circ}$, $\theta = 30^{\circ}$ and $\theta = 60^{\circ}$ meridional planes of casing 15 are given in Figs. 7.26, 7.27 and 7.28 respectively. The distribution in the $\theta = 0^{\circ}$ and $\theta = 30^{\circ}$ planes of casing 12 are given in Figs. 7.29 and 7.30 respectively.

7.3.2 Hoop strains in the casing

From Test 4, casing 2, the distribution in the $\theta = 0^{\circ}$ meridional plane is given in Fig. 7.31.

From Test 5, casing 4, the distribution in the $\theta = 0^{\circ}$ meridional plane is given in Fig. 7.32.

From Test 7, casing 9, the distribution in the $\theta = 0^{\circ}$ meridional plane is given in Fig. 7.33.

From Test 8, the distribution in the boss fillet radius hoop plane of casing 19 and casing 17 are given in Figs. 7.34 and 7.35 respectively. A plot of hoop strain against Log(time) for the inside and outside surfaces of casing 19 in the $\theta = 0^{\circ}$ meridional plane in the cylinder, 2.25 in from the cylinder joint, is given in Fig. 7.36.

From Test 9, a plot of hoop strain against Log(time) for the inside and outside surfaces of casing 15 in the $\theta = 0^{\circ}$ meridional plane in the cylinder, 1.875 in from the cylinder joint, is given in Fig. 7.37.

7.3.3 Hoop strains in the flange fillet radius

The distribution of hoop strains round the flange fillet radius is not continuous, since the bolt hole counterbores cut into the casing. For all tests other than test 9, the gauge positions were in small isolated groups, so those results were plotted individually against time. The results from tests 4, 5, 7 and 8 are given in Figs. 7.38, 7.39, 7.40 and 7.41 respectively. No results were obtained from test 6, since all the gauges in the flange fillet radius were lost on clamping up, when the rubber pads extended and either cut or short circuited the wires.

In Test 9, a more extensive coverage was made, and these results were plotted as distributions round the flange. Although the results are presented as a meridional distribution, the section is not meridional, but parallel to the $\theta = 90^{\circ}$ meridional section and displaced by the thickness of the flange. Again, the discontinuity of the fillet means that the distribution is schematic.

The distributions on the right hand side of casing 12 and the left hand side of casing 15, on the same side of the assembled model, are given in Figs. 7.42 and 7.43 respectively. The distribution on the right hand side of casing 15 is given in Fig. 7.44.

7.4 Meridional strains in the Casing

7.4.1 Clamping strains

Results from the photoelastic tests (Chapter 4) and the finite element elastic analysis carried out by Parkes showed that the bolt loading alone should produce negligible meridional strains in the $\theta = 0^{\circ}$ meridional plane remote from the boss. Meridional strains in the $\theta = 30^{\circ}$ meridional plane should also be negligible, although more is expected in the $\theta = 60^{\circ}$ meridional plane.

However, it can be seen from Figs. 7.7 to 7.30 that significant meridional strains appear in the $\theta = 0^{\circ}$ and $\theta = 30^{\circ}$ meridional planes when the simulated bolt loading is applied by clamping up the models in the clamping rig.

The magnitude of this clamping strain appears to be quite random from test to test, although top and bottom casings in each test usually show clamping strains of the same order. The meridional strain distribution in the toroid section, however, is similar in every casing, showing tensile strains on the inside surface and compressive strains on the outside surface.

This difference between inside and outside surfaces indicates bending in the sense of trying to open out the meridional curve, as if there were an axial tension acting on the boss ends. In tests 7, 8 and 9 this bending reduces or reverses near the boss, implying rigidity; but in test 6 the bending increases, implying that the boss is bending also.

Although the curvature and the geometry of the domed ends would produce higher bending stresses on the inside surface than on the outside from a pure bending moment, these appear to be a combination of direct tension and bending in the $\theta = 0^{\circ}$ meridional plane in all casings. The component of direct tension reduces round to the $\theta = 30^{\circ}$ plane and further to the $\theta = 60^{\circ}$ plane, supporting the hypothesis of meridional bending of the entire casing.

The following explanations for the clamping strains were considered;

(i) Interference of the distribution bar (Fig. 6.3)

The pillars representing the bolt washers are positioned close against the casing, and were made only $\frac{1}{2}$ inch long to reduce the chances of tilting over under the large compressive load, should the flange creep non-uniformly. The rubber pads do not add much to the height, since they are compressed to very thin sheets. The distribution bar must act over the centre of the pillars, and be wide enough to support the rubber pads.

Because of the thin flange, this means that the outside surface of the casing does not clear the inside edge of the distribution bar by a large margin, and it was found in the early tests that great care had to be taken when aligning the distribution bars to avoid digging into the casing when clamping up. This problem is aggravated at the toroid end near the boss by the prolonged near-vertical casing wall, and often strain gauge wires were severed in that area.

Since the toroid section was the important, instrumented end, the distribution bar was moved clear, while trying to avoid fouling at the hemispherical end. This was not successful. Despite careful alignment before each test, evidence was found afterwards that the distribution bars fouled on the casings at one side or the other, near the boss of the hemispherical end, over a length of about one inch.

However, it seems unlikely that the fouling of the distribution bars can account for the clamping strains. The effect could extend to the toroid end in only two ways; from local deformations being transmitted through the casing and from an end load acting on the casing as a whole.

The effect of local deformations would die out very quickly along the casing, particularly since the fouling took place near the junction of the flange and the boss where the casing is fairly rigid. When clamped up,

the friction between the flange, the pillars and the distribution bar is so great that the effect of the end load would also be lost well before the toroid end. Furthermore, if the effect were felt at the toroid end, the result would be an axial compression of the casing, producing bending strains of the opposite sense to those measured.

(ii) Interference of the rubber pads

The large compressive loads transmitted to the pillars cause the rubber pads to be compressed to a very thin sheet, squeezing the rubber out against the casing. In some places this side force has been sufficient to leave marks on the casing, and can occur anywhere round the casing.

However, as in the case of the distribution bar, any effect from the rubber pads would produce clamping bending strains in the opposite sense to those measured.

(iii) Misalignment of dummy bolts

The pillars which represent the bolts are not firmly located or aligned. Positioning depends on a short peg, which fits into the bolt hole loosely and allows 0.020 in lateral movement; and alignment depends on the machined surface of the flange and the spot facing being parallel.

Misalignment, aggravated by creep of the flange, would affect only the hoop strains in most of the casing. Only those pillars round by the boss would cause meridional bending in the casing, and the sense of this bending would probably be opposite to that shown by the model test results.

(iv) Uneven application of clamping force

The straightening of the toggle linkages on clamping up (Section 6.1.3 and Fig. 6.5) involves a peak of resistance at about half the travel of each piston. This means that the toggles straighten one at a time. Due to the positioning of the pivot arms (Fig. 6.4) along the distribution bar, the precompression of the springs at the toroid end is less than that of the

hemispherical end, so the two toggles at the toroid end always straighten first.

On clamping up, therefore, the distribution bars, each of which form a flat rigid plane, close together first at one corner of the toroid end, then at the other, then at one corner of the hemispherical end, and finally at the last corner to make the planes parallel again. The clamping load, therefore, is only distributed evenly among the pillars when all the toggles are straight, and when only one corner is clamped, a large proportion of one spring load is carried by only two or three pillars.

Since the distribution bars form flat planes, there is no twisting of the model due to this uneven closing, but in one corner of the toroid section the flange could be overloaded for a few seconds during clamping up, causing meridional bending in the casing of the opposite sense to that measured. If this overloading is sufficient to cause yield in the flange, the relaxing of this load as the clamping up continues might lead to small meridional bending in the same sense as that measured in the casing. This residual stress would be similar, though not necessarily same in both top and bottom casings.

(v) Squeezing of model

If the model were squeezed across the flanges on clamping up, the boss ends would be forced apart, causing an axial tension. As discussed earlier, this would be compatible with the model clamping strains measured. However, the rigid framework of the distribution bars was designed to resist such sideways faces.

(vi) Longitudinal bending of the casings

Bending in both the top and bottom casings from clamping up could be caused either by interference at the ends or by gaps in the flange joint of cylindrical section, which will close up when the model is clamped.

Interference might arise from the shaft ends or from wires being trapped between the flanges when the two half-casings of the model are put together. However, the sleeves on the shaft ends (Fig. 6.1) were made with 0.010 in radial clearance to avoid just such a problem. Trapped wires are easily detected since they cause a large gap between the flanges, and great care is taken to ensure that the flanges come together when assembled. A 0.003 in feeler gauge is used to check that the flanges are mated.

Several times before, and at final assembly, the pairs of half casings are put together. No significant gap between the flange surfaces has been detected, although most casings have been checked only at the outside edge. While the machining techniques were being developed, the flange faces of early casings were checked all over for flatness, but once the techniques were established, detailed checking was discontinued, and a mating check at the outside edge was considered sufficient.

A further unknown has been introduced, however, in the form of the silicone rubber seal of the joint faces. The forming of the seal, described in Section 6.1.5, leads to very thin films of silicone rubber on the flange joint face, particularly along the cylindrical section where a dry joint had previously sealed adequately. The curing time allowed was $1\frac{1}{2}$ to 2 hours, but it is possible that the thin films in the flange joint, away from the air take longer than this.

If this is the case, the rubber in some parts of the flange joint will still be liquid when the model is clamped, while in other parts it will be solid. In this way, the resulting unevenness of the flange face could cause bending in the casings, and the bending would be similar in top and bottom casings.

Summary

The evidence of the strain results indicates that longitudinal bending of the casings is taking place in a plane perpendicular to the flange plane. Unevenness of the flange faces or unequal curing of the silicone rubber seal or both would account for the symmetry of behaviour between top and bottom casings, while allowing for the randomness of the magnitude of clamping strains from test to test. Misalignment of the dummy bolts could explain the differences between top and bottom casings in each test. Implications for future tests are as follows;

(i) More positive location of the dummy bolts,

(ii) More detailed checking of the machined flange face,

(iii) Tests should be carried out to determine the minimum curing time for thin films of silicone rubber. Sealed casings should be left for times greater than this before loading.

(iv) The pivot arms on each side of the clamping rig should be rigidly linked by a shaft. Clamping up will then take place first on one side, then on the other, thus avoiding overloading of any of the dummy bolts.

(v) Future tests will be carried out on models with much thicker flanges, so there is no danger of the distribution bars fouling on the casing.

7.4.2 General features of Test 9

The distribution of meridional strains in the toroid section of the top and bottom casings (Figs. 7.26 to 7.30) shows clearly the shape predicted by the elastic analysis (Figs. 4.15 to 4.17) emerging above the clamping strains. Since the clamping strains arise from an unexpected loading pattern, however, the magnitude of the strain increase may not correspond to that predicted (Section 7.5.2); but if the analysis of the clamping is valid, the strains should be of the same order, top and bottom.

The closeness of the strain distribution lines after 0.11 hours, 1.03 hours and 10 hours show that the strain rates are very small. This confirms the conclusion arrived at in Section 7.1.3 that the difference between the elastic strain distribution and the distribution after about 0.1 hour is less than the experimental error.

$\theta = 0^{\circ}$ Meridional Section

Comparing the meridional strains in $\theta = 0^{\circ}$ meridional plane of top and bottom casings (Fig. 7.26 and Fig. 7.29), the differences in shape of the elastic distributions can be accounted for by the difference in shape of the clamping strain distributions. The shift from the clamping to the total elastic distributions are of the same order top and bottom, but the difference in the shape of the clamping strain distributions has resulted in a shift of the position of the peak strain of casing 15 (base) towards the cylinder.

The elastic strains shown at position 'e', the boss fillet radius, are very much smaller than those expected from the elastic distribution (Fig. 4.15). However, the very steep strain gradient in the fillet means that the average strain over the length of the strain gauge, which is all that the strain gauge will show, will be very much less than the peak. The radius of the fillet is $\frac{1}{8}$ in, which means an arc length of about 5 mm. The gauge length of the strain gauges in the fillet is 3 mm, so allowing for inaccuracy of gauge positioning, the average strain measured could be half the peak value. Furthermore, the very high stress in the fillet will induce very rapid creep, and will redistribute quickly to a lower value.

As expected, the positions of large total elastic strain are also the positions of large creep strain, the strain distribution changing to emphasise the high points. The separation of the distribution curves at the various test times shows that the creep strain rate is all the time slowing down. This is expected from the uniaxial creep calibration for the

material (Section 3.2), which showed only the primary stage of creep, even from high stress tests over long periods.

On the outside surface in the toroid section, the total strains indicate stresses too small to produce much creep unless there are very large hoop stresses. The initial movement is therefore probably elastic, as creep on the inside surface redistributes more load onto the rest of the section.

The distribution after 407 hours shows a big shift in the distribution both on the outside surface and on the inside surface at points with only small previous creep strains. This indicates that significant redistribution has taken place as the section bends. The position of the bending 'crossover' point between positions e and j, which was previously a pivot point for bending strains on the surface, has now moved. This means that the casing has deformed, and the direction of the redistribution indicates that the end boss has rotated in a sense that would separate the flanges on the outside (Fig. 7.26).

$\theta = 30^{\circ}$ Meridional Section

The elastic meridional strain distribution in the $\theta = 30^{\circ}$ plane is expected to be similar to that of the $\theta = 0^{\circ}$ plane, but of smaller magnitude. Fig. 7.27 and Fig. 7.30 show this to be the case, although the influence of the clamping strains is proportionately greater. The creep behaviour is also similar, though the smaller total initial strains have lead to smaller magnitude of creep strains.

At position '1' in Fig. 7.27, the strain gauge on the inside surface failed after 10 hours. A check under the gauge after the test did not reveal any defect in the casing.

$\theta = 60^{\circ}$ Meridional Section

In this test no strain bridges were available for the $\theta = 60^{\circ}$ meridional plane in the top casing. In the bottom casing (Fig. 7.28) the expected elastic strain distribution is smothered by the clamping strains, though the flattening of the inside surface total elastic distribution, reversed by the clamping, shows the influence of the expected peak of the pressure distribution (Fig. 4.17) at position '1'.

7.4.3 Comparison with Tests 4 to 8 casing strains

In general, the strain distributions are similar to those obtained from Test 9. Apart from test 6, however, where the pressure is lower than that of Test 9, the results of these tests are likely to be affected by separation of the flanges at the inside edge, inducing hoop bending all along the casing, and some meridional bending where the flange comes round to the boss ends. Because of the high value of Poisson's ratio for lead alloys, this hoop bending can affect the meridional strains significantly.

Test 4

Fig. 7.7 shows the meridional strain distribution to be very similar to that predicted by the elastic analysis (Fig. 4.15). The strain gauge positions cover a larger part of the $\theta = 0^{\circ}$ meridional plane than was covered in Test 9, although the peaks were missed due to lack of information about the elastic distribution (Section 7.1.2). Because of the high pressure, the total elastic strains are much less affected by the clamping strains, and give a clearer picture of the expected distribution.

In spite of the short duration of the test, the high pressure stresses lead to a distinct change of strain magnitudes due to creep, and a test time much shorter than for the other tests much be taken to obtain the elastic distribution.

Test 5

The strain gauge positions in Test 5 have missed the peak meridional strains in the toroid in the $\Theta = 0^{\circ}$ meridional plane, as in Test 4. However, the distribution around the cylinder joint (Fig. 7.8) show very much the same pattern as expected from the elastic analysis (Fig. 4.15).

Test 6

The low test pressure of Test 6 means that the total strains are much affected by the clamping strains. Allowing for this, the general pattern conforms with that of Test 9 and the expected distribution.

In the $\Theta = 0^{\circ}$ meridional plane the strain behaviour of the bottom casing (Fig. 7.9) is consistent with that of the other tests. But the top casing (Fig. 7.12) shows large strain rates at position 'ℓ' early in the test, on both the inside and the outside surfaces. These strains are probably not due to creep, but to an increase in the elastic bending stresses at that position, suggesting some deformation in the casing and deflection of the boss end early in the test. The strain rates in the bottom casing, too, are higher than expected, considering the magnitude of total initial elastic strains, particularly on the outside surface.

In the $\Theta = 30^{\circ}$ and $\Theta = 60^{\circ}$ meridional planes the strains also behave unexpectedly, (Figs. 7.10, 7.11 and 7.13) increasing rapidly on the inside surface towards the end of the test when they ought to be slowing down, and showing an unusually big change between 0.104 h and 10.4 h on the outside surface.

If there were early elastic changes, they are not thought to have been connected with additional, external loads. It is more likely that there was some initial restriction of the axial growth arising from the elastic deformations, so that at first, the full elastic stresses were not generated. This initial restriction, if it was there, may have been connected with the interference of the rubber pads at the toroid end, which severed and short

circuited the leads of some strain gauges located around the fillet radius of the flange near the boss end.

Test 7

The meridional strain distributions obtained from Test 7 (Fig. 7.14 to Fig. 7.19) show all the general features that were found in Test 9. The strains in and opposite the boss fillet radius (position 'e') are proportionally much larger than those of Test 9, probably due to the high pressure opening the flanges at the toroid end, leading to extra bending of the toroid boss.

Test 8

The meridional strain distributions obtained from Test 8 (Fig. 7.20 to Fig. 7.25) again show all the general features of Test 9. As in Test 7, the high pressure has opened the flanges at the inside edge, causing bending in the boss and hence the high strains at position 'e'.

In this test, however, there is a significant difference in the elastic strain magnitudes of top and bottom casings (see Section 7.4.4). This difference is apparent in all the meridional planes.

7.4.4 Comparison of Test 6 to Test 9 with predicted behaviour

For comparison, the meridional strains are taken at one position on the inside surface only in each casing. This is position 'ℓ' on the $\theta = 0^{\circ}$ meridional section, where the peak elastic strains are expected in the toroid.

Table 7.3 gives the experimental strain results for each casing. The total elastic strains are divided into their clamping and pressure components, and the creep strains are given at test times of 10 hours, 100 hours and at the maximum test time.

Table 7.4 shows the stresses and strains predicted from the elastic analysis. The predicted creep strains have been derived from the material uniaxial creep law obtained in Chapter 3, assuming the multiaxial creep

criteria described in Section 2.1.3, and assuming that there is no redistribution of the stresses. It can be seen that there is little correlation between Tables 7.3 and 7.4.

The elastic strains due to pressure agree fairly well in the experimental results top and bottom, except for Test 8, but correlation between tests is variable. The ratios shown of the meridional elastic pressure strain to test pressure indicate similar behaviour in Tests 7, 8 and 9, although these ratios and those of Test 6 do not agree with the predicted values given in Table 7.4. The base casing of Test 8, the odd one out among the experimental results, is the only casing where the experimental pressure strain agrees with the predicted value.

Variations of wall thickness (Table 7.3), which would lead to variations in both the direct stress and bending stress in the toroid under pressure, are not large enough to account for this difference. However, the clamping strains (see Section 7.4.1) introduce an unknown factor. These clamping strains are brought about by some unexpected distortion in the casing, and it is possible that this distortion will be modified by the pressure; in which case a linear response to pressure would not be expected.

The difference between the experimental and predicted pressure strains in addition to the experimental clamping strains result in experimental total elastic strains which are much higher than those predicted by theory. This results in the large differences between the predicted creep strains as shown in Table 7.4 and the experimental creep strains shown in Table 7.3. It can be seen that, in general, the high levels of total elastic strains in the experimental results lead to the high creep strains, particularly for test times of 100 hours or less.

To attempt to provide some correlation for the meridional experimental results, Table 7.5 was drawn up. Using the same theoretical criteria as for Table 7.4 in the method described in Appendix 6, the elastic stresses were

calculated for the comparison point in each casing which would produce the experimental total initial meridional strain and the subsequent experimental meridional creep strain after 100 hours test time, as given in Table 7.3. Using the same calculated stresses, the meridional creep strains after 10 hours and at maximum test time were also calculated. The experimental creep strains given in Table 7.3 are reproduced in Table 7.5 with the calculated values for comparison.

It can be seen from Table 7.5 that the calculated total meridional stresses in each test are similar in top and bottom casings. The difference in total strains between top and bottom casings comes from the difference in hoop stresses. This agrees well with the conclusion of Section 7.4.1 that there is meridional bending in the plane perpendicular to the flange plane, which would produce the same bending moments, and hence the same bending stresses, in top and bottom casings. It is much easier to account for the difference in the hoop stresses from misalignment of the dummy bolts or from radial misalignment of the flange faces.

The calculated stresses also give close agreement with the creep strains after 10 hours and at the maximum test time for each test. It was not possible to find an exact solution for the stresses in the bottom casing of Test 9, so the nearest values were taken. This accounts for the discrepancy at 100 hours, but taking them into account the stresses still give good agreement with the experimental results. The results for the top casing of Test 6, however, could not be matched in this way.

Since there were no strain gauges in the hoop direction at this point in any of the casings, it is not possible to verify the calculated values of Table 7.5, but these values do provide a reasonable correlation between the elastic and creep behaviour of the casings and could well indicate the true states of stress at those positions.

7.5 Hoop strains in the Casing (cylinder)

7.5.1 General features of Test 4 to Test 9

The concentration on the meridional strains in the toroid section and on the strains in the fillet radius has resulted in a scarcity of gauges for measuring hoop strains in the casing (see Section 7.1.2). In Tests 4 and 5 sufficient positions were gauged to enable the hoop strain distribution on the inside and outside surfaces of the cylindrical section in the $\theta = 0^{\circ}$ meridional plane to be mapped (Fig. 7.31 and 7.32) but for Tests 7, 8 and 9 only single positions are available (Figs. 7.33, 7.36 and 7.37). Although the results for Test 7 are plotted as a distribution (Fig. 7.33), the two gauges in the cylinder are so far apart that the lines joining the points should be considered only as a guide, and for both these gauges the pair on the inside surface failed. No hoop results were available for Test 6.

Elastic

Section 7.2 describes the elastic behaviour due to pressure expected in the $\theta = 0^{\circ}$ meridional plane of the cylindrical section, and in general, the creep test initial pressure strain behaviour agrees well with the conclusions of that section.

Test 9 is the only test where the flanges are not expected to separate and for which there are some hoop strain results (Fig. 7.37). The large clamping strains cause the big difference between the inside and the outside surface hoop strains (see Section 7.4.1), but the elastic strains due to pressure are, as expected, of about the same magnitude and are in the same direction.

Test 5 (Fig. 7.32) and Test 8 (Fig. 7.36) are at the same pressure of 55 lbf/in^2 at which the flanges are expected to separate and produce some hoop bending at the $\theta = 0^{\circ}$ meridional section. At the measurement position of Test 8 (between 's' and 't'), the clamping strains are different,

but small; and the elastic pressure strains for both tests are of the right order and show hoop bending in the manner expected. The strain distribution of test 5, allowing for the bending, agrees well with that predicted by the elastic analysis (Fig. 4.35).

The hoop strain due to pressure on the outside surface in Test 7 (Fig. 7.33) in the same position agrees well with those of tests 5 and 8, allowing for the difference in pressure; although the lack of results on the inside surface prevents any conclusion about the mean strain and the bending. However, the strain distribution along the $\theta = 0^{\circ}$ meridional section on the outside surface is also similar to that of Test 5, and suggests that the behaviour of Test 7 is consistent with the other tests.

Test 4, however, shows completely unexpected behaviour (Fig. 7.31). Instead of the flat hoop strain distribution found in the other tests and predicted by the elastic analysis, both the mean and the bending components of the surface elastic hoop strains increase rapidly towards the middle of the cylindrical section, where the strain on the inside surface is nine or ten times the expected value. The sense of the bending and the rapid growth in strain towards the middle of the cylinder suggests that the thin flange has twisted along its straight portion, separating the flange joint by a large amount in the middle of the cylinder. The large rotation would not only cause greatly increased bending strains in the $\theta = 0^{\circ}$ meridional plane, but would also produce sufficient deflections to increase the mean tension in the casing.

This twisting open did not occur at high pressure in Test 2 (see Section 7.2), which suggests that in Test 4 the flange was not properly clamped in the cylindrical section.

Additional hoop strains were measured in the boss at the toroid end in Tests 5, 7 and 8. In the boss fillet radius (position 'd' in the meridional plane) the results from Test 8, top and bottom (Fig. 7.34 and

Fig. 7.35), and from Test 5 agree with each other and the predicted elastic results. Test 7 is also consistent in that position; and although it shows larger hoop strains than expected in the middle of the boss, it can be seen from Fig. 7.33 that this is due to the clamping.

Creep

In general, as with the meridional strains in the toroid, the positions of large total elastic strains are also those of large creep strains.

For Test 9 (Fig. 7.37), the difference in initial strain levels (and, by implication, stress levels) between the inside and outside surfaces due to the clamping means that the outside surface alone will creep. But as it does so, the stresses are relieved on the outside and more of the pressure load must be carried by the inside. Hence, creep at the outside surface will be accompanied by an increase in the elastic strain at the inside surface.

A similar argument applies to Test 8 (Fig. 7.36), although here the small clamping and the bending induced by the pressure opening the flanges means that it is the inside surface which begins to creep. The elastic strain on the outside surface increases as the load is redistributed and the pressure bending stress reduced.

7.5.2 Comparison of Tests 8 and 9 with predicted behaviour

From Tests 8 and 9, the elastic pressure hoop strains in the cylinder on the inside and outside surfaces in the $\theta = 0^{\circ}$ meridional section, 2.25 in from the cylinder joint in Test 8 (Fig. 7.36) and 1.875 in from the cylinder joint in Test 9 (Fig. 7.37), are presented again in Table 7.6 with the elastic strains predicted by the finite element analysis of Parkes at the same positions.

It can be seen that in Test 9, where the flanges did not separate, the experimental elastic pressure strains agree very closely with the predicted values. In Test 8, where the flanges did separate, the experimental mean

hoop strain again agrees closely with the predicted value, but, as expected from Test 2 (Section 7.2), the bending strains are much larger.

The bending component of the Test 8 result is 80 μs, which gives a ratio of microstrain to pressure equal to 1.48. From the elastic casing results of Test 2 (Fig. 7.4 and Fig. 7.5) the expected value of the ratio would be nearer to 2. This suggests that the flanges have not separated as much in Test 8 as they did in Test 2, which could be the effect of the silicone rubber seal in Test 8 (not present in Test 2) preventing the pressurising oil from penetrating as far into the joint face.

7.6 Hoop strains in the flange fillet radius

7.6.1 General features of Test 9

The flange fillet radius strains were studied in detail in Test 9. Fig. 7.42 and Fig. 7.43 show the strain distributions in the right and left hand sides of the bottom casing, and Fig. 7.44 shows the strain distribution in the right hand side of the top casing (opposite the left hand side of the bottom casing). Because of the counterbores of the bolt holes, which cut into the casing at the junction with the flange, the fillet is not continuous, so the distribution lines shown should be regarded as schematic only.

As expected from the elastic analysis, the fillet hoop strains in the cylindrical section (holes 9 and 10) are small. However, in the toroid section, from the boss round to the junction with the cylinder, the hoop strain levels are very high. The strengthening effect of the boss is reflected in the falling off of strain between holes 1 and 2.

It can be seen that the application of pressure in the model has very little effect on the fillet strains. Considering the high clamping strains, the strain changes could be attributed almost entirely to creep. This would agree with the elastic analysis of Parkes (42) which predicts a negligible elastic strain due to pressure when the flanges do not separate.

The distribution in the toroid section, therefore, must be considered in the light of the unexpected clamping behaviour as discussed in Section 7.4.1. The direction of the gauges in the flange fillet radius round by holes 1, 2, 3 and 4 is nearly parallel to the $\theta = 0^{\circ}$ meridional section, so longitudinal bending of the casing as described in Section 7.4.1 might be expected to produce the kind of peaks in the flange fillet that were experienced in the boss fillet radius in the $\theta = 0^{\circ}$ meridional plane. The combination of bending and torsion which would be transmitted round the flange could extend into the cylindrical section before dying away, and produce the large strains between holes 4, 5 and 6.

The distributions of the matching top right hand and bottom left hand sides agree fairly well, except for the possibly freak result from the bottom casing between holes 3 and 4. As with the boss fillet radius, the steep gradients in the flange fillet radius can lead to big differences in measured strain from small inaccuracies of gauge location.

The right hand side of the bottom casing agrees with the other results at the boss and the junction with the cylinder, but does not show the peaks round the toroid. This probably reflects the different clamping behaviour of one side from another, and agrees more with the expected behaviour since the strains become smaller round where the toroid end becomes more rigid.

The creep strains are very small, considering the large initial strains. This indicates that a rapid redistribution has taken place on clamping up.

7.6.2 Comparison of Test 4 to Test 8 with Test 9

Of the other tests, only Test 6 was of a pressure low enough to prevent separation of the flanges, and there are no flange fillet radius results for this test. Flange separation will cause hoop bending in the casing and hence bending strains in the flange fillet radius (Fig. 7.6).

Bending in the flange fillet is shown most dramatically in the high pressure test, Test 4 (Fig. 7.38). As the pressure builds up, large bending strains appear in the flange fillet, particularly in the cylindrical section. In the toroid section, although the clamping strains show the same pattern as in Test 9, with large initial strains in the region of holes 2, 3, 4 and 5, the rigidity of the toroid prevents large flange rotations, and hence bending as the pressure is applied is smaller.

Again, in Test 5 (Fig. 7.39) the pattern is repeated - large clamping strains and small pressure strains in the toroid, and small clamping strains and large pressure strains in the cylindrical section. In Test 7 (Fig. 7.40)

the flange rotation is small with only 45 lbf/in^2 pressure, although there were no gauges to show the behaviour in the cylinder.

Although Test 8 follows the pattern of clamping strains (Fig. 7.41), and agrees with Test 5 (at the same pressure) in the toroid section, the single gauge in the cylindrical section shows very little flange rotation. This is probably due to faulty location of the gauge.

7.7 Errors

7.7.1 Build up of errors

Some of the differences between the theoretical prediction of the model creep strain behaviour and the experimental results can be attributed to errors in the prediction and to errors in the strain measurement. The flow chart in Fig. 7.45 shows how these errors build up if the multiaxial creep criteria described in Section 2.1.3 are assumed valid.

The error analysis is concerned with the prediction of the true behaviour of the models under test, so that differences in material composition and test temperature between the uniaxial specimens and the model casings are shown in Fig. 7.45 as leading to errors in the material uniaxial creep law.

7.7.2 Errors in predicted stresses

The elastic stresses in the models were obtained in two ways. The photoelastic analysis was subject to its own experimental errors, and the large deflections involved (Chapter 4) do not represent the behaviour of the lead models exactly. The finite element analysis of Parkes does not suffer from these defects, though there are necessarily discontinuities of stress at the junction of the elements, and the infinitesimally small deflections involved equally do not represent the elastic behaviour of the lead models. However, where the two analyses are in close agreement, as in the toroid, the elastic stresses can be predicted with some confidence.

In the cylindrical section in Tests 8 and 9, the results show 15% and 1% prediction error in the elastic mean hoop stress respectively (see Table 7.6). This difference is probably accounted for by the separation of the flanges at the higher pressure of Test 8, so it is probable that the average of the elastic analyses allow prediction of mean stresses in Test 9, to within 5%.

However, this accuracy applies to the elastic pressure stresses only. The clamping stresses, particularly in the meridional direction, were very different from those expected, but the cause was thought to be additional loading on the model (Section 7.4.1).

The bending stresses are inversely proportional to the square of the thickness. Table 7.3 shows the wall thickness at the comparison position in the toroid to be an average 0.011 inch thicker than the standard 0.375 inch, an error of 3%.

Errors in model loading would include model self weight and varying pressure. No consistent difference between the elastic behaviour of top and bottom casings was detected in the results, so it was considered that the self weight effect was negligible. Because of friction in the seal-less piston of the pressure rig, there is an increase in the model pressure of nearly 5 lbf/in^2 while the pump is operating. Tests with the U/V recorder showed that this pulse lasts less than 3% of the piston cycle time, but there is evidence (Section 2.1.5) that the effect of pressure cycling in creep is much greater than that predicted by theory.

Hence, probable errors in surface stresses

$$\frac{\Delta\sigma}{\sigma} = 0.05 + 2(0.03) = 0.11$$

7.7.3 Errors in Predicted Creep Law

Where a material has been calibrated to derive a creep law, and this law is then used to predict the behaviour of a model, the error analysis of the model prediction must lead back to the experimental errors in the calibration, for the special case where the model is of the calibration specimens.

Errors in determining the constants of the Uniaxial Creep Law

Although a curve fitting program was used in the material calibration (Section 3.2.4), the method used was basically graphical. The program was used merely to draw the 'best' line through the points, so the error analysis must be based on the graphical determination of the creep constants. The experimental results were fitted to the law:

$$\varepsilon_c = A\sigma^n t^s \qquad (1)$$

and the constants 'n' and 's' were obtained from the slopes of graphs of log(strain) against log(stress),

i.e. $\text{Log}\ \varepsilon_c = n\ \text{Log}\ \sigma + \text{Log}\ At^s$ (2) where $\text{Log}\ At^s$ is constant

and of a graph of log(strain) against log(time),

i.e. $\text{Log}\ \varepsilon_c = s\ \text{Log}\ t + \text{Log}\ A\sigma^n$ (3) where $\text{Log}\ A\sigma^n$ is constant.

The constant 'A' is also determined from the graph of equation (3), where a particular value of creep strain, ε_1, produced in the corresponding time t_1 from a stress σ_1 gives,

$$\text{Log}(A\sigma_1^n) = \text{Log}\ \varepsilon_1 - s\ \text{Log}\ t_1 \qquad (4)\ \text{Hence A.}$$

From (4) $\Delta\left[\text{Log}(A\sigma_1^n)\right] = \Delta\left[\text{Log}\ \varepsilon_1\right] - \Delta\left[s\ \text{Log}\ t_1\right]$ for small changes.

If there is an error of $+\Delta s$ in the measured time index, 's', and an error of $+\Delta n$ in the measured stress index, 'n', and an error of $+\ \Delta\varepsilon_1$ in the value of the particular strain level, ε_1,

then $$\Delta\left[\text{Log}\ \varepsilon_1\right] = \text{Log}(\varepsilon_1 + \Delta\varepsilon_1) - \text{Log}\ \varepsilon_1 = \text{Log}\left(1 + \frac{\Delta\varepsilon_1}{\varepsilon_1}\right)$$

and $$\Delta\left[s\ \text{Log}\ t_1\right] = \Delta s\ \text{Log}\ t_1$$

and $$\Delta\left[\text{Log}(A\sigma_1^n)\right] = \text{Log}\left[(A + \Delta A)\sigma_1^{(n + \Delta n)}\right] - \text{Log}\ A\sigma_1^n =$$

$$= \text{Log}\left[\left(1 + \frac{\Delta A}{A}\right)\sigma_1^{\Delta n}\right]$$

then from equation (4)

$$\text{Log}\left[\left(1+\frac{\Delta A}{A}\right)\sigma_1^{\Delta n}\right] = \text{Log}\left(1+\frac{\Delta\varepsilon_1}{\varepsilon_1}\right) - \Delta s\ \text{Log}\ t_1$$

i.e. $$1+\frac{\Delta A}{A} = \left(1+\frac{\Delta\varepsilon_1}{\varepsilon_1}\right) t_1^{-\Delta s}\ \sigma_1^{-\Delta n} \qquad (5)$$

Errors from use of experimental creep law

If A', n', s' are the true values of the creep constants, and σ', t' are the true stress and time, the true creep strain, ε_c', is given by

$$\varepsilon_c' = A'\ \sigma'^{n'} t'^{s'}$$

If A, n, s are the experimentally determined values of the creep constants, and σ, t are the estimated values of stress and time, then the predicted creep strain ε_c is given by equation (1)

$$\varepsilon_c = A\sigma^n t^s$$

Let the experimental errors be of the form $x + \Delta x = x'$ as usual,

Hence $$\varepsilon_c + \Delta\varepsilon_c = \varepsilon_c'$$

i.e. $$A\sigma^n t^s + \Delta\varepsilon_c = (A+\Delta A)(\sigma+\Delta\sigma)^{(n+\Delta n)}(t+\Delta t)^{(s+\Delta s)}$$

i.e. $$1+\frac{\Delta\varepsilon_c}{\varepsilon_c} = \frac{1}{A\sigma^n t^s}\Bigg[A\left(1+\frac{\Delta A}{A}\right)\sigma^{(n+\Delta n)}\left(1+\frac{\Delta\sigma}{\sigma}\right)^{(n+\Delta n)} t^{(s+\Delta s)}\left(1+\frac{\Delta t}{t}\right)^{(s+\Delta s)}\Bigg]$$

taking first order terms only,

$$1+\frac{\Delta\varepsilon_c}{\varepsilon_c} = \left(1+\frac{\Delta A}{A}\right)\left(1+n\frac{\Delta\sigma}{\sigma}\right)\sigma^{\Delta n}\left(1+s\frac{\Delta t}{t}\right)t^{\Delta s} \qquad (6)$$

The error in the creep constant A is given by equation (5),

hence, $$1+\frac{\Delta\varepsilon_c}{\varepsilon_c} = \left(1+\frac{\Delta\varepsilon_1}{\varepsilon_1}\right)t_1^{-\Delta s}\sigma_1^{-\Delta n}\left(1+n\frac{\Delta\sigma}{\sigma}\right)\sigma^{\Delta n}\left(1+s\frac{\Delta t}{t}\right)t^{\Delta s}$$

i.e. $$1+\frac{\Delta\varepsilon_c}{\varepsilon_c} = \left(1+\frac{\Delta\varepsilon_1}{\varepsilon_1}\right)\left(1+n\frac{\Delta\sigma}{\sigma}\right)\left(1+s\frac{\Delta t}{t}\right)\left(\frac{\sigma}{\sigma_1}\right)^{\Delta n}\left(\frac{t}{t_1}\right)^{\Delta s} \qquad (7)$$

If second order terms are ignored, equation (7) can be simplified

$$1 + \frac{\Delta\varepsilon_c}{\varepsilon_c} = \left(1 + \frac{\Delta\varepsilon_1}{\varepsilon_1} + n\frac{\Delta\sigma}{\sigma} + s\frac{\Delta t}{t}\right)\left(\frac{\sigma}{\sigma_1}\right)^{\Delta n}\left(\frac{t}{t_1}\right)^{\Delta s} \qquad (7a)$$

If equation (7) is to be used to predict the strain errors in the original calibration tests, in particular for the point from which the constant 'A' was determined, the results reduce to the expected errors. In this case the stress is σ_1, the time is t, and the creep strain is ε_1. The errors in stress and time are taken as zero, expressing all experimental error in terms of strain. Equation (7) then becomes

$$\frac{\Delta\varepsilon_c}{\varepsilon_c} = \frac{\Delta\varepsilon_1}{\varepsilon_1} \quad \text{as expected.}$$

Examining equation (7), the effect of errors in the stress and time indices can be large if the test stress and time lie outside the range of the calibration stress and time. This shows how large errors can arise from extrapolation of the range of the calibration tests.

From Section 3.2.4, the value of $s \pm \Delta s = 0.513 \pm 0.052$; i.e. $\frac{\Delta s}{s} \simeq 10\%$

and the value of $n \pm \Delta n = 5.417 \pm 0.55$; i.e. $\frac{\Delta n}{n} \simeq 10\%$

The particular stress, strain and time values have been taken from the middle of the range of the group 2 uniaxial specimens, the average error in the strain level being given by the standard deviation.

Hence, $\sigma_1 = 1400$ lbf/in^2; $t_1 = 30$ hours; $\frac{\Delta\varepsilon_1}{\varepsilon_1} = 0.219$

i.e. from equation 7(a),

$$1 + \frac{\Delta\varepsilon_c}{\varepsilon_c} = \left[1.219 + 5.417\frac{\Delta\sigma}{\sigma} + 0.513\frac{\Delta t}{t}\right]\left(\frac{\sigma}{1400}\right)^{\pm 0.55}\left(\frac{t}{30}\right)^{\pm 0.052} \qquad (7b)$$

7.7.4 Errors in predicted creep strains

Considering the casing as thin walled, the Von-Mises-Hencky equivalent stress is given by (see Appendix 6);

$$\sigma_e = \sigma_1\sqrt{1 - \alpha + \alpha^2} \qquad \text{where } \frac{1}{\alpha} = \sigma^1/\sigma_2$$

differentiating, $$\frac{\Delta\sigma_e}{\sigma_e} = \frac{\Delta\sigma_1}{\sigma_1} + \frac{\alpha(2\alpha - 1)}{2(1 - \alpha + \alpha^2)}\frac{\Delta\alpha}{\alpha}$$

and $$\frac{\Delta\alpha}{\alpha} = \frac{\Delta\sigma_1}{\sigma_1} + \frac{\Delta\sigma_2}{\sigma_2}$$

In the $\theta = 0^\circ$ meridional plane σ_1 is the meridional stress and σ_2 is the hoop stress. In Section 7.4.4, results and prediction were compared at position 'ℓ' on the inside surface of the toroid in the $\theta = 0^\circ$ meridional plane. From Table 7.3, the predicted value of α at this point is 0.39 and the predicted value of σ_e is 400 lbf/in^2. The bending stress error due to section thickness is the same for σ_1 and σ_2 (Section 7.7.2), so the error in α will arise only from the mean stress errors.

i.e. $$\frac{\Delta\alpha}{\alpha} = 0.05 + 0.05 = 0.10$$

Hence $$\frac{\Delta\sigma_e}{\sigma_e} = 0.11 + (0.056)(0.10) = \underline{0.116}$$

Substituting these values in equation (7b), the error in the equivalent creep strain after 100 hours, when $\Delta t/t$ is negligible, ε^* is given by,

$$1 + \frac{\Delta\varepsilon^*}{\varepsilon^*} = \left[1.219 + 5.417(0.116) + 0\right]\left(\frac{400}{1400}\right)^{\pm 0.55}\left(\frac{100}{30}\right)^{\pm 0.052}$$

$$\therefore \quad 1 + \frac{\Delta\varepsilon^*}{\varepsilon^*} = (1.849)(1.99)(1.065) = 3.93$$

$$\therefore \quad \frac{\Delta\varepsilon^*}{\varepsilon^*} = 2.93$$

From Appendix 6 , the meridional creep strain is given by

$$\varepsilon_{1c} = \frac{\varepsilon^*}{\sigma_e}\sigma_1\left(1 - \tfrac{1}{2}\alpha\right)$$

differentiating,

$$\frac{\Delta\varepsilon_{1c}}{\varepsilon_{1c}} = \frac{\Delta\varepsilon^*}{\varepsilon^*} - \frac{\Delta\sigma_e}{\sigma_e} + \frac{\Delta\sigma_1}{\sigma_1} - \frac{\alpha}{2(1-\frac{1}{2}\alpha)}\,\frac{\Delta\alpha}{\alpha}$$

Substituting,

$$\frac{\Delta\varepsilon_{1c}}{\varepsilon_{1c}} = 2.93 - 0.116 + 0.11 - (0.243)(0.1) = \underline{\underline{2.90}}$$

Note Since the error values have been given a particular sign for calculating the errors in σ_e, α and ε^*, these signs must be preserved in the calculation of $\frac{\Delta\varepsilon_{1c}}{\varepsilon_{1c}}$.

Hence the average error in predicting the meridional creep strain at position 'ℓ' on the inside surface in the $\theta = 0^\circ$ meridional plane was 290%.

7.7.5 Errors in measured creep strains

The electrical strain calibration described in Section 6.2 bypasses any calculation involving the strain bridge circuit, and so eliminates any errors in the settings of voltage, amplifier gain, bridge resistance and DVM reading. Only drift and variation of resistance in the gauges which make up the individual half-bridge circuits will lead to errors.

These strain gauges, which are of the same type as those used on the model, were checked for resistance and were found to vary less than 0.5 Ω in approximately 120 Ω. The maximum possible resistance ratio variation in the half-bridge was therefore less than 1%.

Drift due to zero drift in the DVM and temperature drift in the gauges was allowed for in the processing of the results (Section 6.3), and the errors here were expected to be negligible - particularly since the creep tests took place in a temperature-controlled room ($\pm 1^\circ$C).

The most serious measurement error was due to the limit of sensitivity of the DVM. The last 'window' could show only 0 or 5 (microvolts), allowing a possible error in each reading of $2\frac{1}{2}\,\mu$V. The processing of the results

involved four calculations involving addition and subtraction of readings, leading to a possible error of $10\,\mu V \simeq 5\,\mu S$.

The gauge factor error was unknown, since no information was supplied by the manufacturers, but it was thought to be about 5%.

$\therefore$ Total error (allowing 1% for drift variations) = $6\% + 5\,\mu S$.

for a strain reading of $100\,\mu S$, error = 6 + 5 = <u>11%</u>

7.7.6 Discussion

The uncertainty of results from small total strains and low stresses is immediately apparent. The large prediction errors in Section 7.7.4 are strongly connected with the factor of 1.99 which arose from extrapolation from uniaxial test results around 1400 lbf/in^2 to model tests at 400 lbf/in^2. If the uniaxial tests and model tests could be conducted within the same range of stresses, this factor would be reduced to 1.

TABLE 7.1 SURVEY OF TURBINE CASINGS

* to be decided

MAKE OF CASING	DIAMETER (D)	LENGTH	WALL THICKNESS (t) (INCH)	PRESSURE lbf/in^2	MEAN HOOP STRESS lbf/in^2	TEMPERATURE ^oC	YOUNG'S MODULUS (E) $lbf/in^2 \times 10^{-6}$	$\frac{D}{D_L}$	$\frac{t}{t_L}$	$\frac{E}{E_L}$	HOOP STRAIN CORRESPONDING LEAD MODEL PRESSURE lbf/in^2
Lead Model	6.625 in	14 in	0.375	*	*	20	2.85	-	-	-	-
English Electric I.P. Nosing Outer Casing	11 ft	10 ft	2.75	223	5350	435	24.0	19.9	7.35	8.0	75.5
English Electric I.P. Inner Cylinder	5.5 ft	5.3 ft	4.0				23.0	9.95	10.7	7.66	
English Electric H.P. Outer Casing	7 ft	10 ft	4.5	1045	9750	435	24.0	12.7	12.0	8.0	138.0
English Electric H.P. Inner Casing	4 ft	3.5 ft	5.0	758	3640	535	23.0	7.25	13.35	7.66	53.7
Parsons I.P. Outer Casing	8.5 ft	13 ft	3.25	240	3800		24.0	15.4	8.7	8.0	53.3
Parsons I.P. Inner Casing	5 ft	6 ft	3.25	318	2940		23.0	9.1	8.7	7.66	43.3
Parsons H.P. Outer Casing	6 ft	8.5 ft	3.375	610	6500		24.0	10.85	9.0	8.0	92.0
Parsons H.P. Inner Casing	3.5 ft	7 ft	3.0	1190	8330		23.0	6.35	8.0	7.66	123.0

TABLE 7.2 SUMMARY OF MODEL TESTS

TEST NO.	Sb CONTENT	PRESSURE lbf/in^2	TEST TIME hours	REMARKS
1	6%	Various		Trial of rig and instrumentation
2	6%	Various		Test of elastic response
3	6%	75	200	Creep test trial
4	1.2%	75	1.5	Test at max. pressure and further sealing trials
5	1.2%	55	96	Test at new max. pressure without leaks
6	1.2%	30	667	Test at minimum pressure for creep with correct gauge locations
7	1.2%	45	453	Middle range test. (correct gauge locations)
8	1.2%	55	576	Repeat of test 5 with correct gauge locations and repeatability check
9	1.2%	35	407	Optimum pressure test (correct gauge locations). For comparison with finite element analysis.

TABLE 7.3 EXPERIMENTAL RESULTS FOR POSITION *l* ($\phi = 53^\circ$) IN THE $\theta = 0^\circ$ MERIDIONAL PLANE (inside surface)

		TEST 6		TEST 7		TEST 8		TEST 9	
PRESSURE (lbf/in^2)		30		45		55		35	
MAX. TEST TIME (hours)		667		453		576		407	
CASING		TOP	BASE	TOP	BASE	TOP	BASE	TOP	BASE
WALL THICKNESS (in)		0.388	0.386	0.379	0.385	0.393	0.392	0.384	0.385
INITIAL MERIDIONAL STRAIN ε_m (μS)	Clamping	-25	40	100	85	25	40	80	150
	Pressure	75	75	235	220	285	180	150	165
	Total	50	115	335	305	305	220	230	315
	Total ε_m/p	2.5	2.5	5.2	4.9	5.2	3.3	4.3	4.7
MERIDIONAL CREEP STRAIN (μS)	after 10 h.	50	5	85	70	55	30	20	40
	after 100 h.	110	50	195	175	170	95	70	100
	at end of test	-	85	355	350	440	220	160	150

TABLE 7.4

PREDICTED STRAINS FROM ELASTIC ANALYSIS AND MATERIAL CREEP LAW AT POSITION '1' ($\phi = 53^{\circ}$) IN THE $\theta = 0^{\circ}$ MERIDIONAL PLANE - INSIDE SURFACE

		TEST 6	TEST 7	TEST 8	TEST 9
PRESSURE (lbf/in^2)		30	45	55	35
MAX. TEST TIME (hours)		667	453	576	407
CASING		Top & base	Top & base	Top & base	Top & base
ELASTIC STRESSES (lbf/in^2) pressure	clamp	0	0	0	0
	meridional	315	472	578	368
	hoop	120	183	220	140
	α	0.38	0.38	0.38	0.38
INITIAL MERIDIONAL STRAIN (μS)	clamp	0	0	0	0
	pressure	94	141	172	105
	$\varepsilon_{m/p}$	3.14	3.14	3.14	3.14
MERIDIONAL CREEP STRAIN (μS)	after 10 h.	0.07 (50 / 5)	0.70 (85 / 70)	3.8 (55 / 30)	0.15 (20 / 40)
	after 100 h.	0.21 (110 / 50)	2.1 (195 / 175)	12.5 (170 / 95)	0.5 (70 / 100)
	after max. time	0.44 (- / 85)	4.7 (355 / 350)	30.5 (440 / 220)	1.0 (160 / 150)

The figures in brackets are the corresponding experimental values of meridional creep strain (μS) from Table 7.3 (TOP / BASE)

TABLE 7.5 CALCULATED RESULTS TO PRODUCE EXPERIMENTAL INITIAL ELASTIC STRAINS AND CREEP STRAINS AFTER 100 HOURS AS GIVEN IN TABLE 7.3 (Resulting creep strains after 10 h. and max. test time compared)

		TEST 6		TEST 7		TEST 8		TEST 9	
PRESSURE (lbf/in^2)		30		45		55		35	
MAX. TEST TIME (hours)		667		453		576		407	
CASING		TOP	BASE	TOP	BASE	TOP	BASE	TOP	BASE
INITIAL ELASTIC STRESSES (lbf/in^2)	Meridional	not solvable	753	1100	1125	1115	975	940	955
	Hoop		1009	374	640	614	878	715	143
	κ (ratio)		1.45	0.34	0.57	0.55	0.89	0.76	0.15
INITIAL MERIDIONAL STRAIN (μS)		50	115	335	305	305	220	230	315
MERIDIONAL CREEP STRAIN (μS)	after 10 h.	-	13 (5)	60 (85)	54 (70)	52 (55)	28 (30)	21 (20)	37 (40)
	after 100 h.	-	44 (50)	194 (195)	176 (175)	170 (170)	93 (95)	69 (70)	120 (100)
	after max. time	-	116 (85)	421 (355)	382 (350)	416 (440)	229 (220)	142 (160)	246 (150)

TABLE 7.6

COMPARISON OF EXPERIMENTAL AND PREDICTED (PARKES, 42)
ELASTIC PRESSURE HOOP STRAINS IN THE CYLINDER

		TEST 8		TEST 9	
PRESSURE (lbf/in^2)		55		35	
MEASUREMENT POSITION		Cylinder joint + 2.25 in		Cylinder joint + 1.875 in	
Strains due to pressure		Experimental	predicted	Experimental	predicted
ELASTIC HOOP STRAINS (μS)	ε inside	245	146	95	99
	ε outside	85	143	86	86
	ε mean	165	145	90.5	92.5
	ε bending	80	1	4.5	6.5

STRAIN GAUGES ON MODEL

FIG. 7·1

CYLINDER - $\theta = 0°$, $z = 2{\cdot}50$ in

MODEL TEST 2 (position A)

FIG. 7·2

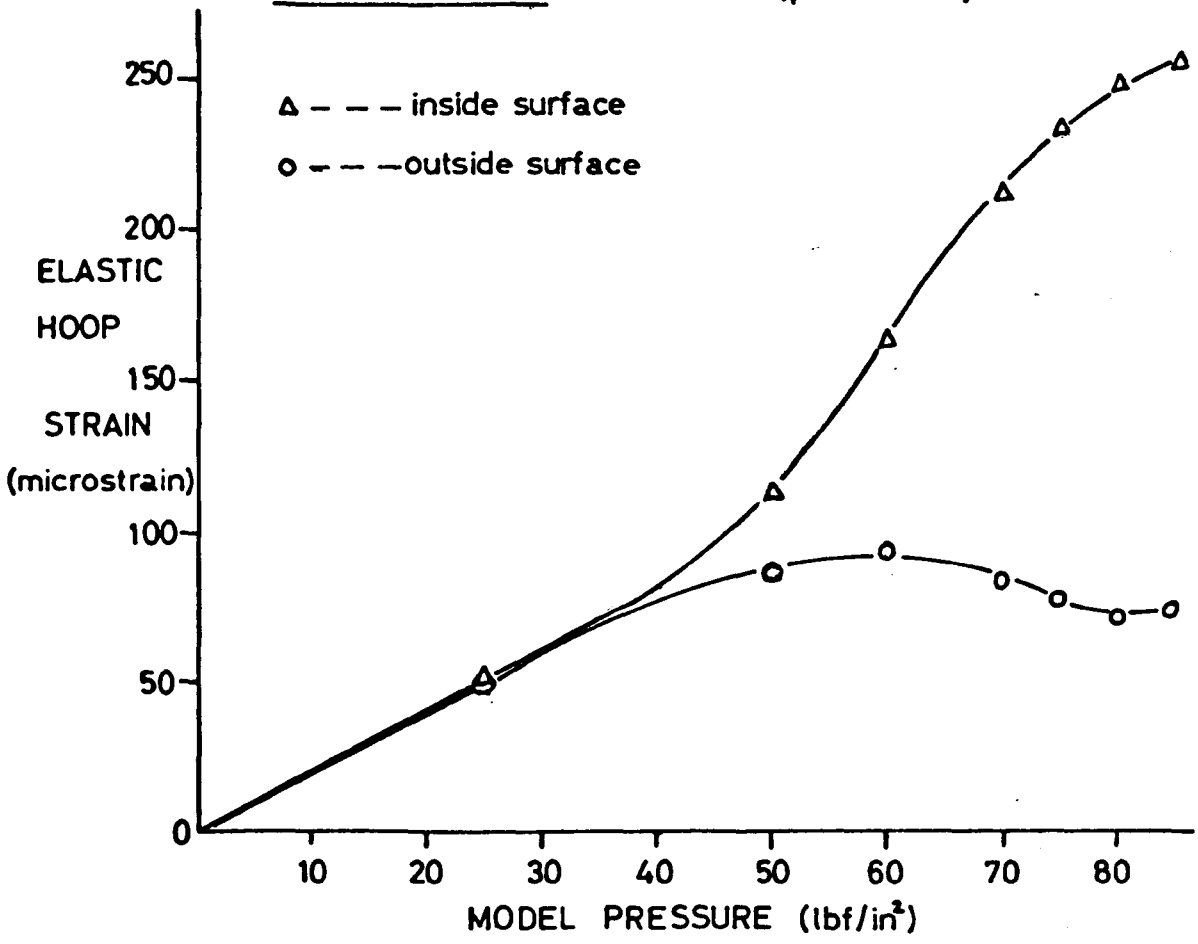

MODEL TEST 2

CYLINDER - $\theta = 0°$, $z = 3{\cdot}35$ in (position B)

FIG. 7·3

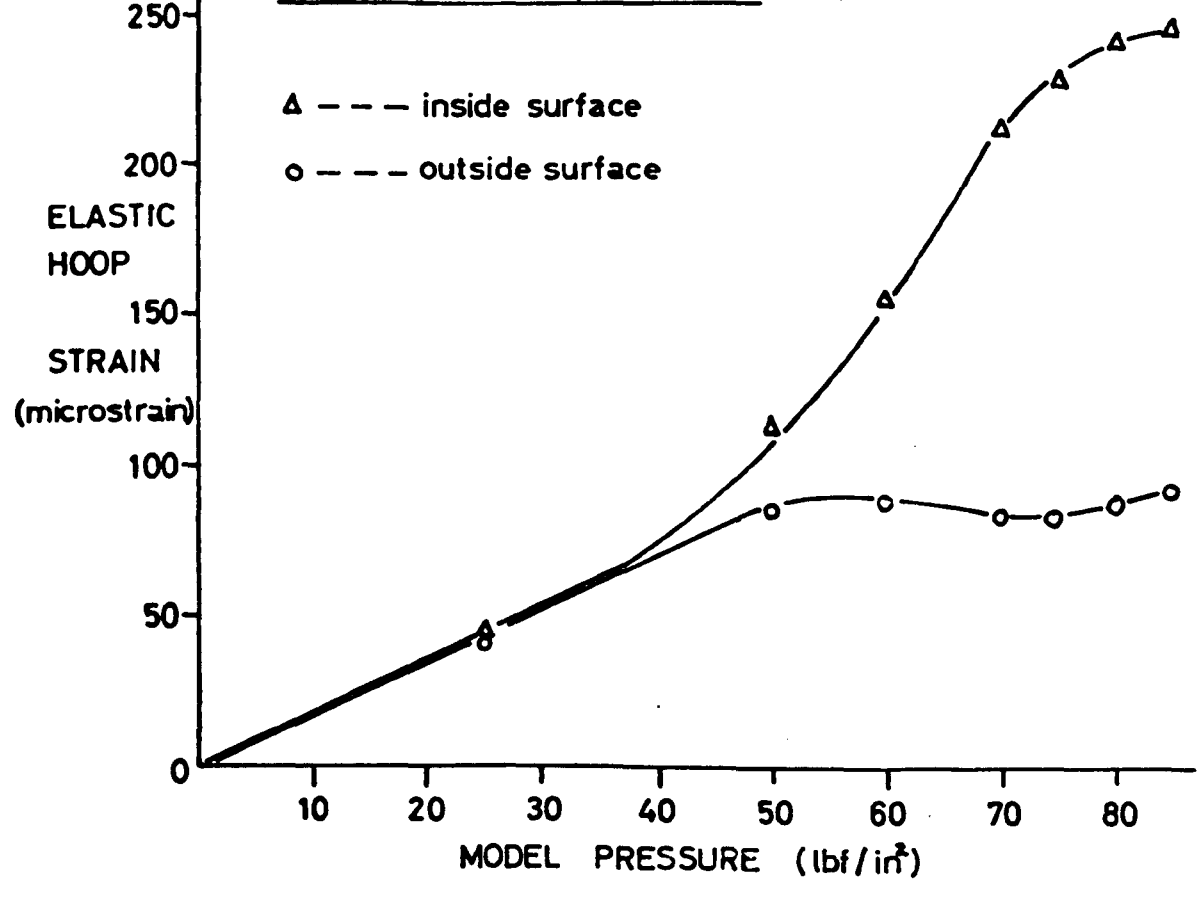

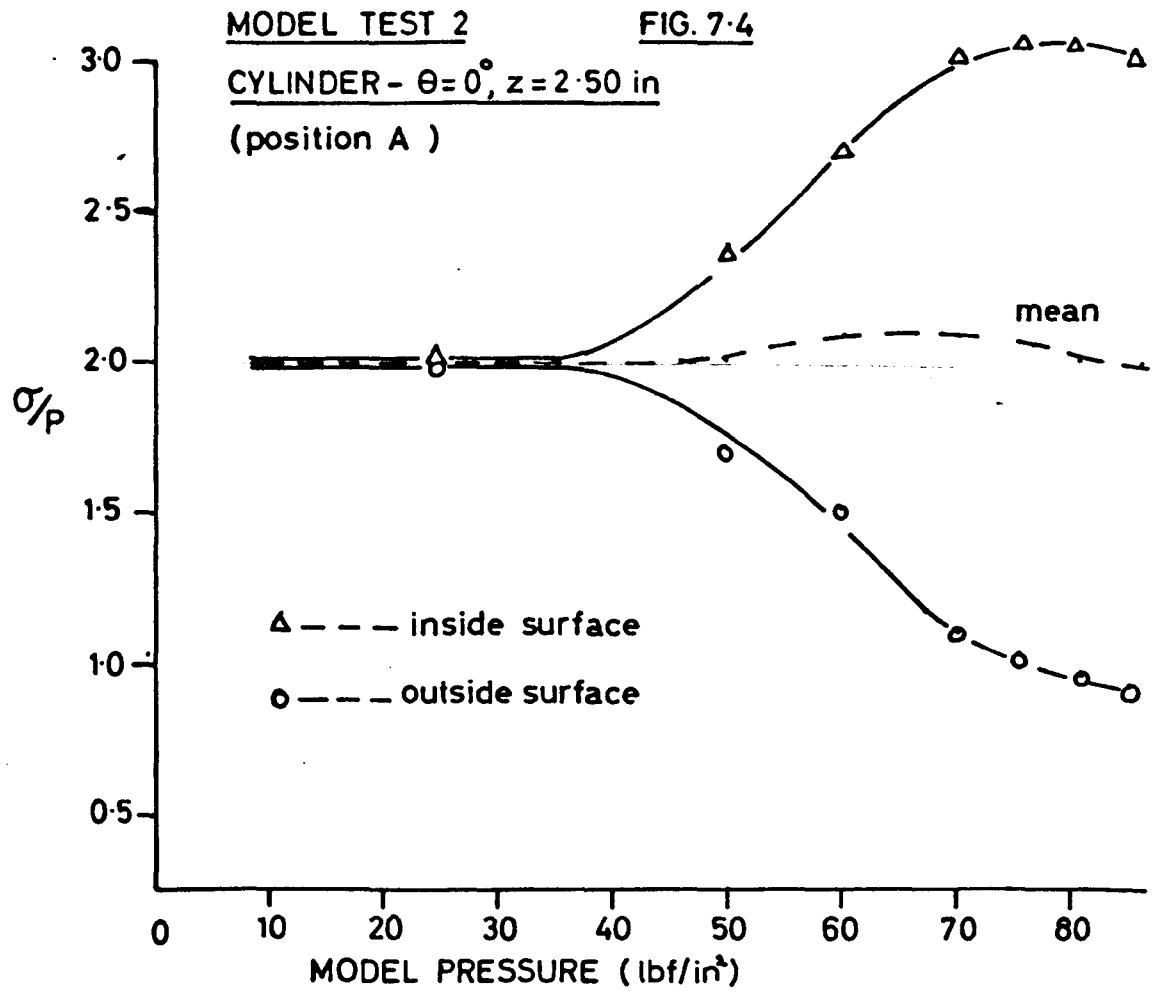
MODEL TEST 2
FIG. 7·4
CYLINDER - θ = 0°, z = 2·50 in
(position A)
mean
σ/p
inside surface
outside surface
3·0
2·5
2·0
1·5
1·0
0·5
0
10
20
30
40
50
60
70
80
MODEL PRESSURE (lbf/in²)

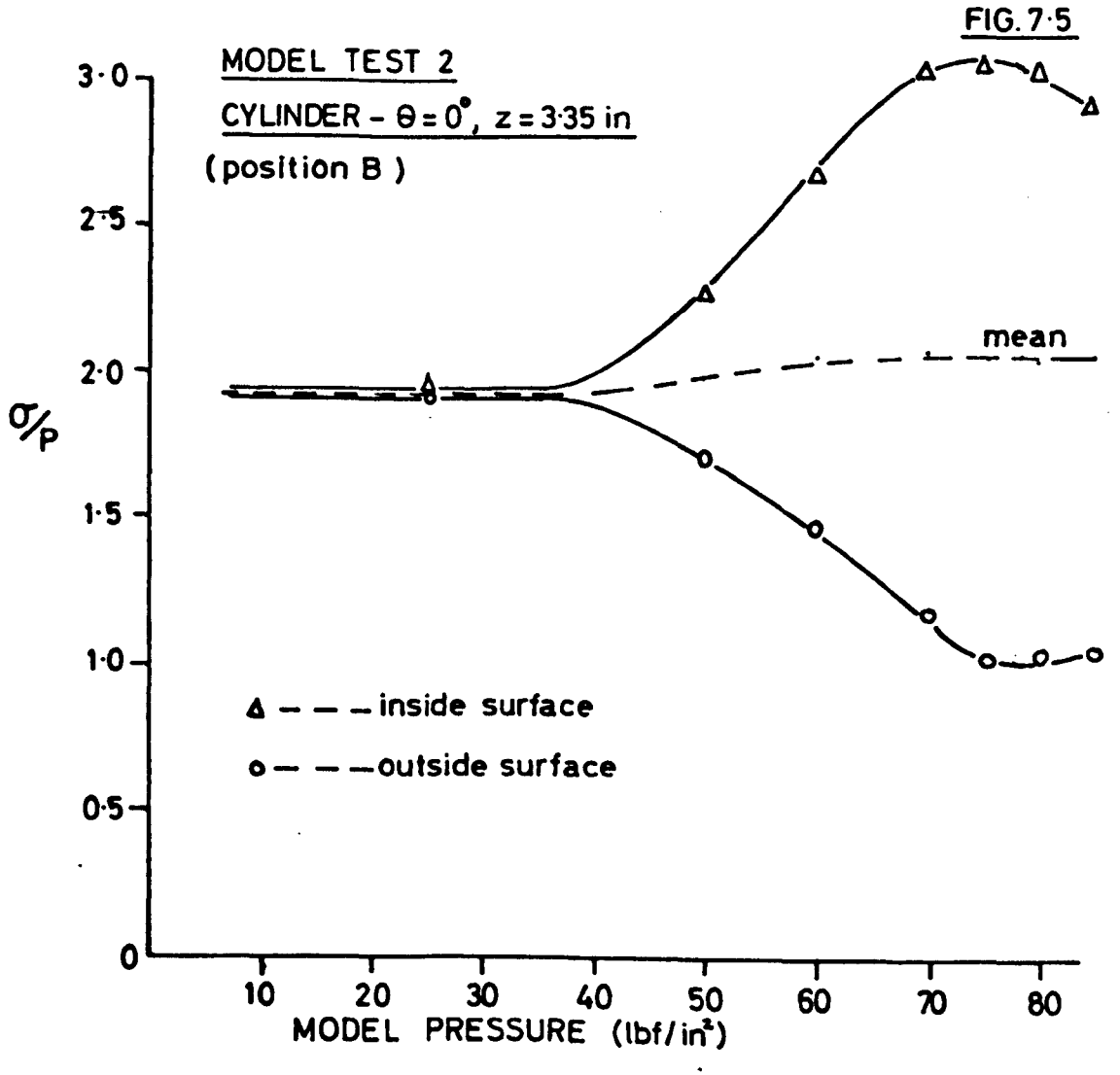
FIG. 7·5
MODEL TEST 2
CYLINDER - θ = 0°, z = 3·35 in
(position B)
mean
σ/p
inside surface
outside surface
3·0
2·5
2·0
1·5
1·0
0·5
0
10
20
30
40
50
60
70
80
MODEL PRESSURE (lbf/in²)

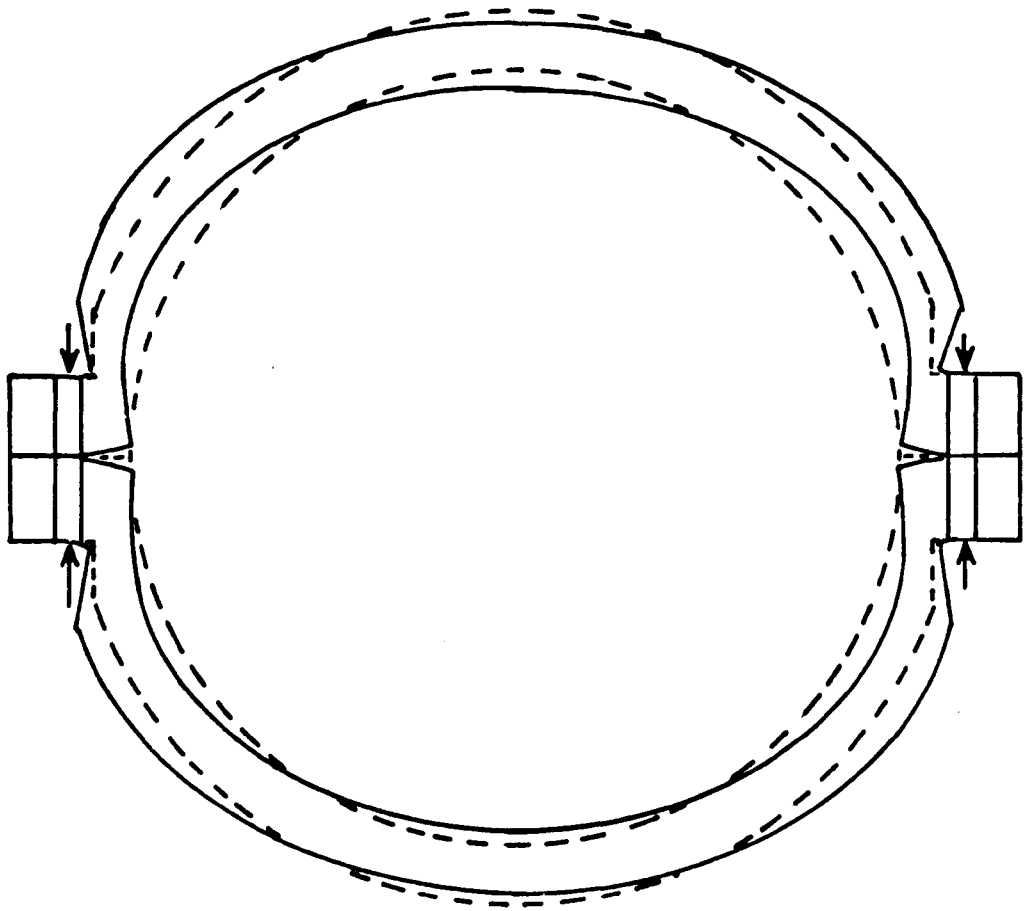

FIG. 7·6

FIG. 7·6 hoop bending in cylinder as flanges separate.

MODEL TEST 4 PRESSURE = 75 lbf/in FIG. 7·7

CASING No 2 (base)

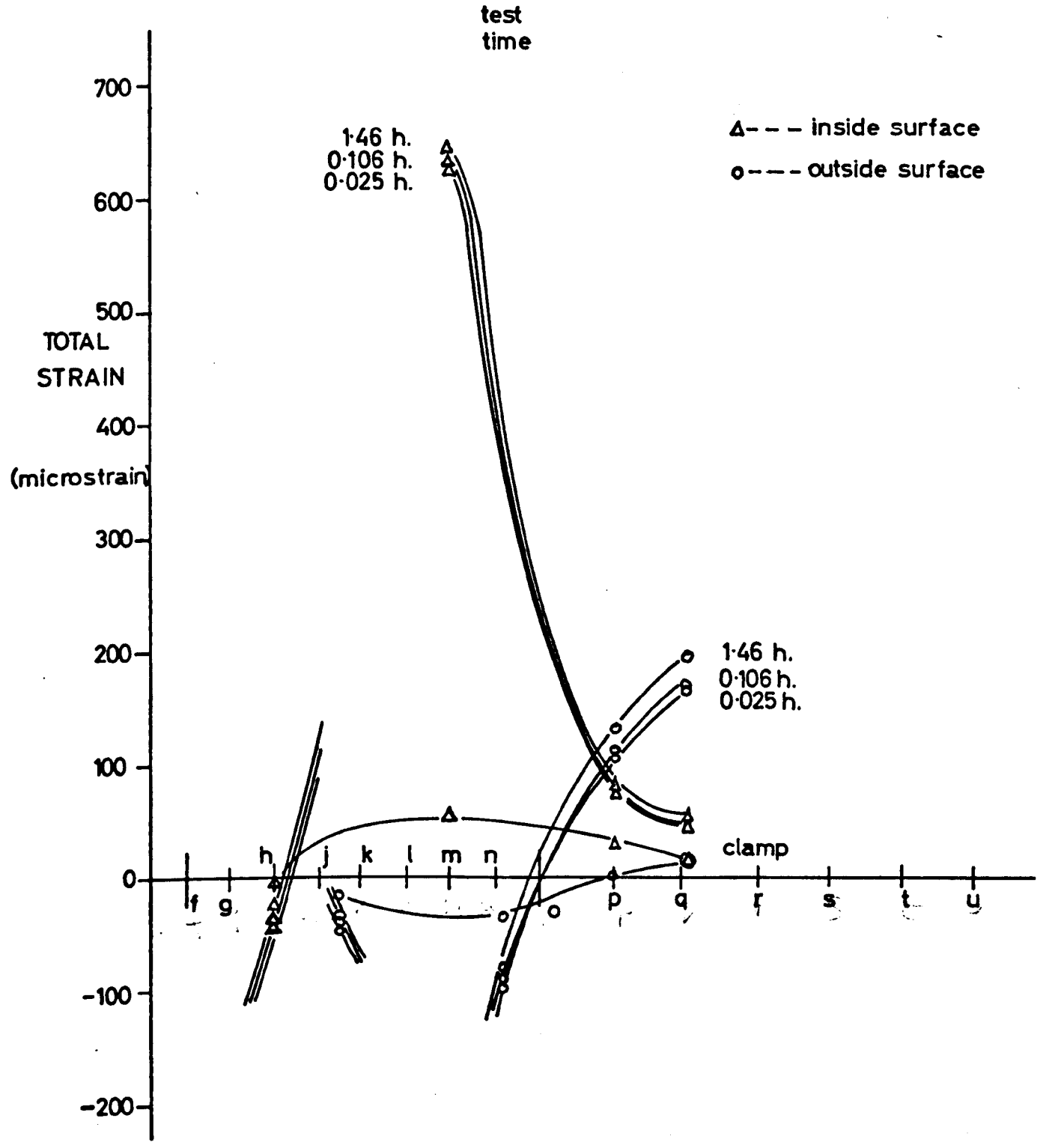

MERIDIONAL STRAIN DISTRIBUTION

$\theta = 0^{\circ}$ MERIDIONAL SECTION

MODEL TEST 5 PRESSURE = 55 lbf/in^2 FIG. 7·8

CASING No. 4 (base)

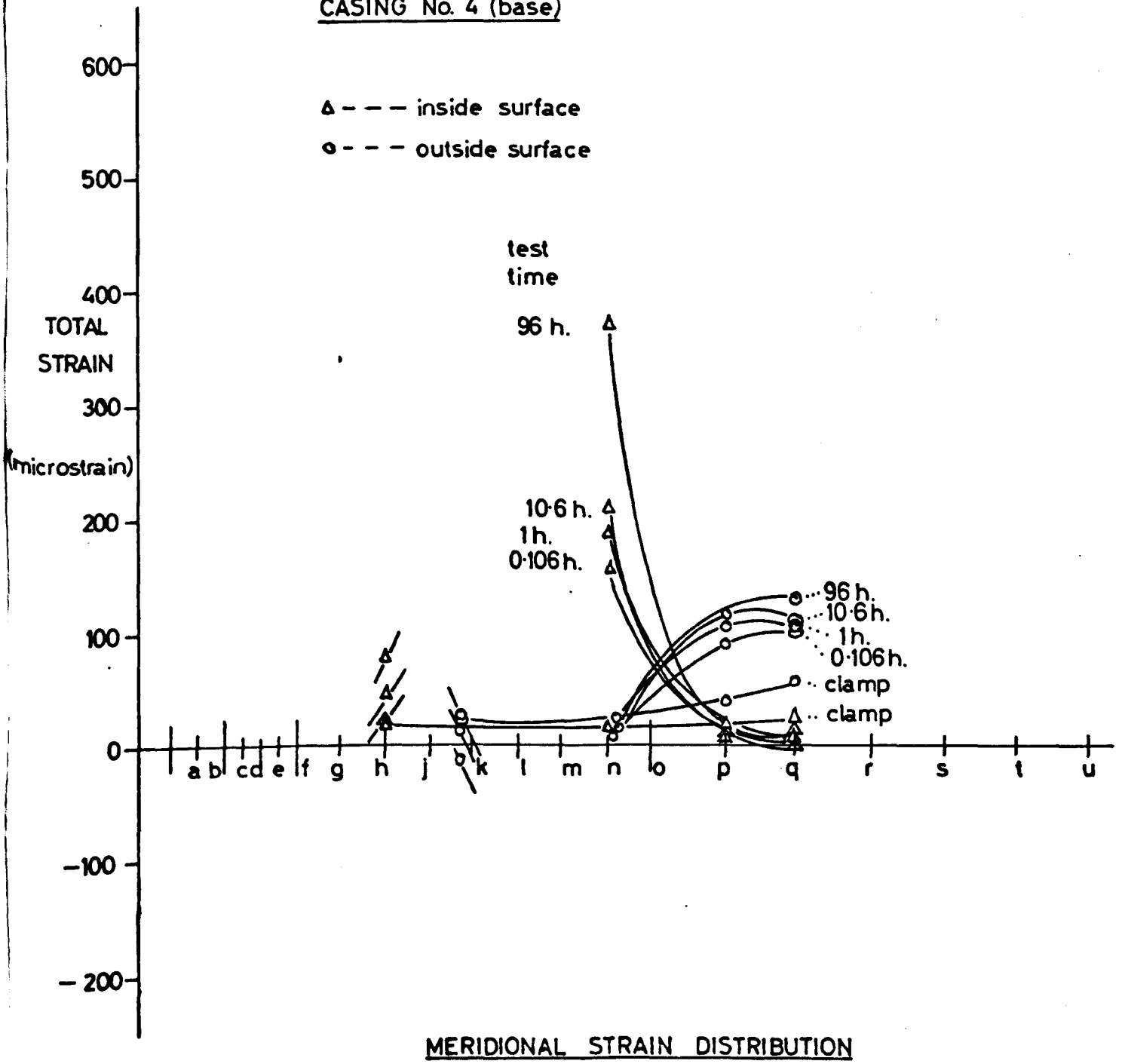

MERIDIONAL STRAIN DISTRIBUTION

$\theta = 0^{\circ}$ MERIDIONAL SECTION

MODEL TEST 6 PRESSURE = 30 lbf/in^2 FIG. 7·9

CASING No. 13 (base)

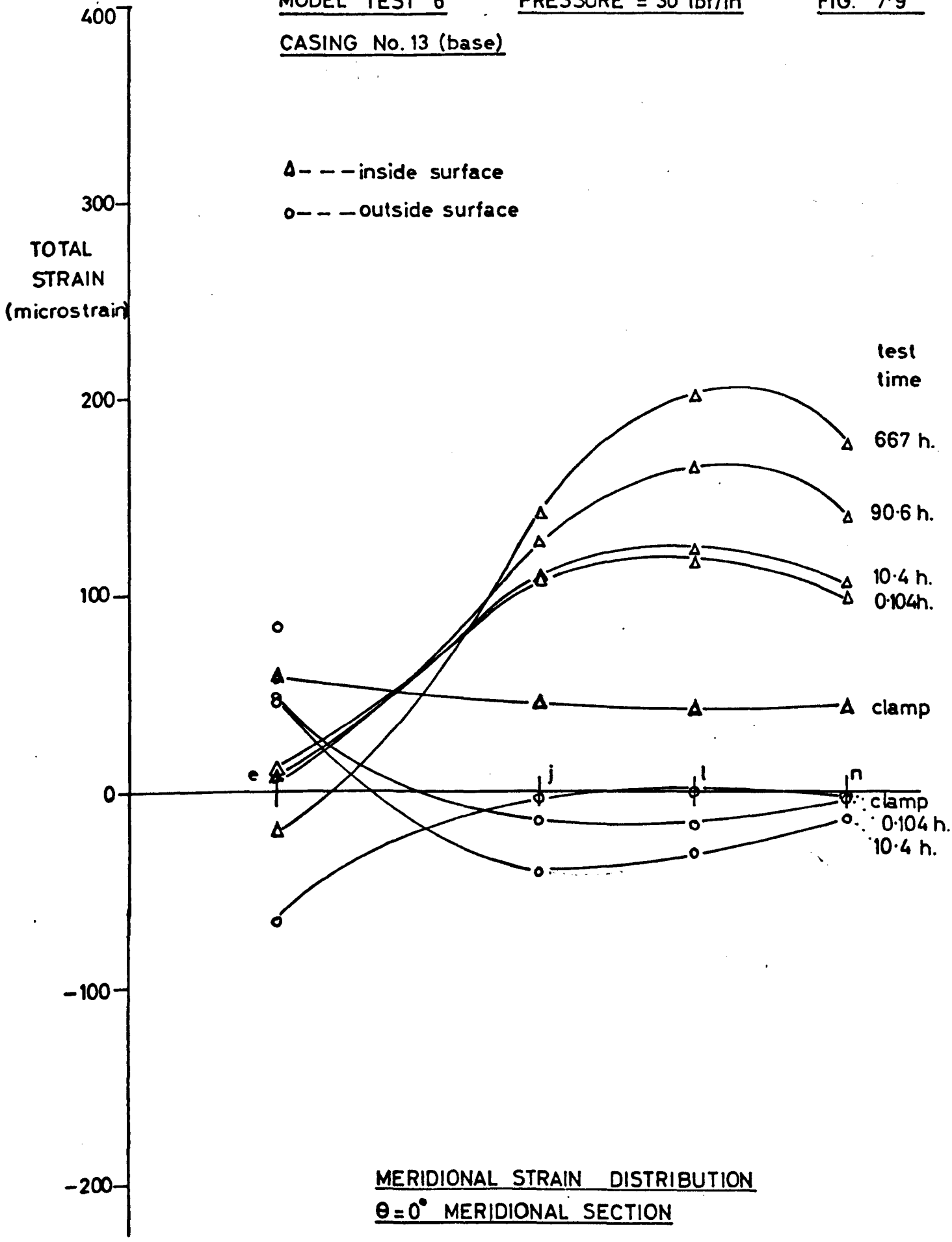

MERIDIONAL STRAIN DISTRIBUTION

$\theta = 0°$ MERIDIONAL SECTION

MODEL TEST 6 PRESSURE = 30 lbf/in² FIG. 7·10

CASING No. 13 (base)

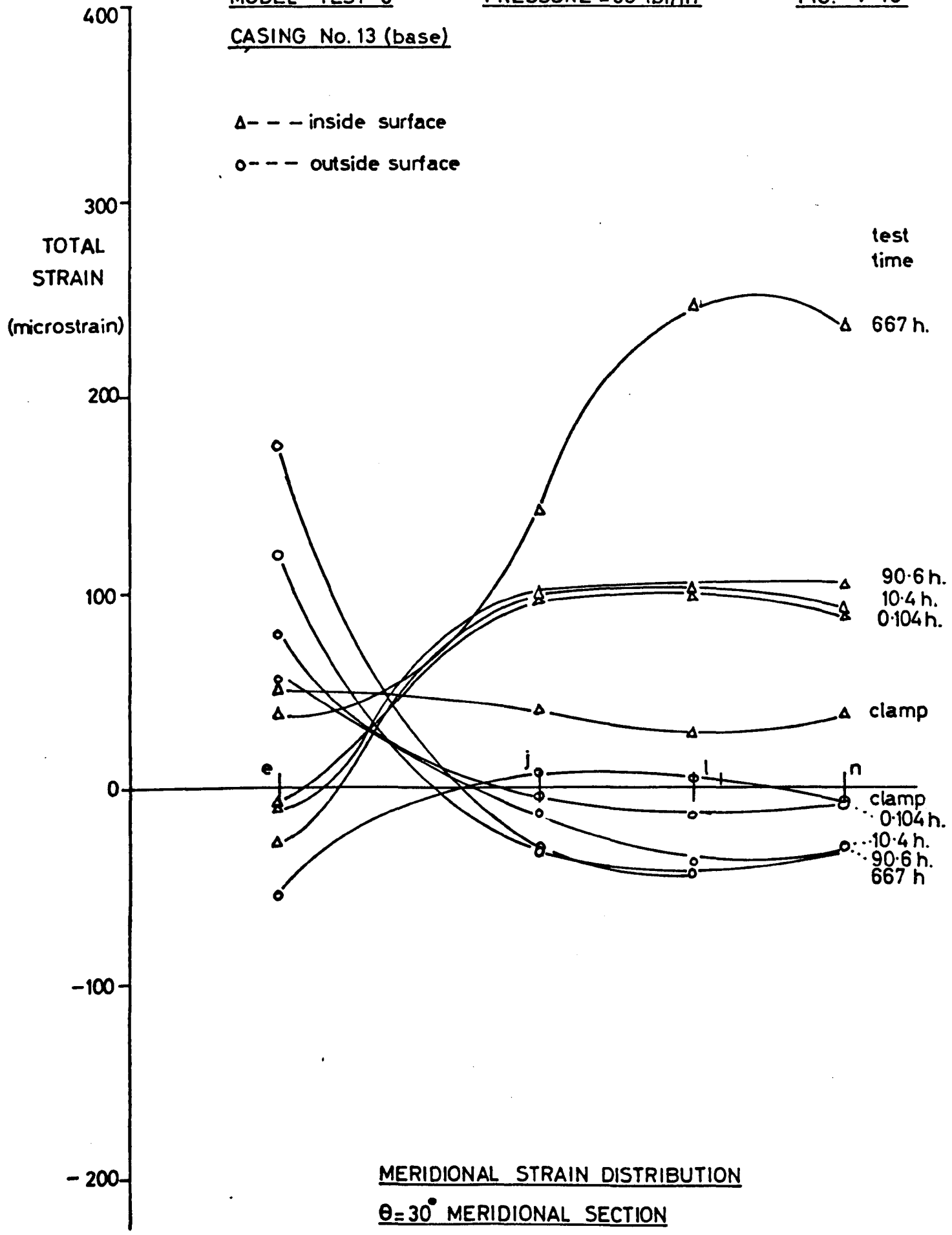

MERIDIONAL STRAIN DISTRIBUTION

$\theta = 30^{\circ}$ MERIDIONAL SECTION

MODEL TEST 6 PRESSURE = 30 lbf/in^2 FIG. 7·11

CASING No. 13 (base)

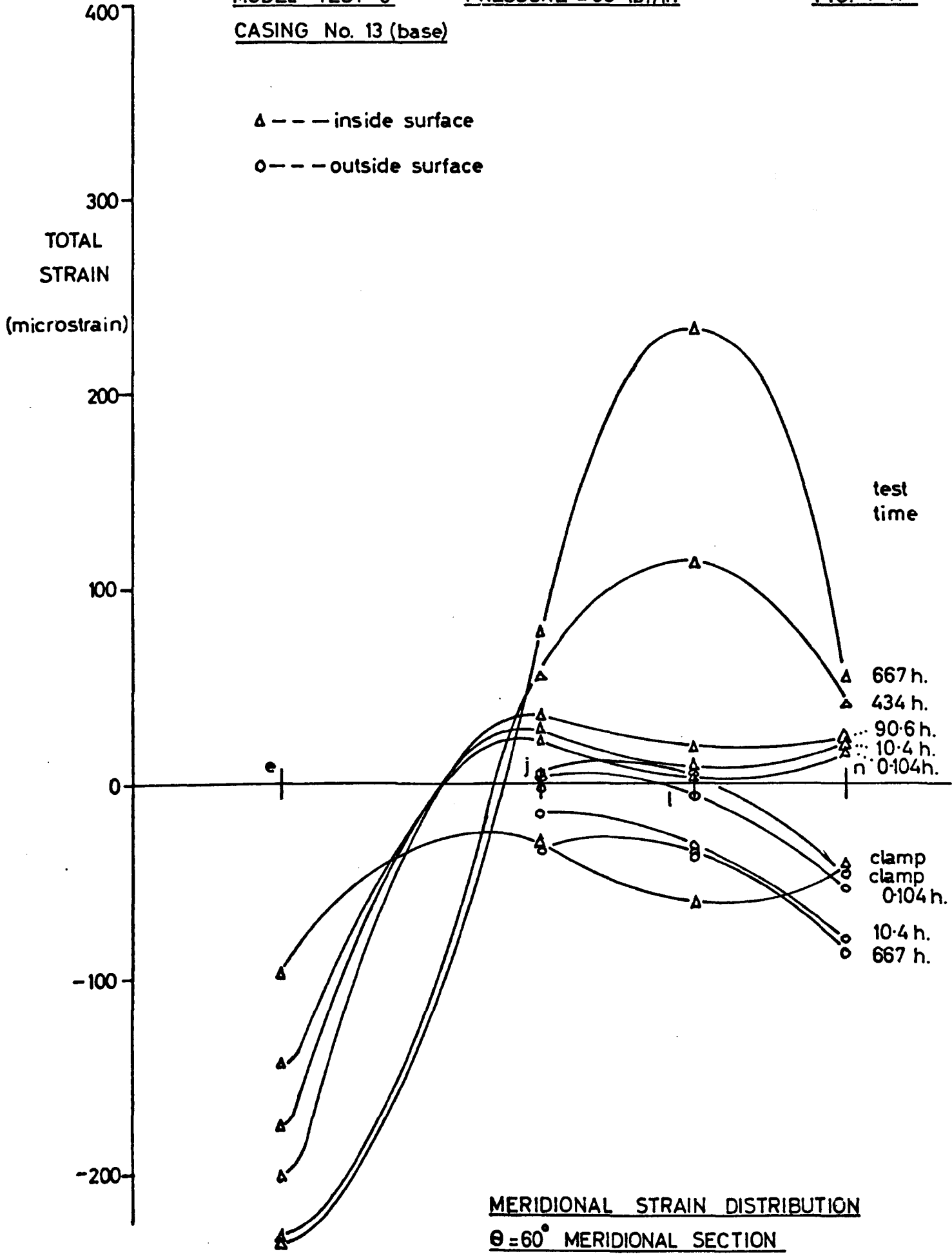

MERIDIONAL STRAIN DISTRIBUTION

$\theta = 60^\circ$ MERIDIONAL SECTION

MODEL TEST 6 PRESSURE = 30 lbf/in² FIG. 7·12

CASING No. 14 (top)

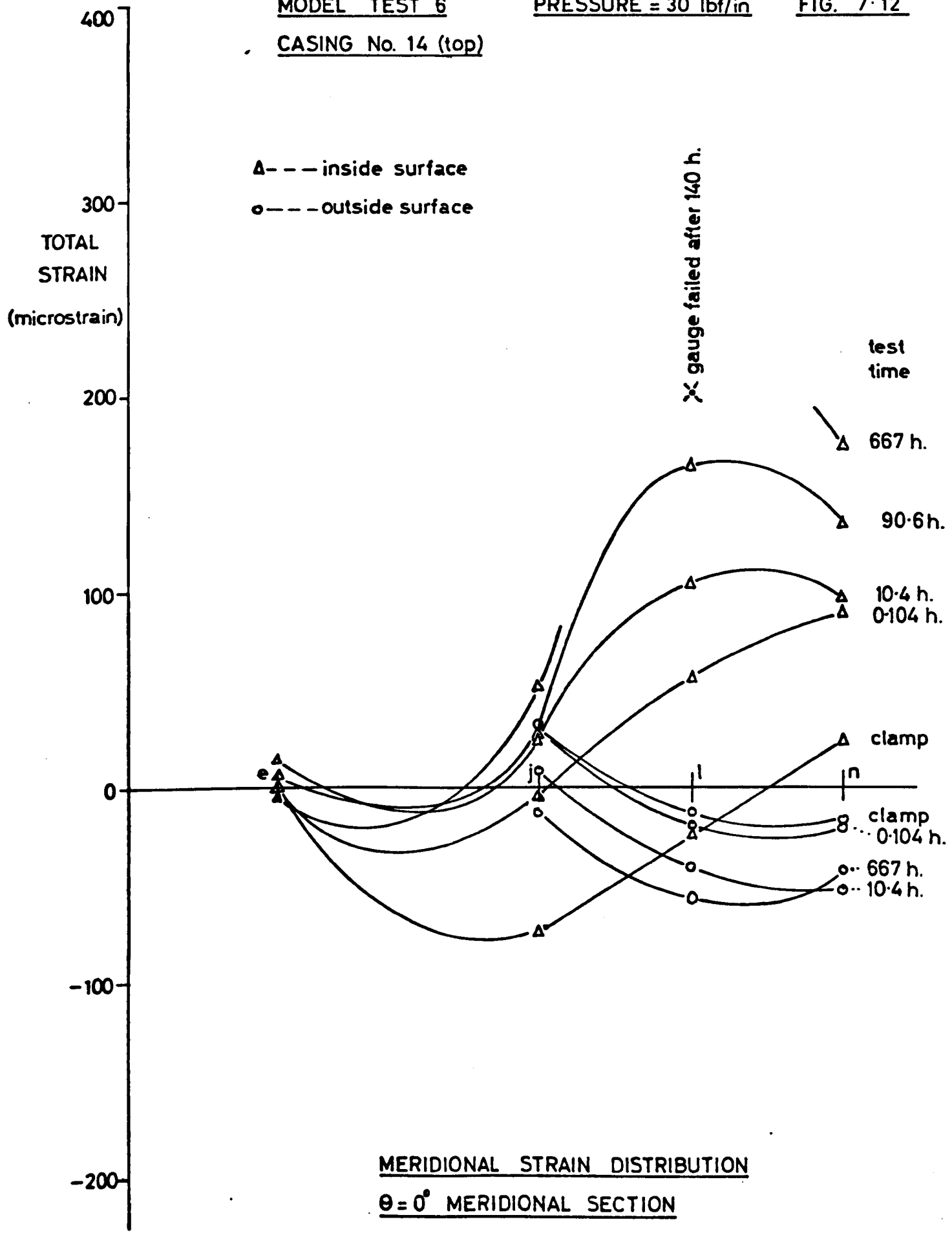

MERIDIONAL STRAIN DISTRIBUTION

$\theta = 0^\circ$ MERIDIONAL SECTION

MODEL TEST 6 PRESSURE = 30 lbf/in FIG. 7·13

CASING No.14 (top)

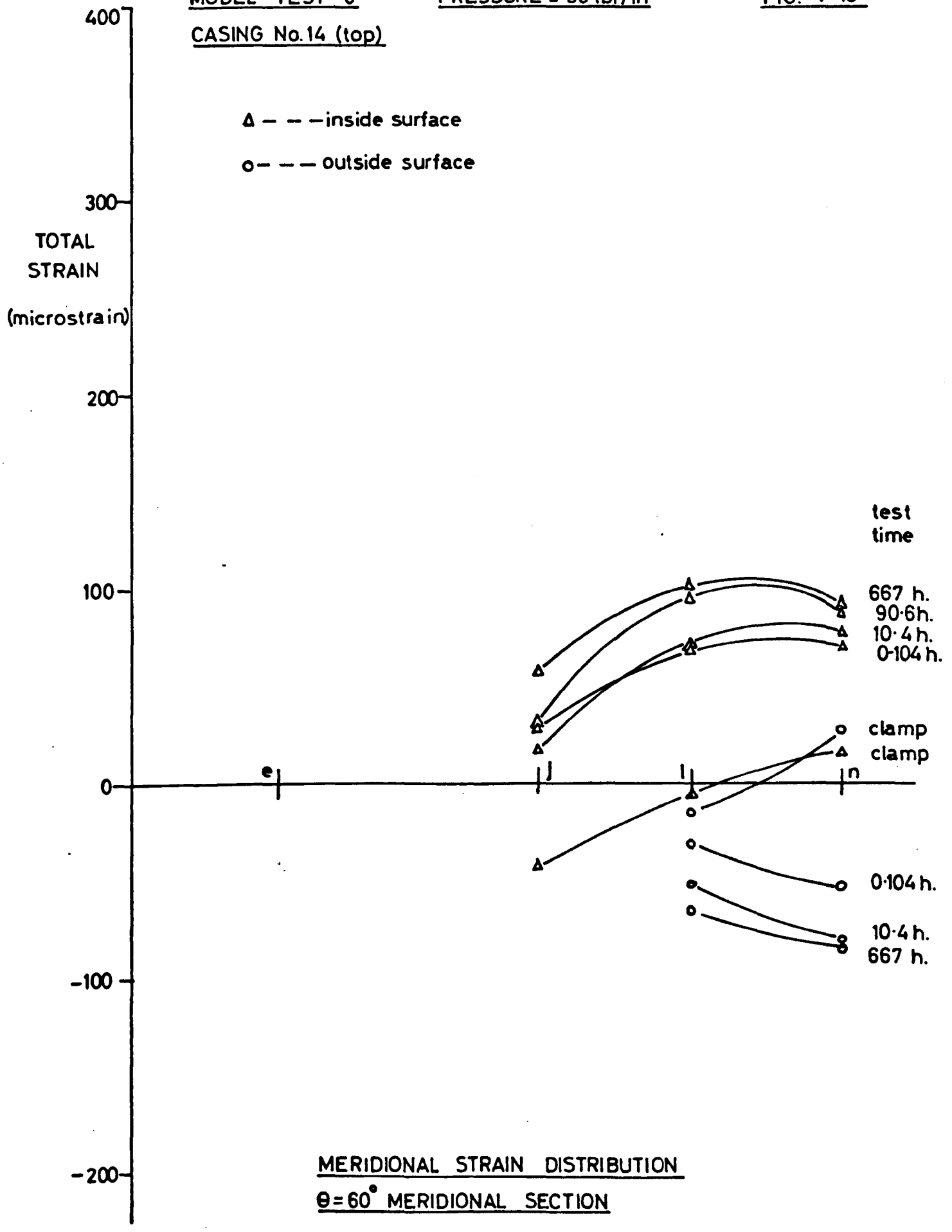

MERIDIONAL STRAIN DISTRIBUTION

$\theta = 60^{\circ}$ MERIDIONAL SECTION

MODEL TEST 7 PRESSURE = 45 lbf/in² FIG. 7·14

CASING. No. 9 (base)

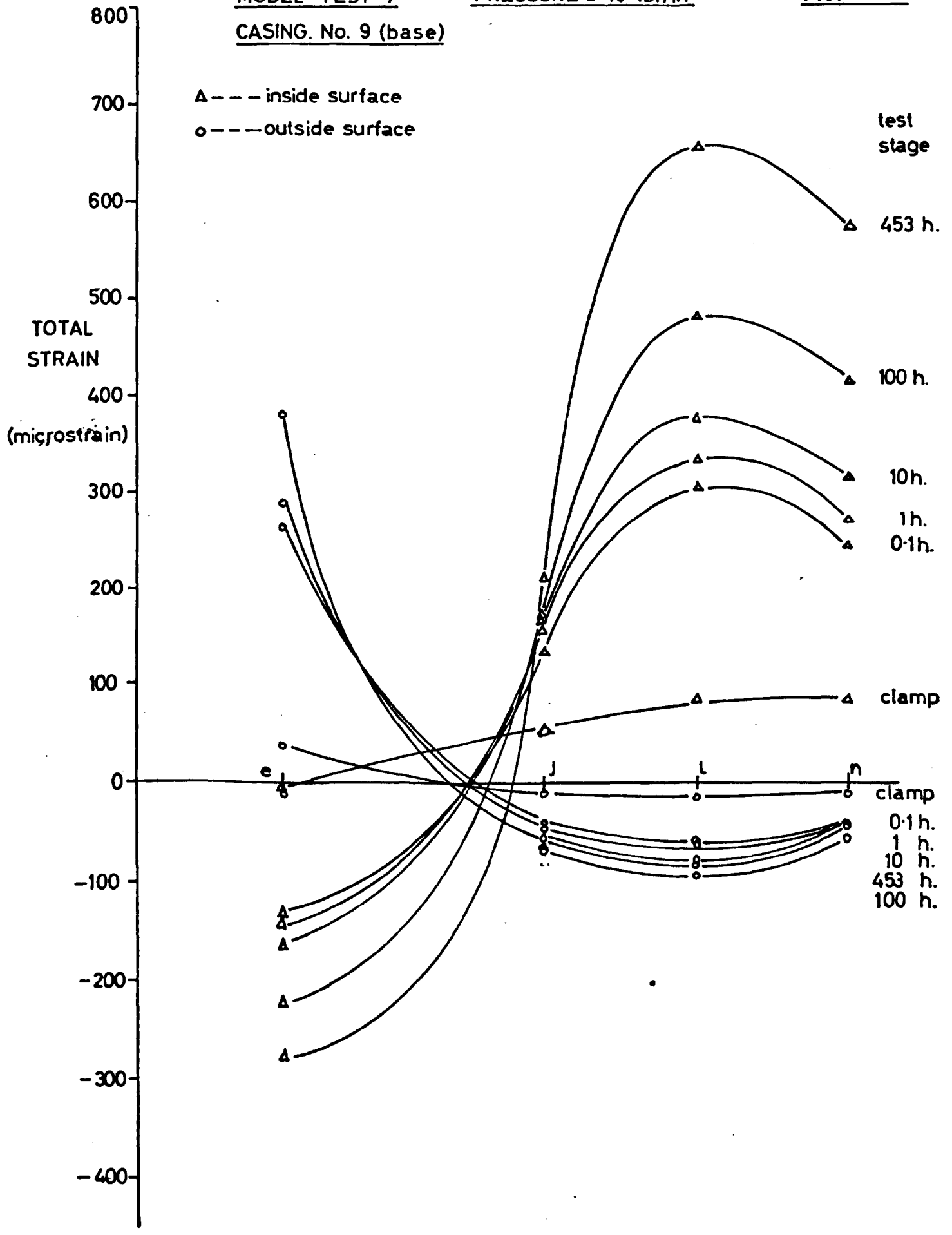

MERIDIONAL STRAIN DISTRIBUTION

$\theta = 0^{\circ}$ MERIDIONAL SECTION

MODEL TEST 7 PRESSURE = 45 lbf/in² FIG. 7·15

CASING No. 9 (base)

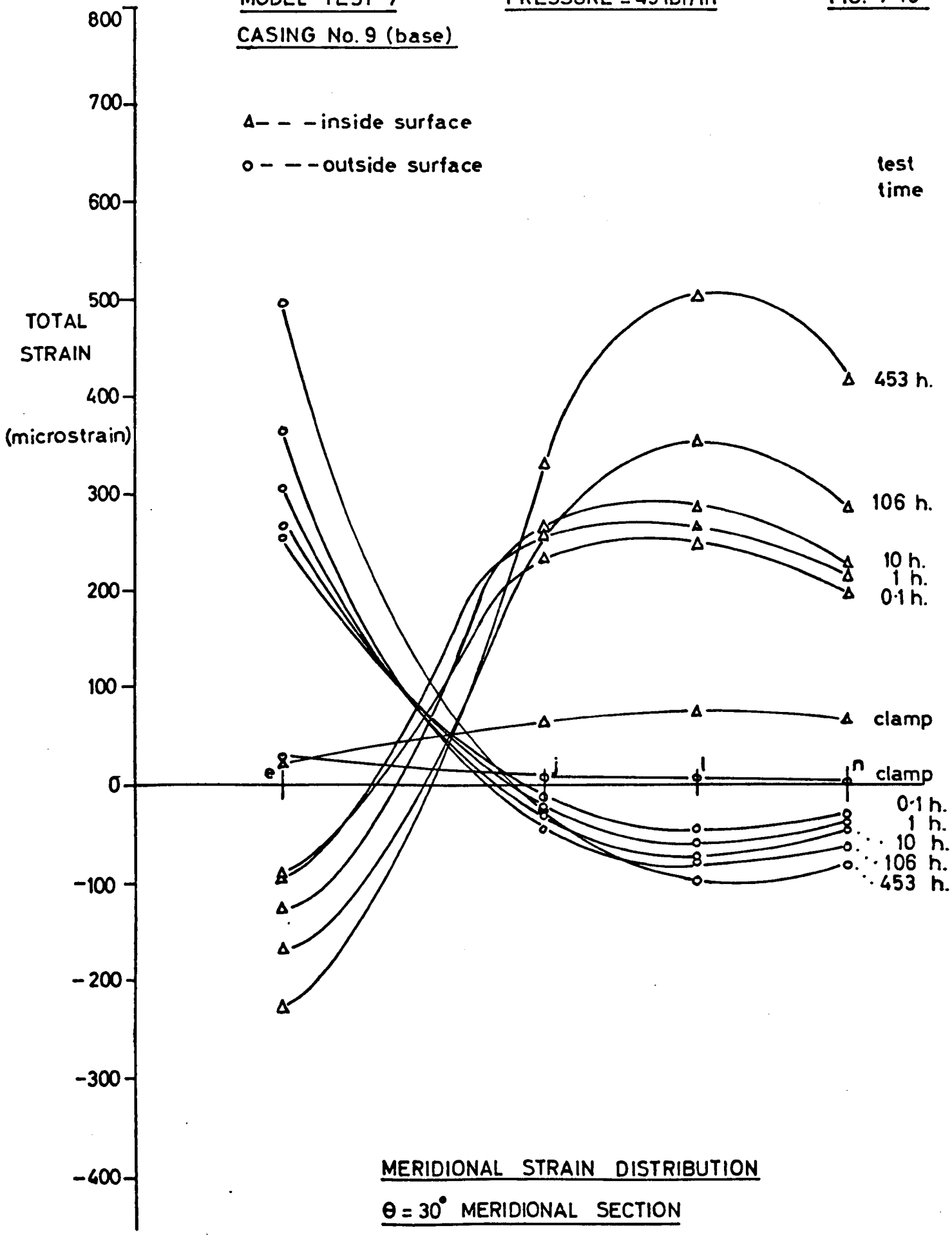

MERIDIONAL STRAIN DISTRIBUTION

$\theta = 30^{\circ}$ MERIDIONAL SECTION

MODEL TEST 7 PRESSURE = 45 lbf/in^2 FIG. 7·16

CASING No. 9 (base)

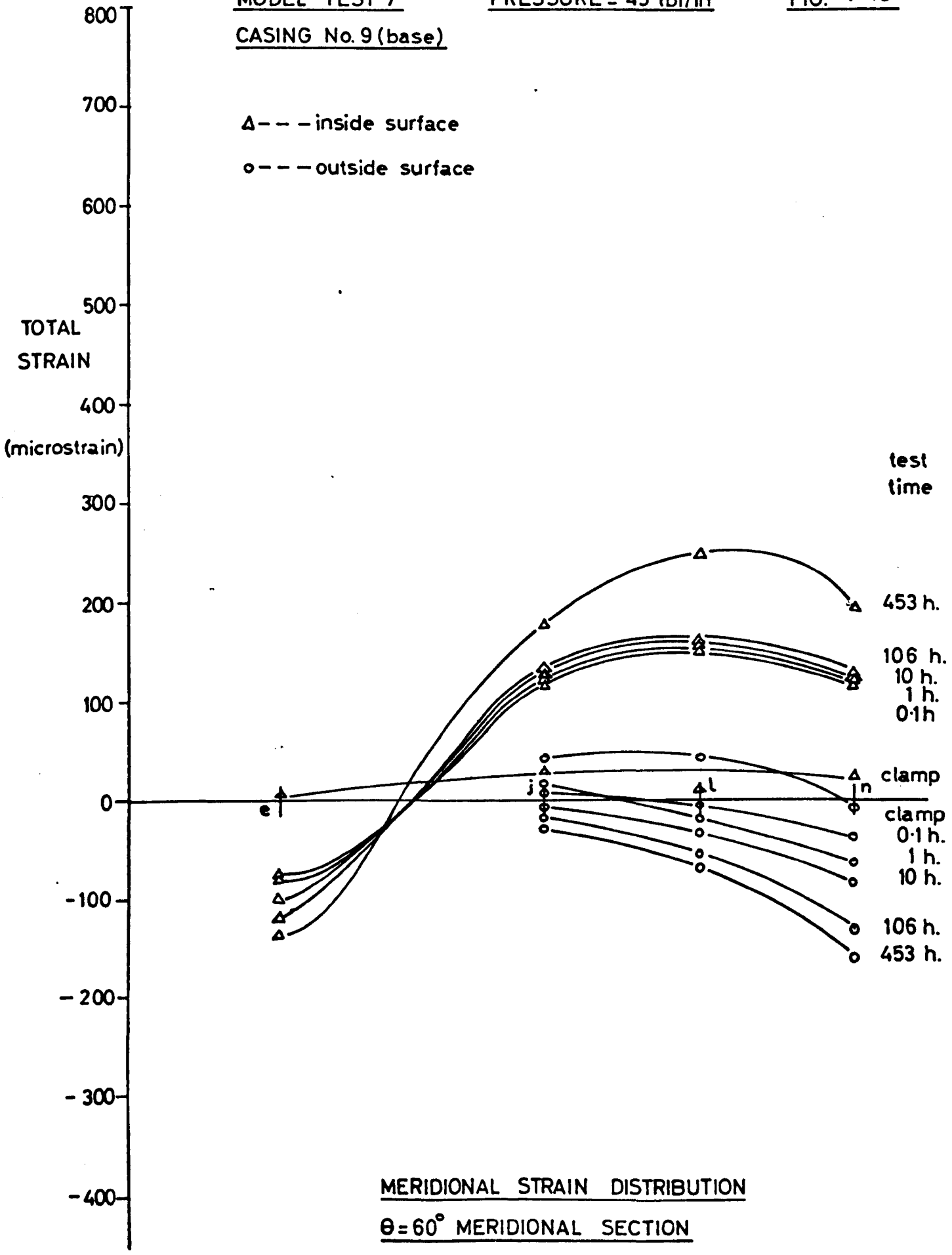

MERIDIONAL STRAIN DISTRIBUTION

$\theta = 60^\circ$ MERIDIONAL SECTION

MODEL TEST 7 PRESSURE = 45 lbf/in^2 FIG. 7·17

CASING. No.10 (top)

Δ— — —inside surface

o— — —outside surface

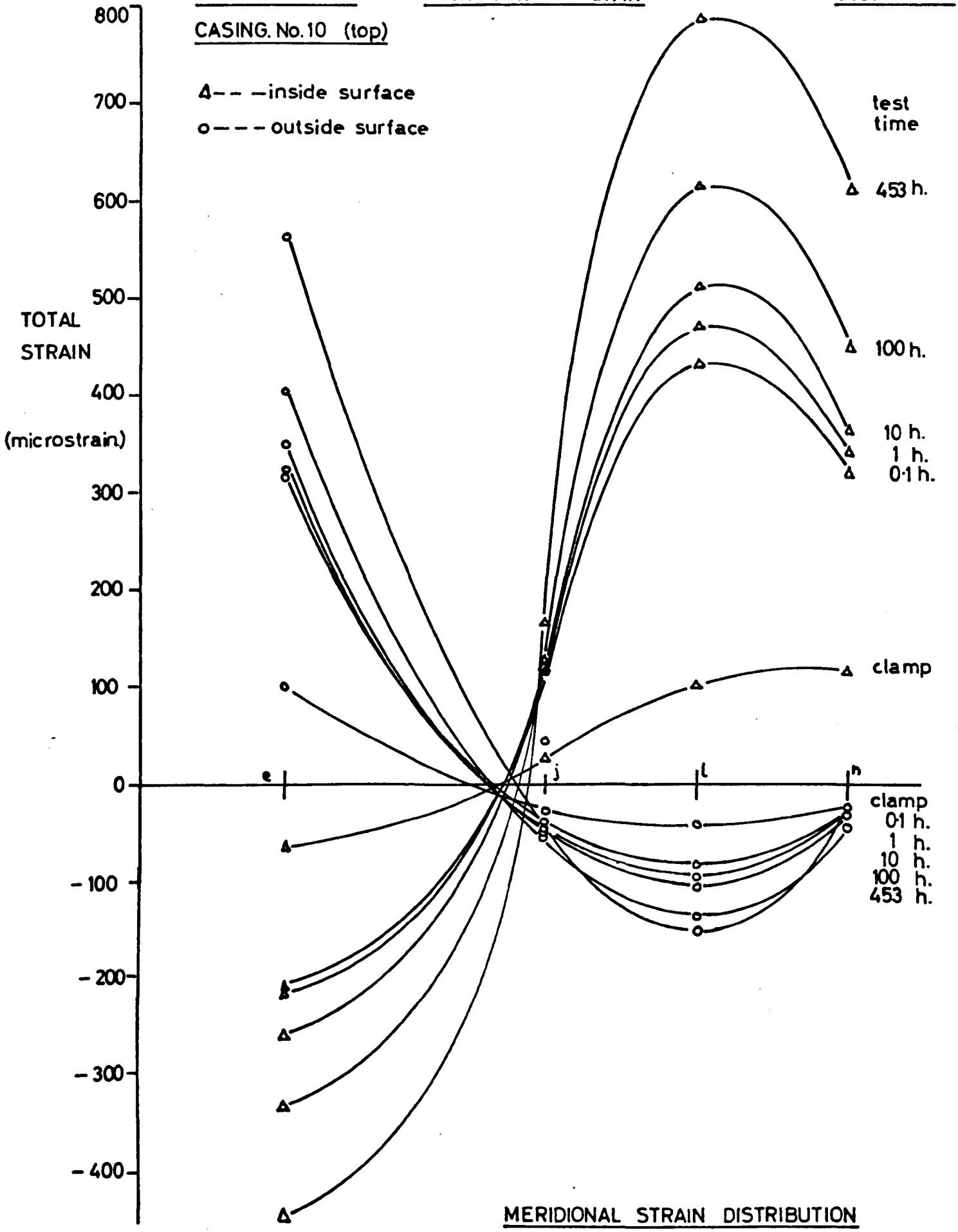

MERIDIONAL STRAIN DISTRIBUTION

$\theta = 0^\circ$ MERIDIONAL SECTION

MODEL TEST 7 PRESSURE = 45 lbf/in² FIG. 7·18

CASING No. 10 (top)

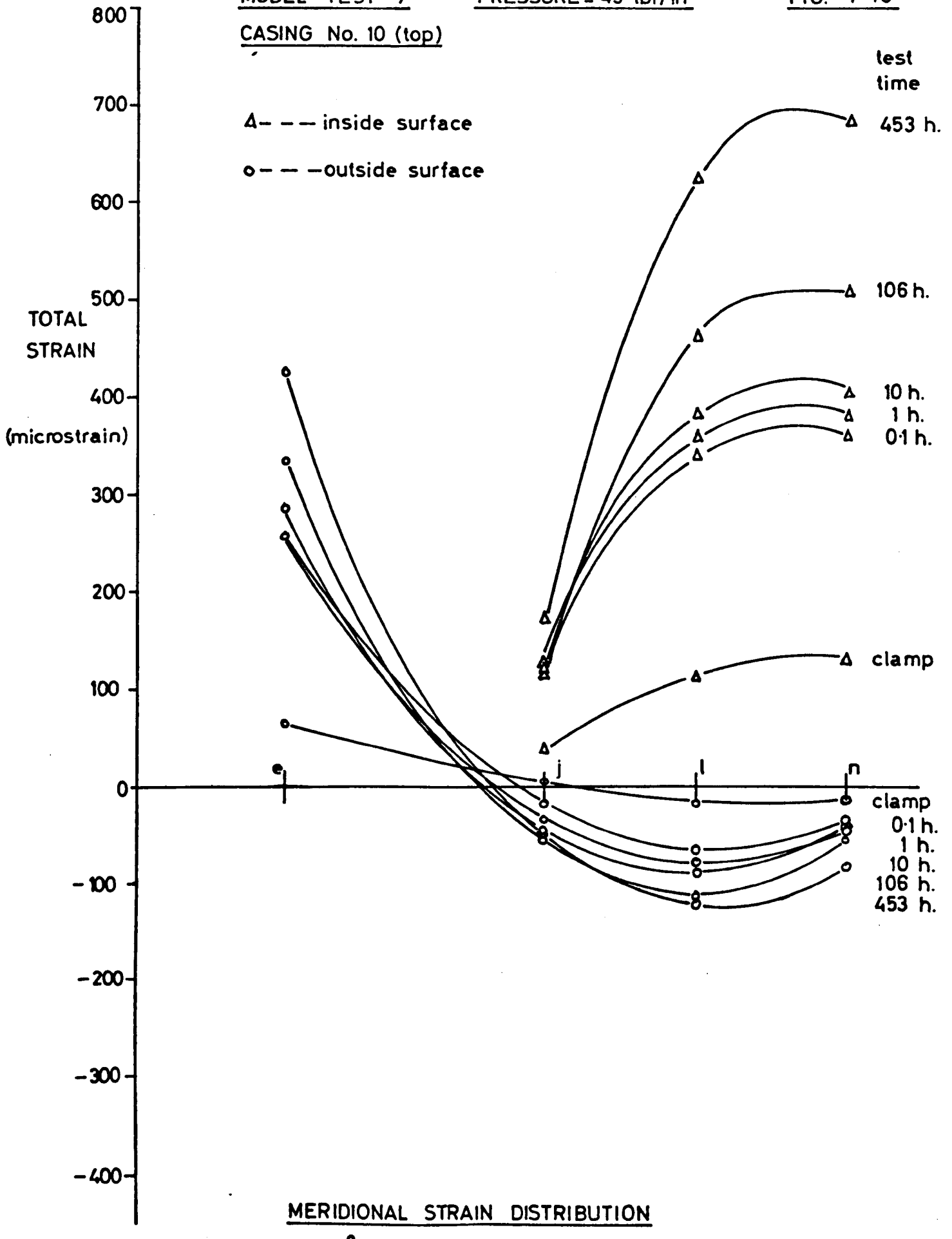

MERIDIONAL STRAIN DISTRIBUTION

$\theta = 30^{\circ}$ MERIDIONAL SECTION

MODEL TEST 7 PRESSURE = 45 lbf/in^2 FIG. 7·19

CASING. No. 10 (top)

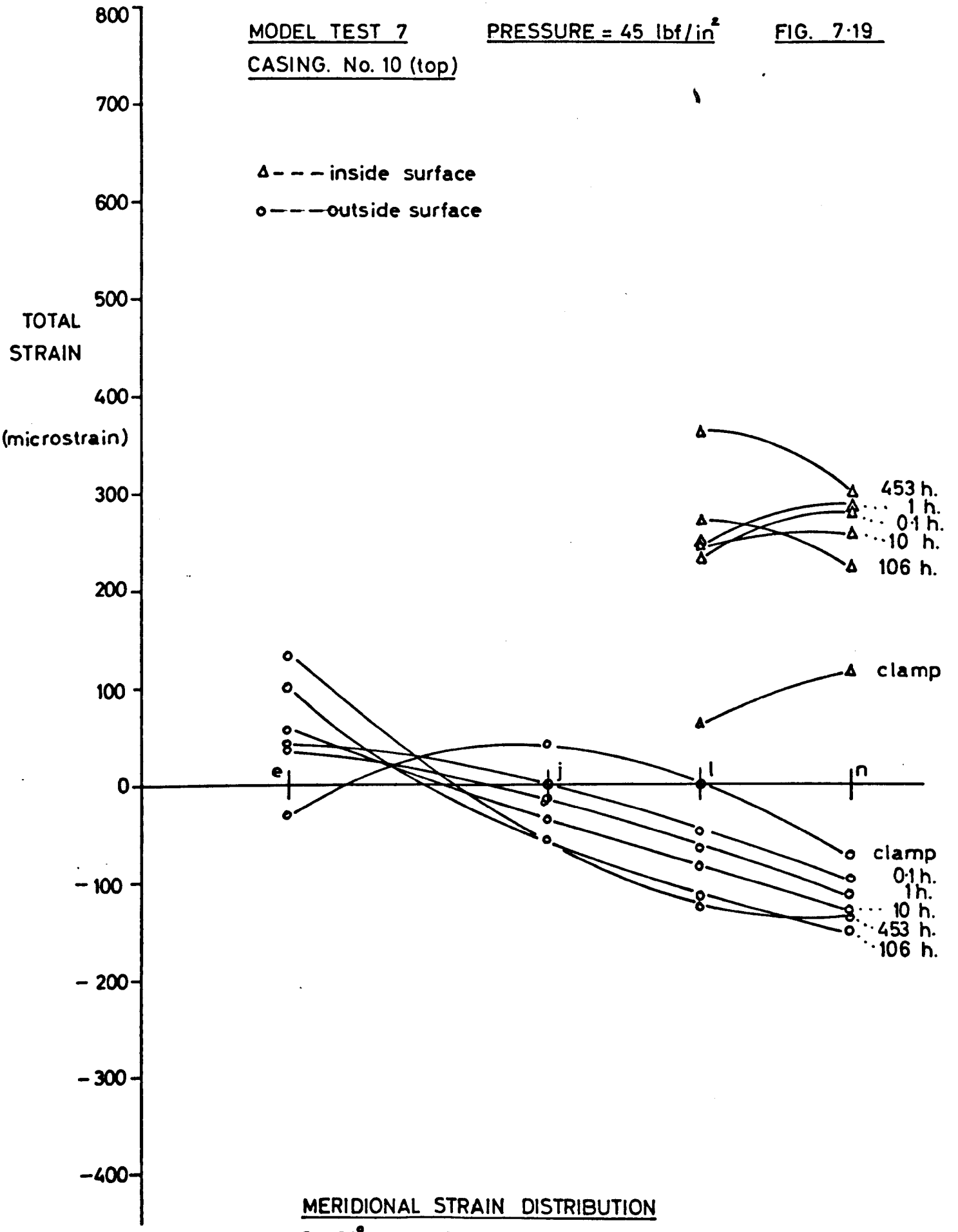

MERIDIONAL STRAIN DISTRIBUTION

$\theta = 60^\circ$ MERIDIONAL SECTION

MODEL TEST 8 PRESSURE = 55 lbf/in^2 FIG. 7·20

CASING No. 19 (base)

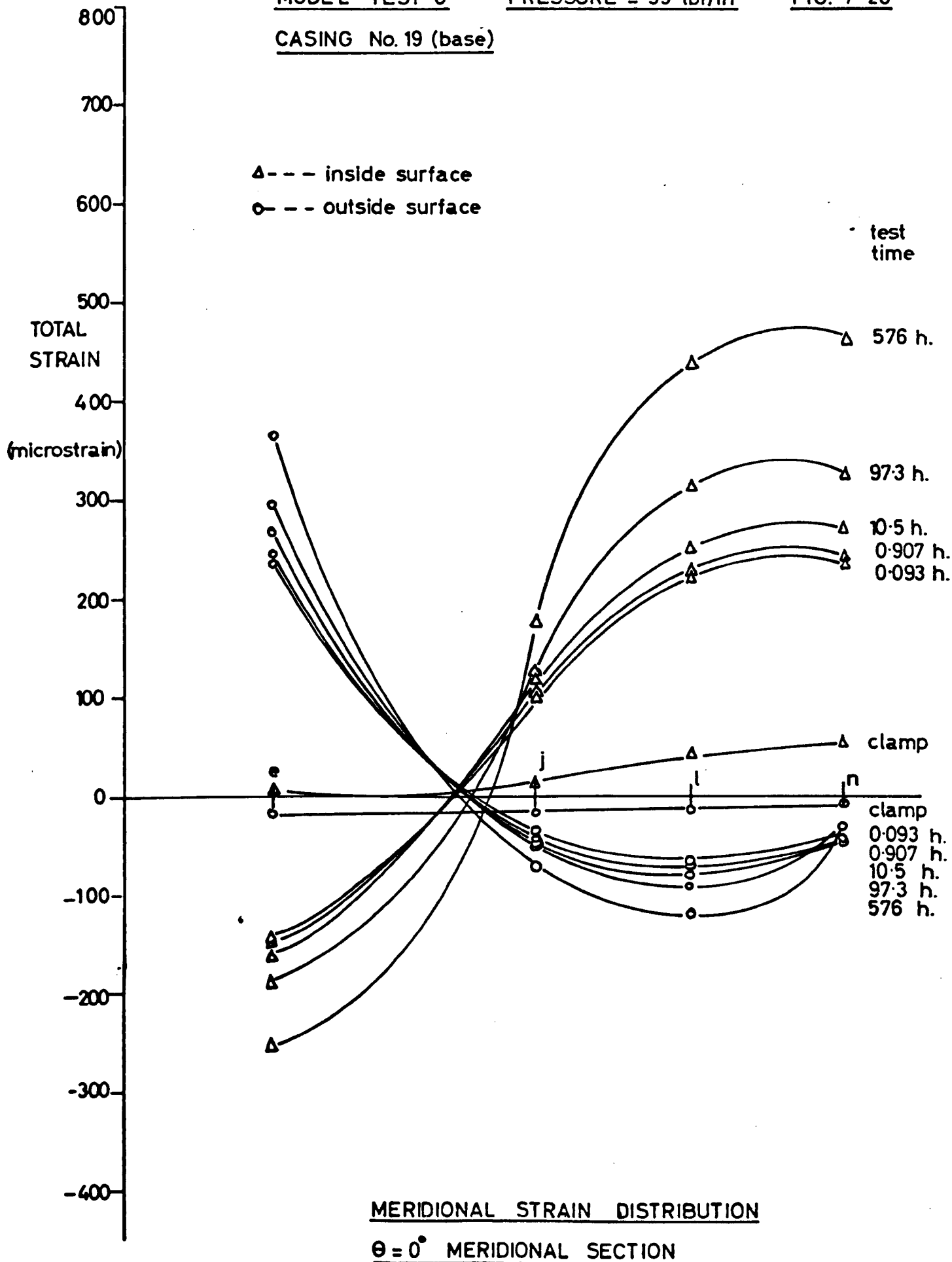

MERIDIONAL STRAIN DISTRIBUTION

$\theta = 0^\circ$ MERIDIONAL SECTION

MODEL TEST 8 PRESSURE = 55 lbf/in² FIG. 7·21

CASING No. 19 (base)

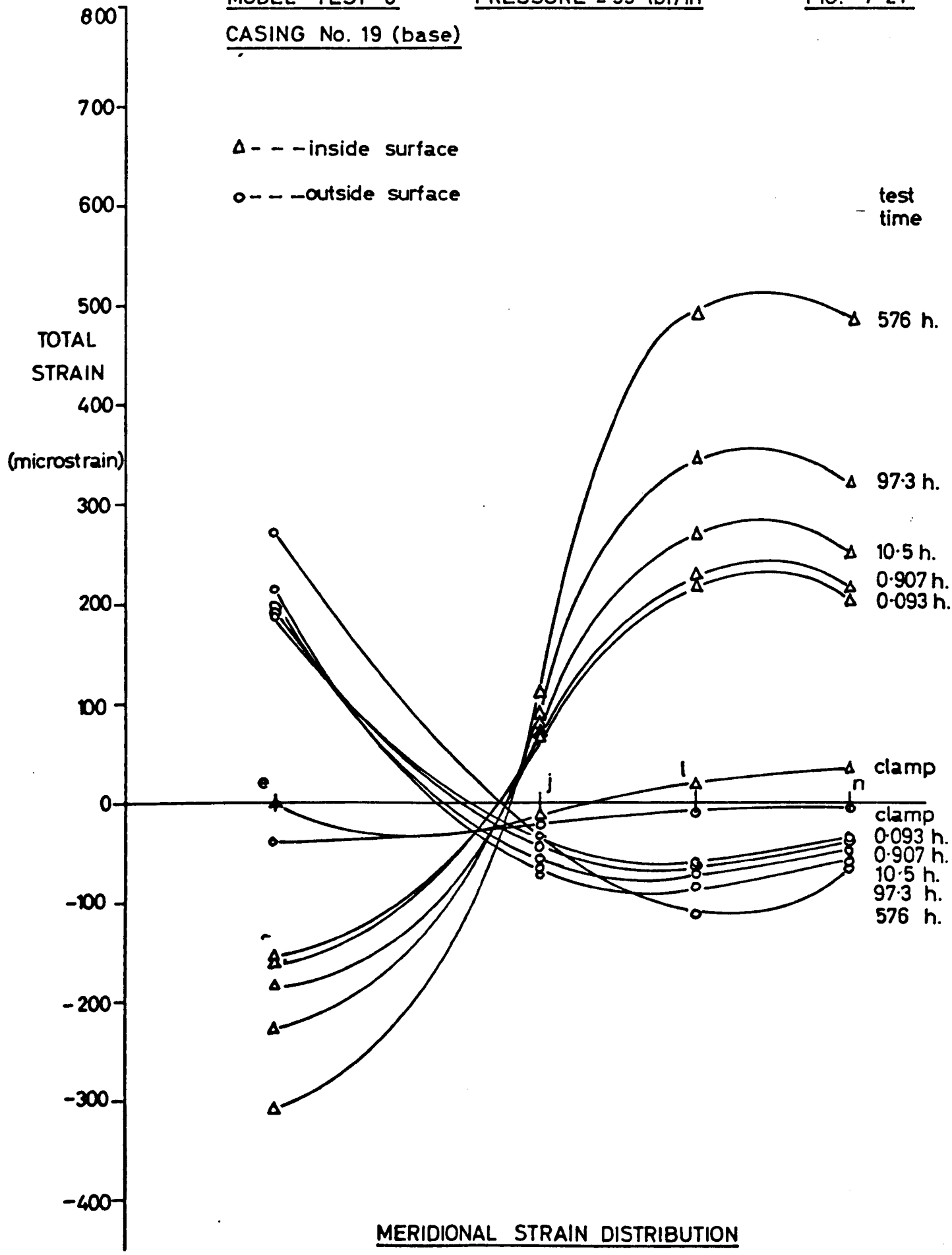

MERIDIONAL STRAIN DISTRIBUTION

$\theta = 30^{\circ}$ MERIDIONAL SECTION

MODEL TEST 8 PRESSURE = 55 lbf/in FIG. 7·22

CASING No. 19 (base)

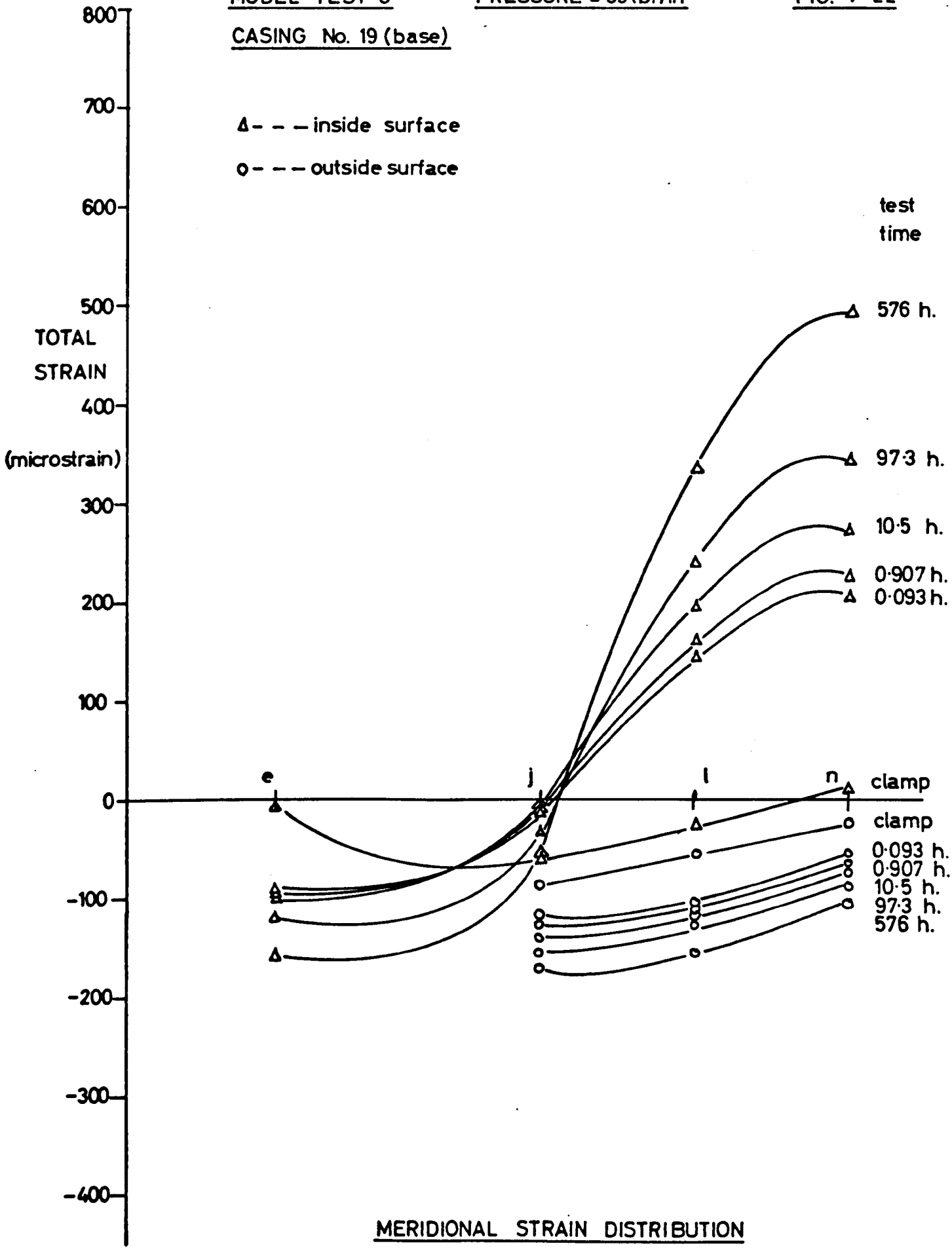

MERIDIONAL STRAIN DISTRIBUTION

$\theta = 60^{\circ}$ MERIDIONAL SECTION

MODEL TEST 8 PRESSURE = 55 lbf/in FIG. 7·23

CASING No. 17 (top)

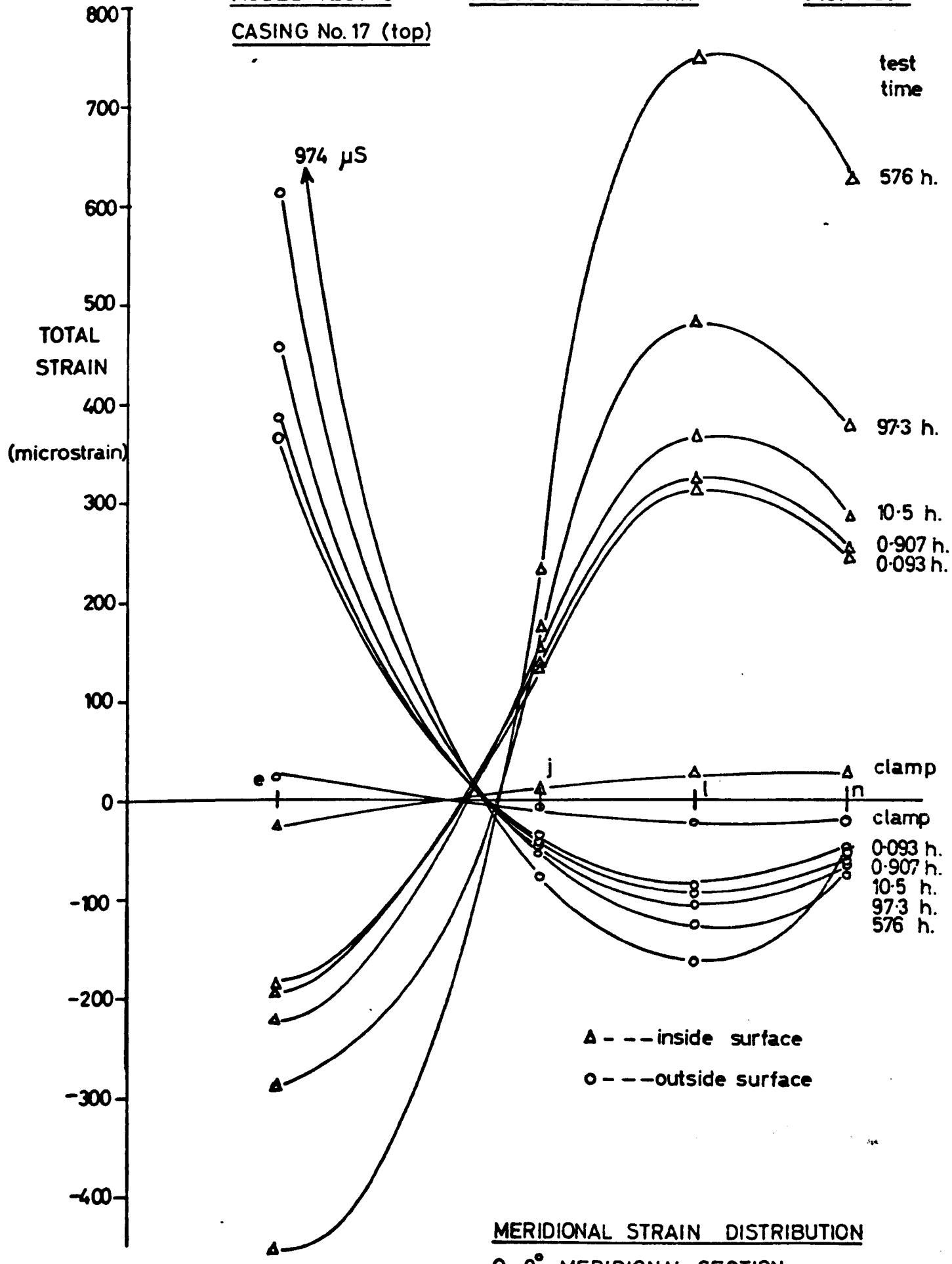

MERIDIONAL STRAIN DISTRIBUTION

θ = 0° MERIDIONAL SECTION

MODEL TEST 8 PRESSURE=55 lbf/in

CASING No.17 (top)

FIG. 7·24

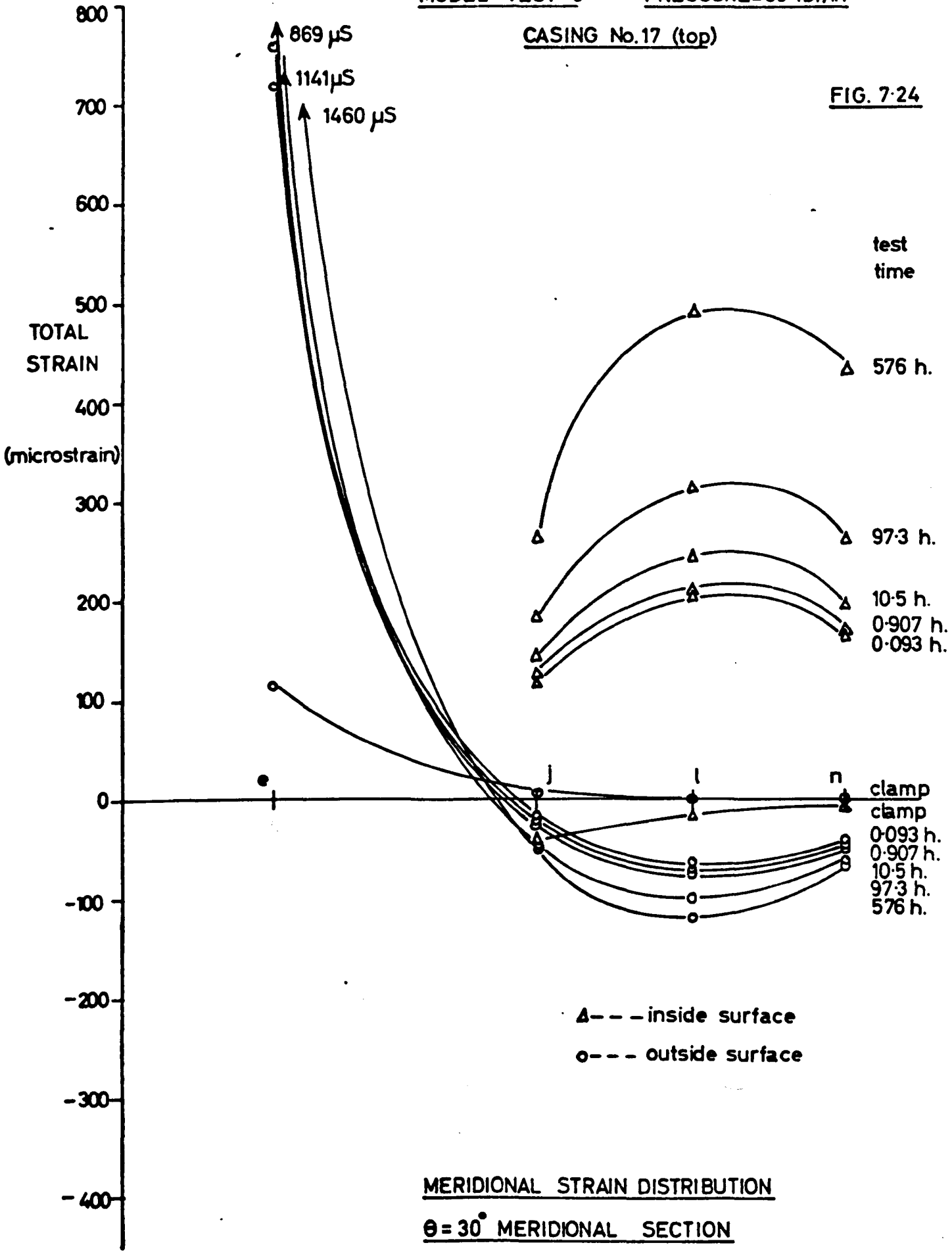

MERIDIONAL STRAIN DISTRIBUTION

$\theta = 30^{\circ}$ MERIDIONAL SECTION

MODEL TEST 8 PRESSURE = 55 lbf/in FIG. 7·25

CASING No. 17 (top)

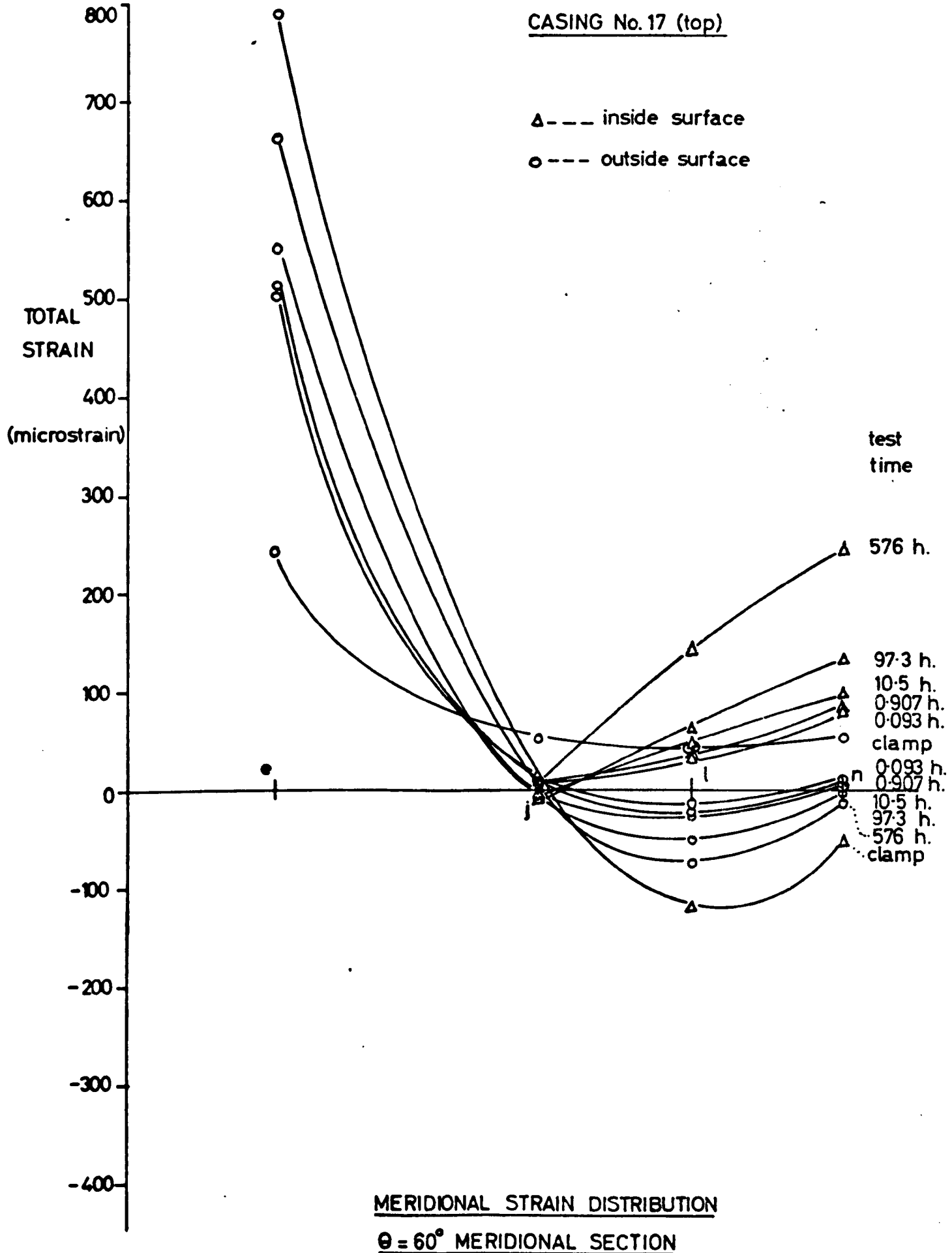

MERIDIONAL STRAIN DISTRIBUTION

$\theta = 60°$ MERIDIONAL SECTION

MODEL TEST 9 PRESSURE = 35 lbf/in FIG. 7·26

CASING No. 15 (base)

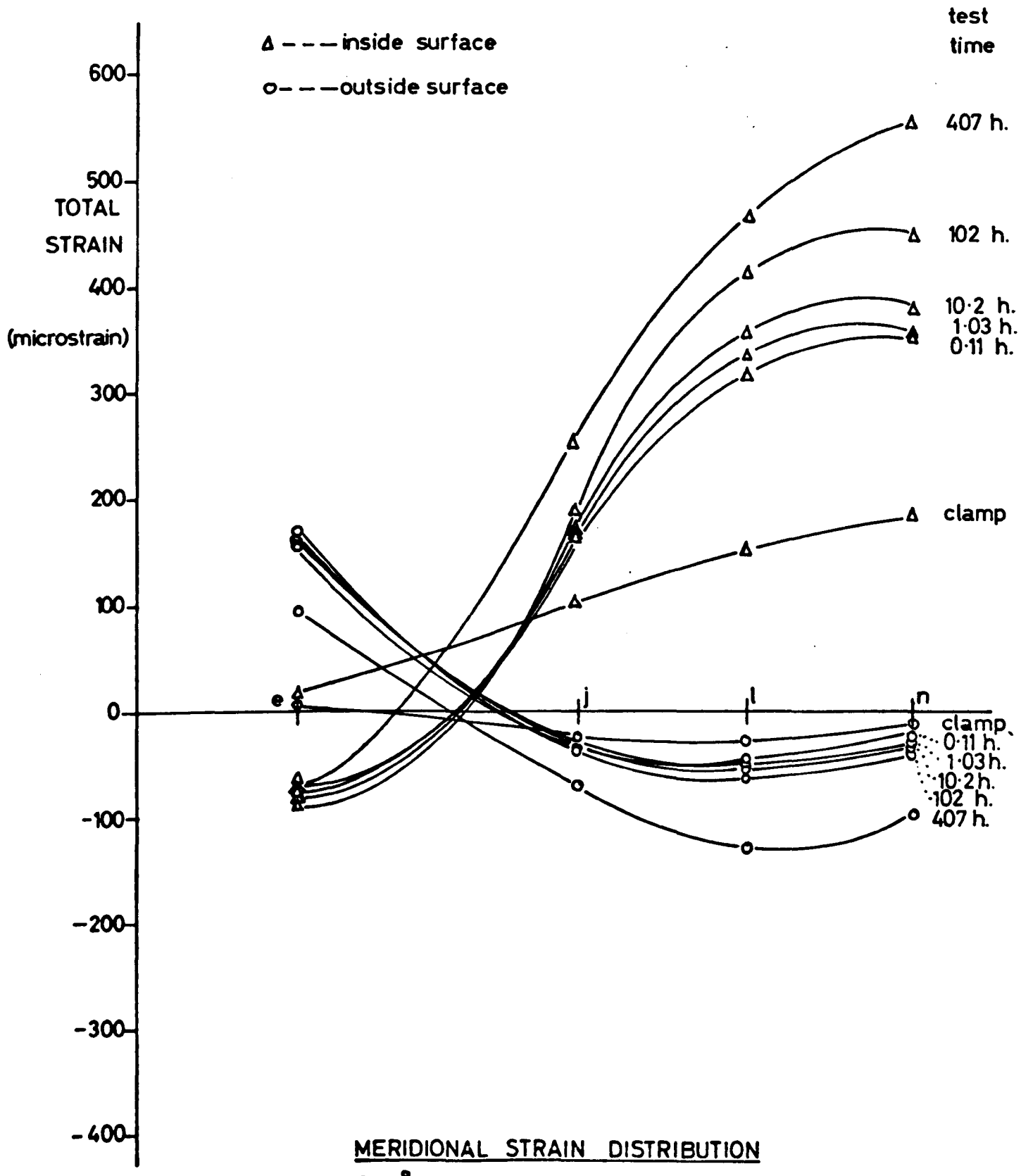

MERIDIONAL STRAIN DISTRIBUTION

$\theta = 0^{\circ}$ MERIDIONAL SECTION

MODEL TEST 9 PRESSURE = 35 lbf/in FIG. 7·27

CASING No. 15 (base)

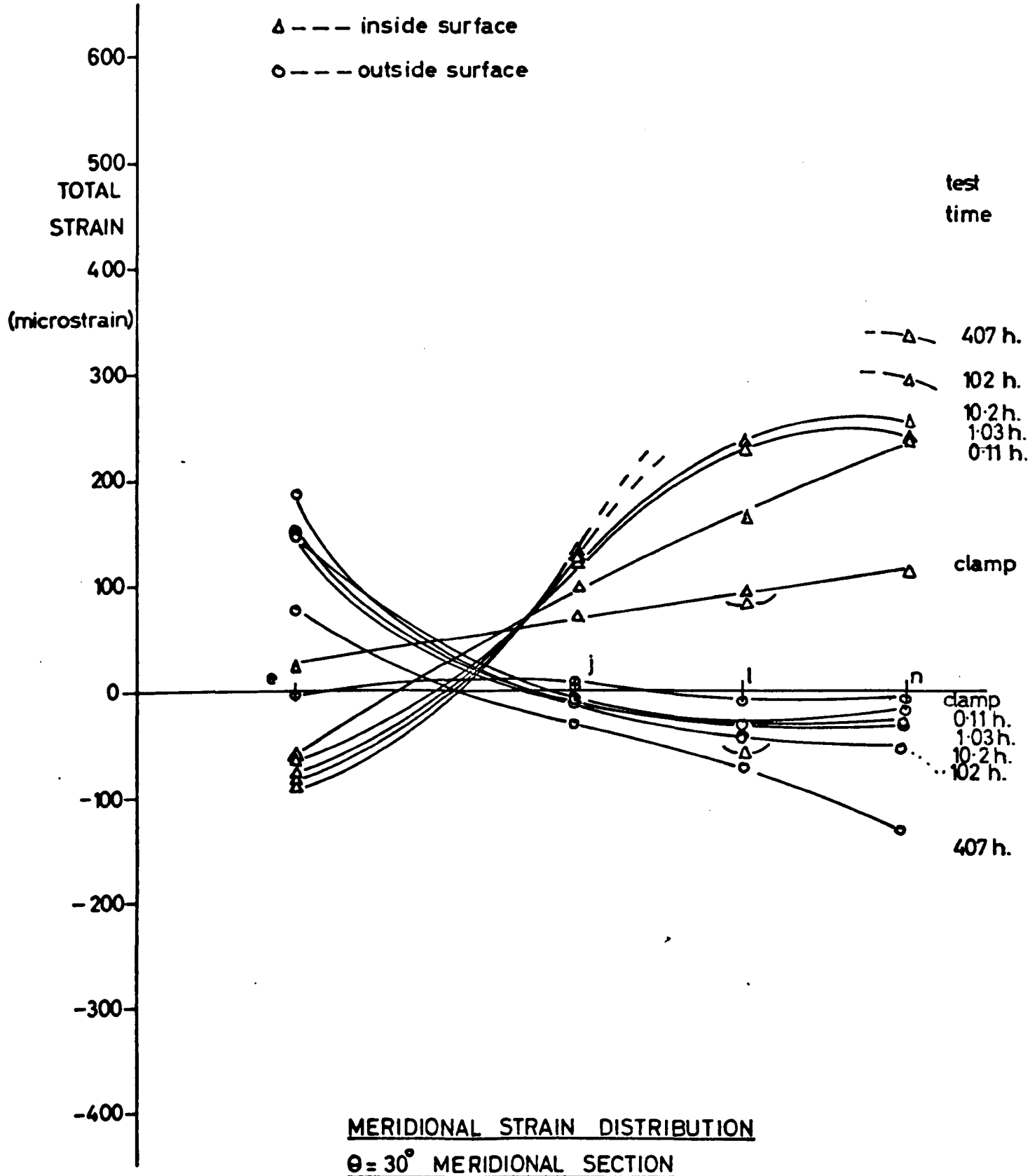

MERIDIONAL STRAIN DISTRIBUTION

$\theta = 30^{\circ}$ MERIDIONAL SECTION

MODEL TEST 9 PRESSURE = 35 lbf/in FIG. 7·28

CASING No.15 (base)

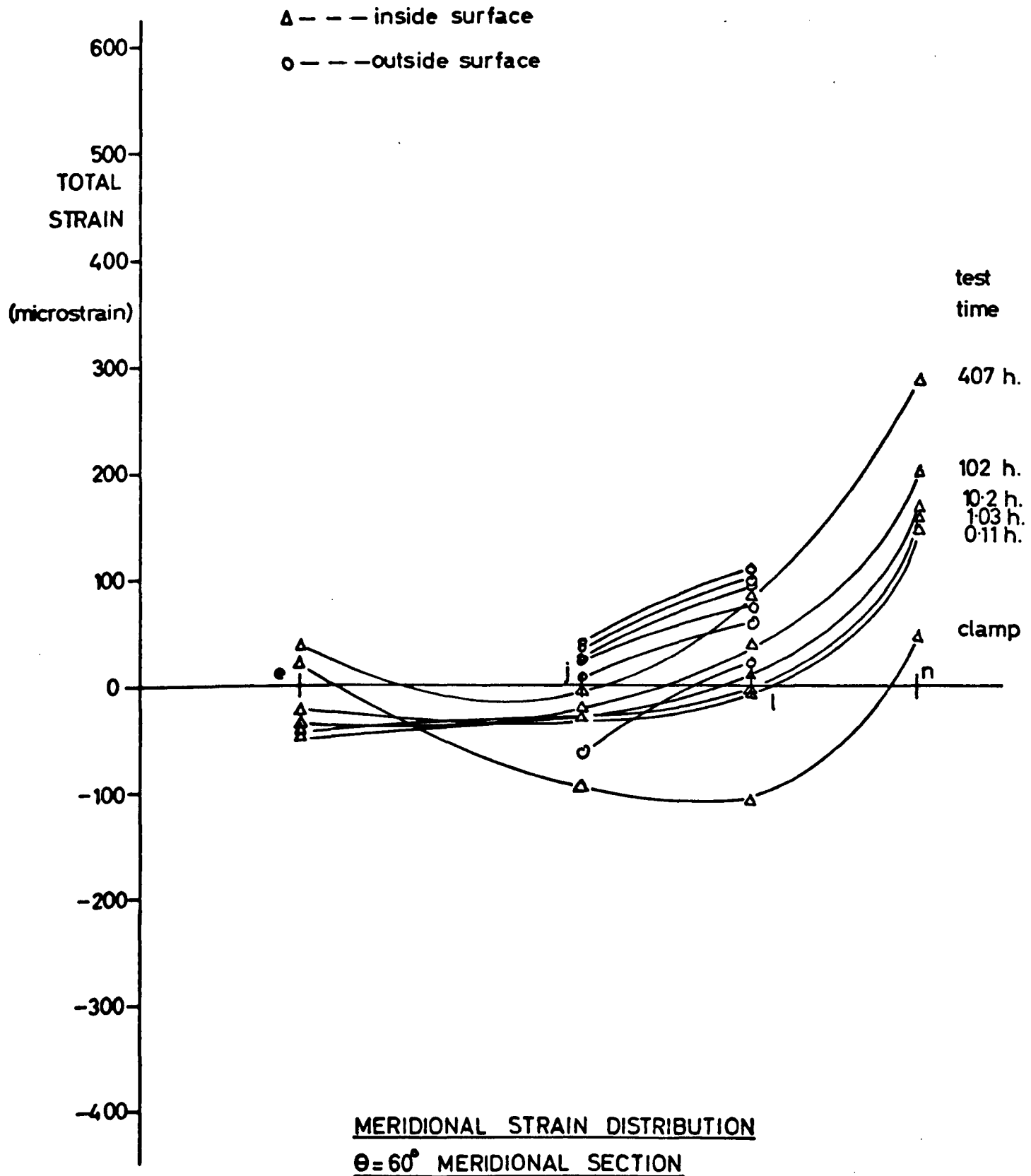

MERIDIONAL STRAIN DISTRIBUTION

$\theta = 60^{\circ}$ MERIDIONAL SECTION

MODEL TEST 9 PRESSURE = 35 lbf/in FIG. 7·29

CASING No. 12 (top)

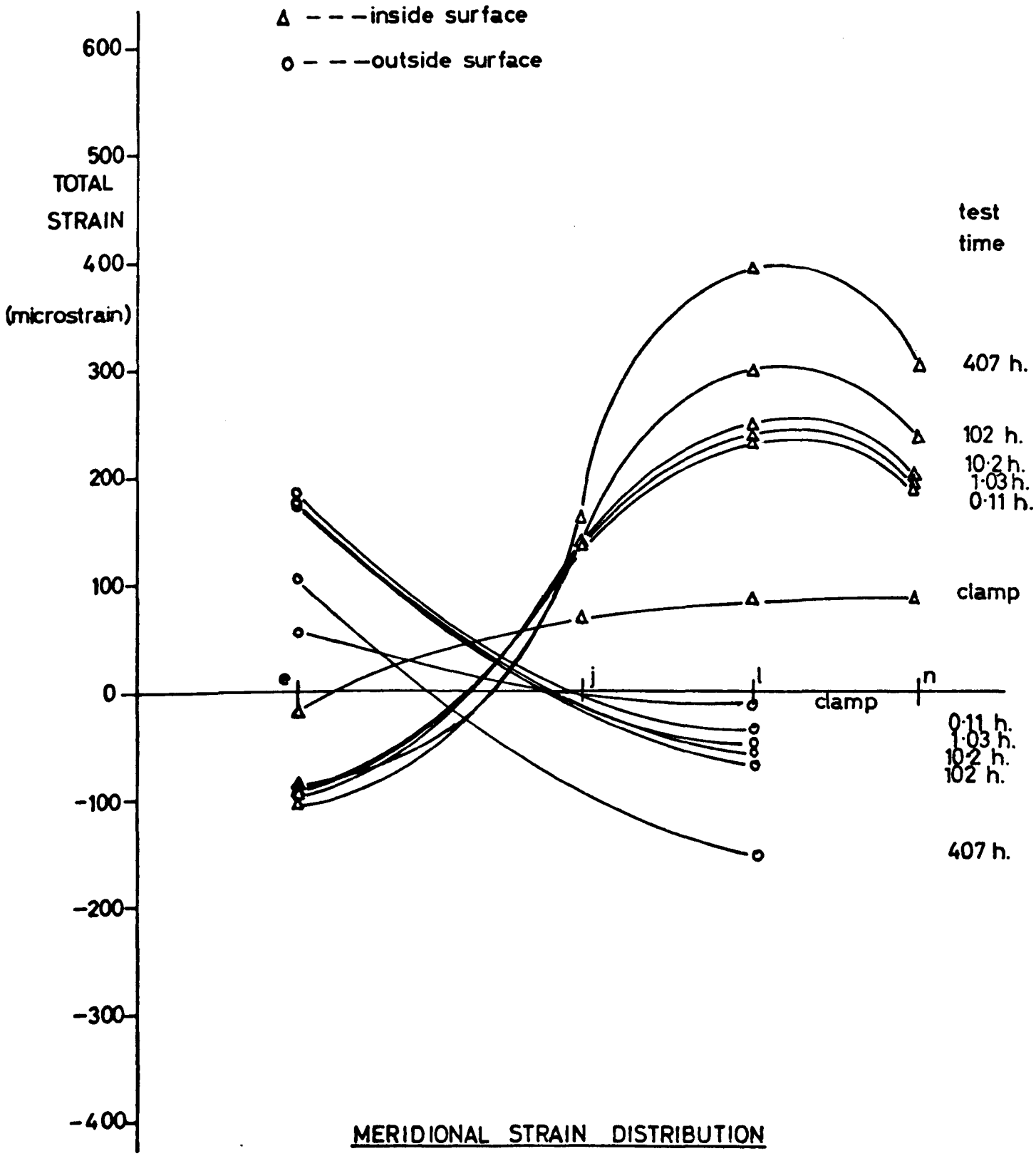

MERIDIONAL STRAIN DISTRIBUTION

$\theta = 0^{\circ}$ MERIDIONAL SECTION

MODEL TEST 9 PRESSURE = 35 lbf/in FIG. 7·30

CASING No. 12 (top)

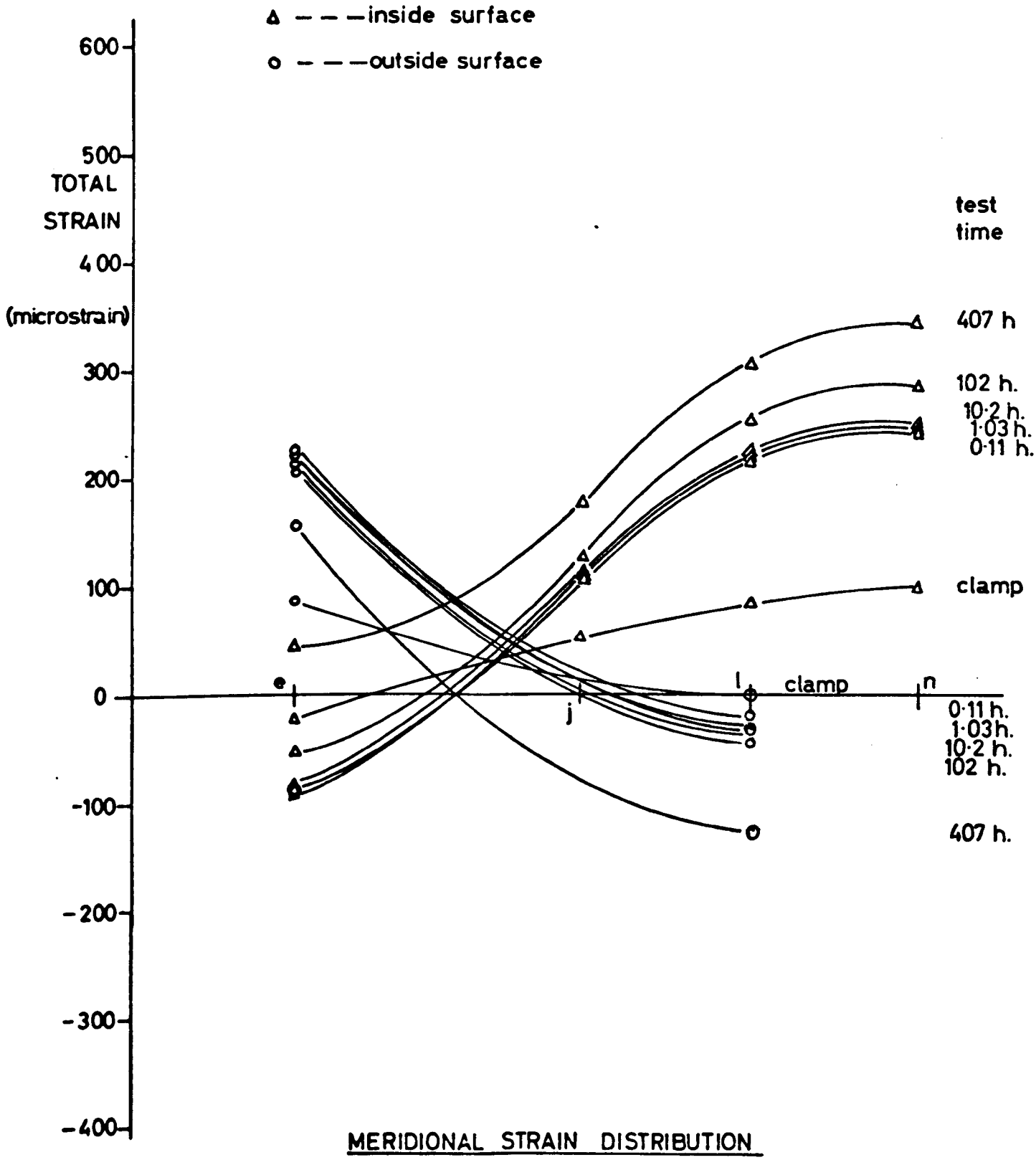

MERIDIONAL STRAIN DISTRIBUTION

$\theta = 30°$ MERIDIONAL SECTION

FIG. 7·31

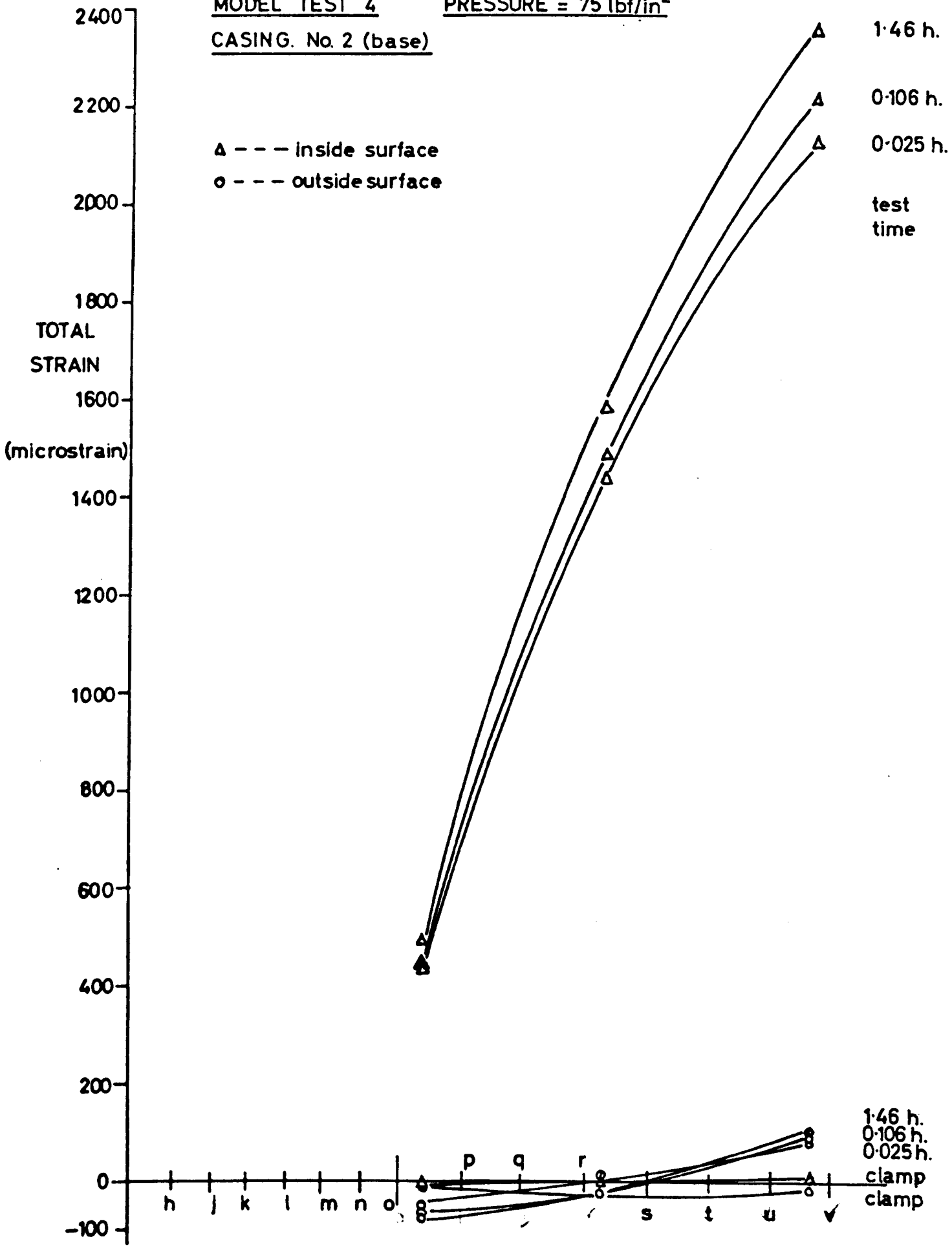

HOOP STRAIN DISTRIBUTION

$\theta = 0°$ MERIDIONAL SECTION

MODEL TEST 5 PRESSURE = 55 lbf/in² FIG. 7·32

CASING No. 4 (base)

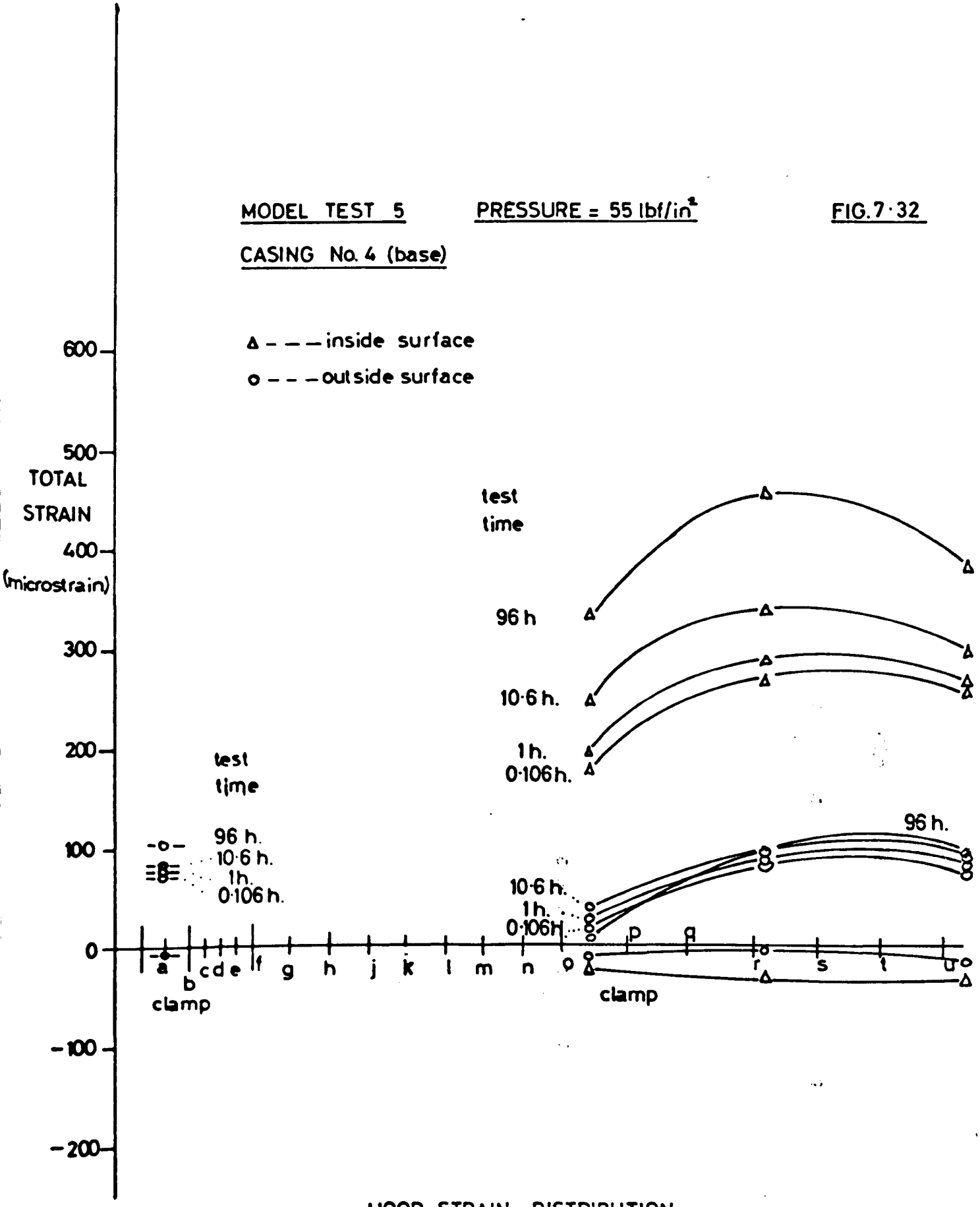

HOOP STRAIN DISTRIBUTION

$\theta = 0^{\circ}$ MERIDIONAL SECTION

MODEL TEST 7 PRESSURE = 45 lbf/in FIG. 7·33

CASING No. 9 (base)

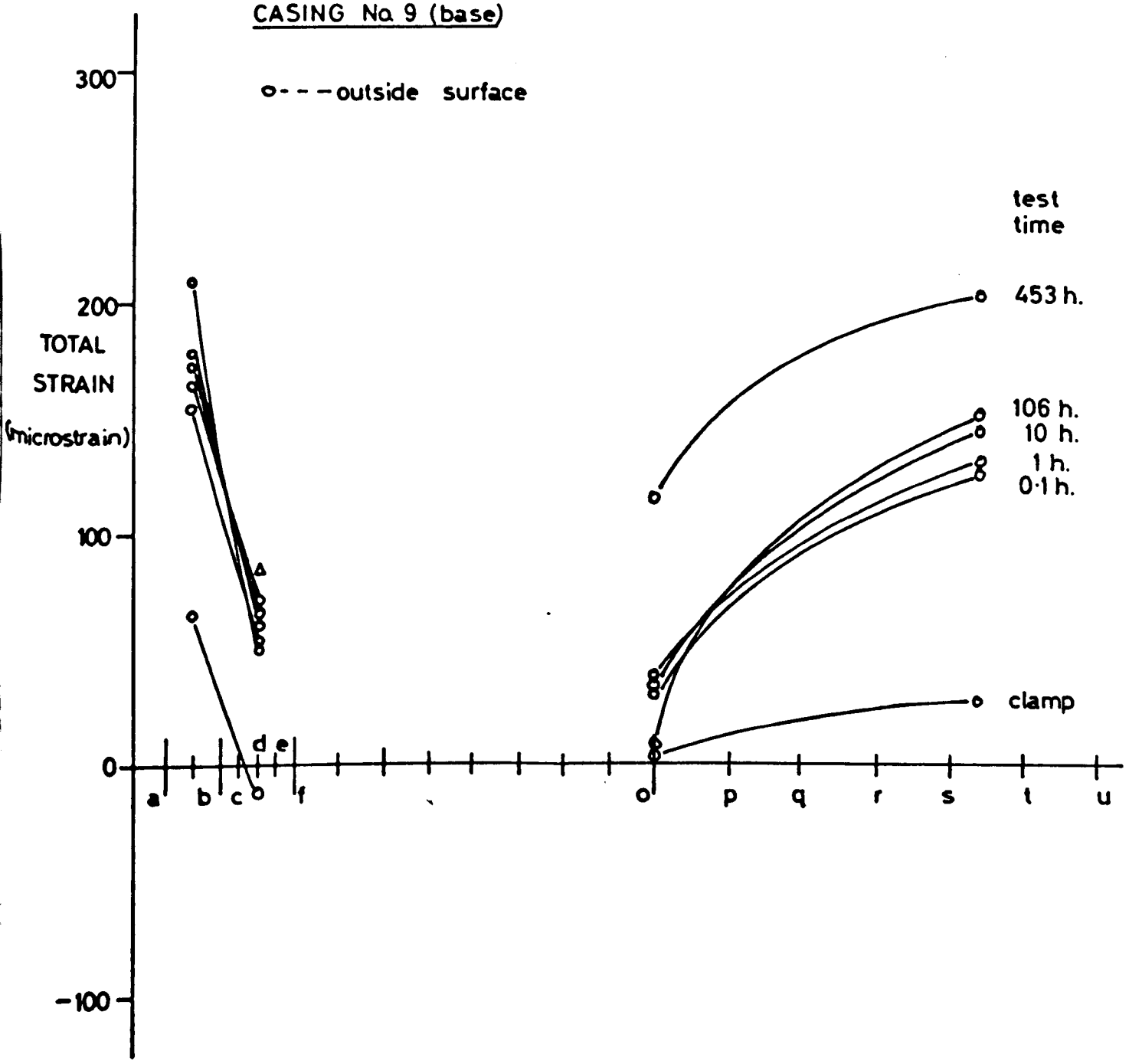

HOOP STRAIN DISTRIBUTION

$\theta = 0^{\circ}$ MERIDIONAL SECTION

MODEL TEST 8 PRESSURE= 55 lbf/in

CASING No.19 (base) FIG. 7·34

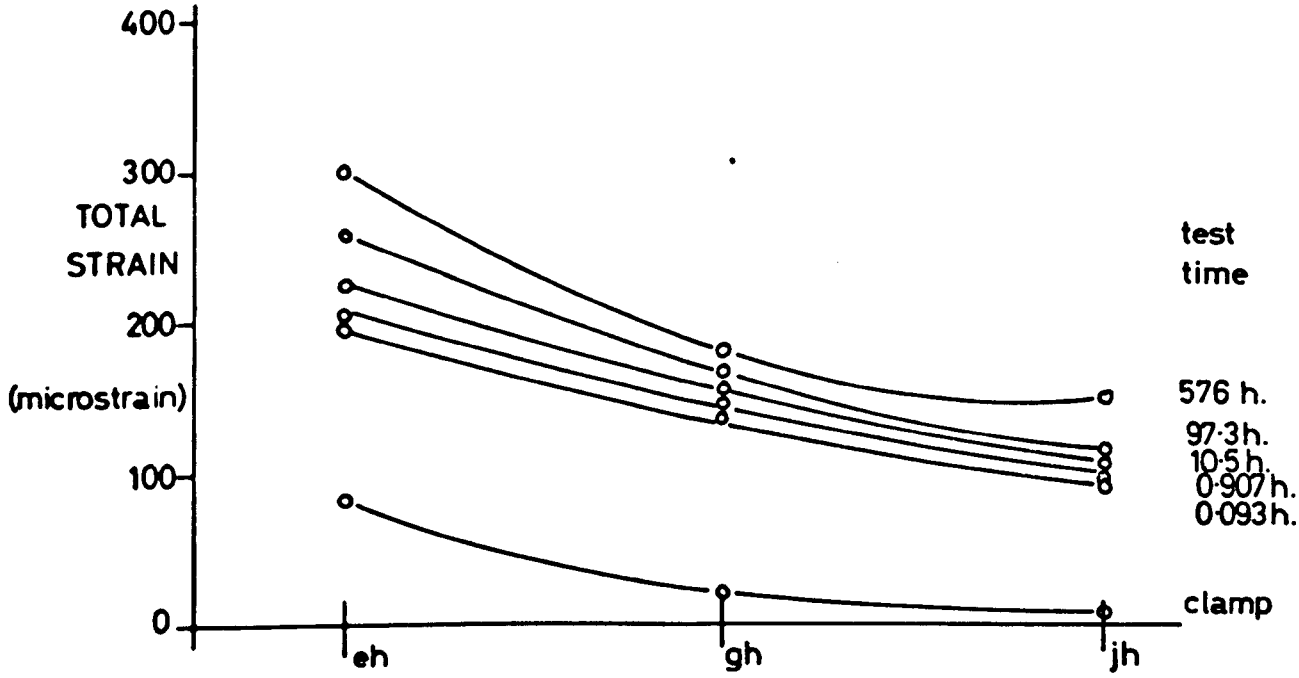

HOOP STRAIN DISTRIBUTION

BOSS FILLET RADIUS HOOP SECTION

CASING No.17 (top) FIG. 7·35

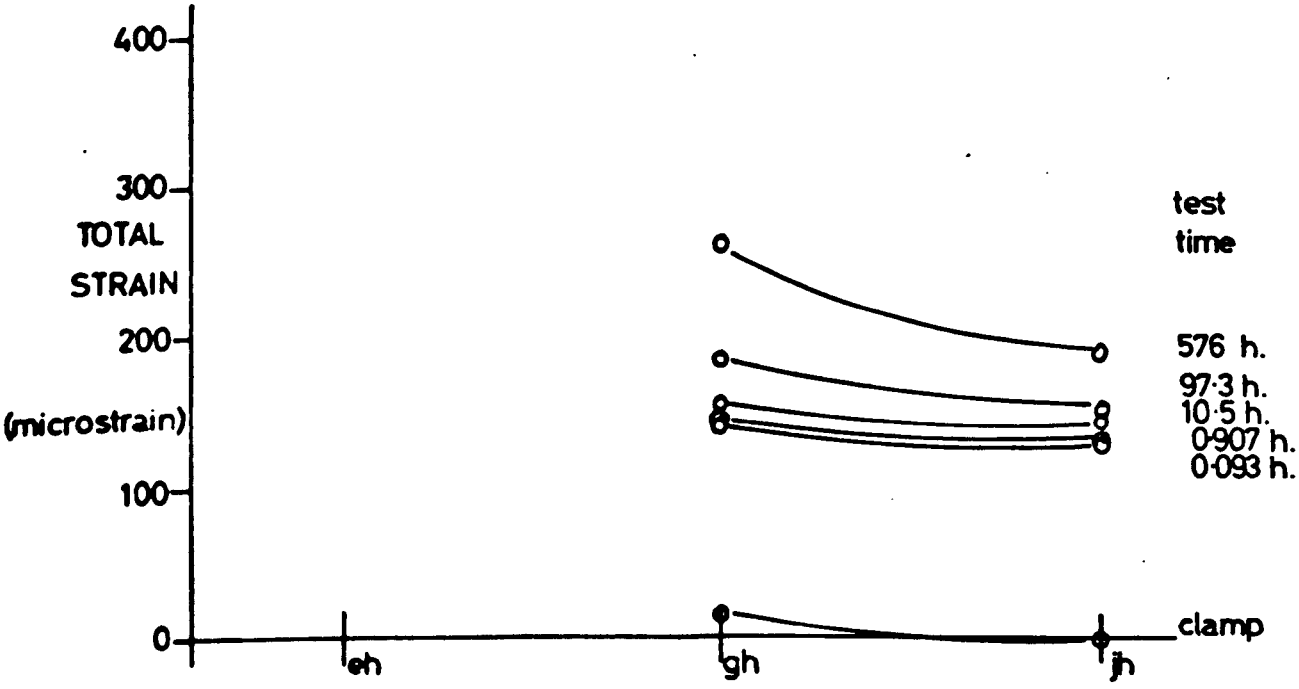

HOOP STRAIN DISTRIBUTION

BOSS FILLET RADIUS HOOP SECTION

MODEL TEST 8 PRESSURE = 55 lbf/in² CASING No. 19 (base) FIG. 7·36

CYLINDER HOOP STRAINS - θ = 0° MERIDIONAL SECTION
CYLINDER JOINT + 2·25 in HOOP SECTION

△- - - inside surface
o- - - outside surface

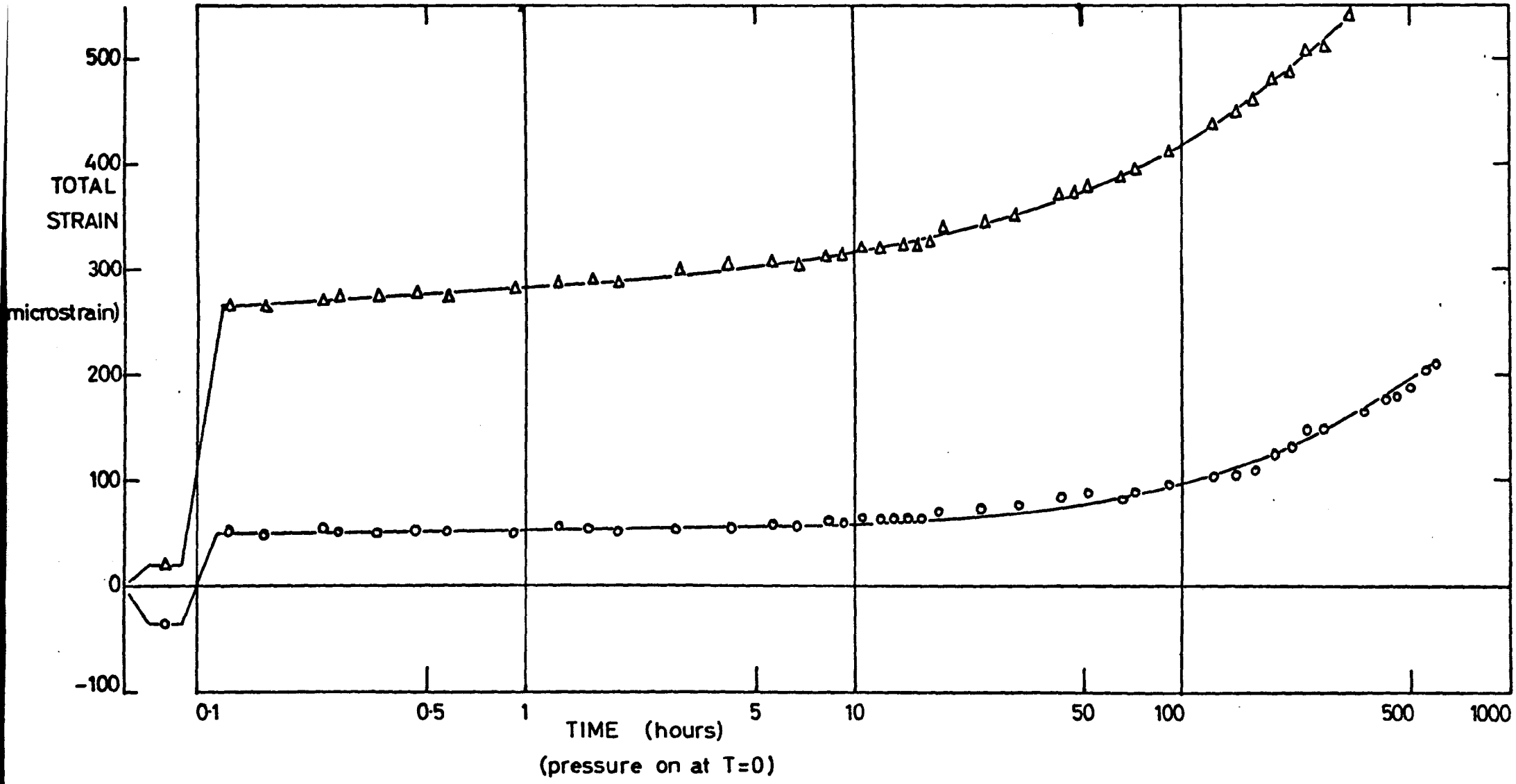

MODEL TEST 9 PRESSURE = 35 lbf/in² CASING No. 15 (base) FIG. 7·37

CYLINDER HOOP STRAINS - θ = 0° MERIDIONAL SECTION
CYLINDER JOINT + 1·875 in HOOP SECTION

△---inside surface
○---outside surface

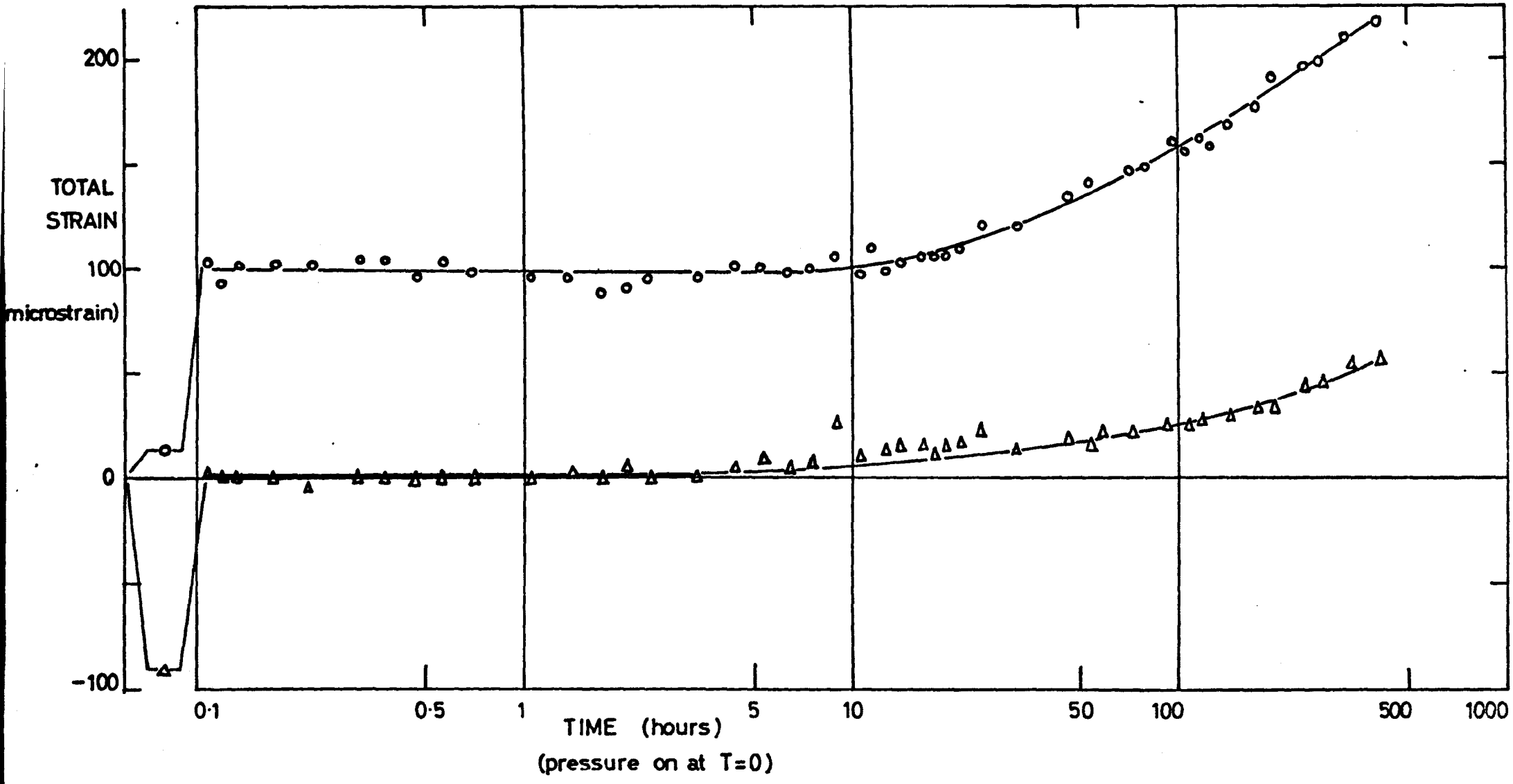

MODEL TEST 4 PRESSURE = 75 lbf/in²

FIG. 7·38

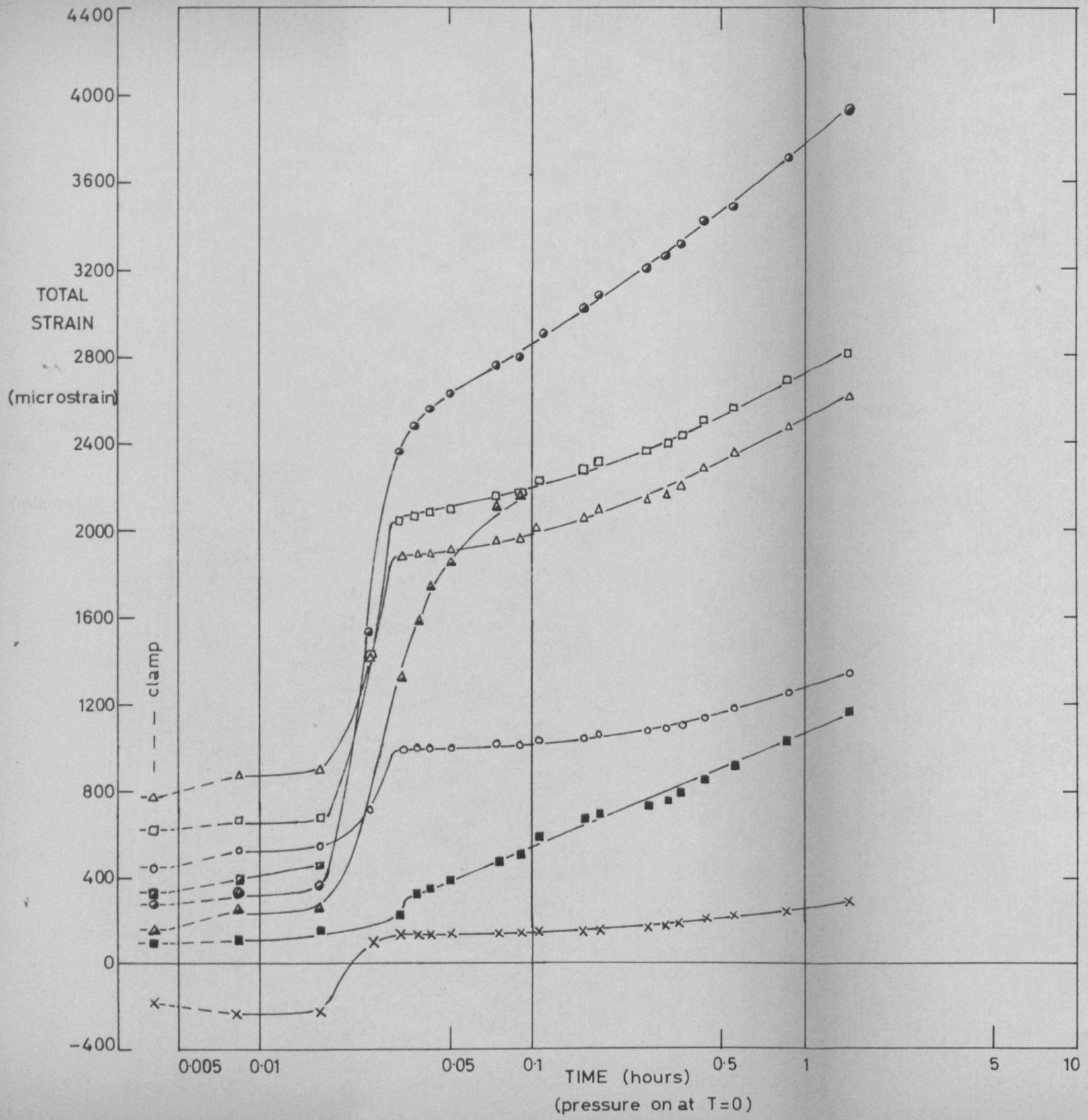

HOOP STRAINS

CASING No. 2 (base)

FLANGE FILLET RADIUS (BETWEEN BOLT HOLES)

△ - - - toroid Ø = 75° hoop section (holes 1/2)
○ - - - toroid Ø = 53° hoop section (holes 2/3)
□ - - - toroid Ø = 12° hoop section (holes 4/5)
◒ - - - cylinder joint + 1·1 inch hoop section (holes 6/7)
◭ - - - cylinder joint + 3·1 inch hoop section (holes 9/10)
◪ - - - cylinder joint + 3·8 inch hoop section (holes 10/11)

Θ=80° MERIDIONAL SECTION (ABOVE COUNTERBORE)

× - - - toroid Ø = 42° (hole 3)
■ - - - cylinder joint + 3·5 inch (hole 10)

MODEL TEST 5 PRESSURE = 55 lbf/in

FIG. 7·39

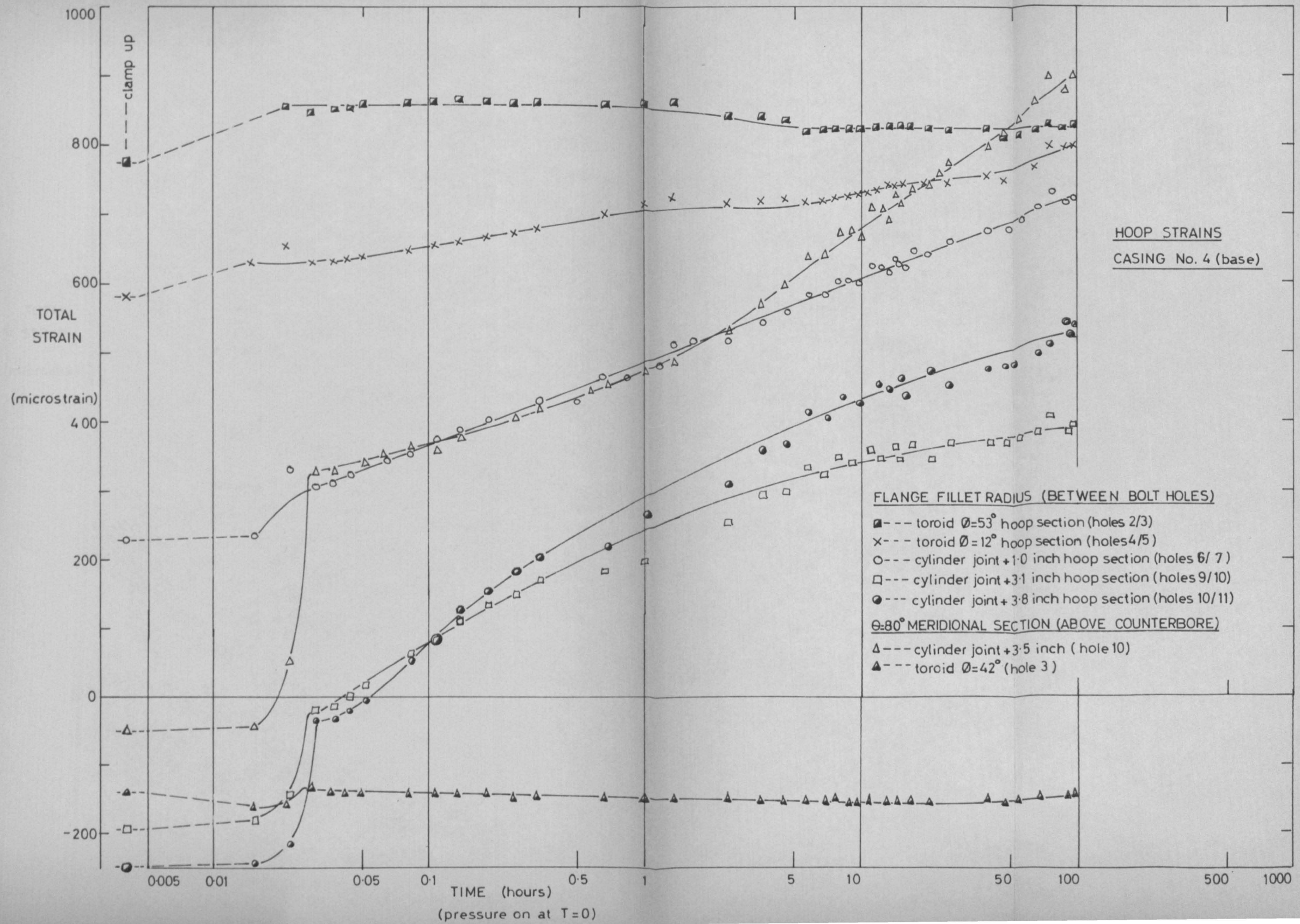

MODEL TEST 7 PRESSURE = 45 lbf/in FIG. 7·40

HOOP STRAINS IN FLANGE FILLET RADIUS (BETWEEN BOLT HOLES) CASING No. 9 (base)

Δ – – – toroid Ø = 12° hoop section (holes 4/5)
□ – – – toroid Ø = 32° hoop section (holes 3/4)
o – – – toroid Ø = 53° hoop section (holes 2/3)
X – – – toroid Ø = 75° hoop section (holes 1/2)

– – – – clamp up

TOTAL STRAIN (microstrain)

1200
1000
800
600
400
200
0

0·005 0·01 0·05 0·1 0·5 1 5 10 50 100 500 1000

TIME (hours)
(pressure on at T = 0)

MODEL TEST 8 PRESSURE = 55 lbf/in²

FIG. 7·41

HOOP STRAINS CASING No. 19 (base)

FLANGE FILLET RADIUS (BETWEEN BOLT HOLES)

o – – – toroid Ø = 75° hoop section (holes 1/2)
□ – – – toroid Ø = 32° hoop section (holes 3/4)
◪ – – – toroid Ø = 12° hoop section (holes 4/5)
Δ – – – cylinder joint +4·6 in. hoop section (holes 11/12)

TOTAL STRAIN (microstrain)

4400
4000
3600
3200
2800
2400
2000
1600
1200
800
400
0
-100

– – – clamp

0·005 0·01 0·05 0·1 0·5 1 5 10 50 100 500 1000

TIME (hours)
(pressure on at T = 0)

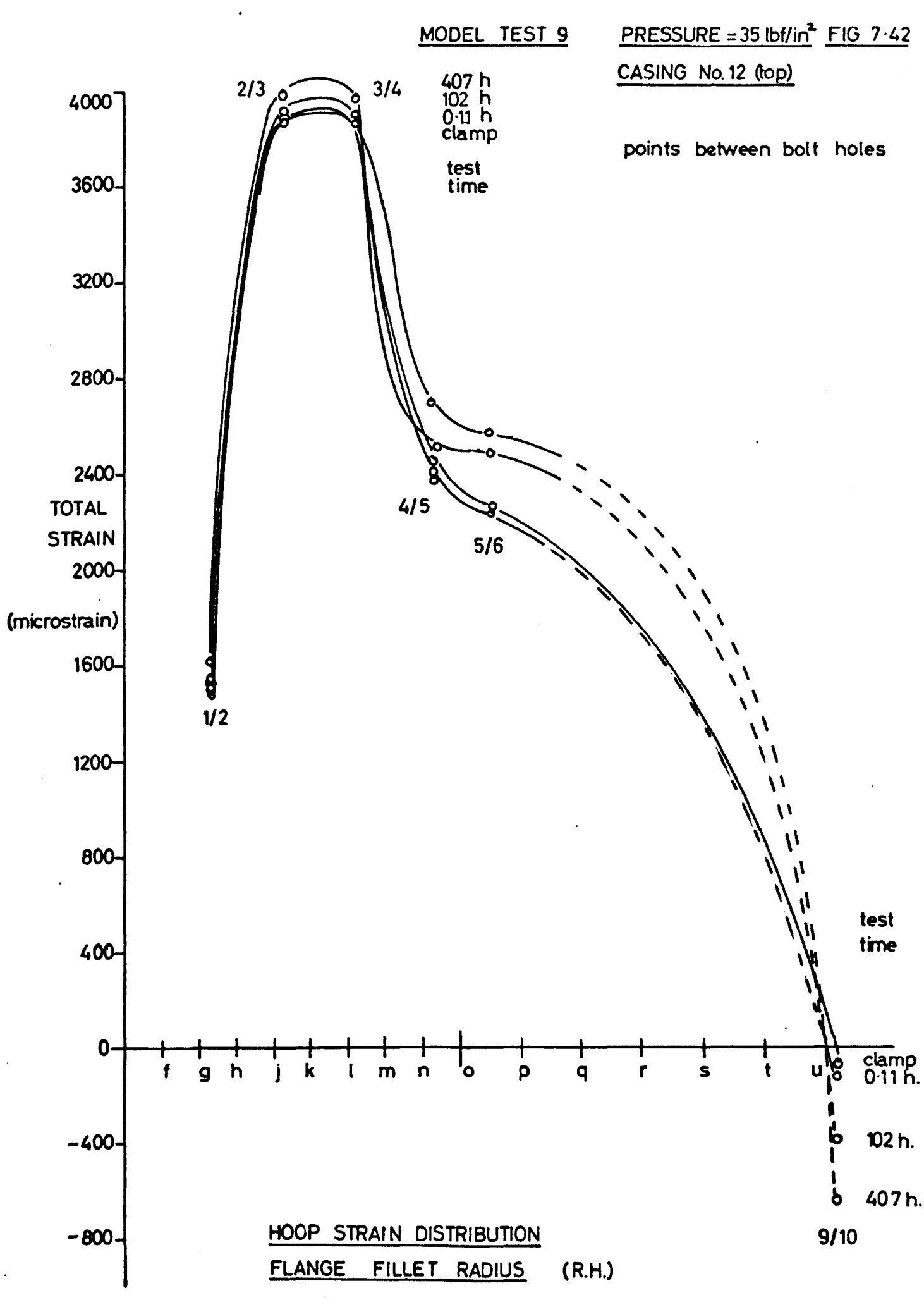
MODEL TEST 9
PRESSURE = 35 lbf/in²
FIG 7·42
CASING No. 12 (top)
points between bolt holes
407 h
102 h
0·11 h
clamp
test time
2/3
3/4
4/5
5/6
1/2
9/10
4000
3600
3200
2800
2400
2000
1600
1200
800
400
0
-400
-800
TOTAL STRAIN (microstrain)
f g h j k l m n o p q r s t u
clamp 0·11 h.
102 h.
407 h.
HOOP STRAIN DISTRIBUTION
FLANGE FILLET RADIUS (R.H.)

MODEL TEST 9 PRESSURE = 35 lbf/in^2 FIG. 7·43

CASING. No. 15 (base)

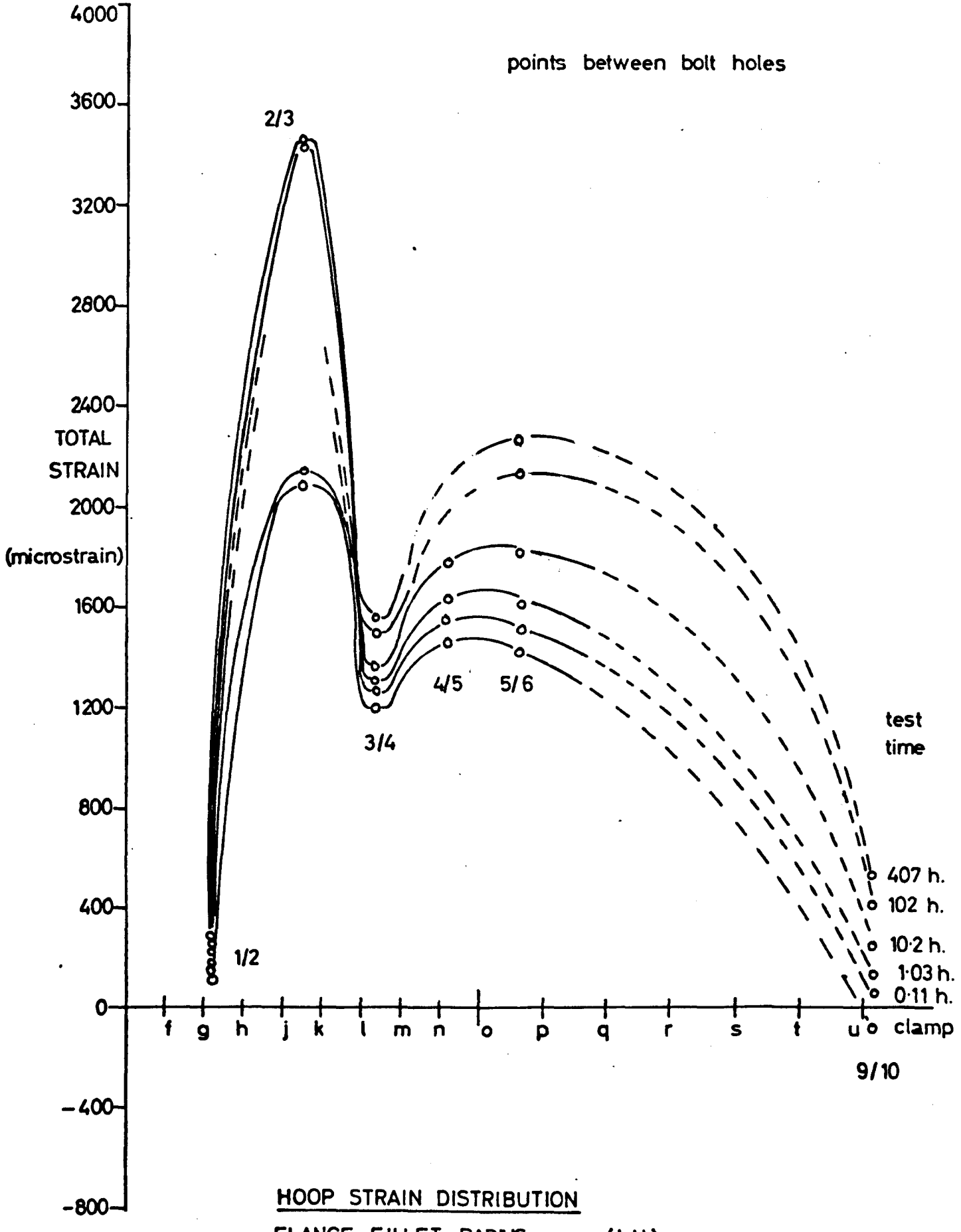

HOOP STRAIN DISTRIBUTION

FLANGE FILLET RADIUS (L.H.)

MODEL TEST 9 PRESSURE = 35 lbf/in² FIG. 7·44

CASING No. 15 (base)

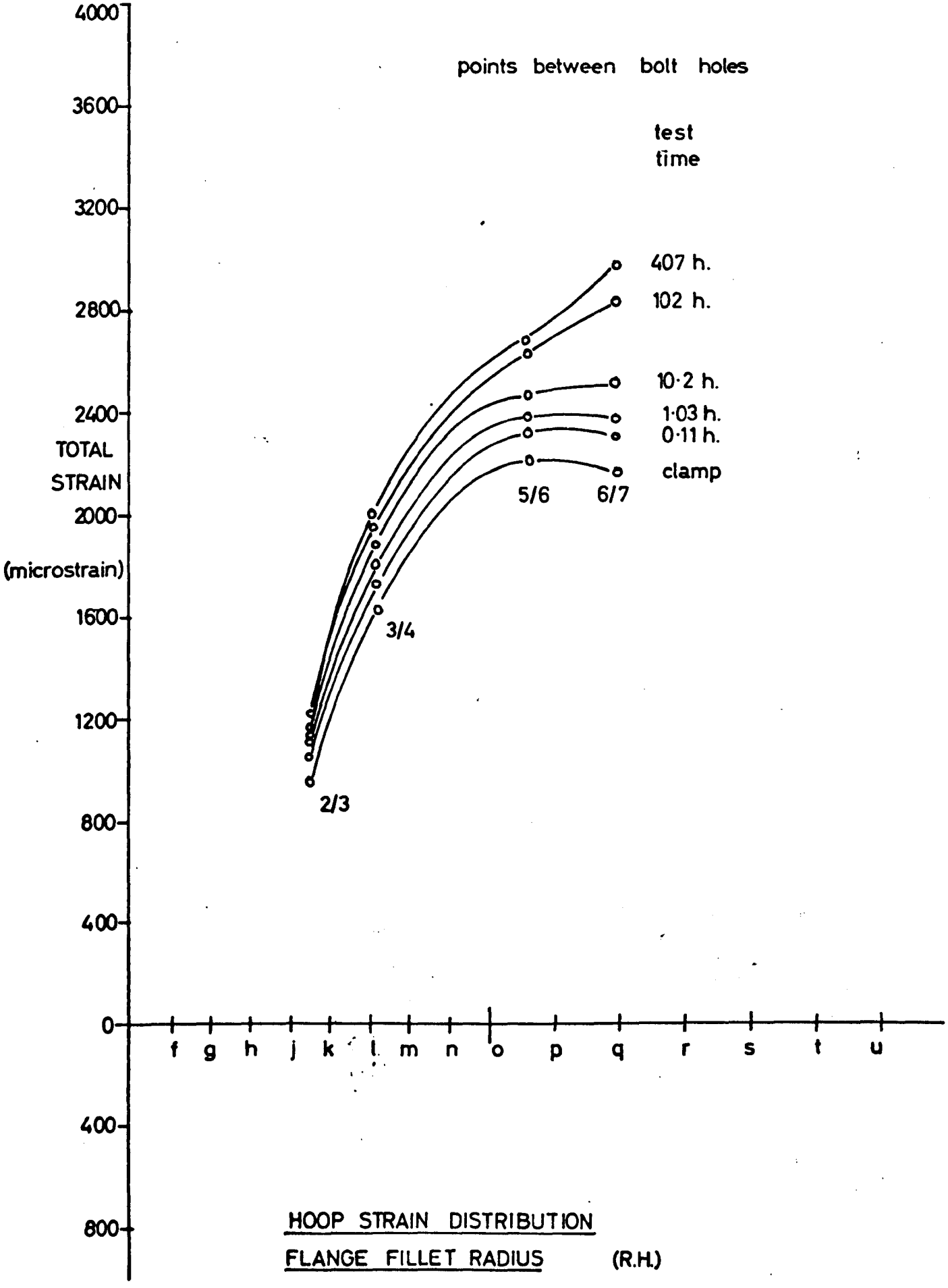

HOOP STRAIN DISTRIBUTION

FLANGE FILLET RADIUS (R.H.)

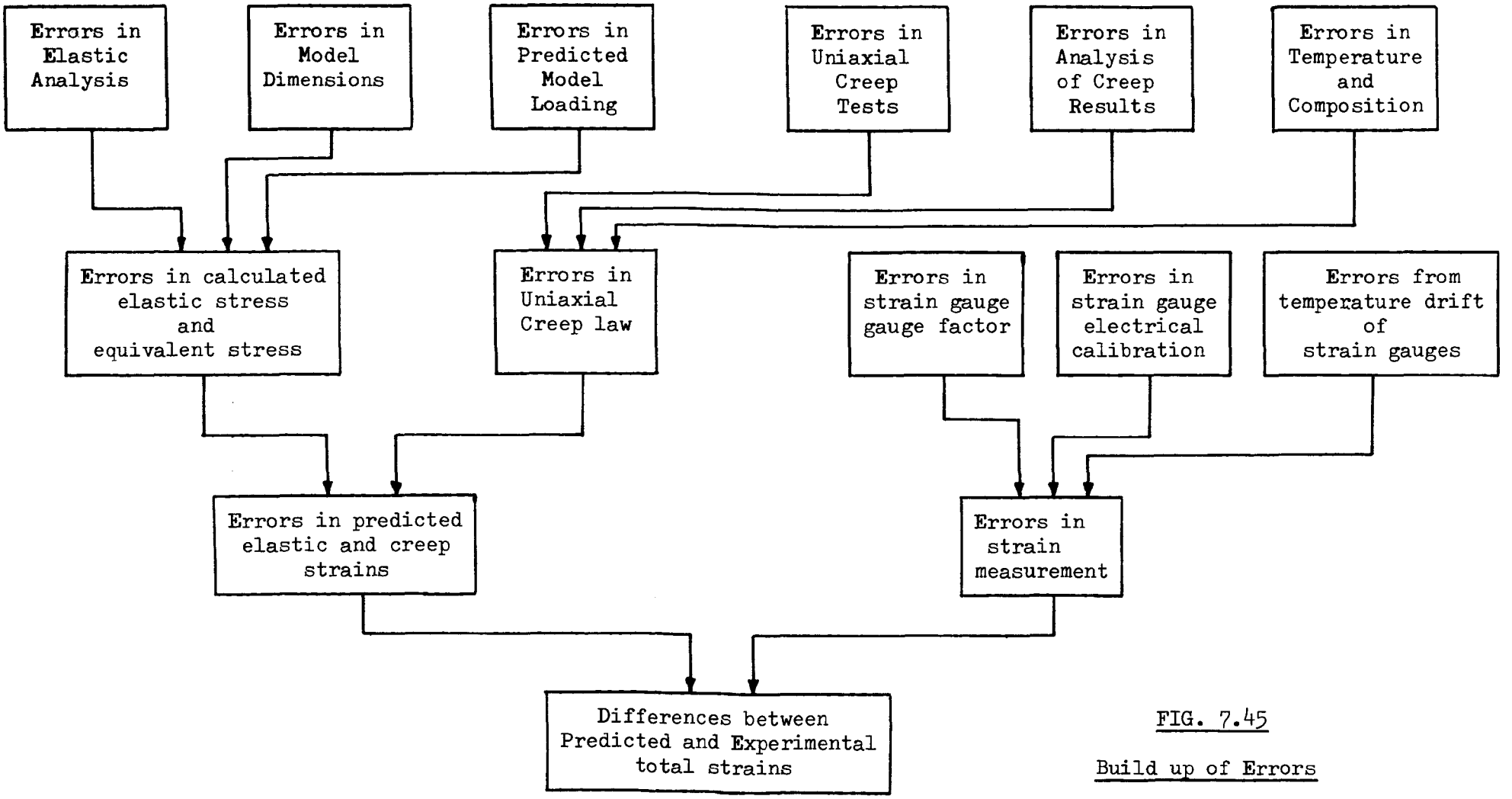

FIG. 7.45

Build up of Errors

8. CONCLUSIONS

(i) A castable material has been developed for the accelerated creep testing of model structures. This material is 1.2% Antimony 0.12% Arsenic alloy of lead, and the creep properties of castings made of this material are given in Section 3.2.4.

(ii) Chill casting techniques for modelling a flanged steam turbine casing in the lead alloy have been developed (Chapter 5).

(iii) The elastic stress distribution in the model casing due to internal pressure was obtained using the photoelastic stress freezing technique. The results are given in Chapter 4.

(iv) Similarity conditions for the model and prototype have been established in creep (Section 2.2) for materials with a creep law of the form given in Section 3.2.4.

(v) The suitability of electric resistance strain gauges for measuring strains in lead structures has been established. A system for monitoring 80 strain gauges at intervals during a creep test lasting up to 4 weeks has been developed.

(vi) The techniques for conducting creep tests in model pressure vessels for long periods at room temperature have been established.

(vii) Although elastic hoop strains measured in the model tests agreed well with those predicted (Section 7.5), unexpected meridional bending of the model casings (Section 7.4.1) prevented agreement with prediction of creep strains. However, the model tests showed some consistency, and it was demonstrated (Section 7.4.4) that some correlation was possible.

9. RECOMMENDATIONS FOR FURTHER WORK

9.1 The immediate program

1. The cause of the meridional bending in the model casings on clamping up should be identified and eliminated.

2. Model creep tests should be carried out on casings with much thicker flanges. Many of the difficulties experienced would have been avoided if the design of casing selected had been one with a flange of at least double the thickness of that used.

3. The location of strain gauges should be restricted to the $\theta = 0^{o}$ meridional plane, the flanges and the boss ends.

4. To be able to compare experimental results with theoretical predictions, the distributions of both meridional and hoop strains should be monitored.

5. Any changes in casting conditions or model shape require the cast material to be recalibrated in uniaxial creep.

6. Photoelastic analyses of split pressure casings should be carried out under internal pressure, for stability. The models for these tests should have the mating flanges cast in one piece, since only hoop splits can be effectively joined and sealed.

9.2 Future Developments

When sufficient experience is gained from the simple flanged casings, the design of the mould allows the addition of inlet nozzles, and end closures of different profiles.

The most important material defect is its porosity. It might be possible to find additional alloying elements which will reduce the solidification contraction of the material without impairing its grain size and age hardening characteristics.

The techniques developed are applicable to any three-dimensional structure, and a split turbine casing with inlet nozzles represents a more difficult modelling problem than many other structures in which creep is important.

ACKNOWLEDGEMENTS

The author wishes to thank Professor A. G. Smith, Head of the Department of Mechanical Engineering, for providing the facilities for this research. The author also wishes to thank Dr. H. Fessler for his encouragement and guidance during the project.

This work was sponsored by the Science Research Council, and in addition the author wishes to thank the Department of Civil Engineering for the loan of the Data logging equipment.

The author is particularly grateful to Mr. B. Russel-Smith, the Experimental Officer engaged on this project, whose assistance enabled the work to cover a wide field.

The helpful assistance of Dr. J. J. Webster and Dr. A. Lichtarowicz is much appreciated, as is the assistance given by the technicians of the Faculty of Applied Science, particularly Messrs. S. McCausland, B. K. Stochaj, R. Pickard, B. Mynett, S. Raines and J. Unwin.

Finally, the author wishes to thank Miss J. Rigley for typing this thesis.

REFERENCES

1. Finnie, I. and Heller, W.R. "Creep of Engineering Materials". McGraw-Hill, New York, 1959.
2. Mclean, D. "Grain Boundaries in Metals". Oxford: Clarendon Press, 1957.
3. Hoffmann, W. "Lead and Lead Alloys". Springer-Verlag Berlin, 1970.
4. Rotherham, L. "Creep of Metals". Inst. of P., 1951.
5. Warren, J.W.L. "A Survey of the Mechanics of Uniaxial Creep Deformations in Metals". Aeronautical Research Council, London, Current papers no. 919 (1967).
6. Hult, J. "Primary Creep in Thick Walled Spherical Shells". Trans. Chalmers. Univ. No. 264 (1963).
7. Rabotnov, Y.N. "Some problems on the Theory of Creep". N.A.C.A. Tech. Memo. 1353 (1948).
8. Dorn, J.E. and Mote, J.D. "Physical Aspects of Creep".
9. Goldhoff, R.M. "Uniaxial Creep Rupture Behaviour of Low Alloy Steel under Variable Loading Conditions". Trans. A.S.M.E. 87D (J. Basic Eng.) 2, 374-378, (June 1965).
10. Taira, S., Koterazawa, R. and Ohtami, R. "Creep of Thick Walled Cylinders under Internal Pressure at Elevated Temperatures". Proc. 8th Japan Congress on Testing Materials, Kyoto, Japan. The Soc. of Matls. Sci. (1965).
11. King, R.H. and Mackie, W.W. "Creep of Thick Walled Cylinders". J. Basic Eng. Trans. A.S.M.E. 89D, 4, 877-884. (Dec. 1967).

12. Ohji, K. and Marin, J. "Creep of Metals under Non-steady Conditions of Stress". Proc. I.Mech.E., 1963-64, 178 Pt 3L, 126.

13. Clarke, J.M. "A Comparison of some Methods for Predicting Creep Strain and Rupture under Cyclic Loading". Aeronautical Research Council, London, Current papers no. 1020 (1968).

14. Marriott, D.L. and Leckie, F.A. "Some Observations on the Deflections of Structures during Creep". Proc. I.Mech.E. 1965.

15. Lubahn, J.D. and Felgan, R.P. "Plasticity and Creep of Metals", Wiley (1961)

16. Gill, P.A.T. "Development and Application of a Model Material for Accelerated Creep Testing". Ph.D. Thesis, 1968, Nottingham Univ.

17. Ohuami, M. Motoie, K. and Yoshida, N. "Experimental Examinations for Creep Analysis of High Pressure Cylindrical Tubes at Elevated Temperatures". Proc. 10th Japan Congress on Testing Materials, Kyoto, Japan. The Soc. Matls. Sci., 54-59, (1967)

18. Taira, S. Ohtani, R. and Ishibaka, A. "Creep and Creep Fracture of a Low Carbon Steel under Combined Tension and Internal Pressure." Proc. 11th Japan Congress on Testing Materials, Tokyo 1967. The Soc. Matls. Sci., 76-78 (1968).

19. Johnson, A.E. "Creep under Complex Stress Conditions at Elevated Temperatures". Proc. I.Mech.E., 164 (1951), p. 432.

20. Johnson, A.E. "Complex-stress Creep of Metals". Metallurgical Review, 5, 447 (1960).

21. Hoffmann, W. and Malotki, V. Z. Metallkunde, 55 (1964), 135.

22. Mackenzie, A.C. "Generalised stress/strain rate relations for Creep of Thin Shells: A Comparison of 'Exact' and Approximate Relations". Applied Scientific Research 20, 6, 393 (June 1969)

23. Fairburn, J. and Mackie, W.W. "A Simple Method of Obtaining Creep Rates of a Thick Walled Cylinder under Internal Pressure". J.Mech. Eng. Sci. 10, 3, 286-288 (June 1968).

24. Smith, E.M. "Estimation of the Useful Life and Strain History of a Thick Tube Creeping under Non-steady Conditions". J.S.A. Vol. 1, 44-49 (1965).

25. Ohnami, M. and Motoie, K. ,"Creep and creep Rupture of Cylindrical Tube Specimens Subject to Combined Axial Load and Internal Pressure at Elevated Temperatures". Proc. 9th Japan Congress on Testing Materials, Tokyo 1965, The Soc. Matls. Sci., 39-43 (1966).

26. Murakami, S. and Iwatsuki, S. "Transient Creep of Circular Cylindrical Shells", Int. J. Mech. Sci., 11, 11, 897-912 (Nov. 1969).

27. Penny, R.K., Ellison, E.G. and Webster, G.A. "Specimen Alignment and Strain Measurement in Axial Creep Tests". Matls. Res. & Stand. 6, 2, 76-84 (Feb. 1966).

28. Dutton, R. "A Survey of Compression Creep Testing of Metals". Matls. Res. & Stand. 9, 11-17 (Apr. 1969).

29. Penny, R.K. and Leckie, F.A. "The Mechanics of Tensile Testing". J. Mech. Sci., (1968), Vol. 10, 265-273.

30. Gifkins, R.C. "Transitions in Creep Behaviour". J. Matls. Sci. 5, 2, 156-165 (Feb. 1970).

31. Gifkins, R.C. and Snowden, K.V. Trans. Met. Soc. AIME 239 (1967), 910.

32. Woodford, D.A. "Measurement and Interpretation of the Stress Dependence of Creep at Low Stresses". Matls. Sci. and Eng. 4, 213, 146-154 (May 1969).

33. Moore, H.F. Betty, B.B. and Dollins, C.W. — University of Illinois Bulletin, 35 (1938) Bulletin 306.

34. Ca — J. Appl. Phys., 21 (1950) 1289.

35. Waller, K.F.A. And Graham, A. — "On the extrapolation and Scatter of Creep Data". Aeronautical Research Council, London, Current papers, no. 680 (1963).

36. Greenwood, J.N. and Warner, H.K. — "Types of Creep Curves obtained with Lead and its dilute Alloys". J.I.M., Vol. 64, 135 (1939)

37. Bluth, A. and Haneman, K. — Z. Metallkunde, 29 (1937), 48.

38. Hopkin, L.M.T. and Thwaites, C.J. — J. Inst. Metals, 81 (1952/53), 181.

39. Williams, J.D — "The effect of Arsenic on the Age Hardening of Lead-Antimony Alloys". Metallurgia (Sept. 1966), 105-108.

40. Nishikawa, S. and Tsumuraya, K. — "The effects of Small Arsenic Additions on the Precipitation Kinetics of Lead-Antimony Alloys".

41. Winegard, W.C. — "An Introduction to the Solidification of Metals". Inst. Metals Monograph & Report No. 29 (1964).

42. Parkes, D.A.C. — Finite Element Analysis of Stresses and Creep in Turbine Casings. Ph.D. Thesis submitted to Nottingham University in 1973.

43. Frederick, C.O. — "Model Correlations for Investigating Creep Deformations and Stress Relaxation in Structures", J.Mech. Eng. Sci. 7, 1, 57-66 (Mar. 1965).

APPENDIX 1

Calculation of Creep Law

The functions given in Section 3.2.4, equations (4), (5) and (6), are fitted to the uniaxial creep data using a least squares method. The calculation is performed on the Nottingham University ICL 1900 computer at the Cripps Computing Centre, and a flow chart of the program is given in Fig. 3.14.

Use is made in the program of a standard subroutine E04CCF. A function FF is specified in the program in terms of variables V1, V2, V3, etc., and the subroutine E04CCF, when called, finds values for V1, V2, V3, etc. which minimise the function FF. The method is iterative, and if the specified number of steps is reached before a minimum is found, the current values are given. This enables the program to be re-run, using these values as initial values for V1, V2, V3, etc.

In the creep law calculations, the variables 'V' are made the creep law constants. The function FF is calculated as the sum of the squares of the difference between the experimental creep strain values for a given time, and the calculated values of creep strain at the same time, according to the creep law with the current values of V1, V2, etc. as creep constants.

APPENDIX 2

Stress Separation for Pressure Loaded Photoelastic Model

In the pressure loading of the Araldite model described in Section 4.2.2, the value of the pressure given by the manometer (Fig. 4.8) can be taken only as a rough guide. The true value of the pressure must be obtained from equilibrium considerations.

Consider a small section of the casing in cylindrical coordinates (Fig. A.1). The equilibrium of a small segment at radius 'r', thickness 'δr' is given by;

$$\frac{\partial \sigma_r}{\partial r} + \frac{1}{r}\frac{\partial \tau_{r\theta}}{\partial \theta} + \frac{\partial \tau_{rz}}{\partial z} + \frac{\sigma_r - \sigma_\theta}{r} = 0 \qquad (A.2.1)$$

If the segment is taken from the $\theta = 0^\circ$ meridional plane (Fig. 4.3), by symmetry, $\frac{\partial \tau_{r\theta}}{\partial \theta} = 0$ when $\theta = 0^\circ$.

In the $\theta = 0^\circ$ meridional slice (Fig. 4.10) in the middle of the cylindrical section, the fringe order ($\propto \tau_{rz}$) was found to be constant along the length.

i.e. $\frac{\partial \tau_{rz}}{\partial z} = 0$ at $\theta = 0^\circ$ and in the middle of the cylinder.

A small section of casing was therefore cut from the $\theta = 0^\circ$ meridional slice, in the middle of the cylindrical section, where equation (A.2.1) becomes,

$$\frac{\partial \sigma_r}{\partial r} + \frac{\sigma_r - \sigma_\theta}{r} = 0$$

i.e. $$\Delta \sigma_r = -(\sigma_r - \sigma_\theta)\frac{\Delta r}{r} \qquad (A.2.2)$$

But, $\sigma_r - \sigma_\theta = \frac{Fn_r}{t_r}$ the stress-optic law

where F is the material fringe value (Section 4.2.3); n_r is the fringe order at radius r of the hoop face of the segment, and t_r is the axial thickness of the section at radius r.

If t, F are constant across the segment

$$\Delta\sigma_r = -\frac{F}{t}\,\Delta r\,\frac{n_r}{r}$$

Therefore, taking small equal steps Δr across the section

$$\sigma_r = \frac{F\,\Delta r}{t}\quad\sum -\frac{n_r}{r} \qquad \text{(A.2.3)}$$

The section was divided into twenty segments of equal height, the fringe order and radius being measured at each segment. On the outside surface, $\sigma_r = 0$. On the inside surface $\sigma_r = -p$. Hence, using equation (A.2.3), the internal pressure 'p' was calculated.

$$\underline{\underline{p = 1.531\ \text{lbf/in}^2}}$$

APPENDIX 3

Etching of Lead Specimens

Antimony alloys of lead are among the more difficult materials to etch and photograph. Many techniques were attempted, and the following method gave the best results.

The lead sections were bandsawed, and then smoothed with a file. Because lead is soft, all abrasive processes leave a fine skin of metal which has burnished over, and the problem is to clean off this skin.

After polishing the specimen was polished with metal polish on a Selvyte cloth, then dipped in a weak solution of nitric acid (10:1). This process was repeated several times; the acid eating through the burnished skin, and the light polishing with the Selvyte cloth keeping the surface smooth without increasing the skin by much. The last dip in the acid needed to be only 15 seconds to reveal the grain structure. Longer than that caused overetching, and the surface became blackened.

It was not found possible to photograph in direct light under a microscope to show the grain structure clearly. The photographs of Fig. 5.10 were taken in diffuse artificial light by a standard camera (with an extension tube for close-up), after spraying the etched surface with Shellsoll to enhance the detail.

APPENDIX 4

Program for Processing Results

The punched tape output from the recording equipment (Section 6.2.2) had to be read into the computer from an ALGOL program, while the main program was written in FORTRAN. Also, the channel number of the D.V.M. was punched, along with the voltage reading, so the tape reading subroutine involved a step by which it stored only every second value read. Card output of the processed results was available for use on the graph plotter.

Flow diagram of program

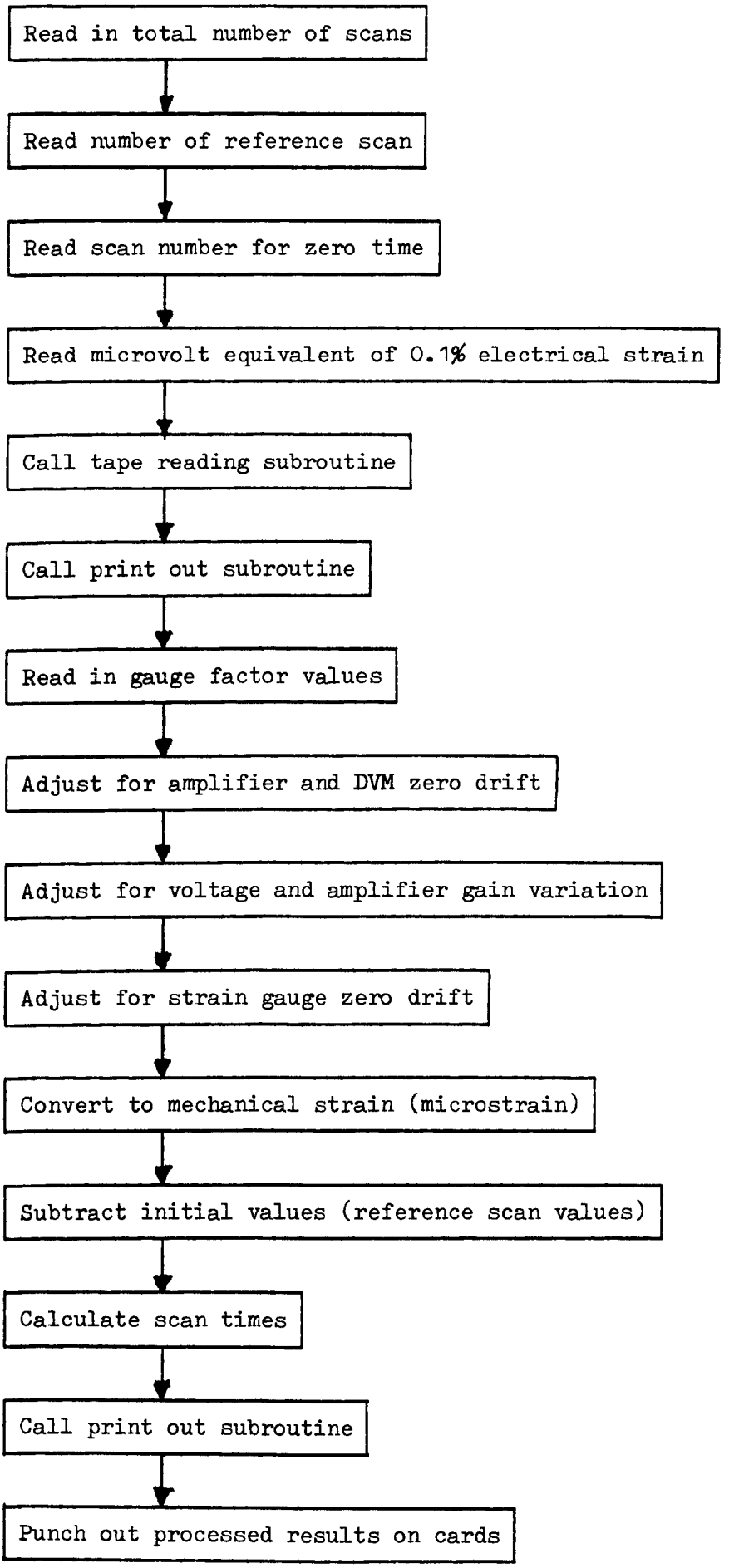

APPENDIX 5

Bolt load calculation

The simple flange bolt load calculation is based on the configuration shown in Fig. A.2. A length of flange equal to one bolt pitch is considered, and the following assumptions are made;

(i) The bolt load, F, acts as a concentrated load.

(ii) Thin shell theory applies to the pressurised cylinder.

(iii) The tensile load in the casing wall can be considered as a point load, Q, acting on the rectangular flange section.

(iv) The pressure load Q acts through the intersection of the casing mid-thickness and the flange joint AB.

(v) The pressure load Q acts in the plane of the bolt load F.

(vi) The flange depth d is sufficient to distribute the point loads evenly along the flange joint AB.

(vii) The minimum bolt load requirement is that the resultant stress in the flange joint at the inside edge (point B) should be compressive and equal to the internal pressure (p).

Area of flange joint considered = $w\,l$

I of section = $\frac{l\,w^3}{12}$

Net force on section = Q - F (tensile forces and stresses are +ive)

Net moment on section = Q.a - F.b

Direct stress on flange joint = $\frac{(Q - F)}{w.l}$

Bending stress at inside edge (position B) = $(Q.a - F.b)\frac{12}{l\,w^3} \cdot \frac{w}{2}$

$$= \frac{6}{l\,w^2}(Qa - Fb)$$

$$\therefore \text{ Total stress at B} = \frac{(Q - F)}{w\ell} + \frac{6}{\ell w^2}(Qa - Fb)$$

But $Q = \ell Rp$ and Total stress at B $= -p$

$$\therefore -p = \frac{(\ell Rp - F)}{w\ell} + \frac{6}{w^2\ell}(\ell Rpa - F.b)$$

Hence $$F = \frac{\ell.p\left[R(1 + 6\frac{a}{w}) + w\right]}{1 + 6\frac{b}{w}}$$

In this case $R = 3.125$ in

$\ell = 0.700$ in

$w = 0.875$ in

$a = 0.25$ in

$b = 0$

$$\therefore \quad F = 6.57\ p$$

i.e. if total load is 11200 lbf (= 5 tonf) and there are 44 bolts,

If the end closures act in the same way as the cylinder,

max load/bolt = 254 lbf

$\therefore$ max pressure = 38.6 lbf/in^2

APPENDIX 6

Calculation of Stresses to Produce Test Elastic and Creep Strains (Section 7.4.4)

Let meridional stress = σ_1, hoop stress = σ_2, radial stress = σ_3

If thin shell, $\sigma_3 = 0$ Let $\sigma_2 = \alpha \sigma_1$

Elastic meridional strain $\varepsilon_{1e} = \frac{1}{E}\left[\sigma_1 - \nu(\sigma_2 + \sigma_3)\right] = \underline{\underline{\frac{\sigma_1}{E}(1 - \nu\alpha)}}$ (A.6.1)

Equivalent stress (Von Mises) $\sigma_e = \frac{1}{\sqrt{2}}\sqrt{(\sigma_1 - \sigma_2)^2 + (\sigma_2 - \sigma_3)^2 + (\sigma_3 - \sigma_1)^2}$

$$\therefore \quad \underline{\underline{\sigma_e = \sigma_1\sqrt{1 - \alpha + \alpha^2}}} \qquad (A.6.2)$$

Equivalent creep strain $\varepsilon^* = A\,\sigma_e^{\,n}\,t^s$ (the creep law given in Chapter 3)

$$\therefore \quad \varepsilon^* = A\,\sigma_1^{\,n}\,(1 - \alpha + \alpha^2)^{\frac{n}{2}}\,t^s \qquad (A.6.3)$$

Meridional creep strain $\varepsilon_{1c} = \frac{\varepsilon^*}{\sigma_e}\left[\sigma_1 - \frac{1}{2}(\sigma_2 + \sigma_3)\right]$

$$\therefore \quad \underline{\underline{\varepsilon_{1c} = At^s\,\sigma_1^{\,n}\,(1 - \alpha + \alpha^2)^{\frac{1}{2}(n-1)}(1 - \tfrac{1}{2}\alpha)}} \qquad (A.6.4)$$

From (A.6.1) and (A.6.4)

$$\varepsilon_{1c} = At^s\,\frac{(\varepsilon_{1e}E)^n}{(1 - \nu\alpha)^n}\,(1 - \tfrac{1}{2}\alpha)(1 - \alpha + \alpha^2)^{\frac{1}{2}(n-1)}$$

Hence $$\underline{\underline{\frac{\varepsilon_{1c}}{At^s(\varepsilon_{1e}E)^n} = \frac{(1 - \frac{1}{2}\alpha)(1 - \alpha + \alpha^2)^{\frac{1}{2}(n-1)}}{(1 - \nu\alpha)^n}}} \qquad (A.6.5)$$

At a given point, the L.H.S. of equation (A.6.5) is known, so the corresponding value of α can be determined. Substituting back into equation (A.6.1) will yield σ_1, and hence σ_2.

FIG. A·1

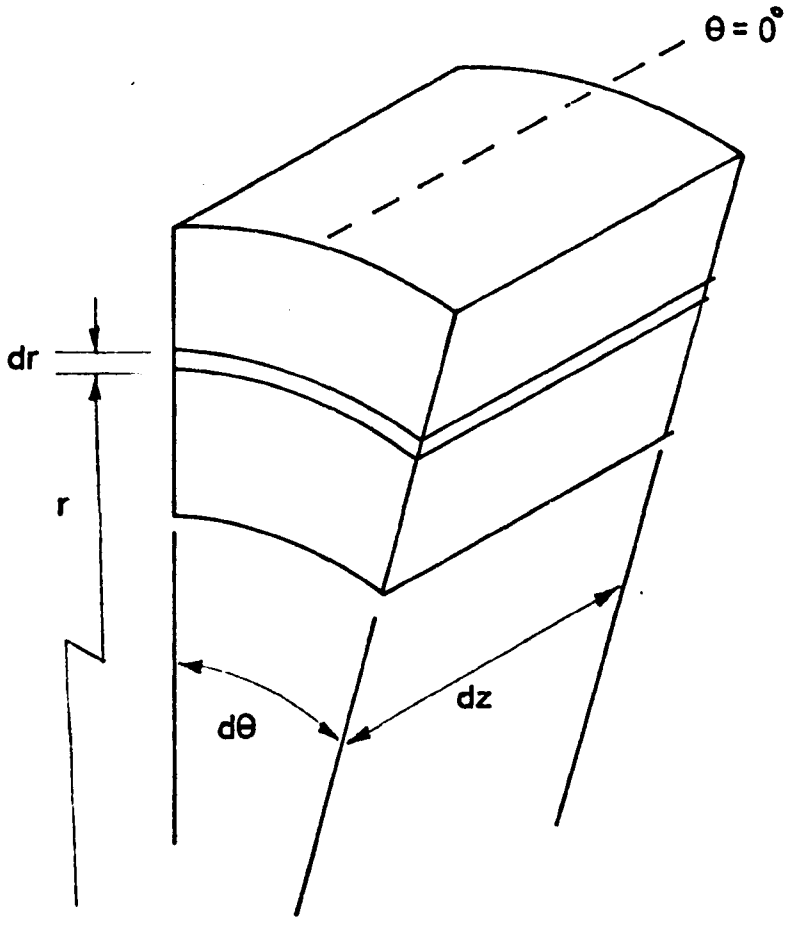
θ = 0°
dr
r
dθ
dz

FIG. A·2

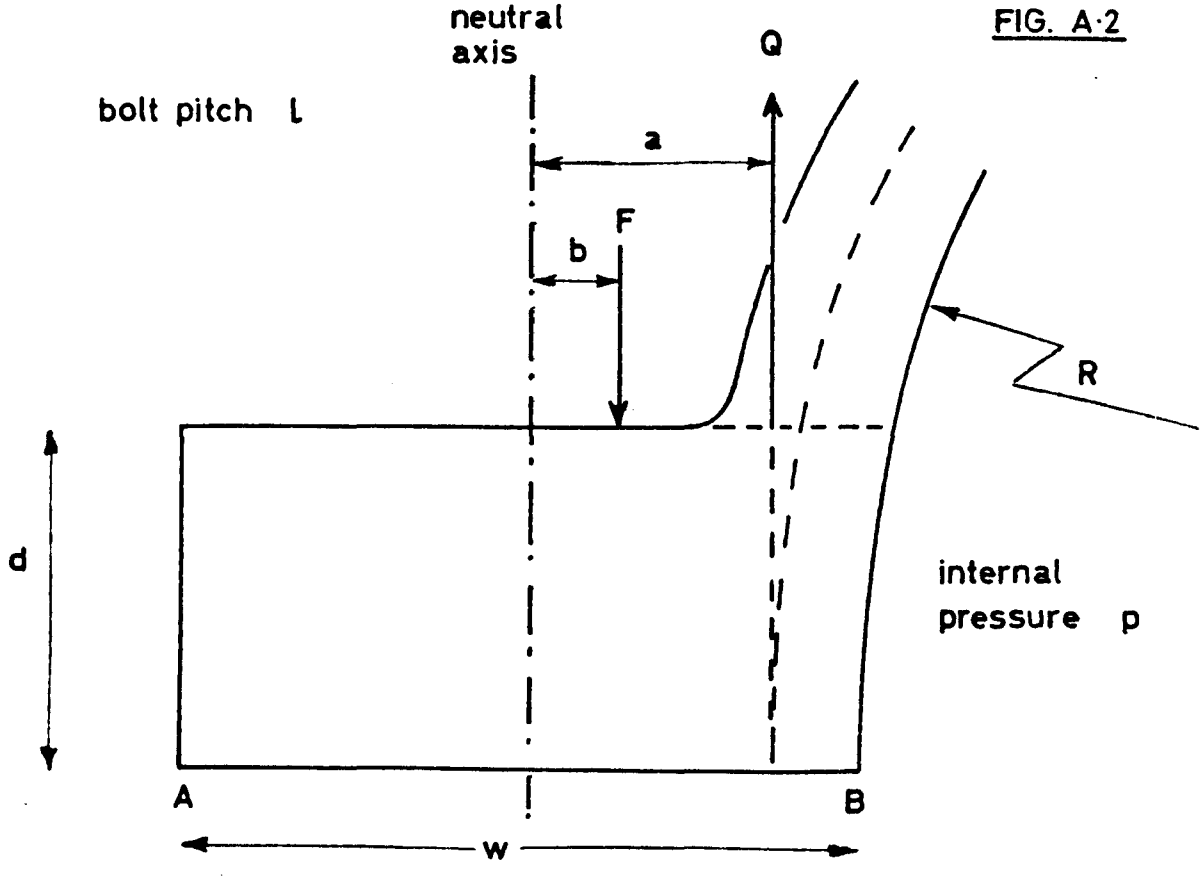
neutral axis
Q
bolt pitch l
a
F
b
R
d
internal pressure p
A
B
w